



HAL
open science

Photodissociation and relaxation dynamics of small Polycyclic Aromatic Hydrocarbon (PAH) monomer and dimer cations stored in electrostatic ion storage rings

Abdulaziz Al Mogeeth

► **To cite this version:**

Abdulaziz Al Mogeeth. Photodissociation and relaxation dynamics of small Polycyclic Aromatic Hydrocarbon (PAH) monomer and dimer cations stored in electrostatic ion storage rings. Physics [physics]. Université de Lyon, 2021. English. NNT: 2021LYSE1115 . tel-03815117

HAL Id: tel-03815117

<https://theses.hal.science/tel-03815117>

Submitted on 14 Oct 2022

HAL is a multi-disciplinary open access archive for the deposit and dissemination of scientific research documents, whether they are published or not. The documents may come from teaching and research institutions in France or abroad, or from public or private research centers.

L'archive ouverte pluridisciplinaire **HAL**, est destinée au dépôt et à la diffusion de documents scientifiques de niveau recherche, publiés ou non, émanant des établissements d'enseignement et de recherche français ou étrangers, des laboratoires publics ou privés.



N°d'ordre 2021LYSE1115

2021

THESE de DOCTORAT DE L'UNIVERSITE DE LYON
Opérée au sein de
L'Université Claude Bernard Lyon 1

Ecole Doctorale 52
ECOLE DOCTORALE DE PHYSIQUE ET D'ASTROPHYSIQUE

Spécialité de doctorat : PHYSIQUE ATOMIQUE, MOLECULAIRE ET OPTIQUE
Discipline : PHYSIQUE

Soutenue publiquement le 08/07/2021, par :
Abdulaziz Al Mogeeth

**Photodissociation and relaxation dynamics
of small Polycyclic Aromatic Hydrocarbon
(PAH) monomer and dimer cations stored in
electrostatic ion storage rings**

Devant le jury composé de :

M. COTTANCIN Emmanuel	Professeur des Universités Université Lyon 1 UMR 5306 - ILM	Président
Mme. DOMARACKA Alicja	Chargée de Recherche CNRS Caen UMR 6252 – CIMAP	Rapporteuse
M. MANIL Bruno	Professeur des Universités Université Sorbonne Paris Nord UMR 7538 – LPL	Rapporteur
M. COTTANCIN Emmanuel	Professeur des Universités Université Lyon 1 UMR 5306 - ILM	Examineur
Mme. JOBLIN Christine	Directrice de Recherche CNRS Toulouse UMR 5277 - IRAP	Examinatrice
M. BERNARD Jérôme	Maître de Conférences Université Lyon 1 UMR 5306 - ILM	Directeur de thèse

Université Claude Bernard – LYON 1

Président de l'Université	M. Frédéric FLEURY
Président du Conseil Académique	M. Hamda BEN HADID
Vice-Président du Conseil d'Administration	M. Didier REVEL
Vice-Président du Conseil des Etudes et de la Vie Universitaire	M. Philippe CHEVALLIER
Vice-Président de la Commission de Recherche	M. Jean-François
MORNEX Directeur Général des Services	M. Pierre ROLLAND

COMPOSANTES SANTE

Département de Formation et Centre de Recherche en Biologie Humaine	Directrice : Mme Anne-Marie SCHOTT
Faculté d'Odontologie	Doyenne : Mme Dominique SEUX
Faculté de Médecine et Maïeutique Lyon Sud - Charles Mérieux	Doyenne : Mme Carole BURILLON
Faculté de Médecine Lyon-Est	Doyen : M. Gilles RODE
Institut des Sciences et Techniques de la Réadaptation (ISTR)	Directeur : M. Xavier PERROT
Institut des Sciences Pharmaceutiques et Biologiques (ISBP)	Directrice : Mme Christine VINCIGUERRA

COMPOSANTES & DEPARTEMENTS DE SCIENCES & TECHNOLOGIE

Département Génie Electrique et des Procédés (GEP)	Directrice : Mme Rosaria FERRIGNO
Département Informatique	Directeur : M. Behzad SHARIAT
Département Mécanique	Directeur M. Marc BUFFAT
Ecole Supérieure de Chimie, Physique, Electronique (CPE Lyon)	Directeur : Gérard PIGNAULT
Institut de Science Financière et d'Assurances (ISFA)	Directeur : M. Nicolas LEBOISNE
Institut National du Professorat et de l'Education	Administrateur Provisoire : M. Pierre CHAREYRON
Institut Universitaire de Technologie de Lyon 1	Directeur : M. Christophe VITON
Observatoire de Lyon	Directrice : Mme Isabelle DANIEL
Polytechnique Lyon	Directeur : Emmanuel PERRIN
UFR Biosciences	Administratrice provisoire : Mme Kathrin GIESELER
UFR des Sciences et Techniques des Activités Physiques et Sportives (STAPS)	Directeur : M. Yannick VANPOULLE
UFR Faculté des Sciences	Directeur : M. Bruno ANDRIOLETTI

بِسْمِ اللَّهِ الرَّحْمَنِ الرَّحِيمِ

{ رَبِّ أَوْزِعْنِي أَنْ أَشْكُرَ نِعْمَتَكَ الَّتِي أَنْعَمْتَ عَلَيَّ وَعَلَىٰ وَالِدَيَّ وَأَنْ أَعْمَلَ صَالِحًا تَرْضَاهُ وَأَدْخِلْنِي بِرَحْمَتِكَ فِي عِبَادِكَ الصَّالِحِينَ }

"My Lord, inspire me to be thankful for the blessings You have granted me and my parents, and to do good deeds that please You; admit me by Your grace into the ranks of Your righteous servants"

"Permetts-moi Seigneur, de rendre grâce pour le bienfait dont Tu m'as comblé ainsi que mes père et mère, et que je fasse une bonne oeuvre que tu agrées et fais-moi entrer, par Ta miséricorde, parmi Tes serviteurs vertueux"

*To the souls of my parents and brother
May Allah have mercy on them*

ACKNOWLEDGMENTS

I would like to express my thanks to all the people who contributed to accomplishing my Ph.D. thesis and all those who shared all the pleasant years in Institut Lumière Matière (ILM), Université Claude Bernard Lyon 1 (UCBL), France, from 2017-2021.

First and foremost, I would like to express my sincere gratitude and my deepest thanks to my supervisor Dr. Jerome Bernard, without whom I would not have completed this research. Thanks for allowing me to join the team, where I certainly acquired enormous skills. There is not enough space here to describe how much I learn from this project. Thanks so much for the consistent support, guidance step by step, and encouragement, kindness, and patience during the running of my thesis work, for the correction of my manuscript, and the care of my living in Lyon (especially le garant de mon logement).

Special thanks to my co-supervisor, Prof. Serge Martin, for his guidance and limitless scientific discussions, and the help through my research work.

I am also grateful to the director of ILM, Prof. Philippe Dugourd, for the support. I am also grateful for all the help and support offered to me by all ILM staff and UCBL. Thanks to Guillaume Montage and other technical staff for their help; thank you to Clothilde as well.

I also express my thanks to our collaborators, Prof. Christine Joblin from UPS-OMP, IRAP, Toulouse, and Prof. Mathias Rapacioli from LCPQ, IRSAMC, Toulouse.

I would like to thank the DESIREE facility staff, Stockholm, Sweden. We had spent a fantastic two weeks conducting a part of experimental work in that beautiful city; many thanks to all people there, especially Dr. Ji Ming Chao and Dr. Naoko Kono, for their help in running the experiment until a late time of night.

Thank you to the Graduate students at ILM, with who I have had pleasant times, especially those in the same office, Sebastien, Marine, Mathilde, Hussein, Lina, Sara, and Katerina. Good luck to all of them in their life.

Finally, I would like to thank my family, brothers, and sisters for their encouragement during difficult times and their unlimited support. Thanks to all my friends, especially Dr. Hamed Algarni, Dr. Mohammad Al-Amri, Magboul Athubiti, Mohammed Alshaharni, Yahya Al-Ammari, Mohammed Al Moghni Alahmari, and others with who I have had unforgettable times during the years.

ABSTRACT

Polycyclic Aromatic Hydrocarbons (PAHs) are ubiquitous complex molecules present in different regions of the universe. They are expected to be possible carriers of the unidentified infrared bands and emitters of the diffuse interstellar bands. The energy relaxation dynamics of such isolated species are of particular interest in understanding their lifetime, stability, and role in the universe. Electrostatic storage devices, such as the Mini-Ring and DESIREE used in the present work have proven to be powerful tools to investigate such isolated molecules over long time observation up to seconds in ultrahigh vacuum. Ion beams of cationic PAH monomers and dimers were produced using electron cyclotron resonance ion sources under special tuning conditions and stored in the two storage rings. The present results about phenanthrene cations confirmed the existence of a fast radiative cooling attributed to recurrent fluorescence. Conversely, for PAH dimer cations, the radiative cooling process is much slower than for monomer cations because of the absence of the recurrent fluorescence process. The photodissociation spectra of dimer cations show two peaks attributed to the charge resonance (CR) and the local excitation bands. These spectra are interpreted using a semi-empirical model and DFTB-EXCI theory. Naphthalene dimer cations were stored up to 30 s in the cryogenic ring DESIREE. The evolution of the CR line was measured as a function of storage time. The time evolution of the center of the CR line is used to estimate the cooling rate of the naphthalene dimer cations.

Key words: PAHs monomer cations, PAHs dimer cations, electrostatic storage devices (ESD), relaxation dynamics, photodissociation, radiative cooling, recurrent fluorescence, internal energy distribution.

Les hydrocarbures aromatiques polycycliques (HAPs) sont des molécules complexes présentes dans différentes régions de l'univers et supposées être à l'origine des bandes infrarouges non identifiées et des bandes interstellaires diffuses. La dynamique de relaxation de ces espèces isolées est d'un intérêt particulier pour comprendre leur durée de vie, leur stabilité et donc leur rôle dans l'univers. Les dispositifs de stockage électrostatique, comme Mini-Ring et DESIREE ont récemment démontré leur efficacité pour étudier ces molécules isolées sur de très longues durées (jusqu'à 1 s). Des faisceaux de monomères et dimères de HAP cationiques ont été produits en utilisant une source à résonance cyclotron électronique, puis stockés dans ces anneaux électrostatiques. Les résultats pour le phénanthrène ont confirmé l'existence d'un refroidissement radiatif rapide attribué à la fluorescence récurrente. Inversement, pour les cations dimères de HAP, le processus de refroidissement radiatif est beaucoup plus lent que pour les monomères en raison de l'absence du processus de fluorescence récurrente pour les dimères. Le spectre de photodissociation des dimères de 400 à 2000 nm contient deux bandes : l'une est attribuée à la résonance de charge (RC), l'autre à l'excitation locale. Ces spectres sont interprétés à l'aide d'un modèle semi-empirique et de la théorie DFTB-EXCI. Les cations de dimère de naphthalène ont été stockées jusqu'à 30 s dans l'anneau cryogénique DESIREE. L'évolution de la bande RC a été étudiée en fonction du temps de stockage. L'évolution temporelle du centre de la bande RC est utilisée pour estimer le taux de refroidissement du dimère de naphthalène cationique.

Mots clés: cations monomères HAP, cations dimères HAP, dispositifs de stockage électrostatique (ESD), dynamique de relaxation, photodissociation, refroidissement radiatif, fluorescence récurrente, distribution d'énergie interne.

RESUME

Les Hydrocarbures Aromatiques Polycycliques (HAP) sont des molécules complexes omniprésentes dans différentes régions de l'univers, en particulier le milieu interstellaire. Elles sont supposés être à l'origine d'émissions infrarouge caractéristiques, comme les bandes infrarouges dites non-identifiées, et de bande d'émission dans le visible, connues sous le nom de bandes interstellaires diffuses. La dynamique de relaxation de ces espèces isolées est d'un intérêt particulier pour comprendre leur durée de vie, leur stabilité et donc leur rôle dans l'univers. Cependant, à ce jour, aucune espèce individuelle n'a été identifiée. L'étude de ces processus, dont certains peuvent être ultra-lents, nécessite une longue période d'observation, permettant aux degrés de liberté interne de ces molécules d'être refroidis par émission radiative vibrationnelle. Les dispositifs de stockage électrostatique ont récemment démontré leur efficacité pour étudier ces molécules isolées sur de très longues durées jusqu'à quelques secondes (voir quelques heures) dans un vide ultra-poussé, dans des conditions contrôlées et compatibles avec celles du milieu interstellaire.

Dans la présente thèse, les anneaux de stockage électrostatique, Mini-Ring et DESIREE, sont utilisés pour étudier de petits monomères et dimères de HAP cationiques. Le Mini-Ring, qui a été construit sur la base du piège linéaire compact, du Conetrap et de l'anneau ELISA, a compilé les caractéristiques des anneaux de stockage et des pièges à faisceau d'ions électrostatiques. En raison de la relative compacité, avec une circonférence d'environ 0,7 m, la courte période de révolution des ions stockés (quelques microsecondes) permet d'échantillonner finement les déclins dus induits par absorption laser, tout en permettant l'étude de la dynamique de refroidissement des ions moléculaires jusqu'à une centaine de millisecondes. Mini-Ring a été principalement utilisé dans le présent travail pour étudier la dynamique de refroidissement des petits HAPs, en particulier les cations phénanthrène et les dimères cationiques du benzène, du naphthalène et du pyrène et pour enregistrer les spectres de photodissociation de ces dimères cationiques. De plus, en raison de la nécessité d'un temps de stockage plus long (jusqu'à quelques secondes) et d'une température cryogénique pour permettre le refroidissement des ions stockés, d'une semaine de temps de faisceau a été utilisée sur l'installation DESIREE pour étudier les dimères cationiques de naphthalène.

Les espèces étudiées (monomères ou dimères de PAH) ont été préparées dans le plasma d'une source d'ion à résonance cyclotron électronique et accélérées à 12 keV et transportées à travers des modules d'optique ionique, puis stockées dans le Mini-Ring pour des temps de stockage jusqu'à 100 ms. Des conditions très spéciales de réglage de la source ECR sont requises pour produire les cations de phénanthrène: une très faible puissance de la microonde et une pression suffisante pour garder le plasma aussi froid que possible. Les conditions pour la production de cations de dimères sont cruciales et très critiques.

Pour l'étude des cations de phénanthrène, les fragments neutres issus des processus de dissociation ont été détectés à chaque tour du paquet d'ions dans le Mini-Ring en fonction du temps de stockage. Durant les premières millisecondes de stockage, l'énergie interne est dissipée soit par dissociation unimoléculaire soit par le processus radiatif de fluorescence récurrente. Le déclin naturel présente trois régions distinctes : au temps courts (1 à 2 ms), la dissociation unimoléculaire domine, puis les processus de dissociation sont réduits, limités par l'influence du refroidissement radiatif rapide dû à la fluorescence récurrente, enfin, le refroidissement radiatif domine et les fragments neutres détectés sont dus aux collisions avec le gaz résiduel.

Pour quantifier les effets de la fluorescence récurrente sur l'évolution de la distribution interne les ions de phénanthrène stockés dans Mini-Ring, on induit des processus de dissociation par absorption laser à différents temps de stockage et avec différentes longueurs d'onde. Les

RESUME

fragments neutres résultants de la dissociation induite par laser donnent des déclin qui sont analysés par deux différentes méthodes. (i) les déclin sont ajustés par des lois de puissance en $t^{-\alpha}$ et donc caractérisés par la “facteur de déclin”, α , qui est étroitement relié à la forme de la distribution d’énergie. Les résultats montrent que le facteur de déclin décroît lorsque la distribution d’énergie interne se décale vers les basses énergies. En comparant les valeurs de α à des temps de stockage différents et pour différentes longueurs d’onde, on a pu estimer que la vitesse de refroidissement est de l’ordre de 100 eV/s (ii) On ajuste les déclin expérimentaux avec des déclin simulés à partir de taux de dissociation connus et d’une fonction gaussienne paramétrée représentant la distribution d’énergie interne. L’énergie au niveau du front descendant (du côté des hautes énergie) de la distribution d’énergie interne diminue régulièrement en fonction du temps de stockage avec une vitesse de refroidissement moyen de l’ordre de 100 eV/s, en accord avec la méthode précédente. Cette vitesse de refroidissement est bien trop grande pour être attribuée au processus classique de refroidissement par émission vibrationnelle dans l’infrarouge, qui est habituellement de l’ordre de quelques eV/s. Ce refroidissement est attribué au processus de fluorescence récurrente pour lequel on a pu calculer un taux d’émission radiative de l’ordre de quelques centaine de s^{-1} , en accord avec les mesures. Les mesures de vitesse de refroidissement pour le cation de phénanthrène sont du même ordre de grandeur que celles obtenues dans des travaux précédents pour, un de ces isomères, le cation d’anthracène.

Dans la deuxième partie de de travail de thèse, nous montrons que les dimères cationiques de PAH se comportent très différemment des monomères. Pour les cations de benzène, de naphthalène et de dimère de pyrène, le déclin naturel ne montre pas de réduction de la dissociation attribuable à un processus de refroidissement radiatif. Ce résultat démontre que le refroidissement radiatif de ces dimères cationiques est beaucoup plus lent que celui des monomères et que les conditions pour la fluorescence récurrente, c’est-à-dire, la possibilité de peupler un état électronique excité stable par l’intermédiaire du processus conversion interne inverse, ne sont pas remplies pour ces dimères.

Les spectres photodissociation de ces trois dimères cationiques ont été enregistrés dans la gamme de 400 à 2400 nm. Deux larges bandes ont été observées dans les trois cas : la bande de résonance de charge (RC) est due à la transition électronique de l’état fondamental vers le premier état excité, et la bande d’excitation locale (EL) est due à la transition électronique de l’état fondamental vers le deuxième état excité.

Pour les dimères de naphthalène, les bandes RC et de EL sont centrées, respectivement, à environ 1 et 2.2 eV. L’énergie de dissociation, estimée à partir de la moitié de l’énergie de la transition RC serait alors de 0,5 eV. Cette valeur est en bon accord avec les travaux expérimentaux précédents, mais pourtant plus faible d’un facteur de 2 par rapport aux calculs théoriques. Ce désaccord peut éventuellement être attribué à des effets de température induisant éventuellement des isomérisations, ou bien, peut-être plus probablement, à une estimation trop grossière de cette valeur par la moitié de l’énergie de transition de la bande RC. D’autres effets peuvent contribuer à une augmentation ou à une diminution de l’écart des niveaux RC, comme par exemple, des effets de polarisation. Un modèle semi-empirique basé sur des potentiels de Morse effectifs a été proposé pour l’interprétation des spectres de photodissociation. On s’attend à ce que ces potentiels effectifs moyennent les effets de température qui entraînent une diminution de la différence d’énergie entre l’état fondamental et l’état excité dissociatif en raison des modes de vibrations de rotation autour de l’axe intermoléculaire des dimères.

Le spectre de photodissociation des dimères cationiques de pyrène a été enregistré, pour la première fois, dans la gamme de 400 à 2000 nm. De manière similaire au cas du naphthalène, deux larges bandes d’absorption ont été observées à 550 (2,25 eV) et 1560 nm (0,79 eV) et sont attribuées respectivement aux bandes LE et CR. Des simulations théoriques réalisées par nos collaborateurs (M. Rapacioli et al. du LCPQ à Toulouse) du spectre d’absorption en fonction

RESUME

de la température. La simulation utilise une approche de type « tight binding » (liaison forte) basée sur la fonctionnelle de la densité incluant un schéma étendu d'interaction de configuration (DFTB-EXCI) pour déterminer la structure électronique. La simulation prend en compte les 5 premiers états excités, non-interdits pour des transitions dipolaires électriques, D_2 à D_6 des monomères et une exploration Monte-Carlo de la surface de potentiel de l'état fondamental. Les simulations montrent trois bandes principales à 1,0, 2,1 et 2,8 eV. Ces résultats permettent d'attribuer la bande expérimentale à 1560 nm à l'absorption par l'état excité de résonance de charge (CR) corrélé avec l'état fondamental du monomère D_0 . La bande à 550 nm est attribuée aux états de dimère corrélés avec les états excités D_2 - D_4 dans du monomère. Les simulations montrent également que la bande CR s'élargit et se déplace vers les plus grandes longueurs d'onde avec une température croissante car la différence d'énergie entre l'état fondamental et le premier état excité dépend des variations de la géométrie en fonction de la température. La comparaison du spectre expérimental avec les spectres théoriques à différentes températures nous a permis d'estimer la température des dimères de pyrène stockés dans Mini-Ring dans la gamme de 300 à 400 K, ce qui est conforme à la température attendue déduite de l'analyse du déclin naturel.

Lors d'une semaine de campagne d'expériences, les dimères cationiques de naphthalène ont été stockés jusqu'à 30 s dans l'anneau cryogénique DESIREE pour enregistrer des spectres de photodissociation. L'évolution de la bande RC a été étudiée en fonction du temps de stockage, donc en fonction de la température car ces longs temps de stockage permettent aux dimères de se refroidir par émission vibrationnelle dans l'infrarouge. L'évolution temporelle de la position du centre de la bande CR a pu être utilisée pour déterminer un taux de refroidissement d'environ $5,2 \text{ s}^{-1}$ pour les dimères de pyrène.

Table des matières

Acknowledgments.....	I
ABSTRACT.....	II
RESUME.....	III
Table des matières.....	I
1 INTRODUCTION.....	1
1.1 Polycyclic Aromatic Hydrocarbons (PAHs).....	2
1.2 The motivation of the present studies on PAHs.....	3
1.2.1 The Interstellar medium (ISM).....	3
1.3 AIBs and DIBs.....	5
1.3.1 Expectations on the size of PAHs.....	6
1.3.2 The Formation of PAHs in space.....	6
1.3.3 Possible role of ionic, fragmented species, dimer, and cluster formation...	11
1.4 Experimental and theoretical Studies on PAHs.....	11
1.5 Electrostatic Storage Devices (ESDs).....	13
1.5.1 Electrostatic storage rings (ESRs).....	14
1.5.2 Electrostatic ion beam traps (EIBTs).....	22
1.6 Conclusion.....	26
2 THEORETICAL BACKGROUND.....	27
2.1 Standard methods in quantum physics and chemistry.....	28
2.1.1 The Schrödinger equation.....	28
2.1.2 Hamiltonian for polyatomic molecules.....	29
2.1.3 Born-Oppenheimer approximation.....	29
2.1.4 Beyond the Born-Oppenheimer approximation.....	31
2.1.5 Electronic transition (photon absorption or emission).....	32
2.1.6 Franck-Condon Principle.....	33
2.1.7 Potential energy surface.....	36
2.2 Theory for dimer cations.....	36
2.2.1 The charge resonance (CR) and local excitation (LE) transitions.....	36
2.2.2 DFTB calculations to account for charge resonance.....	38
2.2.3 Morse PECs and photo-dissociation spectra of PAH dimer cations.....	38
2.3 Statistical Models for the relaxation processes of isolated systems.....	42
2.3.1 RRKM theory.....	42
2.3.2 The microcanonical temperature for small isolated systems.....	43
2.3.3 Relaxation of internal energy.....	44

Table des matières

2.3.4	Recurrent/Poincaré fluorescence.....	48
2.3.5	IR vibrational emission - IR cooling.....	49
2.3.6	Power-law decay	50
2.3.7	Time evolution of the shape of the IED	51
2.4	Decay rates for collision-induced dissociation of stored ions.....	53
2.5	Conclusion	54
3	THE EXPERIMENTAL SET-UP	55
3.1	Principles of magnetic and electric deflection of charged particles.....	56
3.1.1	Deflection via magnetic field.....	56
3.1.2	Deflection via electric field.....	57
3.1.3	Comparison between electrostatic and magnetic rings.....	58
3.2	The Mini-Ring experiment and the beam-line.....	59
3.2.1	General overview of the experimental set-up	59
3.2.2	ECR ion sources.....	60
3.2.3	Transport beam line	66
3.2.4	The Mini-Ring.....	69
3.3	Laser Equipment	77
3.3.1	General description of the laser system	78
3.3.2	Setting the overlap between the laser beam and stored ions.....	81
3.4	Timing of the experiment.....	84
3.4.1	Storage sequence.....	84
3.4.2	Time structure of recorded neutral fragments.....	84
3.5	Computer control and Data acquisition	85
3.5.1	The National Instruments PCI (NI-6229)	85
3.5.2	Time to digital converter (TDC V4)	87
3.6	The experimental set up in DESIREE at Stockholm	88
3.6.1	The Double ElectroStatic Ion Ring ExpEriment, DESIREE	88
3.7	Conclusion	91
4	PRODUCTION OF ION BEAM OF PAHs	92
4.1	Short review of different ion sources for the production of PAH and PAH dimer cations in the gas phase	92
4.2	General source conditions inside the ion source.....	93
4.2.1	Roles of HF power and pressure	93
4.2.2	Estimation of the pressure inside the ion source.....	94
4.3	Production of ion beams of phenanthrene monomer cations.....	95
4.4	Production of ion beams of dimer cations	97
4.4.1	Dimers of naphthalene	98

Table des matières

4.4.2	Dimers of pyrene.....	99
4.4.3	Dimers of benzene	100
4.5	Possible mechanism of formation of dimer cations of PAHs	101
4.6	Conclusion	102
5	EXPERIMENTAL RESULTS OF PHENANTHRENE MONOMER CATIONS	103
5.1	The natural decay of monomer phenanthrene cations	103
5.2	Laser-induced dissociation.....	105
5.3	Time evolution of the internal energy distribution	107
5.3.1	Energy Distribution of ions.....	107
5.3.2	Time and energy window.....	108
5.3.3	Modeling the neutral yield	112
5.3.4	Experimental Laser-induced decay curves	114
5.3.5	Determination of the energy shift rate using photon energies	116
5.3.6	Time evolution of HEE of the IED	118
5.3.7	The measured population decay rate.....	120
5.4	Conclusion	123
6	EXPERIMENTAL RESULTS FOR DIMER CATIONS	124
6.1	The natural decay of cationic dimers	125
6.2	Prompt dissociation.....	128
6.3	Dissociation pathway - Coincidence experiments	130
6.4	Experimental photodissociation spectra of cationic dimers.....	131
6.4.1	Method	131
6.4.2	Cationic dimers of Naphthalene.....	132
6.4.3	Cationic dimers of benzene.....	134
6.4.4	Cationic dimers of pyrene	137
6.5	Semi-empirical Modelling	138
6.5.1	Cationic dimers of naphthalene.....	138
6.5.2	Cationic dimers of benzene.....	141
6.6	Results of DFTB-EXCI Modelling for pyrene dimer cations.....	143
6.6.1	The photo-absorption spectrum	143
6.6.2	Photo-absorption spectra dependence on temperature.....	144
6.6.3	The potential energy surfaces in reduced dimensionality.....	145
6.6.4	Comparison of the theoretical absorption spectrum with the experimental photodissociation spectrum	146
6.7	IR radiative cooling of the dimer of naphthalene at DESIREE	147
6.8	Fragmented dimer cations	149
6.9	Conclusion	151

Table des matières

7	CONCLUSION AND OUTLOOK.....	152
	Bibliography.....	155

1 INTRODUCTION

1	INTRODUCTION	1
1.1	Polycyclic Aromatic Hydrocarbons (PAHs)	2
1.2	The motivation of the present studies on PAHs	3
1.2.1	The Interstellar medium (ISM)	3
1.3	AIBs and DIBs	5
1.3.1	Expectations on the size of PAHs	6
1.3.2	The Formation of PAHs in space	6
1.3.3	Possible role of ionic, fragmented species, dimer, and cluster formation... 11	11
1.4	Experimental and theoretical Studies on PAHs	11
1.5	Electrostatic Storage Devices (ESDs)	13
1.5.1	Electrostatic storage rings (ESRs)	14
1.5.2	Electrostatic ion beam traps (EIBTs)	22
1.6	Conclusion	26

The purpose of the present thesis work is inscribed in general studies on polycyclic aromatic hydrocarbons (PAHs) that have some relevance in astrophysics. The energy relaxation dynamics of phenanthrene cations and the photo-dissociation spectroscopy of two PAH dimer cations (naphthalene and pyrene) and benzene dimer cations have been studied using electrostatic ion storage rings, the Mini-Ring for the major part of this work, and DESIREE for naphthalene dimer cations only. PAHs are presently considered as the most probable carriers of some astrophysical spectral signatures, known as the aromatic infrared bands (AIBs), which correspond to emissions from their typical stretching and bending vibration modes and are possible carriers for the UV-visible diffuse interstellar bands (DIBs). The origin, formation, growth, destruction, stability, and role of such complex species in the universe has motivated various experimental and theoretical studies over decades in order to investigate and understand their intrinsic features. Gas-phase experiments at cryogenic temperatures would be ideal to study isolated systems in absence of interaction with the environment and to investigate some of the astrophysical-related processes in conditions that are relevant for astrophysics. Studying such processes require long observation timescales up to seconds, allowing for quantitative investigations on ultra-slow processes such as the cooling dynamics. The cooling dynamics plays an important role in the stability of PAHs and their dimers. The possible presence and relative abundance of PAHs and their dimers in the interstellar medium (ISM) are conditioned by the competition between radiative cooling and dissociation. These studies should be carried out under controlled physical conditions, e.g., temperature, pressure, radiations, etc., that are compatible with those in interstellar space. Hence, electrostatic storage devices have been utilized to respond to most of the needs to study such ions over long timescales.

The present work is focused on studying the stability and formation processes of PAHs and their dimer cations after absorbing a photon. The energy relaxation processes such as the

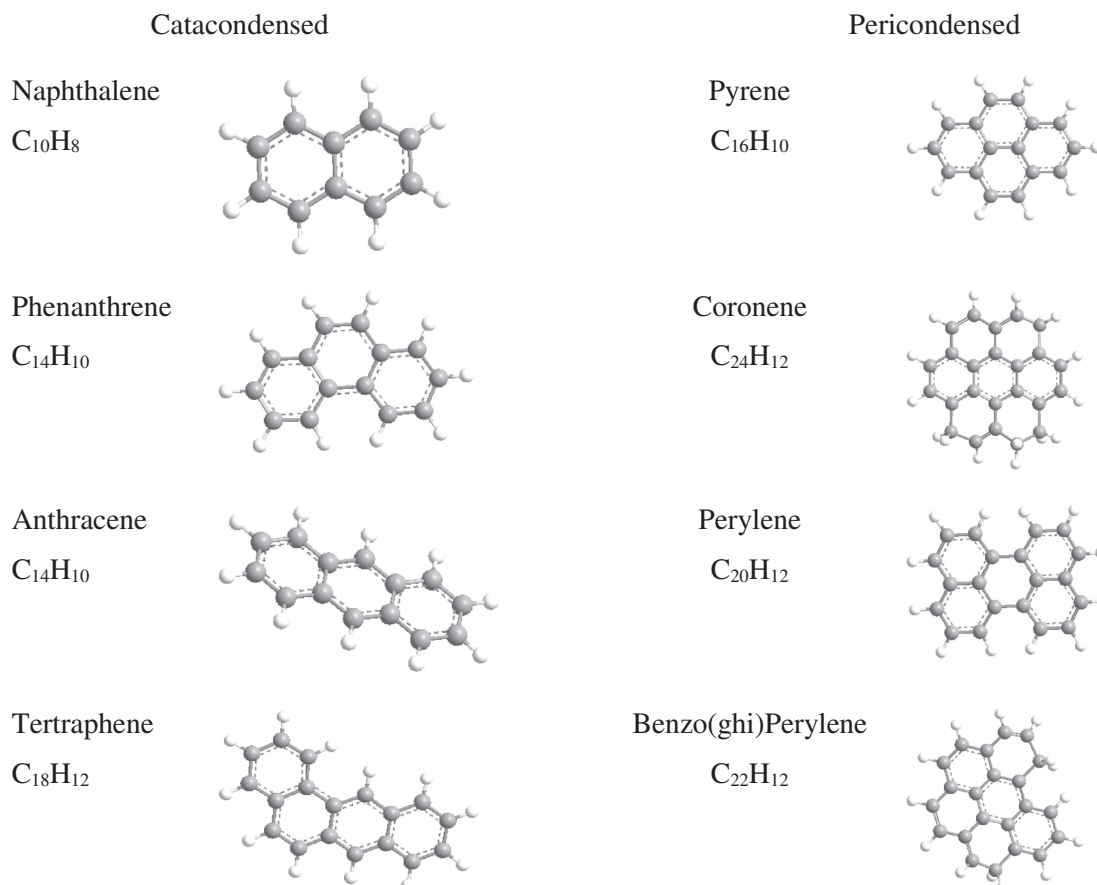
INTRODUCTION

cooling dynamics and photodissociation of the stored molecular ions are studied. The laser probing technique is employed to study the time evolution of the internal energy distribution of PAHs, and the action spectroscopy technique is also used to give information on the cooling rates.

The present chapter is divided into three sections. The first section is to provide a brief introduction to polycyclic aromatic hydrocarbons (PAHs). The general motivation of the present study, essentially related to astrophysics and astrochemistry considerations, is presented in the second section of this chapter. Whereas the third section deals with electrostatic storage devices as powerful tools for studying isolated ions in the gas phase on long time ranges.

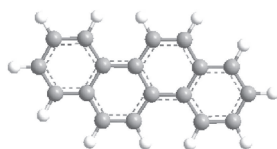
1.1 Polycyclic Aromatic Hydrocarbons (PAHs)

Polycyclic Aromatic hydrocarbons molecules (PAHs) designate a family of planar molecules that are composed of carbon and hydrogen atoms with two kinds of characteristic lattice structures of multiple fused benzene rings. In peri-condensed structures, carbon atoms can be shared by more than two rings, whilst in the cata-condensed structures, each carbon atom can share no more than two rings. These rings are resulting from the overlap between π electrons on adjacent carbon atoms to form π bonds. This leads to the delocalization of electrons above and below the molecular plane, which has an important role in the stability of PAHs. Figure 1-1 shows several members of the PAH family in both structures [1,2]. Another family of molecules tightly related to PAHs is fullerenes, e.g., the quasi-spherical C_{60} molecule, which is only made of carbon atoms. In addition, one or more of the carbon atoms in PAHs can be replaced by other atomic species, e.g., N or O, and can have the same aromatic properties [3]. Benzene (C_6H_6) is not considered a member of the PAH family since it is not polycyclic. However, as it is the elementary brick of PAHs, it is worthy to investigate this molecule in the present thesis work.



INTRODUCTION

Chrysene
 $C_{18}H_{12}$



Antanthrene
 $C_{22}H_{12}$



Figure 1-1: Examples of peri-condensed and cata-condensed PAHs.

Over the last three decades, many experimental and theoretical studies have been focused on studying these PAH molecules because of their possible astrophysical relevance. Many laboratory studies about their physical-chemistry properties (absorption lines and cross-sections, dissociation rates, etc.) [4–10] were carried out to evaluate if they could be considered as possible candidates for the AIBS and DIBs. It was also important to determine in which astrophysical and astrochemical environments these species could be formed and survive despite the presence of X, UV, or other cosmic radiations.

1.2 The motivation of the present studies on PAHs

1.2.1 The Interstellar medium (ISM)

In space between stars and galaxies, gas and dust constitute a gaseous matter, which is subject to constant bombardments by cosmic rays and electromagnetic radiations. These matter and radiations are the main components of the ISM. The dominant sources of energy mainly come from the radiation of stars [1].

The ISM is thought to be filled by hydrogen and helium gas and other small amounts of heavier atoms of carbon, oxygen, and nitrogen, etc., that can be in neutral, ionized, or molecular form in the gas phase or may also form small solid particle less than one micrometer in size (grains) [11].

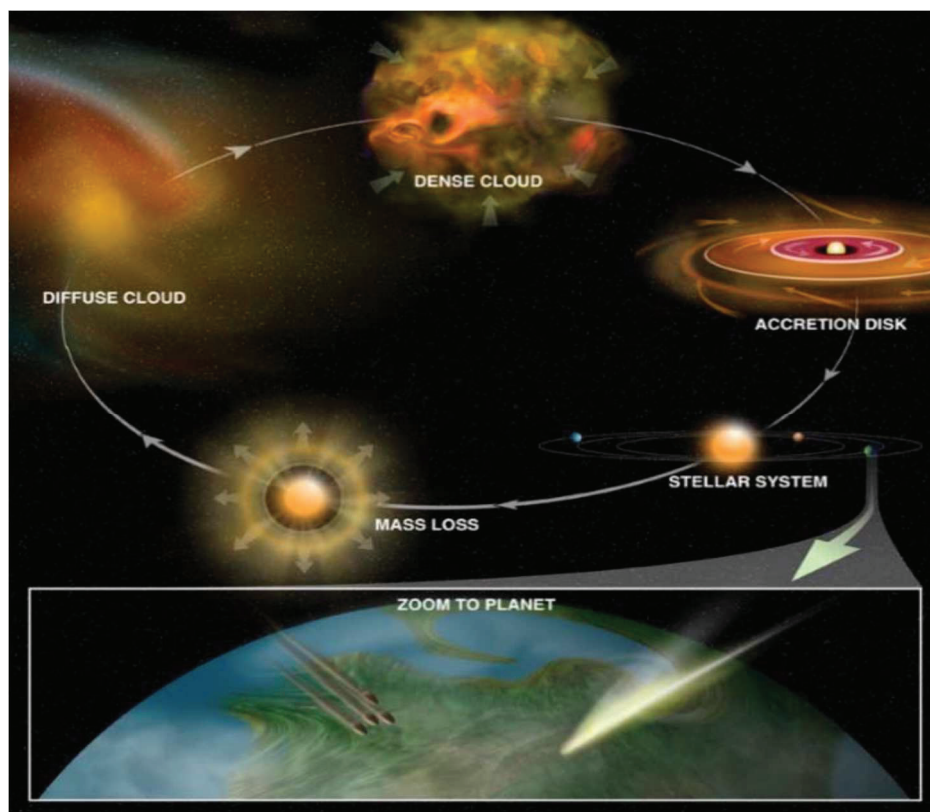


Figure 1-2: The cosmic chemistry cycle Credit: Bill Saxton, NRAO/AUI/NSF [12].

The coldest phase of the ISM, which has a central role in the evolution of galaxies, can be quite classified into four different regions. These regions are diffuse atomic, diffuse molecular,

INTRODUCTION

translucent, and dense molecular clouds. Therefore, ISM is not homogenous, and each region has its own specific features, e.g., density and temperature. For example, the density is varied from the least dense region, the diffuse atomic regions, to the diffuse molecular clouds up to the densest region, dense molecular clouds. The typical densities of diffuse and dense molecular clouds are estimated to be in the range of the order of $100\text{-}500$ and $10^4 - 10^6$ atoms and molecules per cm^3 , respectively, while the temperatures are in the range of several tens of K, i.e., $30\text{-}100$ K, $10\text{-}50$ K, respectively. UV photons play a significant role in the physics and chemistry of diffuse clouds by ionizing and exciting the present molecular species [13].

It is rather challenging to identify the molecular species in the different regions of the ISM since it is expected that more than 200 molecular species comprised of more than 16 different atoms can be present. In order to achieve this goal, observational absorption or emission spectroscopy can be performed in different spectral ranges. Atoms or molecules may be identified via their electronic transitions in the UV/visible ranges or, for molecules, via their rovibrational transitions in the range IR or their rotational transitions in the radio-wave range [13,14].

Several processes such as ionization, the substitution of various atoms, and excitation, as well as the physical conditions such as density, temperature, and radiation fields, can affect the intrinsic properties of complex species such as PAHs. Depending on local conditions, the formation of species can occur in different environments. The ISM provides favorable environments in which PAHs might be formed. Figure 1-2 shows how such complex species can be synthesized in the ISM and also shows how such molecules are delivered to planets via meteorites or comets. In the lifecycle of the ISM, which starts with the injection of gas and dust either as wind or an explosion of stars at the end of their life, materials often circulate between diffuse phases and molecular clouds, and each of these regions in the lifecycle of the ISM has distinctive species, as shown in examples of Figure 1-3 [15,16].

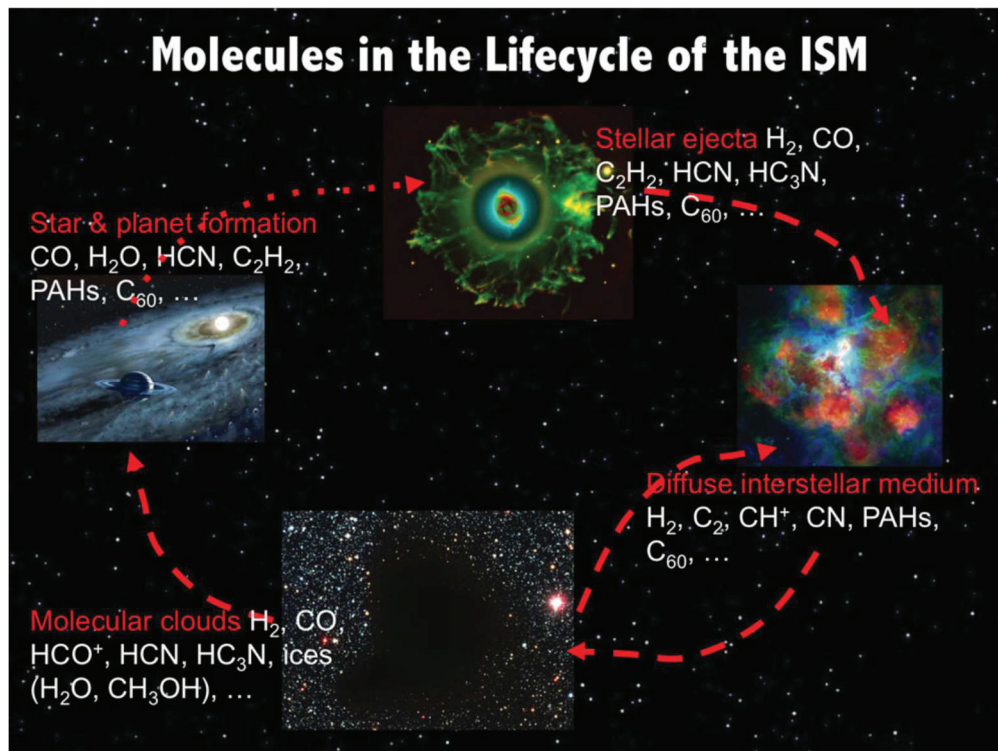


Figure 1-3: The lifecycle of molecules in the ISM [15].

Besides, PAHs may be considered as very abundant complex species in different regions of space with a relative abundance up to 10^{-7} of that of hydrogen nuclei, such as in star-forming regions where they give bright IR bands. When irradiated by young massive stars, they are expected to play a significant role in the heating of neutral gas, the ionization balance, and the

INTRODUCTION

ion-molecule chemistry in molecular clouds [17]. Consequently, PAHs are used as tracers of galactic star formation in both local and distant universe, implying that PAHs may have a significant role in the evolution of galaxies [17]. Figure 1-4 shows an example of a picture taken by the Spitzer space telescope of the Orion region where massive stars are formed and PAHs are expected to be abundant. Moreover, PAHs are thought of having a role in the origin of life as plausible prebiotic membrane components [18] and as precursors of biogenic molecules [19].

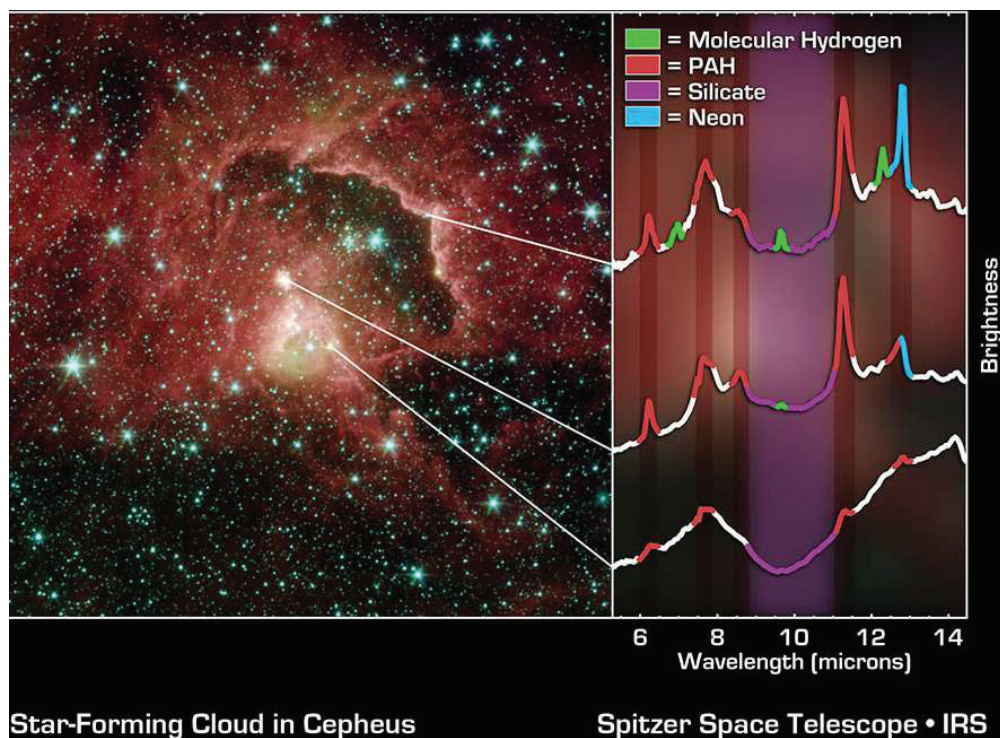


Figure 1-4: The presence of PAHs in the Orion region where massive stars are formed [20].

1.3 AIBs and DIBs

The first infrared (IR) emission spectra of astrophysical objects are dated back to the year 1973 [21]. Since then, several astronomical observations have been performed: spectrophotometric observations of the planetary nebulae NGC 7027 and BD+30° 3639 and NGC 6572 in the range of 8-14 μm and 4-8 μm [21,22], spectra of the nuclear region of the galaxy M82 and the starburst galaxy NGC 253 in the range of 8-13 μm [23], a spectrum of the emission of red rectangular nebula HD 44179 in the range of 8-13 μm [24], and spectrum of the planetary nebulae NGC 7027 in the range of 2-14 μm [22]. These observations have shown intense emission peaks at 3.3, 6.2, 7.7, 8.6, 10, 11.3, and 12.7 μm and other weak bands in a wide variety of objects, such as HII regions, planetary nebulae, reflection nebulae, young stellar objects, nuclei of galaxies and post-asymptotic giant branch Objects (AGB). These spectral bands were called the unidentified infrared emission bands (UIR) because their identification was unclear for several years. Many studies have been conducted to identify which kinds of species could be the possible carriers of these bands. In 1980, Dwek et al. [25] proposed that small hot grains were probably contributors to such emission bands. Soon after, in 1981, Duley and Williams [26] suggested that these emission bands were due to hydrogenated carbon grains. After that, in 1984, PAHs and PAH-like species have been proposed to be responsible for these emission bands [27]. In 1985, Allamandola et al. [28] proposed to attribute these emission bands to a set of partially hydrogenated, positively charged PAHs. Such investigations have led to the so-called PAH hypothesis. Several energetic arguments have supported this PAH hypothesis, including the high feature to continuum ratio that indicates the molecular origin, the low heat capacity of molecules and their stability even after single-photon absorption, the correlation that exists between the different features, and the characteristic C-C and C-H vibrational modes of these species [17,27,28]. Figure 1-5 shows the IR emission spectra of the planetary nebula NGC

INTRODUCTION

7027, the Orion Bar nebula H2S1, and the nuclear region of NGC 4536 and associated vibrations. These IR spectra present very similar features that can be attributed to the C-C and C-H vibrational modes of PAHs. These characteristics emission spectra bands referred to as the aromatic infrared bands (AIBs) have been observed in various locations of the ISM. Therefore, it is expected that the presence of PAHs is ubiquitous in the ISM.

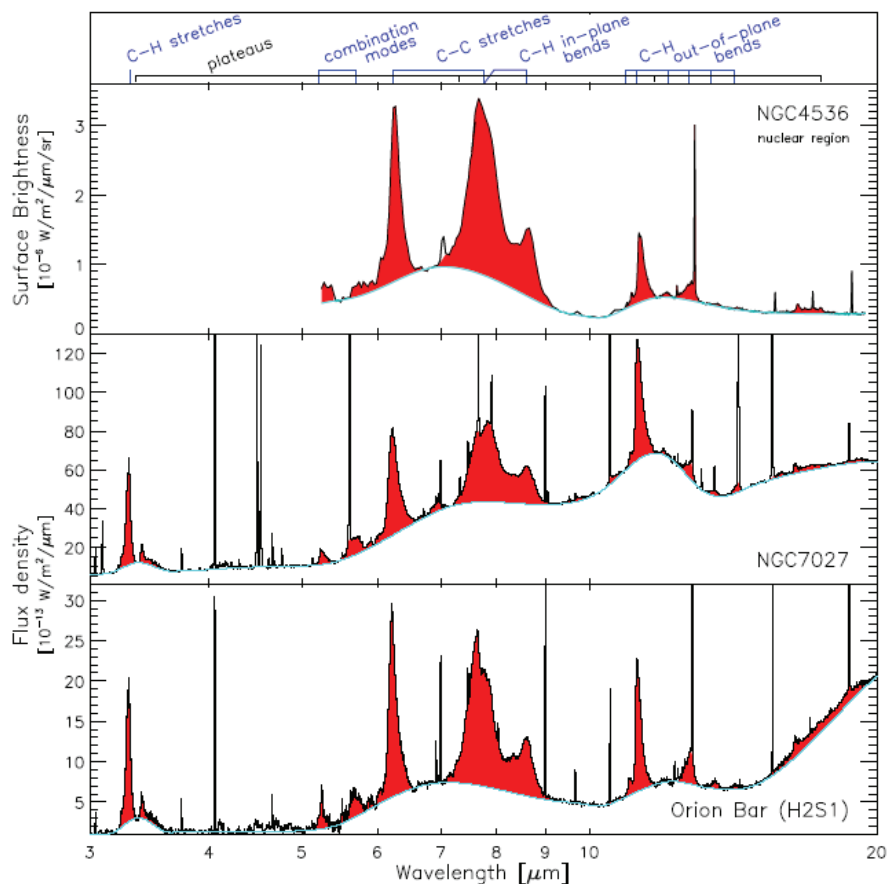


Figure 1-5: Mid-infrared emission from NGC7027, the Orion Bar nebula (H2S1), and the nuclear region of NGC 4536. Main bands have been attributed to C-C and C-H vibrational modes of PAHs [29].

Furthermore, Diffuse interstellar bands (DIBs) are astronomical absorption bands, which are associated with the diffuse phase of the ISM and were discovered about a century ago [30]. Several hundred bands have been observed in the UV, visible, and IR wavelengths. The origin of these bands is still not precisely identified. One of the possible candidates molecular of these bands is the PAH family [31]. Recently, the C_{60}^+ was identified as the carrier of several DIBs [32]. Figure 1-6 displays the extinction curve in the wavelength range 1.5-1.75 μm^{-1} , showing several strong DIBs.

1.3.1 Expectations on the size of PAHs

The question about the size of PAHs has been addressed by a systematic theoretical study of the intensity ratios of the 3.3 and 11.2 bands compared with astronomical observations. The typical size of PAHs has been estimated to be in the range of 50-150 carbon atoms [15,33]. PAHs with a size of less than 50 carbon atoms are expected to be destroyed by UV-photon absorption because of their low heat capacity [34]. The formation of PAHs is still a matter of ongoing research. In the next sections, some studies about the formation of PAHs in the ISM are briefly presented to give a general idea about possible involved mechanisms.

1.3.2 The Formation of PAHs in space

Over the last decades, various studies were performed to get more understanding of the formation of PAHs and their role in astrophysical environments. However, their possible

INTRODUCTION

formation pathways are still elusive. The proposed models can be separated into two categories: the bottom-up and the top-down routes. The first one implies gas-phase chemical reactions between small molecules to form benzene and heavier PAH compounds. The latter one implies the formation of grains, where chemical reaction would occur to form the PAHs and evaporation or detachment of PAH compounds from the grains due to cosmic rays, X, UV, etc., irradiations.

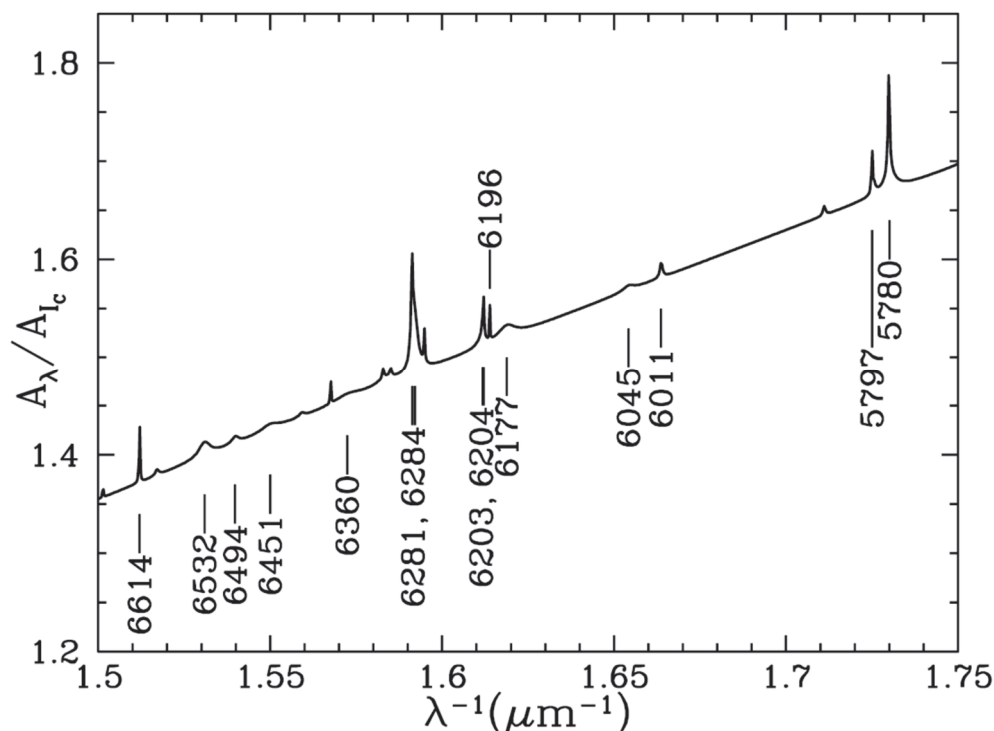


Figure 1-6: DIBs in the 5700-6670 Å region [35].

1.3.2.1 The bottom-up route

Frenklach and Feigelson [36] firstly investigated the formation and growth of PAHs in circumstellar envelopes that can be found in the vicinity of red giant stars using chemical networks that apply to combustion. In these environments, the acetylene abundance is expected to be rather high in a region where temperature can be of about 1000 K. This was expected to provide a suitable environment for the formation of PAHs. In this work, Frenklach and Feigelson involved approximately 100 reactions and 40 molecular species. Figure 1-7 illustrates carbon particles that are thought to be formed in the outflow of carbon stars where small carbon chains, e.g., acetylene, form PAHs which nucleate in turn into larger and clusters PAHs and, eventually, into grains.

Two probable chemical routes have been suggested to lead to the formation of the benzene ring, which is the elementary brick of the PAHs family. The first possible route (route A in Figure 1-8) can begin with an isomerization reaction of acetylene, leading to the formation of vinylidene. Then, vinylidene can react with acetylene again. Next, by eliminating hydrogen and adding another acetylene, benzene may be formed. The abstraction of hydrogen from benzene can then form the phenyl radical, which may react with acetylene to grow further up to the formation of a second cycle (after several reactions). A second possible route can begin with a 3-body reaction between three acetylene molecules leading to the formation of two propargylic radicals, which react with each other to form the phenyl radical [37], as displayed in route B in Figure 1-8.

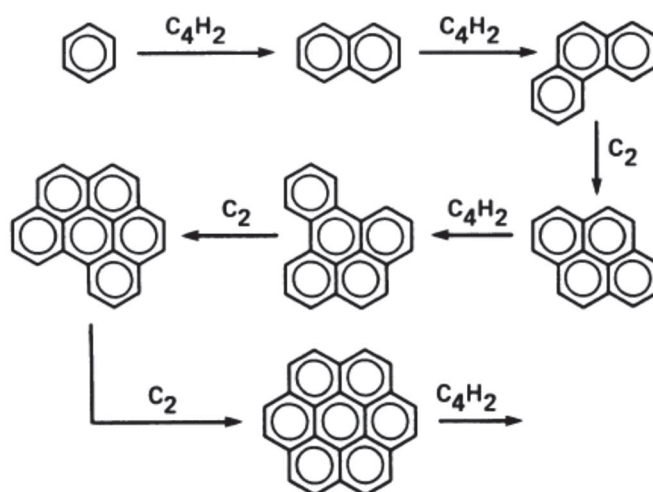


Figure 1-9: The first six members of the high-temperature PAH polymerization route [40].

In another possible mechanism, which is known as HACA, the growth of PAHs can be mainly explained by the hydrogen abstraction-acetylene addition mechanism proposed by Frenklach et al. [42]. In this multistep reaction, an aromatic radical reacts with acetylene radical which is followed by an abstraction of H_2 . A second acetylene molecule can be then added to the ring, followed by ring closure, as shown in Figure 1-10.

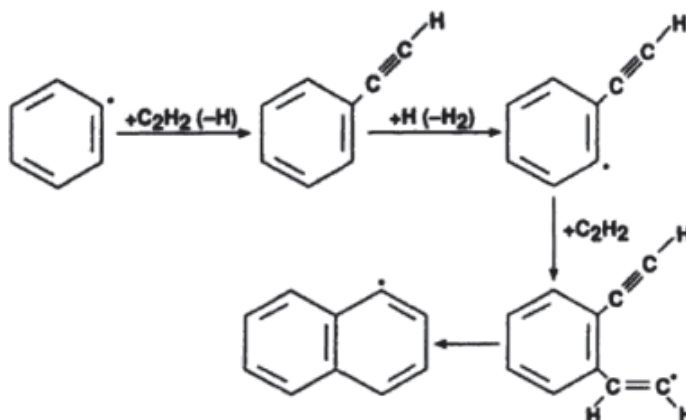


Figure 1-10: Growth of PAHs via (HACA) mechanism, the H abstraction $-C_2H_2$ addition, proposed by Frenklach et al. [42]. Reproduced from [43].

Sabbah et al. [44] studied the role of PAHs in the formation of soot. They show that small clusters of PAHs cannot form initial nuclei in soot formation of hydrocarbon combustions and the formation of carbonaceous particles in astrophysical environments.

Ions are not expected to be present in high quantities in the envelopes of red giant stars. However, in other regions of the ISM, the situation might be different due to the presence of UV light. In this case, ionized or dehydrogenated PAHs may play a significant role in the further growth of PAHs, possibly via the formation of dimers, small clusters up to very small grains (VSG) [45].

Rapacioli et al. [46] and Berne et al. [47] have studied the AIBs in photo-dominated regions, so-called photo-dissociation regions (PDRs) where stars emit the UV photons that excite PAHs. They derived limited sets of the mid-IR emission spectra attributed to neutral PAHs, cationic PAHs, and VSGs, as shown in Figure 1-11 [48]. They concluded that the production of free PAHs could be via the destruction of very small grains (VSGs) when they are irradiated by a UV photon. For this reason, Rapacioli et al. have suggested PAHs to be constituents of these VSGs.

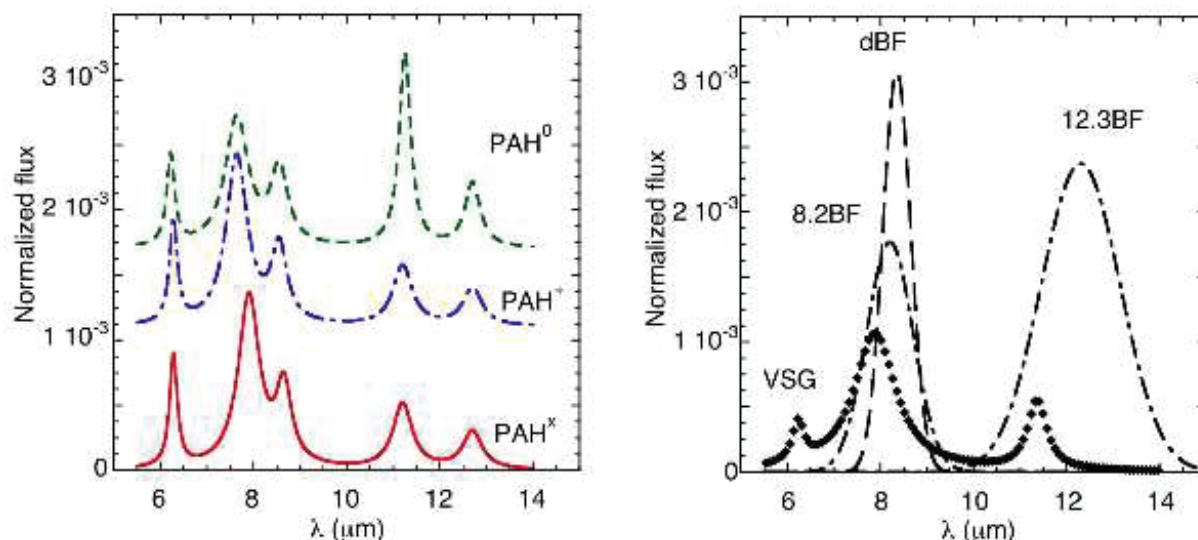


Figure 1-11: The left panel displays various PAH populations: neutral PAHs (PAH^0), ionized cationic PAHs (PAH^+), and large ionized species only clearly observed in highly UV-irradiated environments (PAH^x). The right panel shows the spectrum from VSGs after continuum subtraction and some broad features that are only observed in specific classes of objects: the broad features at 8.2 and 12.3 μm in PNe (8.2 BF and 12.3 BF), and the feature at 8.3 μm (dBF) in disks. Reproduced from [48].

1.3.2.2 Polymerization route

Mukherjee et al. [49] have studied PAHs using high-temperature pyrolysis of pyrene and concluded that direct polymerization and cyclodehydrogenation should be the most important growth pathways. This then led to suggest that soot formation could result from direct polymerization via the initial formation of dimers of PAHs rather than by acetylene addition. Figure 1-12 shows the growth of PAHs via the dimerization and coalescence of PAHs.

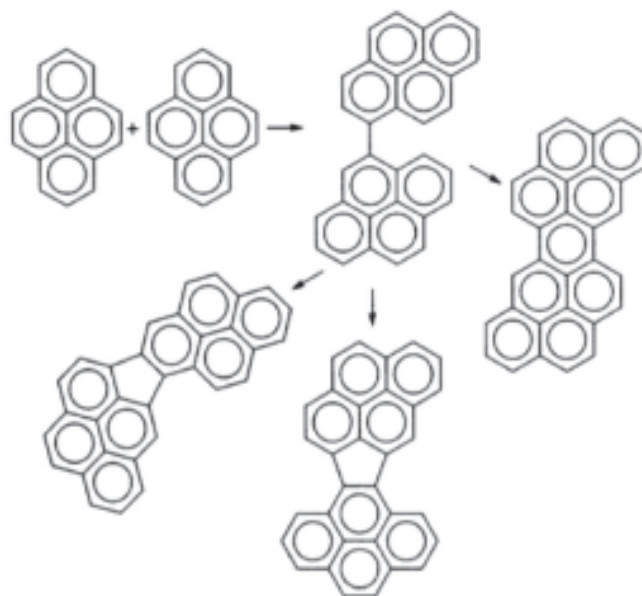


Figure 1-12: Illustration of the growth of PAHs via the dimerization and coalescence of PAHs proposed by [49]. Reproduced from [43].

1.3.2.3 Top-down route

P. Merino et al. [50] have presented recently a new efficient mechanism based on top-down route for the growth of PAHs in red giant stars via the hydrogen processing of SiC dust grains, as can be schematically illustrated in Figure 1-13. They suggested that aromatic species can be formed on the graphitized surface of the abundant silicon carbide stardust upon exposure to atomic hydrogen under conditions similar to those encountered in these environments.

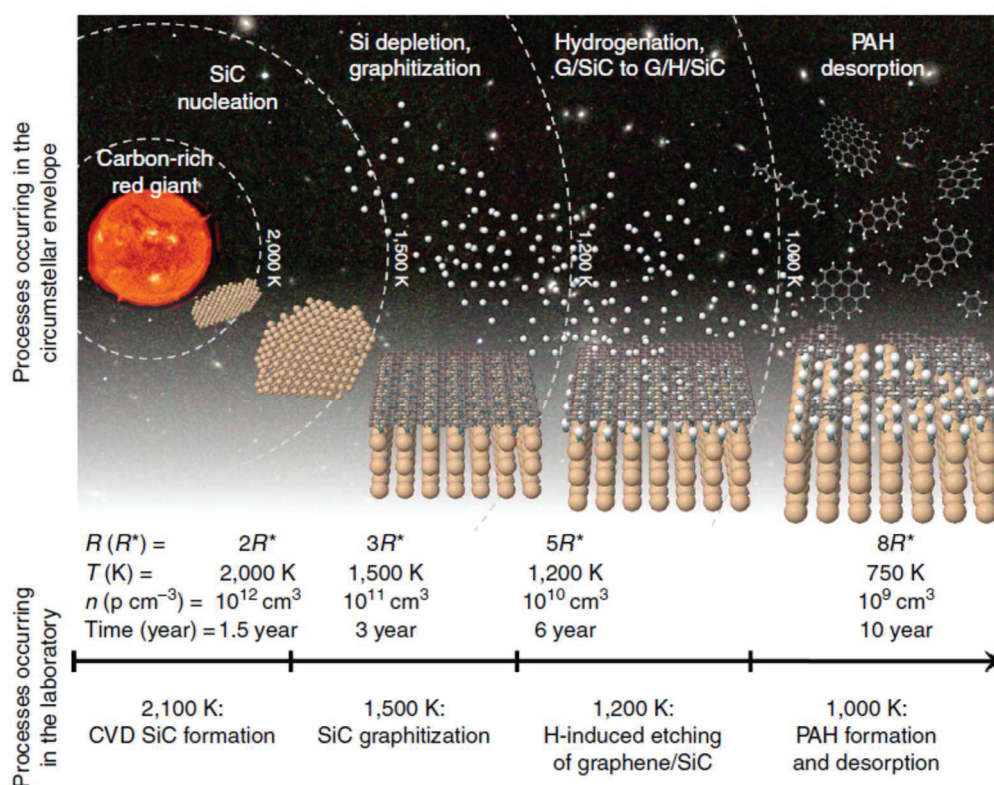


Figure 1-13: Illustration of the four different stages of the formation of PAHs in ISM. (1) The formation of SiC in the gas phase and condensation into μm and nm -sized grains ($T=2000 \text{ K}$; $1-5 R^*$). (2) The annealing of the SiC dust grains to the proximity of the star and the consequent promotion of the surface C-rich phases and graphene ($T=2000-1500 \text{ K}$; $1-5 R^*$). (3) The exposure of the surface to atomic hydrogen, promoting graphitization of the C-rich surface and H passivation of the underlying buffer layer ($T=1500-1200 \text{ K}$; $5-20 R^*$). (4) Etching of the graphene by atomic hydrogen and thermally assisted desorption of PAHs ($T=1200-1000 \text{ K}$, $5-20 R^*$) [50].

1.3.3 Possible role of ionic, fragmented species, dimer, and cluster formation

The PAH population in the ISM is expected to be affected by physical conditions. The dissociation and ionization processes caused by UV photons are expected to compete with recombination with electrons and interaction with gas-phase molecules. Consequently, PAHs are possibly in different states of charge, hydrogenation, dehydrogenation states based on the environments [51,52].

One speculative question is to what extent ionic, fragmented species as well as dimers, and other clusters have a possible role in the growth of PAHs in space, and what is the role of dimers and clusters as precursors of very small grains. Indeed, long-range interactions attractive force between ions and the induced dipole of neutral species may lead to higher cross-sections than neutral-neutral interaction. Therefore, even though these ionic species are in small quantities, their contribution may not be so negligible in the production of clusters because of this higher cross-section. Moreover, ionized fragmented species may also attach to neutral to form new rather strongly bound molecules and contribute to the growth of PAHs [53].

1.4 Experimental and theoretical Studies on PAHs

Over the last decades, numerous observational studies using the Infrared Space Observatory (ISO), Spitzer Space telescope, Midcourse Space Experiment, Infrared Telescope in space missions, but also 8-m class ground-based telescopes such as the Keck Observatory, and very Large Telescope of the European Southern Observatory have been made to study PAHs emission features with a good spectral and spatial resolution in the mid-infrared. The processing, i.e., the formation, destruction, and reactivity of PAHs in the ISM have also been studied. These investigations covered the effects of energetic ion and electron collisions on PAHs in the hot post-shock gas behind interstellar shock waves, in interstellar shock waves,

INTRODUCTION

and the effects of cosmic ray, ion (H, He, CNO, and Fe-Co-Ni), and electron bombardment of PAHs in galactic and extragalactic environments [54,55].

Moreover, various laboratory studies have also been performed to investigate different spectral, physical, and chemical properties such as photolysis, fragmentation, and the evolution of PAHs under conditions similar to those in space.

The unimolecular dissociation of small PAHs has been investigated to measure photodissociation rates. Among others, we may cite: the photofragmentation of anthracene cations irradiated by visible light [9]; the ionization and fragmentation of coronene ($C_{24}H_{12}$), ovalene ($C_{32}H_{14}$), and hexa-peri-hexabenzocoronene (HBC; $C_{42}H_{18}$) cations by exposure to synchrotron radiation in the range of 8–40 eV [56]; the unimolecular dissociation of the pyrene radical cation, $C_{16}H_{10}^{+\bullet}$ [57]; the dissociation of the anthracene radical cation using imaging photoelectron photoion coincidence spectroscopy (iPEPCO) and (APCI-CID); the dissociation of the naphthalene radical cation using tandem mass spectrometry and (iPEPICO) [58,59]; the photostability of a series of PAH cations [60]; the formation of pentalene⁺ in the dissociative ionization of naphthalene [61], etc.

Collision-induced dissociation has been carried out to study the dependence of dissociation channels of PAHs, such as isolated pyrene and coronene molecules, upon their size, the energy, and the nature of colliding particles ions [62]. The effectiveness of molecular hydrogen (H_2) formation from PAHs dissociation is an important issue for astrophysics. It has been investigated by collisions with keV ions, which may induce non-statistical fragmentation, by collisions between (PAH/PAH⁺), by collisions with hydrogen or helium atoms with kinetic energies ranging from 50 eV to 10 keV [63], etc. The latter experiments were made on large cationic PAHs like coronene and *He* atoms, three sets of isomeric of PAHs in collision with *He* at a center-of-mass energy of about 100 eV [64], or by inducing non-statistical fragmentation in PAH-*He* collisions [65]. The dissociation of coronene molecules by stellar wind-like protons was also investigated [66].

Theoretically, many studies have also been done to study different features of PAHs such as dissociation rates of naphthalene cation by RRKM [67] or by density functional theory (DFT) [68], the energies and the fragmentation of neutral and cationic coronene by DFT [69], the interactions of hydrogen and helium atoms with anthracene using molecular dynamic simulation [70], the dissociation of the smallest PAH using DFT [33].

Many models have also been done to study the chemical evolution of PAHs. Bakes et al. [71] have computed the contribution of PAHs and small graphitic grains to interstellar gas heating by the photoelectric effect. Allain et al. [4] have proposed a model, which gave a rather deep view on the stability of interstellar PAHs as a function of their size. Le Page et al. [51] suggested another model which focuses on the charge and hydrogenation states of PAHs in the ISM. Visser et al. [72] proposed a model to describe the evolution of PAHs in protoplanetary disks and the photo destruction of the skeleton of PAHs [73,74]. Montillaud et al. [52] developed a new model that includes multiple-photon events for all photo-dissociation processes and predicted that PAHs smaller than 50 carbon atoms cannot survive in photodissociation regions (PDRs), and carbon clusters could also be end products of PAHs photodissociation.

The stability of PAHs depends on the balance between the dissociation process and radiative cooling. In early models, mid-infrared vibrational emissions were only included. Léger et al. [8,75] considered an additional radiative decay mechanism that would lead to faster radiative cooling, especially at high energies. This mechanism, initially named Poincaré fluorescence, is nowadays referred to as recurrent fluorescence (RF). The first indirect evidence and modeling of this process were reported for anthracene cations by Boissel et al. [9].

INTRODUCTION

Despite various dedicated investigations performed on PAHs, further studies are needed under controlled conditions to address their stability, estimate the size range of astro-PAHs, and understand their evolution and role in the universe.

In order to investigate slow energy relaxation processes of PAHs in astrophysically relevant conditions, experiments should be designed to mimic as closely as possible the interstellar conditions, i.e., very low pressure (below 10^{-8} mbar) and temperature (below 50 K). Most importantly, long observation times are needed in order to observe slow decay processes, which can occur in such isolation conditions. Hence, ion storage devices, such as Paul traps, Penning traps [73,74], electrostatic ion beam traps, and electrostatic storage rings (ESR) [76–78], are commonly used to achieve laboratory experiments aiming at providing data for astrophysical models.

This Ph.D. thesis aims to contribute to answering several questions relevant to PAHs in the ISM. Firstly, how stable are they as a function of their size and their internal energy, or in other words, can small PAHs be more stable than initially expected? Is the RF process ubiquitous for PAH cations? How can PAHs grow in size in the gas phase in low temperature and low-density regions? Can PAHs dimer cations play a role in this growth? Can dimer cations composed of intact and fragmented monomers play a role?

Some clues to these questions have been provided by previous works on anthracene, naphthalene, and pyrene cations. The present study on phenanthrene presented in chapter 5 confirms that RF is of importance for the cooling of small PAHs. For dimer cations, in chapter 6, relaxation processes are addressed, showing the absence of RF in the cooling process of dimer cations.

In this work, a compact electrostatic storage ring, the Mini-Ring, is used to perform experiments with phenanthrene cations and small PAH dimer cations. Although this storage ring is operated at room temperature, it could be used to study the time evolution of the internal energy of the phenanthrene cations and to perform the photo-dissociation spectroscopy of dimers of PAHs. A beam time at the cryogenic DESIREE storage ring in Stockholm has been dedicated to the photodissociation of naphthalene dimer cations in more relevant astrophysical temperature conditions (13 K).

In the following section, a brief description of electrostatic storage devices, i.e., electrostatic ion beam traps and electrostatic ion storage rings, is presented with some examples of the physics recently performed with such devices.

1.5 Electrostatic Storage Devices (ESDs)

Electrostatic Storage Devices (ESDs) usually refer to instruments that achieve ion-beam storage by means of electrostatic fields only. ESDs are generally divided into two categories: the electrostatic storage rings (ESRs), where ions are circulated on racetrack like orbits, and electrostatic ion beam traps (EIBTs), in which ions bounce back and forth between two electrostatic mirrors. Since the first ESR [79] and EIBT [80] were built in the '90s, both kinds of ESDs have been attracting a growing interest for atomic [81], molecular [82–89], carbon [90–94], and metallic [95–100] cluster physics and many related area fields such as gas-phase studies or mass spectrometry of biomolecules [101–106]. The aforementioned references should not be considered exhaustive, but they provide a panel of the different kinds of experiments that have been achieved so far. A comprehensive review of the dynamics of ESD-stored molecular beams has been recently written by K. Hansen [107].

In ESDs, ion beams are bent and/or focused by electrostatic ion optics elements only in contrast with magnetic storage rings where the kinetic energy of the ions is unchangeable. Although the accessible beam energy remains limited for ESDs, up to several tens or hundreds of keV, they do not suffer from some of the drawbacks of magnetic rings, such as hysteresis

INTRODUCTION

effects, long-range fringe fields, etc. Moreover, one of the most important benefits of the electrostatic design is the mass-independent storage conditions, i.e., the voltage on electrodes, provided that kinetic energy is a fixed value often set by placing the ion source inside a high-voltage platform at a given voltage. This property will be discussed in the next section. ESDs can also be cooled down more easily to cryogenic temperatures, achieving in this way one of the requirements of the astrophysical conditions. Another decisive consequence of cryogenic cooling is the very low background gas pressure which is another important feature of astrophysical conditions. Collision with the background gas being the main ion loss process, very long storage times can be reached. Therefore, studies on a very wide time range are possible from tens of microseconds to hours corresponding to eight orders of magnitude.

Several ESDs and EIBTs have been built so far, each of them having different features and specificities (size, geometry, temperature, beam kinetic energy range, etc.) [79,108–112]. Among other studies, lifetime measurements, collision phenomena, action spectroscopy, cooling dynamics, ionization, charge recombination, photodissociation, photo-detachment, and single-component plasma can be performed in such devices [108,113]. Some General advantages of EIBTs and ESRs are summarized in Table 1-1.

Table 1-1: Some advantages of EIBTs and ESRs

EIBTs	ESRs
Better time sampling	Long straight sections
More limited ion beam kinetic energy	Free field
Less easy access to external excitation	More space for interaction with external excitation
Re-bunching effect	Beam moving in a single direction

1.5.1 Electrostatic storage rings (ESRs)

Ion storage rings were initially developed for nuclear and particle physics leading to the building of very big infrastructures such as CERN in Geneva, GSI in Darmstadt, Germany, and many others. Storage rings are also used for electron beam in synchrotron facilities, e.g., ESRF in Grenoble, SOLEIL in Saclay near Paris, . . . , as tunable VUV and X-rays light sources. Smaller infrastructures have been successfully used for atomic physics and molecular physics using much lower energy beams in the range of keV to investigate a wide range of ions, from protons and anti-protons to heavy molecular and cluster ions, e.g., ASTRID in Aarhus. In those storage rings, the ion trajectories are controlled by magnetic bending and focusing optical elements to store and guide the charge particles in well-defined directions with constant energy [114]. In such magnetic storage rings, heavy ions, e.g., biomolecular ions, proteins, clusters. . . , can hardly be stored in the same conditions as lighter ions due to the proportionality of the magnetic rigidity to the square root of the mass (Eq. (1-1)). The magnetic rigidity is defined in Eq. (1-1), as the product of the magnetic field intensity (B) times the radius (ρ) of the trajectory and is a function of the ion mass (m_i), charge (q_i), and kinetic energy (E_i).

$$B\rho = \sqrt{\frac{2E_i m_i}{q_i}} \quad \text{Eq. (1-1)}$$

Electrostatic storage rings have been developed to overcome this problem of high masses since the ion mass is not limited because electrostatic rigidity is independent of ion mass (Eq. (1-2)). Indeed, the electrostatic rigidity, defined as the product of the electrostatic field intensity (E) times the radius (ρ) is proportional to the kinetic energy and the charge (Eq. (1-2)). As already

INTRODUCTION

mentioned in the previous section, the mass independence of the electric rigidity implies that for fixed kinetic energy and charge (often $q_i = \pm 1$), the storage conditions, i.e., the voltages on the electrostatic bending and focusing elements, are independent of mass.

$$E\rho = \frac{2E_i}{q_i} \quad \text{Eq. (1-2)}$$

Presently, several different kinds of ESRs have been built and are in operation all around the world (Denmark, Germany, Sweden, France, Japan, Saudi Arabia, etc.). A list of existing ESRs is given in Table 1-2. In this section, we will shortly review some examples of the research performed using these different ESRs.

Table 1-2: List of electrostatic storage rings (ESR)

Name	City / Country	structure	Circumference (m)	Ion source
ELISA	Aarhus / Denmark	racetrack	6.8	Electrospray
ESR	KEK / Japan	racetrack	8	Electrospray
TMU E-Ring	Tokyo / Japan	racetrack	7.7	Electrospray, cold cathod,...
Mini-Ring	Lyon / France	hexagonal	0.73	ECR
DESIREE	Stockholm / Sweden	racetrack	8.6	Nielsen, ECR, Cs sputter
FLSR	Frankfurt / Germany	racetrack	14.23	Penning(PIG), FR
ELASR	Riyadh/ Saudi Arabia	racetrack	9.2	ECR
SAPHIRA	Aarhus / Denmark	square	1 x 1	Electrospray
CSR	Heidelberg/Germany	square	35	Discharge ion source
RICE	RIKEN / Japan	racetrack	2.9	ECR, ESI, FR
μ E-ring	Tokyo / Japan	racetrack	0.8	Electron impact
USR	Darmstadt/ Germany	square	10 x 10	

The first electrostatic ion storage ring was ELISA (Electrostatic Ion Storage Ring Aarhus), which has been built in 1996 in Aarhus, Denmark [79]. The design and characteristics of ELISA have been followed by the other ESRs; thus, a brief description of ELISA is presented here.

ELISA is composed of electrostatic linear optics with deflection and focusing optical elements and it is suitable for the study of heavy ions in the range 10 s -1000 s. The operating energy E_i is up to 25 keV. In ELISA, the guiding elements are two 160° spherical electrostatic deflectors (SDEH), four 10° parallel plate deflectors (DEH), and four pairs of electrostatic

INTRODUCTION

quadrupoles (QEV, QEH), as shown in Figure 1-14. It has a racetrack-shaped design, i.e., straight sections connected via cylindrical deflectors, with a circumference of about 6.8 m, corresponding to a revolution period of 2.9 μs for H ions and 77 μs for C_{60} ions [115]. Later, the spherical deflectors were replaced by cylindrical deflectors to reduce space charge effects resulting from the strong repulsion between the stored ions at the ion trajectory focal points in the middle of the cylindrical deflectors.

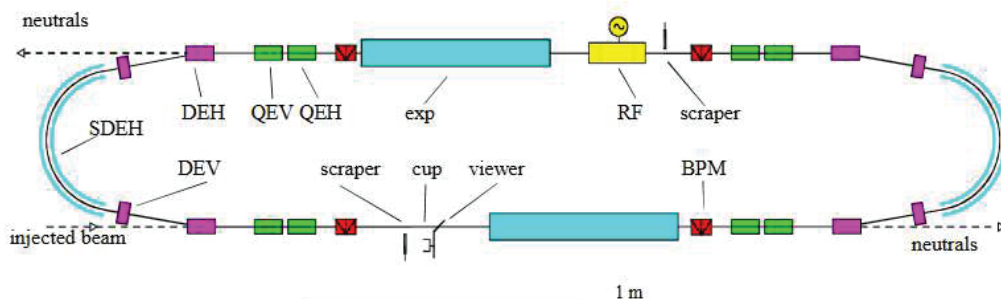


Figure 1-14: Schematic of ELISA ion storage ring [116]

Ions can be provided using different ion sources, e.g., an electrospray ion source or a cold-cathode plasma ion source, and injected into the ring via the straight section. Detectors, placed at the end of one straight section, are used to detect the neutral fragment yields. Laser pulses (Nd:YAG, OPO) are used to excite the stored ions in the merged beam configuration. It is possible to cool or heat the ring. The ring can be cooled to reduce the blackbody radiation and hence achieve a longer storage time. A wide range of experiments with ELISA, such as lifetime studies of metastable negative ions He^- [117] and Be^- [118] through a forbidden autodetachment process, isomerization [119], electron-ion collisions [120,121], and action spectroscopy of bio-molecular ions in the gas phase for which the first absorption spectra were recorded using OPO laser-induced techniques for a chromophore of the green fluorescent protein (GFP) and red fluorescent protein (RFP) and the results were compared with those obtained for proteins in solution (Figure 1-15) [122–126]. Additionally, the cooling dynamics process of various molecular and cluster ions has been investigated. Hansen et al. [115] have first observed the t^{-1} power decay law for stored Ag_5^- cluster ions which was attributed to a broad distribution of internal energy of stored ions.

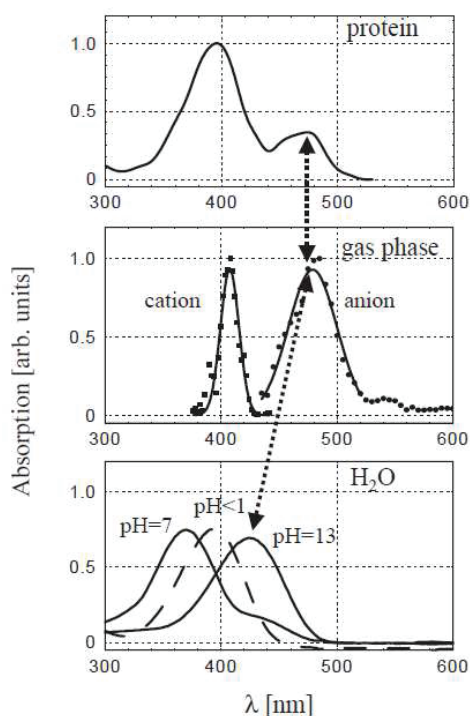


Figure 1-15: The absorption spectrum of GFP in different media, protein, gas phase, and solution [126].

INTRODUCTION

The building and successful operation of a second ESR were reported in 2002 by a Japanese group in Tsukuba (ESRing) [127]. The design of this ESR is very similar to ELISA but with a slightly larger circumference of 8.1 m and maximum energy $E_i = 30$ keV. It has been employed to study electron capture dissociation of complex bio-molecular ions by merging the stored bio-molecular ion beam with an electron beam at low relative velocities [128]. In more recent works, this ESR has been used to study the photodissociation of fluorescein anions [129] of the azo and hydrazone form of orange I monoanions. This group has also used the OPO laser pulse technique to excite the stored ions produced in an electrospray ion source. The absorption was found to be strongly dependent on the storage time before the laser excitation [130].

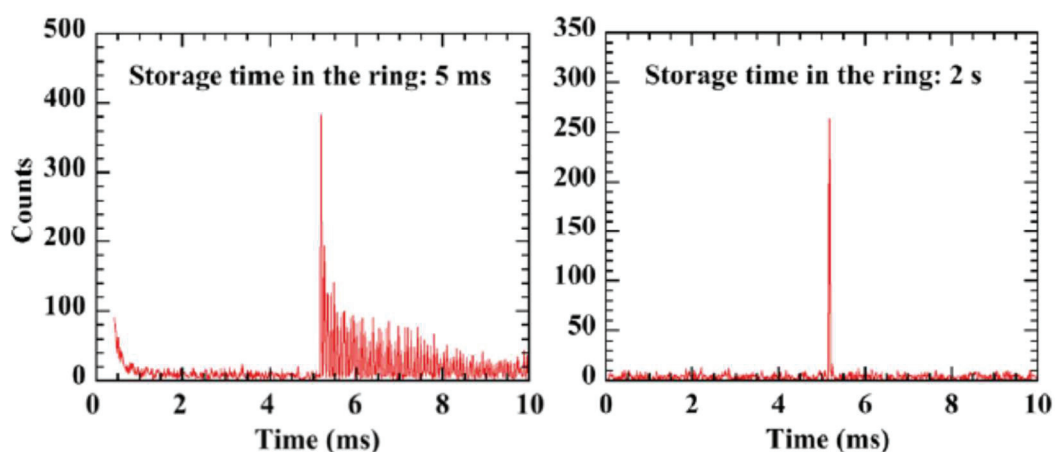


Figure 1-16: Neutral counts as a function of different storage times produced by photodissociation of orange I monoanion [130].

The TMU E-ring at Tokyo Metropolitan University (TMU) was built in Japan in 2004 and with a similar racetrack tape-shaped of about 7.7 m in circumference as an ELISA storage ring. It has been used to study the interaction of the large molecular and cluster ions with electrons, atoms, and molecules. The interesting feature of TMU is that it could be cooled down to the liquid nitrogen temperature [131]. The radiative cooling of highly excited cluster carbon anions with $N = 8, 10, 13-16$ has been investigated. The measured radiative rate was found to be consistent with the fast RF radiative cooling process. The rate constants were determined to be about $3 \times 10^4 \text{ s}^{-1}$ [90].

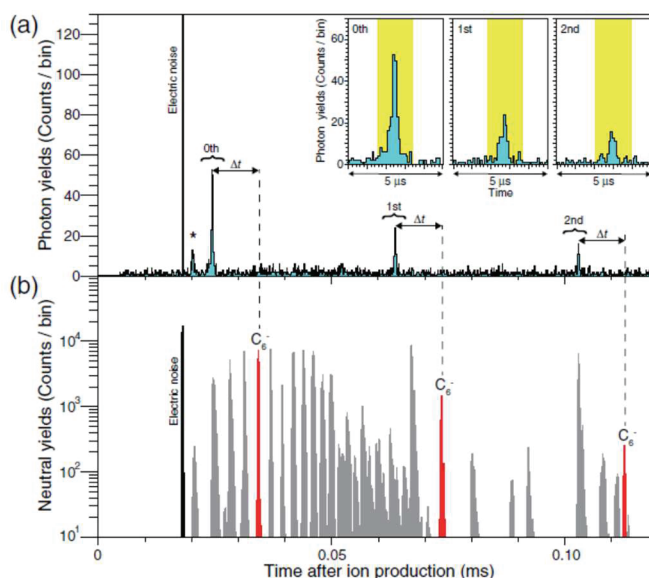


Figure 1-17: RF photons from C_6^- ions. (a) The photon yields as a function of storage time. (b) The neutral fragments yield as a function of storage time [132].

The commissioning of the Mini-Ring in Lyon has been reported in 2008 [109]. It has been intentionally designed to be a much smaller ESD than other existing rings at that time. The ion

INTRODUCTION

trajectory circumference is about 0.73 m, and it is presently operated at a beam energy of 12 keV. ECR ion sources have been used to produce ion beams of atoms and molecules. More detail will be given later in chapter 3 since the experiments performed during this thesis work have been performed with such sources [76,109]. The Mini-Ring was used to study the radiative cooling process of PAH cations such as anthracene, naphthalene, and pyrene via the evolution of the internal energy distribution. These experiments demonstrated that the fast reduction of the internal energy of these cations could be attributed to a fast radiative cooling process, i.e., the RF process. RF rates have been estimated for the first time for these three different cations [76,77,133–136]. Later on, these findings were confirmed at TMU for C_6^- clusters by direct detection of emitted recurrent fluorescence photons (Figure 1-17) [132]. Recently, the direct detection of emitted recurrent fluorescence photons from naphthalene ions has been observed using an electrostatic ion beam trap for a long time up to 10 ms [137].

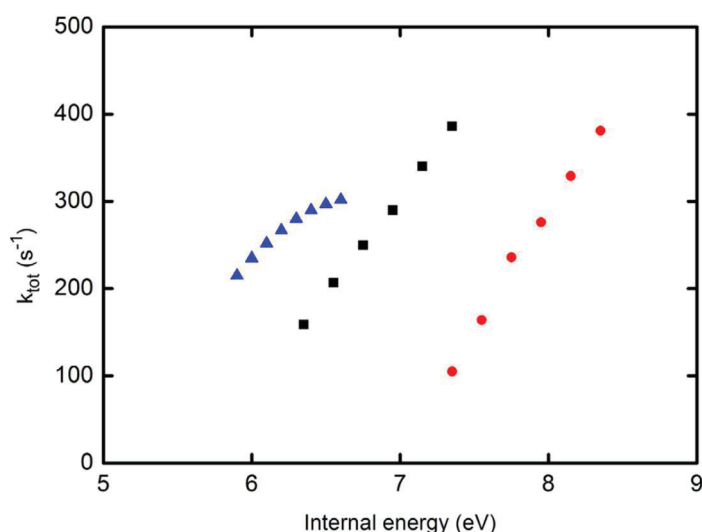


Figure 1-18: total cooling rate obtained for the cation of naphthalene (blue triangles), anthracene (black squares), and pyrene (red dots) as a function of the internal energy [135].

At Stockholm University, Sweden emerged in the 2000's decade the idea of the Double ElectroStatic Ion storage Ring ExpERiment (DESIREE) with a common straight section in order to perform merged-beam experiments between two oppositely-charged ion beams to study mutual neutralization process (Figure 1-19) [138,139]. The commissioning of this project has been reported in 2013 [139]. It is presently operated as a facility, which is open to application for beam time. Some of the experimental results in the present manuscript have been obtained during a one-week beam-time at DESIREE in October 2019. More details about DESIREE will be given in Chapter 3. For comparison with other rings discussed in this section, let us mention that all the elements of DESIREE are placed on a single plate support, and the whole apparatus is sealed inside a single vacuum chamber, which is thermally isolated in order to achieve a cooling down to 13 K. The racetrack type ion trajectories have a circumference of 8.6 m.

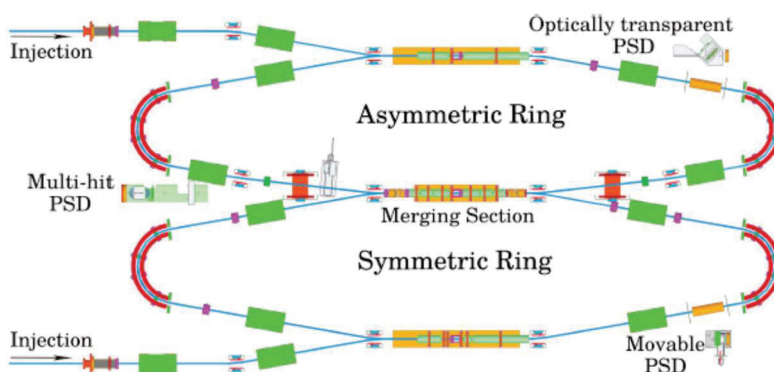


Figure 1-19: Scheme of DESIREE [138].

INTRODUCTION

As an example of the capabilities of DESIREE, let us cite the recent measurement of the spontaneous unimolecular decays of the homo-nuclear dimer anion Ag_2^- performed on the timescale of milliseconds and seconds [140]. Internally hot Ag_2^- ions were produced in a cesium sputter ion source and stored for 10 s. The authors found evidence that the dissociation process dominates the decay signal up to 100 ms of the storage time, and the electron emission dominates the measured decay signal for times larger than 100 ms. They interpreted the faster dissociation process as due to a tunneling effect appearing for high rotational quantum number states and the slower electron emission process as due to a non-adiabatic coupling between the high vibrational states of Ag_2^- and low vibrational states of Ag_2 . Because of the absence of avoided crossing in the potential energy curves, usually mandatory to imply a coupling between electronic and nuclear degrees of freedom, this electron emission is a striking direct observation of a deviation from the Born-Oppenheimer approximation [140].

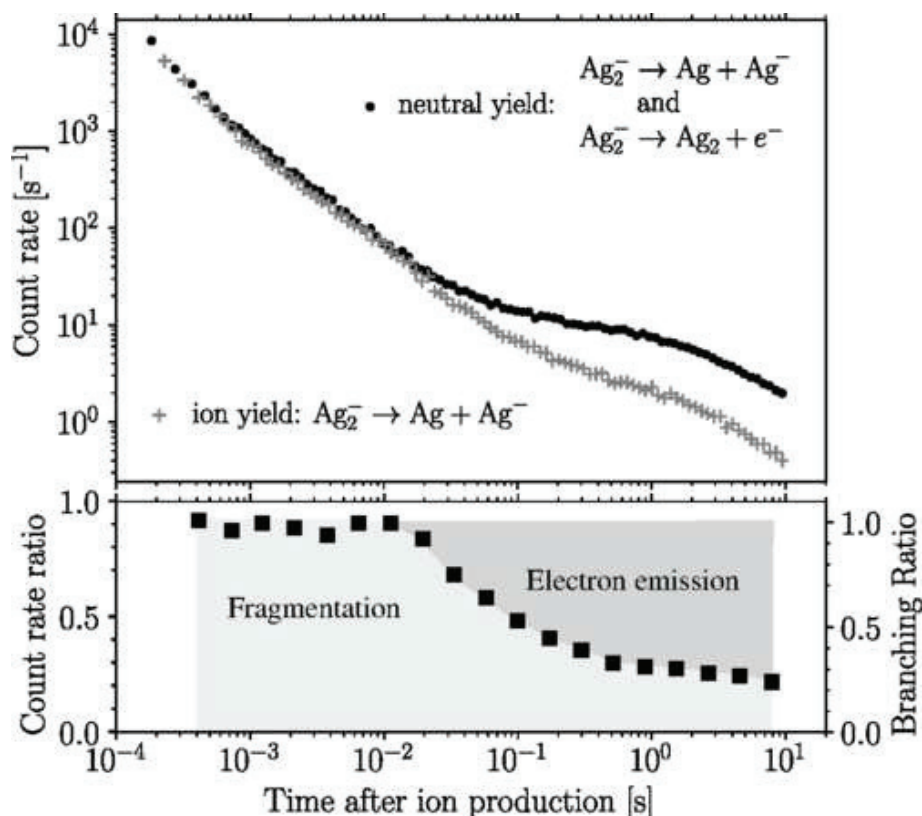


Figure 1-20: Ion and neutral yields measured with the fragment and neutral detectors [140].

The storage ring SAPHIRA constructed and operated in the Aarhus University for studying interactions of ions with photons has a simple square geometry ($\sim 1m \times 1m$) [141]. As an example, we can cite the recent study of the photo-isomerization dynamics of the retinal protonated Schiff base (RPSB) [142]. In this work, electrospray RPSB ions are stored in SAPHIRA for several microseconds before they are excited in a pump-probe scheme with a Femtosecond laser. From the induced dissociation, Kiefer et al. showed that the CIS isomer of RPBS presents a barrier-less fast decay, whereas the all-trans isomer has a much higher barrier-controlled inducing a much slower dissociation pathway [142].

The RIKEN Cryogenic electrostatic ring (RICE) was built in Japan. It is operated in cryogenic conditions down to temperatures of about 4.2 K [143]. Atomic and molecular ions can be stored for a long time up to 1000 s on closed orbits of 2.9 m in circumference and at 15 keV kinetic energy. UV dye lasers with a repetition rate of 10 Hz or 100 Hz were merged with the stored ion beam in order to investigate [144,145] the radiative cooling and the photodissociation spectroscopy of N_2O^+ . Hirota et al. [144] observed that the radiative cooling of the vibrational level populations occurred with a time constant of about 5 s, whereas no changes in the rotational levels could be evidenced within the storage time of 200 s.

INTRODUCTION

Likewise, ELASR, which stands for the ELeCtroStAtic Storage Ring in Riyadh, has been designed and built to be the core of an atomic and molecular collision experimental facility in Saudi Arabia. Figure 1-21 displays a photograph of ELASR. It was built following the standard design of ELISA. It thereby features a racetrack single-bend-shaped ring, with a circumference of 9.2 m, of which the optical lattice consists of two super periods. In the super period, the 180° turns are made up using two cylindrical deflectors (CD) that are inserted in between parallel plate deflectors (PPD) and quadruple doublets. ELASR can store ion beams at energies up to 30 keV, and its lattice is designed in a way that allows the study of laser-ion, electron-ion, and ion-neutral beam interactions [146–148].

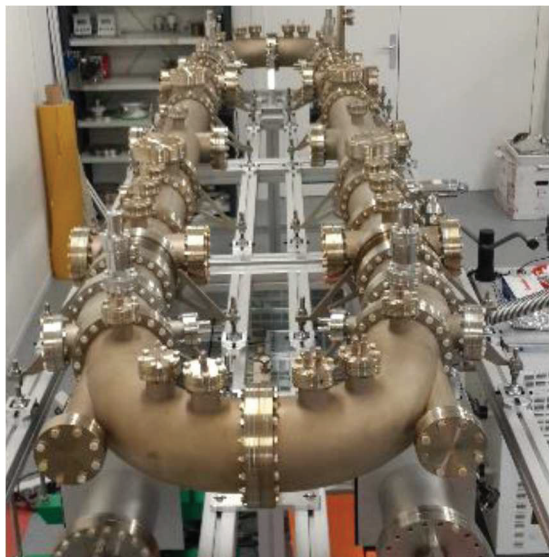


Figure 1-21: A photograph of ELASR in Saudi Arabia [147]

The Frankfurt low energy storage ring (FLSR) is a racetrack room temperature storage ring with a circumference of 14.23 m. The FLSR was constructed at the “Institut für Kernphysik” in Frankfurt University (IKF), Germany, to store molecular ion beams at kinetic energies up to 80 keV [149,150]. The FLSR has been firstly used to study the kinetic energy release (KER) in molecular collisions thanks to its embedded reaction microscope [151,152]. Recently, an RF plasma ion source with a rubidium charge exchange cell has been installed in FLSR to produce and store negative atomic or molecular anions such as He^- , O^- and OH^- [153].

The Cryogenic storage ring (CSR) at the Max Planck Institute for Nuclear physics in Heidelberg is a single square shape cryogenic storage ring of 35 m circumference and with a beam energy of 20-300 keV. One of its important specificities is the presence of a low-energy electron cooler, which is employed to preserve the longitudinal and transversal momentum spread of the stored ions as small as possible. It also gives the opportunity to perform electron attachment reactions. The first ion beam was stored in 2014, the cryogenic operation was set in 2015, and the first electron-cooled ion beam operated in 2017 [154,155]. CSR is composed of a room with a cryogenic vacuum of a diameter of 100 -320 mm and four straight sections of 10 meters long. Electrostatic deflectors, focusing elements, quadrupoles, and an electron source are mounted in the straight sections. Figure 1-21 shows a schematic picture of CSR and the vertical section.

As an example of recent studies on CSR, a near-threshold photodissociation experiment using CH^+ at a temperature below 10 K has been carried out in order to study the cooling of rotational degrees of freedom inside the ring. The stored ion beam was with a kinetic energy of about 60 keV for several minutes. An OPO laser in the ultraviolet was used to induce the reaction



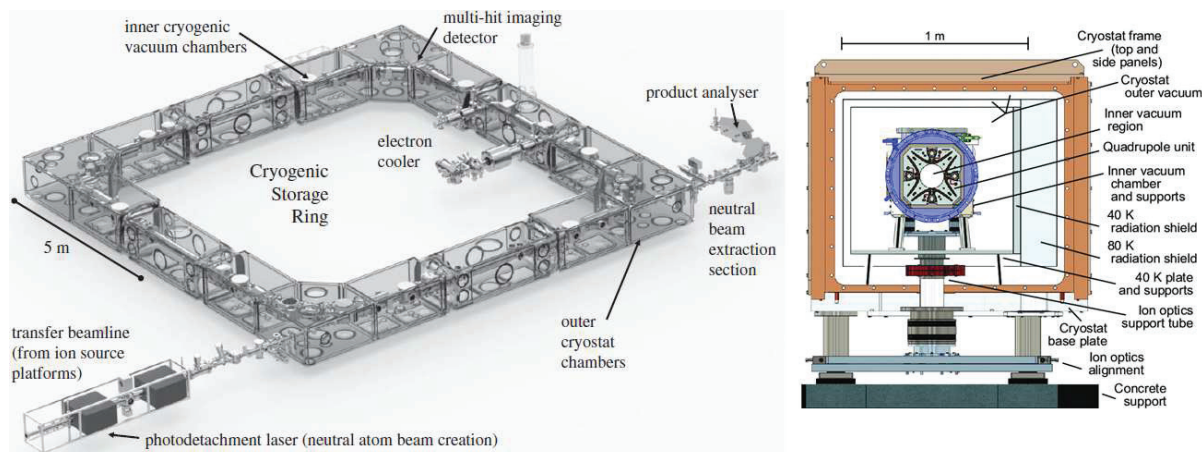


Figure 1-22: Schematic figure of CSR [156] and vertical section [154].

Laser excitation from the $X^1\Sigma^+$ of CH^+ coupled to the $A^1\Pi$ excited state, which correlated to upper $C^+(^2p_{3/2})$. The excitation is thus just above the dissociation threshold, but below the energy of $^2p_{3/2}$ level leads to a predissociation process where non-adiabatic coupling between excited state $^2p_{3/2}$ and lower level $^2p_{1/2}$ takes place before the decay. The two-step dissociation led to a Feshbach resonance near the threshold, which was observed for the rotational levels $J = 0 - 2$. A set of resonances in the photodissociation cross-section just above the threshold for each rotational state and the photodissociation spectra measured near the thresholds for $J = 0 - 2$ states for different storage times are shown in Figure 1-23 [156].

A more recent significant study of recombination rate measurement was to measure quantum state-specific rate coefficients of dissociative recombination (DR). A pronounced decrease of the electron recombination rates for the lowest rotational state of HeH^+ comparing with the measurements obtained at room temperature has been observed, suggesting a high abundance of cold HeH^+ [157].

μ E-ring at Tokyo Metropolitan University is the second table-top electrostatic ion storage ring with a circumference of 0.8 m [158]. The first storage was in 2016. Ar^{n+} $n=1, 2$ have been stored, and the electron capture cross-section for neutral argon has been measured as well [159].

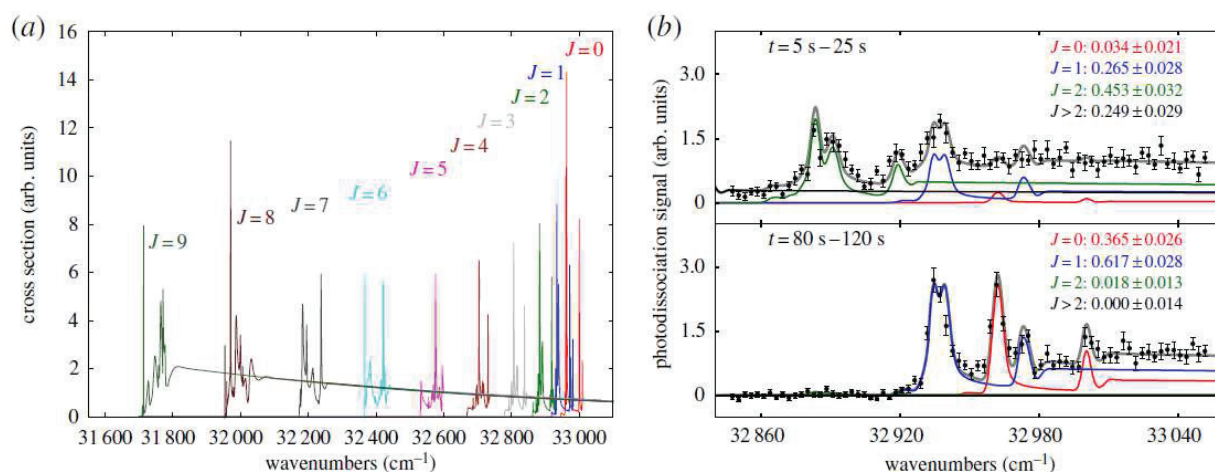


Figure 1-23: (a) Calculated Feshbach resonance for the photodissociation of CH^+ for $J=0-9$. (b) Photodissociation spectrum of CH^+ measured for two different storage time intervals inside the CSR [156].

Finally, we may mention here the Ultra-low energy electrostatic Ring (USR), which is an ongoing project at FLAIR (Facility for Low energy Anti-proton and Ion Research) dedicated to the storage of anti-proton beams in the range 300 keV to 20 keV and with revolution time from 5.6 ms to 32.8 ms [160].

1.5.2 Electrostatic ion beam traps (EIBTs)

The concept of electrostatic ion traps (EIBTs) is based on an analogy with classical geometrical optics. Indeed, ion storage in an EIBT is analog to photon storage between the two mirrors of an optical resonator. The stability condition is related to the focal length f of the mirrors and the distance L between the mirrors (Eq. (1-4)).

$$\frac{L}{4} \leq f \leq \infty \quad \text{Eq. (1-4)}$$

The first EIBTs were built simultaneously and independently in 1996 at the Weizmann Institute of Science in Israel [80] and Berkley [161]. Since then, many experiments using EIBTs have been mounted. We will restrict here the discussion to two important EIBTs, i.e., the so-called Zajfman Trap (from Weizmann Institute) that has been replicated by several other teams [88,89,162–166] and the ConeTrap, initially developed in Stockholm University, Sweden, in 2001 and replicated in Lyon in 2003. The design of the Mini-Ring used in the present thesis work originated from the conic electrodes of the ConeTrap.

1.5.2.1 Zajfman trap

The Zajfman trap is composed of two electrostatic mirrors, which consist of five electrodes labeled E_1 to E_5 , and a free field region in between, as presented in Figure 1-24. The grounded electrode A_1 is used to decrease the electric field outside the trap. The electrodes Z_1 (voltage V_z) and Z_2 (grounded) are used for additional focusing. The Electrodes Z_1 , Z_2 , and E_5 form together an asymmetric Einzel lens. Therefore, only two parameters characterize the ion trap, the stopping and focusing potentials, V_s and V_z , respectively. For injection of ion bunches in the trap, the mirror electrodes on the injection side are set to zero voltage to let ions reach the mirror electrodes on the other side, where the injected ions are stopped and reflected and refocused. Meanwhile, the mirror electrodes on the injection side are switched on to their nominal voltages in order to reflect and focus and the ions that are now trapped in between the two mirrors. In the field-free regions, the ion beam passes following a straight-line trajectory and can be excited by any means, e.g., electron or laser beams, or by collisions with the residual gas. The resulting neutral fragments are detected by micro-channel plates (MCP) outside of the trap [80].

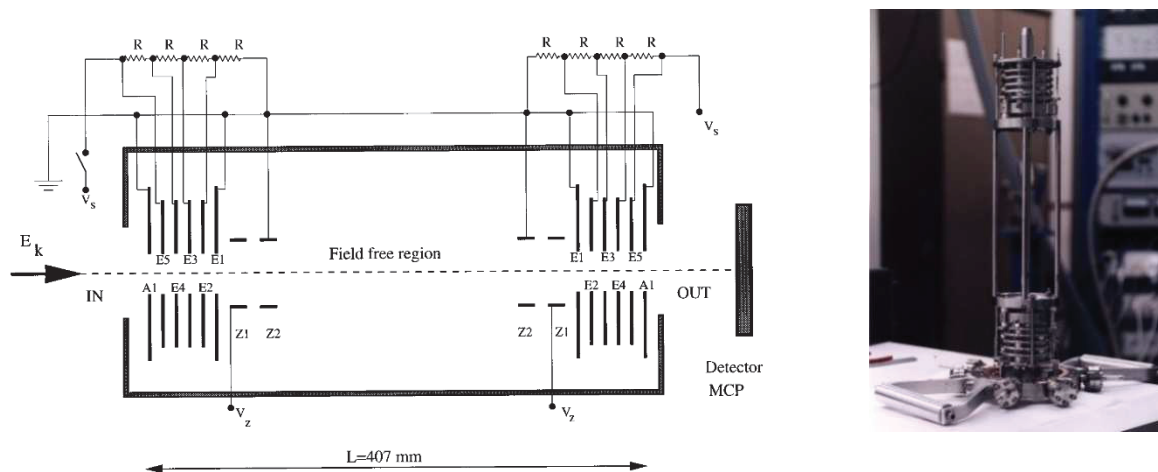


Figure 1-24: Scheme of the Zajfman ion trap built at Weizmann Institute, Revohot, Israel [80].

Among significant initial studies using the Zajfman trap are lifetime measurement of the metastable states of various ions such as He^- [167] and Be^- [168], mass spectroscopy, particularly, self-bunching behavior known as negative mass instability [169]. Electron-ion interactions are also performed by combining electron beam and electrostatic ion traps. In the Zajfman trap at Weizmann institute, an electron target made of only electrostatic elements with a rectangular interaction region was placed in the free region (Figure 1-25) [170]. Therefore,

INTRODUCTION

the electron impact detachment cross-section for different ions such as Al_n^{-1} ($n=2-5$) and Al_n^{-1} ($n=1-9$) [171] could be measured.

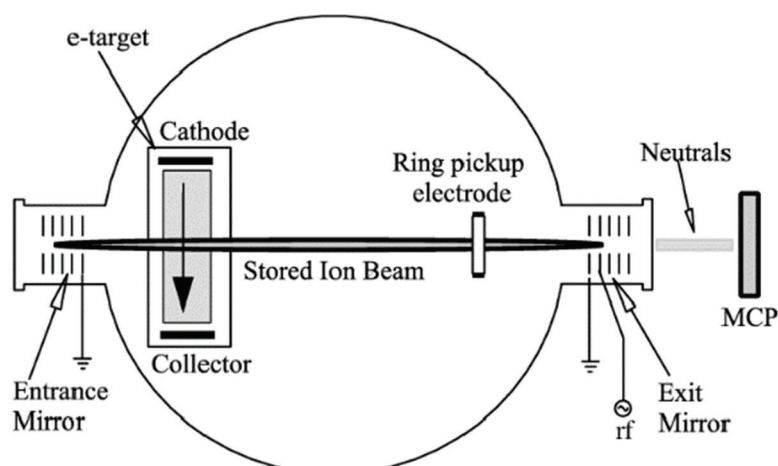


Figure 1-25: The Zajfman trap with an electron target [170]

As an evolution of the Zajfman trap, the Bent Electrostatic Ion trap (BEIBT) has been built to operate as a linear ion trap (EIBT) or in a curved configuration (BEIBT), which enable detecting the neutral and charged fragments simultaneously and determining the average kinetic energy released in the fragmentation. The stored ions have a V-shaped trajectory because of the deflector mounted between the two mirrors, as presented in Figure 1-26. MCP 2 detector is used to collect the charged neutrals, whereas the other two detectors outside the ion trap are used for neutral fragments [97]. One recent study performed with (BEIBT) was the isomerization of C_{10}^- . The ions have been trapped and excited with a laser pulse. It has been found that the isomerization from the linear to the monocyclic conformation occurs on a long timescale, up to hundreds of microseconds [172].

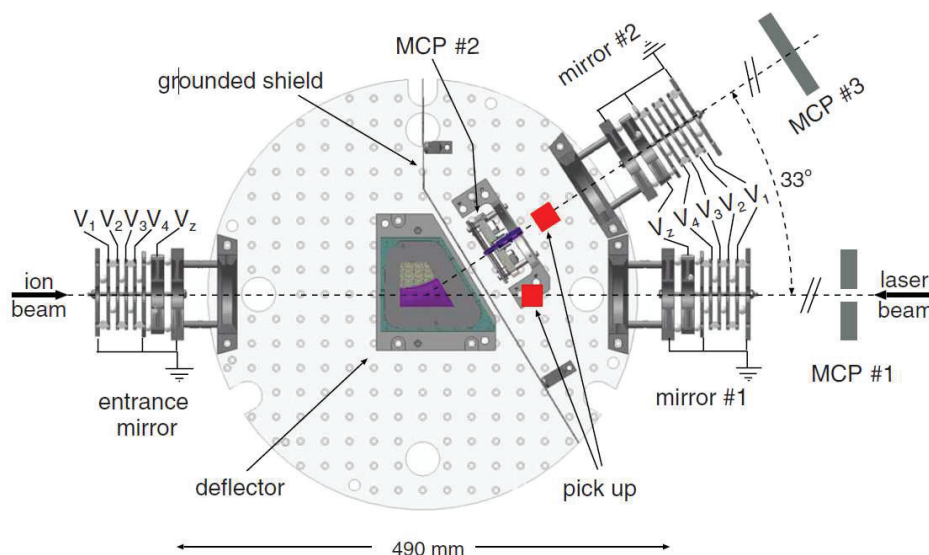


Figure 1-26: schematic view of a Bent Electrostatic Ion trap (BEIBT) [97].

The Cryogenic Trap for Fast ions beams (CTF) has been developed and operated at Max Plank Institute in Germany. It consists of a Zajfman trap that is placed in a vacuum chamber of 3 m long and cryogenically cooled down up to 10 K. The CTF allows to perform experiments on the dynamics of ion beams, especially, in self-bunching mode, as can be shown in Figure 1-27 [173] and to investigate the effect of temperature on cooling anions of Al clusters [162].

One of the experiments performed using CTF was to monitor the internal energy distribution of isolated anion clusters, e.g., CO_4^- by delayed electron detachment, resulting from

INTRODUCTION

single-photon photoexcitation. The ions were produced using a metal ion sputter source and a laser vaporization source. With very narrow internal energy distribution, The study demonstrated that the laser excitation at room temperature provides theory-independent calibration of the radiative emission versus internal energy [174].

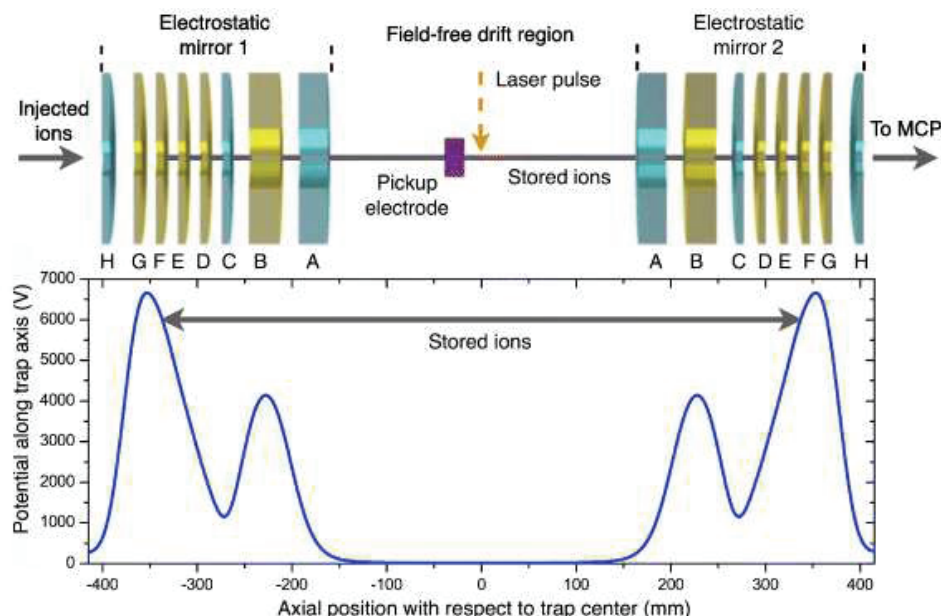


Figure 1-27: Schematic cross-section of CTF electrostatic mirror electrodes employed to trap the ions [173].

More recently, a Hybrid electrostatic Ion Beam Trap (HEIBT) has been designed and simulated by using dichroic mirrors. It is employed to study ion-ion, ion-neutral, and ion-laser collisions where the neutral products of such interactions can be imaged behind the HEIBT mirrors [175].

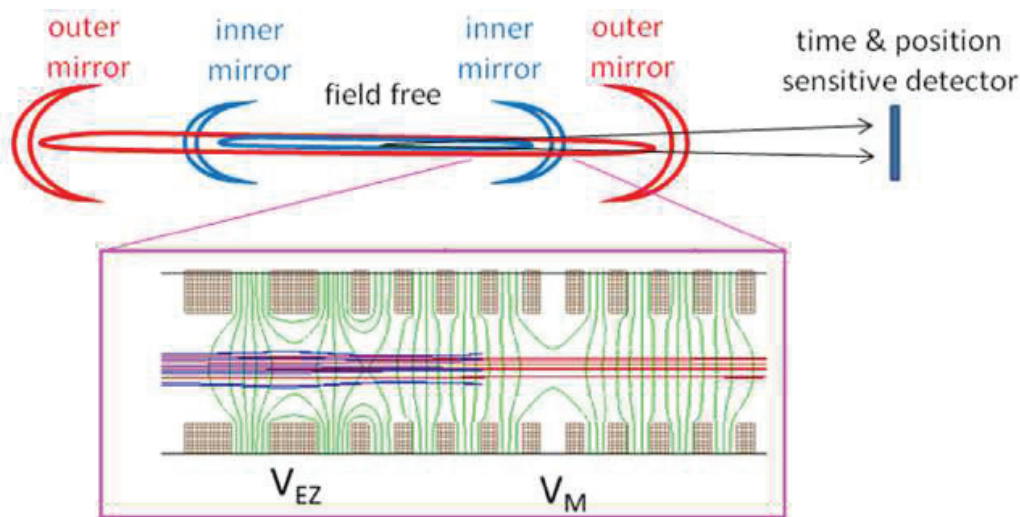


Figure 1-28: Schematic view of a Hybrid electrostatic Ion Beam Trap (HEIBT)[175].

1.5.2.2 The ConeTrap

The compact ConeTrap is the simplest electrostatic ion trap and consists only of three electrodes of a total length of 175 mm, two identical conical shape electrodes, and a cylindrical electrode in between. The name ConeTrap is derived from the conical electrodes, as can be shown in Figure 1-29 [176]. Stable storage conditions are realized by finely setting dimensions and by applying voltage on the electrodes. The ion injection is similar to the Zajfman trap, where the left mirror is set to the ground to inject ions, and then the voltage is raised to the nominal value. The emitted neutral fragments as a function of time can also be collected via a MCP detector placed outside the ConeTrap.

INTRODUCTION

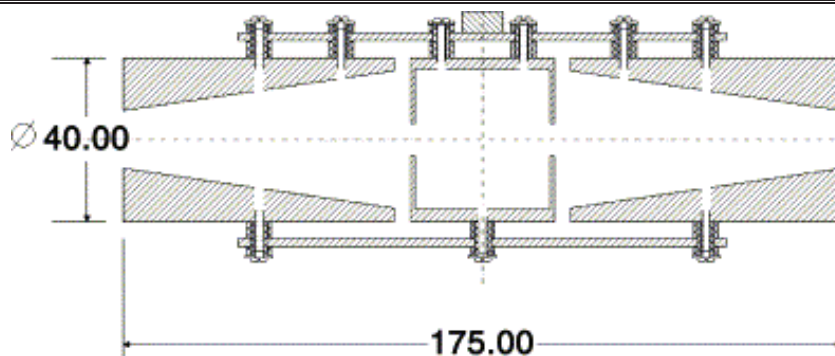


Figure 1-29: The geometry of the ConeTrap and its dimensions in mm [176].

Later, in order to store and measure lifetimes of ions at very low temperature to test DESIREE during the stage of its construction, the ConeTrap was placed at a Cryogenic Vacuum Chamber, as can be shown in Figure 1-30, to cool down the ions up to 10 K [177,178].

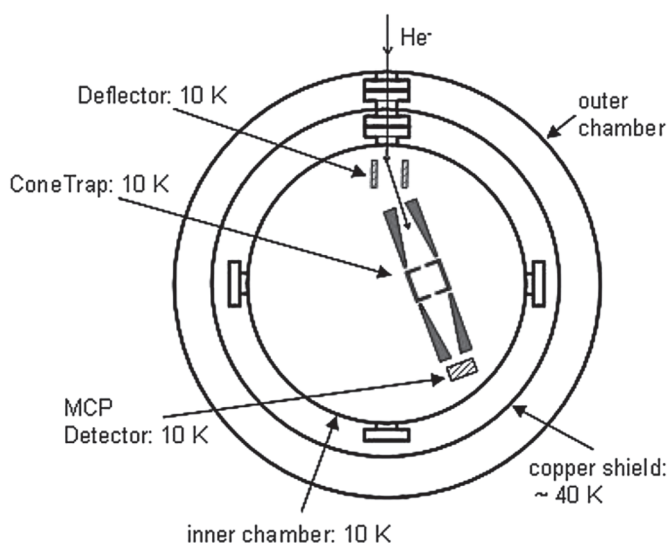


Figure 1-30: Schematic view of the ConeTrap with a cryogenic vacuum chamber [177].

Recently, the application of charge detection mass spectrometry (CDMS) for measuring the masses of large molecules obtained in the gas phase using electrospray ionization (ESI) has been performed using the measurement of the frequency of the stored ions in the EIBT. The study showed that it was possible to determine simultaneously the masses of several ions using CDMS and also to determine their lifetime in the EIBT that was possibly limited due to collisions with the residual gas (Figure 1-31) [179].

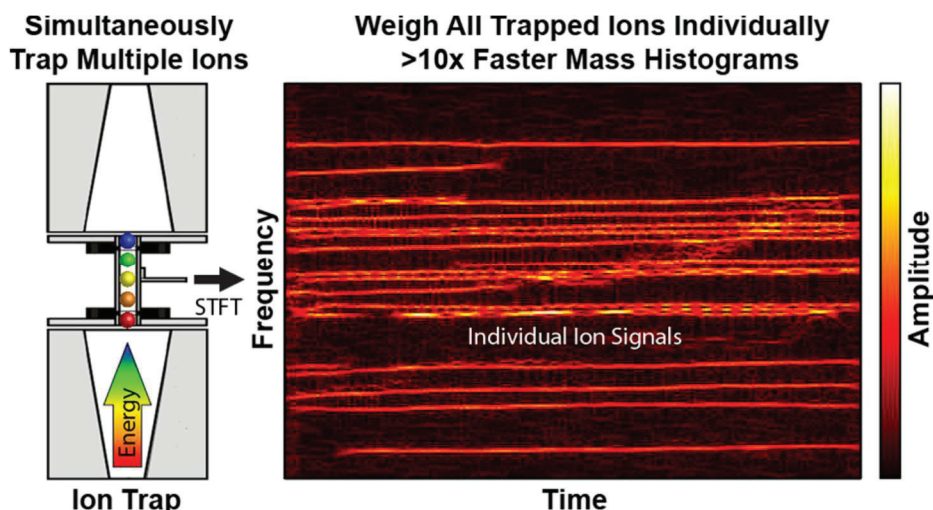


Figure 1-31: Results from a short-time Fourier transform of a single trapping event using 50 ms segments and tracers for RuBisCo ions generated by electrospray ionization [179].

1.6 Conclusion

In this chapter we have introduced firstly PAH molecules, their possible presence in space, and their important role in ISM, as well as their possible formation mechanisms. Then, a brief presentation of ESD setups and a wide range of possible physics experiments performed under controlled conditions has been provided.

The present thesis work is aimed to investigate the energy relaxation processes and the stability of PAH molecules and dimers stored in electrostatic storage rings, the Mini-Ring and DESIREE. By studying the radiative cooling process, we contribute to determining whether the recurrent fluorescence is a general property of PAH cations. The present study on the phenanthrene monomer cations stored in the Mini-Ring shows another example (after previous studies on naphthalene, anthracene, and pyrene) where recurrent fluorescence is an efficient process of the cooling dynamics of such ions. The photodissociation spectroscopy and the cooling dynamics of PAH dimer cations, benzene, naphthalene, and pyrene, are also experimentally investigated in the present thesis on timescales ranging up to 100 ms using the Mini-Ring and for the naphthalene dimer up to 30 s using DESIREE. These experimental results are compared to models based on a semi-empirical method and density functional theory.

The present introductory chapter will be followed by a chapter devoted to the theoretical background and the relaxation processes of isolated systems such as PAHs. Since the experiments were carried out mainly with the Mini-Ring and partly with the DESIREE facility, chapter 3 is devoted to explaining these experimental set-ups. This is followed by chapter 4, which is dedicated to the production of the PAHs and their dimers using the ECR ion source under special conditions. The experimental results lie in two next chapters. Chapter 5 discusses the cooling dynamics of the monomer cations of phenanthrene, and Chapter 6 is dedicated to the PAH dimer cations. The cooling dynamics of dimer cations of PAHs will first be studied, and then the photodissociation spectra will be presented and compared with theoretical models.

2 THEORETICAL BACKGROUND

2	THEORETICAL BACKGROUND.....	27
2.1	Standard methods in quantum physics and chemistry	28
2.1.1	The Schrödinger equation	28
2.1.2	Hamiltonian for polyatomic molecules.....	29
2.1.3	Born-Oppenheimer approximation	29
2.1.4	Beyond the Born-Oppenheimer approximation.....	31
2.1.5	Electronic transition (photon absorption or emission).....	32
2.1.6	Franck-Condon Principle	33
2.1.7	Potential energy surface	36
2.2	Theory for dimer cations.....	36
2.2.1	The charge resonance (CR) and local excitation (LE) transitions	36
2.2.2	DFTB calculations to account for charge resonance.....	38
2.2.3	Morse PECs and photo-dissociation spectra of PAH dimer cations.....	38
2.3	Statistical Models for the relaxation processes of isolated systems.....	42
2.3.1	RRKM theory.....	42
2.3.2	The microcanonical temperature for small isolated systems	43
2.3.3	Relaxation of internal energy	44
2.3.4	Recurrent/Poincaré fluorescence.....	48
2.3.5	IR vibrational emission - IR cooling.....	49
2.3.6	Power-law decay	50
2.3.7	Time evolution of the shape of the IED.....	51
2.4	Decay rates for collision-induced dissociation of stored ions.....	53
2.5	Conclusion	54

The high interest in PAH molecules, their dimers, and their clusters has led theoreticians to carry out various theoretical calculations during the past decade. The first part of this chapter is dedicated to a brief overview of some of the commonly used theoretical frameworks. The next sections are devoted to the theoretical concepts that will be employed in the next chapters of the present work for the interpretation of the experimental results. In particular, the t^{-1} decay law for unimolecular dissociation in a presence of broad internal energy distribution, the recurrent fluorescence process, and its implication in the radiative cooling will be discussed in the case of the monomer PAH cations. For the interpretation of the photodissociation of dimer cations of PAHs, we need to focus on potential energy surfaces (PESs) for the ground and excited electronic states. In addition, a semi-empiric diatomic molecule-like model based on the reflection spectrum will be presented.

2.1 Standard methods in quantum physics and chemistry

This section is dedicated to a short description of some of the computational methods utilized in quantum physics and chemistry. The basics of the methods can be found in many textbooks [180–188]. Since these methods can be used by experts of this field, when needed for the interpretation of the experimental results of the present thesis work, especially about the dimer cations of PAHs (chapter 6), we have collaborated with M. Rapacioli and co-workers of the LCPQ (Laboratoire de Chimie et Physique Quantiques, Toulouse). This collaboration has led to the publication of an article about dimer cations of pyrene [189].

2.1.1 The Schrödinger equation

Obviously, the Schrödinger equation [190] is the basic starting point in physics and chemistry to describe the behavior of microscopic systems in quantum mechanics. Any quantum systems such as particles, atoms, molecules, or clusters have to be described by the Schrödinger equation. When applied to molecules with N_e electrons and N_n nuclei, the time-dependant Schrödinger equation can be written as in Eq. (2-1):

$$i\hbar \frac{\partial \psi(\mathbf{r}, \mathbf{R}, t)}{\partial t} = \hat{H}(\mathbf{r}, \mathbf{R}, t) \psi(\mathbf{r}, \mathbf{R}, t) \quad \text{Eq. (2-1)}$$

Where $\psi(\mathbf{r}, \mathbf{R}, t)$ is the wavefunction containing all information about the system, \hat{H} is the Hamiltonian operator composed of kinetic and potential energies of the system, $\mathbf{r} = (\mathbf{r}_1, \dots, \mathbf{r}_i, \dots, \mathbf{r}_{N_e})$ represents the space coordinates of the N_e electrons, $\mathbf{R} = (\mathbf{R}_1, \dots, \mathbf{R}_i, \dots, \mathbf{R}_{N_n})$ represents the space coordinates of the N_n nuclei, t is the time, and $\hbar = h/2\pi$ is the Dirac constant derived from the Planck constant h .

In case the Hamiltonian does not depend explicitly on time, the wavefunction can be projected based on the time-independent Hamiltonian eigenvectors Eq. (2-2). Hence, discrete energy levels only, i.e. eigenvalues E_k of this Hamiltonian, are available for the system. They are associated with the time-independent wavefunctions $\psi_k(\mathbf{r}, \mathbf{R})$.

$$\hat{H} \psi_k(\mathbf{r}, \mathbf{R}) = E_k \psi_k(\mathbf{r}, \mathbf{R}) \quad \text{Eq. (2-2)}$$

Eq. (2-2) is also known as the time-independent Schrödinger equation.

The corresponding time dependent eigenfunctions are given by:

$$\psi_k(\mathbf{r}, \mathbf{R}, t) = \psi_k(\mathbf{r}, \mathbf{R}) \varphi_k(t) = \psi_k(\mathbf{r}, \mathbf{R}) \times \exp\left(-i \frac{E_k}{\hbar} t\right) \quad \text{Eq. (2-3)}$$

The eigenstate (or wavefunction) of lowest energy ($k = 0$), is generally called ‘ground state’, and the states of higher energies ($k > 0$) are called excited states.

The general solution of the time-dependent Schrödinger equation is then given by an expansion of the wavefunction upon all the eigenstates, which form a complete orthonormal basis (Eq. (2-4)).

$$\psi_k(\mathbf{r}, \mathbf{R}, t) = \sum_k A_k \psi_k(\mathbf{r}, \mathbf{R}) \varphi_k(t) \quad \text{Eq. (2-4)}$$

In Eq. (2-4), the coefficients of the expansion A_k can be found from initial conditions at $t = 0$.

2.1.2 Hamiltonian for polyatomic molecules

For polyatomic molecules consisting of N_n atoms with atomic masses of M_1, \dots, M_{N_n} and atomic numbers $Z_1 \dots Z_{N_n}$, the molecular Hamiltonian can be written as the sum of five contributing terms in Eq. (2-5).

$$\hat{H} = \hat{T}_e + \hat{V}_{e-n} + \hat{V}_{e-e} + \hat{T}_n + \hat{V}_{n-n} \quad \text{Eq. (2-5)}$$

Where \hat{T}_e is the kinetic energy operator for electrons, \hat{T}_n is the kinetic energy operator for nuclei, \hat{V}_{e-n} is the electron-nuclei interaction operator, \hat{V}_{e-e} is the electron-electron interaction operator, and \hat{V}_{n-n} is the nuclei-nuclei interaction operator.

The non-relativistic Hamiltonian is given more explicitly in Eq. (2-6), where the terms are given in the same order as in Eq. (2-5):

$$\hat{H} = - \sum_{i=1}^{N_e} \frac{\hbar^2}{2m_e} \nabla_i^2 - \sum_{\alpha=1}^{N_N} \sum_{i=1}^{N_e} \frac{Z_\alpha e^2}{r_{i\alpha}} + \sum_{i<j}^{N_e} \frac{e^2}{r_{ij}} - \sum_{\alpha=1}^{N_N} \frac{\hbar^2}{2M_\alpha} \nabla_\alpha^2 + \sum_{\alpha<\beta}^N \frac{Z_\alpha Z_\beta e^2}{R_{\alpha\beta}} \quad \text{Eq. (2-6)}$$

For many body systems like polyatomic molecules, the Schrodinger equation cannot be solved analytically since it is composed of $3(N_e + N_n)$ second-order coupled partial differential equations. In principle, numerical computations would remain a possible option, however, the computation time increases dramatically with the number of atoms in the molecule.

Therefore, approximations are necessary to overcome this difficult analytical treatment of such molecular systems and/or to save computation time in numerical calculations. The Born-Oppenheimer is one of the most commonly utilized approximations in the treatment of polyatomic systems.

2.1.3 Born-Oppenheimer approximation

Many theoretical and computational calculations make use of the Born-Oppenheimer approximation (BO) approximation that simplifies Schrodinger by fixing the nuclei at constant positions. Indeed, the basic idea of the Born-Oppenheimer approximation relies on the huge mass difference between electrons and nuclei, resulting in a large difference in their respective velocities. Consequently, one can consider that the electrons move in the static field of fixed nuclei, and when the nuclei move, electrons adiabatically adapt to this movement. As a consequence, the stationary wavefunctions $\psi_k(\mathbf{r}, \mathbf{R})$ can be separated in the product of electronic $\psi_k^e(\mathbf{r})$ and $\psi_k^n(\mathbf{R})$ a nuclei wavefunctions that can be treated independently (Eq. (2-7)).

$$\psi_k(\mathbf{r}, \mathbf{R}) = \psi_k^e(\mathbf{r}; \mathbf{R}) \times \psi_k^n(\mathbf{R}) \quad \text{Eq. (2-7)}$$

In Eq. (2-7), the semicolon in $\psi_k^e(\mathbf{r}; \mathbf{R})$ indicates that the nuclei coordinates \mathbf{R} are not considered as variables but as fixed parameters. The $\psi_k^e(\mathbf{r}; \mathbf{R})$ are eigenfunctions of the electronic Schrödinger equation (Eq. (2-8)).

$$\hat{H}_e(\mathbf{r}; \mathbf{R}) \psi_k^e(\mathbf{r}; \mathbf{R}) = E_k^e(\mathbf{R}) \psi_k^e(\mathbf{r}; \mathbf{R}) \quad \text{Eq. (2-8)}$$

The electronic Hamiltonian accounts for the electron kinetic energy, the electron-nuclei interactions, and the electron-electron interactions (Eq. (2-9)):

$$\hat{H}_e(\mathbf{r}; \mathbf{R}) = \hat{T}_e + \hat{V}_{e-n} + \hat{V}_{e-e} \quad \text{Eq. (2-9)}$$

THEORETICAL BACKGROUND

The basic idea is to repeatedly solve the Schrödinger equation for different fixed values of \mathbf{R} to obtain the energy $E_k^e(\mathbf{R})$. This latter function provides the adiabatic potential energy surface (PES) for the k^{th} eigenstate. This method is very efficient, especially for a first estimation of the PES of the ground state. A minimization procedure is commonly used to determine the geometry of molecules in the ground state.

In a second step of the BO approximation, the nuclei motions are accounted for by reintroducing the nuclei kinetic energy term in the Hamiltonian. The Schrödinger equation becomes (Eq. (2-10)):

$$\left(\hat{T}_n + \hat{H}_e(\mathbf{r}; \mathbf{R})\right) \psi_k(\mathbf{r}; \mathbf{R}) = E(\mathbf{R}) \psi_k(\mathbf{r}; \mathbf{R}) \quad \text{Eq. (2-10)}$$

The separation of the nuclear wavefunction $\psi_k^n(\mathbf{R})$ in the product of translational ψ_t , rotational ψ_r , and vibrational ψ_v wavefunctions (Eq. (2-11)) can be obtained From Eq. (2-10).

$$\psi_k^n(\mathbf{R}) = \psi_t \psi_r \psi_v \quad \text{Eq. (2-11)}$$

In general, the translational motion of the center of mass of the molecule is of no interest. Hence, calculations usually focus on vibrational and rotational motions.

Although the BO approximation reduces significantly the complexity of the resolution of the Schrödinger equation, the electronic equation (Eq. (2-10)) remains a N_e -body problem that cannot be solved analytically and that becomes computationally very demanding as the number of involved electrons (and atoms) increases. For this reason, further approximations are required to effectively solve the Schrödinger equation in real cases.

Quantum physics and chemistry aim to evaluate with the best possible precision, within a reasonable computation effort, the solutions of the electronic Schrödinger equation (Eq. (2-10)) by implementing reasonable strategies. Quantum calculations may then provide important molecular features such as potential energy surfaces, binding energies, vibrational energy levels, rotational energy levels, Frank-Condon factors, etc. A complete discussion of the computational methods employed in quantum physics and chemistry is beyond the scope of the present experimental thesis work; however, let's cite here two commonly used approaches:

(1) Hartree-Fock:

The Hartree-Fock (HF) method is based on the hypothesis that the 'exact' N_e -Body electronic wavefunction can be approximated by the product of N_e individual wavefunctions of each electron evolving in the 'mean field' created by the nucleic and all the other electrons. The purpose of the method was to establish a new 'ab Initio method', i.e., free of empirical parameters, from basic physical principles [191]. V. Fock's contribution was used to add the necessary antisymmetrization with respect to the exchange of two fermionic particles (electrons) [192]. A Slater determinant of the mono-electronic wavefunctions is utilized to express the total wavefunction. This method implies a new so-called 'energy exchange' term in the Hamiltonian.

Although the HF approach remains a reference method in quantum physics and chemistry, it does not account accurately for electron correlation. Various forms of calculations initiate with Hartree-Fock calculation and then correct for individual electron-electron interactions to estimate the correlation energy, which is the difference between the 'exact' and the HF energies. Several approaches have been developed, referred to as post-HF methods, aiming at quantifying this correlation energy. Moller-Plesset [193] perturbation theory (MPn), configuration interaction (CI) [194], coupled-cluster theory (CC) [195] are examples of such Post-Hartree-Fock methods. This latter method makes use of an exponential ansatz in the initial wavefunction and only accounts for single and double excitations, while triple excitations may be added

THEORETICAL BACKGROUND

perturbatively. Although the CC theory is a widely used reference method, its high numerical cost limits its usage to few atom molecules.

(2) Density functional theory:

Density Functional Theory (DFT) is a theoretical approach that is often utilized to define the molecular electronic structure and is assumed to be an ab initio method. Yet, most of the common functionals rely on parameters that emanate from empirical data or more complex calculations. In DFT, the total energy of the system is formulated in terms of the total one-electron density rather than the wavefunction. In this way, the calculation involves an approximate total electron density and an approximate Hamiltonian. The accuracy of the DFT methods can be realized for reasonable computational costs. In essence, the so-called hybrid functional methods combine the density functional exchange with the Hartree-Fock exchange term. Semi-empirical quantum methods rely on the Hartree-Fock formation, but they make use of many approximations and extract parameters from empirical data.

DFT is a key computational theory in many areas in both physical and chemical sciences. It is employed to serve as an approximation of complicated systems such as polyatomic systems. The electron density $\rho(\vec{r})$ is defined as a function of one set of space coordinate and the spin coordinates of all electrons.

$$\rho(\vec{r}) = N \int \dots \int |\psi(r)|^2 ds dr \quad \text{Eq. (2-12)}$$

Since the electrons are indistinguishable, the probability of finding any of the N electrons within volume element dr can be given by

$$P = \int \rho(\vec{r}) d\vec{r} \quad \text{Eq. (2-13)}$$

For the entire space

$$N = \int \rho(\vec{r}) dV \quad \text{Eq. (2-14)}$$

The electron density is an observable and measurable, non-negative function of the three spatial variables and function of three variables contrary to the wavefunction [196].

The average electronic energy can be given a functional of the ground state electron density

$$E[\rho] = \int \rho(\vec{r}) v_{ext}(\vec{r}) dr + F_{HK}[\rho] \quad \text{Eq. (2-15)}$$

where v_{ext} is the external potential generated by all the nuclei and $F_{HK}[\rho]$ is the Hohenberg-kohn functional [197].

2.1.4 Beyond the Born-Oppenheimer approximation

Many experimental results concerning photochemical processes, photodissociation, and unimolecular processes have been found inconsistent with considering adiabatic states [198]. In the Born-Oppenheimer approximation, vibrational excitation energy cannot be transferred to the electronic degrees of freedom (and inversely). However, for complex molecules, including the PAHs studied in the present thesis work, the energy can rapidly convert between electronic and vibrational states when such systems are photoexcited and evolve from electronically excited potential energy surfaces to high vibrational levels of the ground state by a process called internal conversion (IC). The inverse process called inverse internal conversion (IIC)

THEORETICAL BACKGROUND

may also repopulate excited electronic states from the vibrationally excited ground state. These processes may take place in a picosecond timescale at avoided crossings or conical intersections between adiabatic PESs [140].

As mentioned in Chapter 1, for the interpretation of the experimental thesis work about phenanthrene cations, we shall invoke a relaxation process, the recurrent fluorescence (RF) process that implies the conversion of electronic excitation energy to vibrational excitation energy (IC) and its inverse (IIC). This is typically a process that cannot be predicted in the framework of the BO approximation since it implies the coupling between the electronic and nucleic motions.

2.1.5 Electronic transition (photon absorption or emission)

For a quantum molecular system, the atomic orbitals form the molecular orbitals (MO), which have an essential role in determining the electronic structure where electrons are promoted to an empty or partially filled MO. MO depends on the kinds of atoms involved and the internuclear distance. The bonding MO involves the attraction and the overlap of the two atomic orbits, while the antibonding orbits result in repulsion. The occupied bonding MO enhances the stability of the molecule, whilst the occupied antibonding MO contributes to its instability. The probability and intensity of absorption or emission of the electronic transition between an initial state i and a final state f is given by the electronic transition dipole moment

$$D = \langle \Psi_f^t(r, R) | \hat{\mu} | \Psi_i^t(r, R) \rangle \quad \text{Eq. (2-16)}$$

where the integration is performed over the electron space coordinates and $\hat{\mu}$ is the electronic dipole moment operator of the multielectron system, $\hat{\mu}_e = \sum_i e r_i$, Ψ_i^t is the ground state and Ψ_f^t is the excited state.

The total energy of the system is the sum of electronic, vibrational, rotational energies:

$$E_t = E_e + E_v + E_r \quad \text{Eq. (2-17)}$$

However, in this work, we will mostly discuss vibronic transitions, i.e., transitions that may imply electronic and vibrational energy changes, whereas rotational energy is considered small compared to the other energies. The transition between two different states results in absorption and emission lines:

$$h\nu = E_{t_1} - E_{t_2} \quad \text{Eq. (2-18)}$$

After absorption of a photon from a vibrational level v of the ground electronic state to the vibrational level v' of an upper excited state. The absorption oscillator strength between two bound states is given, within the BO approximation where the total wavefunction is $\psi_t = \psi_e(r)\psi_n(R)$, by

$$D = \langle \psi_f^e \psi_f^n | \hat{\mu} | \psi_i^e \psi_i^n \rangle = -e \int \psi_f^e(r) \psi_f^n(R) r \psi_i^e(r) \psi_i^n(R) dr dR \quad \text{Eq. (2-19)}$$

$$D = -e \int \psi_f^e(r) r \psi_i^e(r) dr \int \psi_f^n(R) \psi_i^n(R) dR \quad \text{Eq. (2-20)}$$

where the term $-e \int \psi_f^e(r) r \psi_i^e(r) dr$ is called electronic transition moment, and the term $\int \psi_f^n(R) \psi_i^n(R) dR$ is called vibrational overlap, which determined the breadth and shape of the electronic absorption band.

THEORETICAL BACKGROUND

The transition intensity I_{if} between electronic states is proportional to the square of the transition dipole moment:

$$I_{if} \propto |D|^2 = \left| e \int \psi_f^e(r) r \psi_i^e(r) dr \int \psi_f^n(R) \psi_i^n(R) dR \right|^2 \quad \text{Eq. (2-21)}$$

where the term $\int \psi_f^n(R) \psi_i^n(R) dR$ is called the Frank-Condon factor. It corresponds to the overlap between the vibrational wavefunctions of the initial and final states. It is rewritten in Eq. (2-22), where v and v' stand for vibration quantum numbers of the two states, respectively. The transition is allowed if $D \neq 0$ and forbidden if $D = 0$.

$$FC = f_{vv'} = |\langle \Psi_v^n(R) | \Psi_{v'}^n(R) \rangle|^2 \quad \text{Eq. (2-22)}$$

2.1.6 Franck-Condon Principle

The absorption of photons by a molecular ion follows the general Franck-Condon principle, which gives the relative intensity of the vibrational bands. This principle is explained here in the case of a diatomic molecule for which we consider Morse-like potential curves (PECs), whereas, in polyatomic molecules, higher dimensionality leads to consider multi-dimensional PESs, see section 2.1.7. Since electrons move very much faster, nuclei are assumed fixed during an electronic transition. Thus, it is assumed that an electronic transition is taking place during a much shorter time than the nuclear vibration periodicity. In other words; the electron excitation is instantaneous in the timescale of vibrations. Therefore, electronic transitions can be represented by vertical transitions on the potential energy curves (PECs) of two electronic states. In the lowest vibrational level of a given electronic state ($v = 0$), the radial probability density of presence is maximum around the equilibrium distance, r_e , for the ground state, whereas the maximum is found close to the turning points of excited electronic states of $v' > 0$. Therefore, except in the rare case where the $v = 0$ to $v' = 0$ transition would be possible vertically, the most likely absorption transition would populate $v' > 0$ at one of the turning points of the excited state.

For emission via electronic transitions from excited vibrational levels of an electronically excited state to vibrational levels of a lower electronic state also take place predominantly at a given internuclear distance, r [181]. The allowed vibrational changes associated with electronic transition do not follow any selection rules on vibration. The probability $v \rightarrow v'$ transition is given by Frank-Condon factors, i.e., by the overlap between vibrational wavefunctions.

Figure 2-1 illustrates the Frank-Condon principle with Morse PECs. The nature and shape of the PECs have a major role in the overlap between the vibrational wavefunctions of the initial and final states. If the PECs of the two states are similar with similar equilibrium distances $r_e \simeq r_e'$, the best overlap takes place between $v = 0$ and $v' = 0$, as shown in Figure 2-1(a). If the bonding distance of the two states is different $r_e \neq r_e'$, the best overlap takes place between $v = 0$ and $v' > 0$ resulting in an increase of the vibrational energy of the molecule, illustrated in Figure 2-1(b). The overlap of the wavefunction is illustrated in Figure 2-2 in the case of $v = 0$ and $v' = 2$. It is clearly seen that the transition to $v' = 2$ results in a larger Frank-Condon factor than the transition to $v' = 0$. The displacement to the right of the Morse potential curve in the excited state makes the overlap with the excited vibrational states larger than that for the ground state, so the transition to vibrationally excited states is more likely.

THEORETICAL BACKGROUND

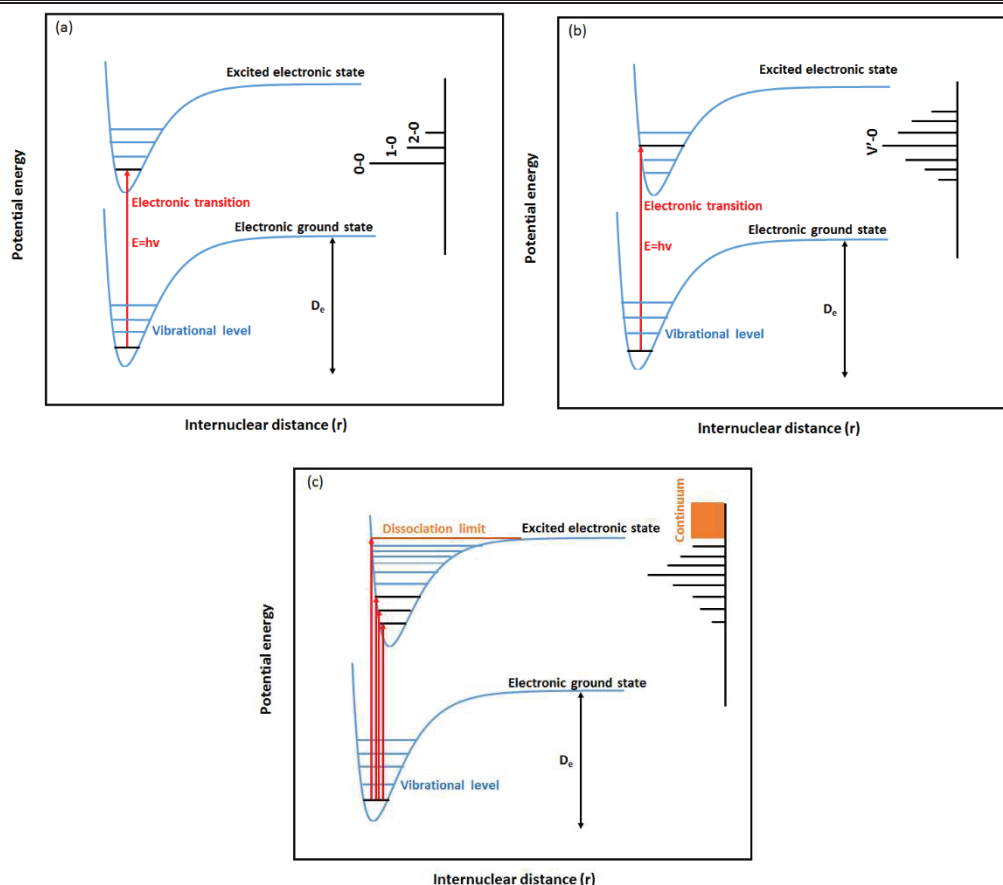


Figure 2-1: Diagram of the Franck-Condon principle. (a) The PECs of the two states are similar with similar equilibrium distances $r_e \approx r_e'$ and the resulting distribution of the absorption probability shown on the right is maximum for $v' = 0$. (b) The PECs of the two states have different equilibrium distances $r_e \neq r_e'$ and the resulting distribution of the absorption probability shown on the right is maximum for $v' > 0$ (c) Extension of Franck-Condon overlap above the dissociation limit [199].

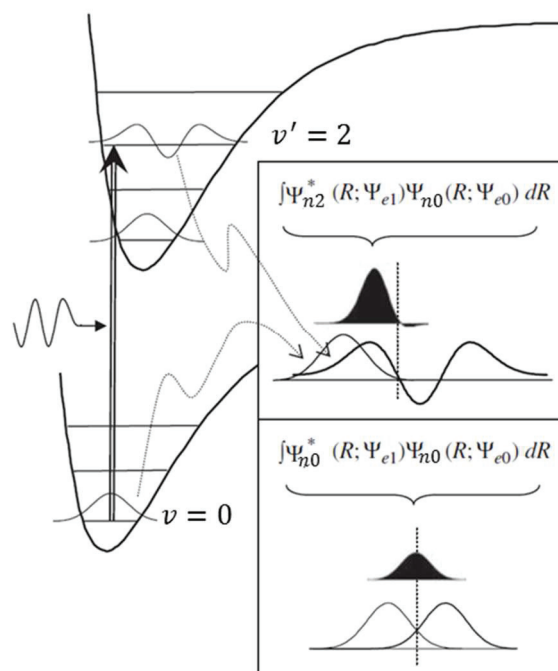


Figure 2-2: The overlap integral for the ground state vibration with $v=2$ vibration in the electronically excited state [200].

In some cases, Franck-Condon overlap extends above the dissociation limit such that excited-state dissociation energies can be measured directly (Figure 2-1(c)). When this is not

THEORETICAL BACKGROUND

the case, but several vibrational levels are excited, it sometimes remains possible to extrapolate the absorption spectrum to determine the dissociation limit.

The Franck-Condon principle for PAH cations is rather complicated because there are many atoms, making the potential as a function of internuclear distances a multi-dimensional PES. However, the Franck-Condon integrals of some electronic transitions have been calculated for a few PAH cations, e.g., anthracene as displayed in Figure 2-3, and line profiles have been simulated at different temperatures to be compared with experimental spectra [201]. In the case of the dimer cations of PAH, when considering the intermolecular bonding, in reduced dimensionality, i.e., treating the different degrees of freedom independently, this reasoning will help interpret the experimental photo-dissociation spectra.

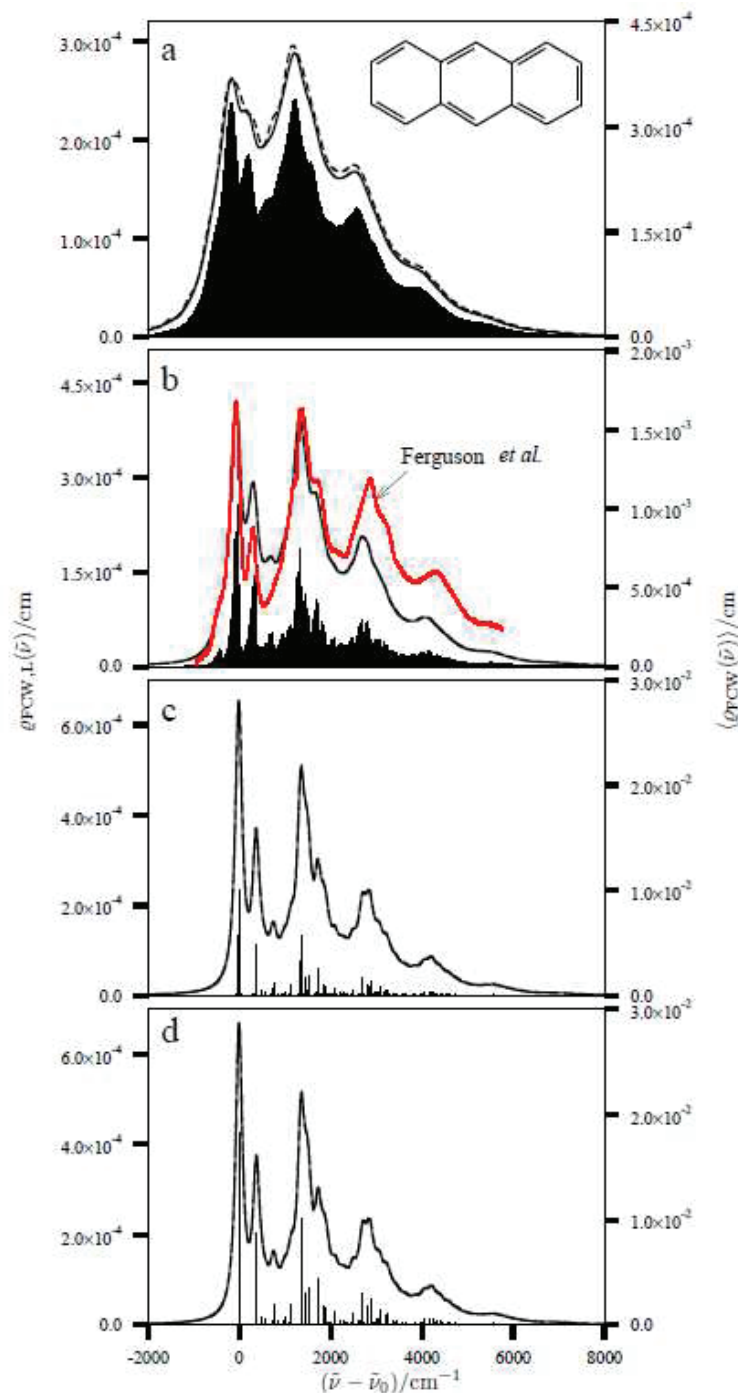


Figure 2-3: Calculated Frank-Condon profiles for the absorption spectra of anthracene molecules at different temperatures (a) 500 K, (b) 300 K, (c) 100 K, and (d) 0 K. The sticks axis represents the average Franck-Condon factors weighted by the density of states [201].

2.1.7 Potential energy surface

The BO approximation leads to obtain the PES of a quantum system and identify the equilibrium configuration of the system with the lowest point on the surface. PESs have an important role in the study of atomic and molecular systems. It is simply defined as a relationship between the total energy of the system as a function of geometric coordinates; as a function of internuclear coordinates. The energy of the molecule is plotted on the vertical axis, and geometric coordinates are plotted on the horizontal axes. For complex molecules (i.e., made of more than two atoms), including PAHs, PESs are highly multidimensional with secondary minima corresponding to isomers. A graphical representation of such PESs is complex because of the large number of degrees of freedom. Figure 2-4 shows a schematic illustration of the potential energy surfaces in one and more dimensions. For multiple dimensions, it is often necessary to reduce the dimensionality for the representation of the PES along some chosen coordinates of special interest. The equilibrium geometry is a minimum energy geometry that matches the positions of the minima in the valleys on a PES. The vibrational spectrum is determined by the shape of the valley around minimum energy, whereas the electronic spectrum is determined by the separation between potential energy surfaces of the electronic states of the system. The physical properties of the system, such as electronic dipole, polarizability are subject to the response of the energy to applied electric and magnetic fields. After the PES is determined, it is possible to solve the nuclear Schrödinger equation. The solution of the nuclear Schrödinger equation allows us to determine a large variety of the properties of the system, such as vibrational energy levels.

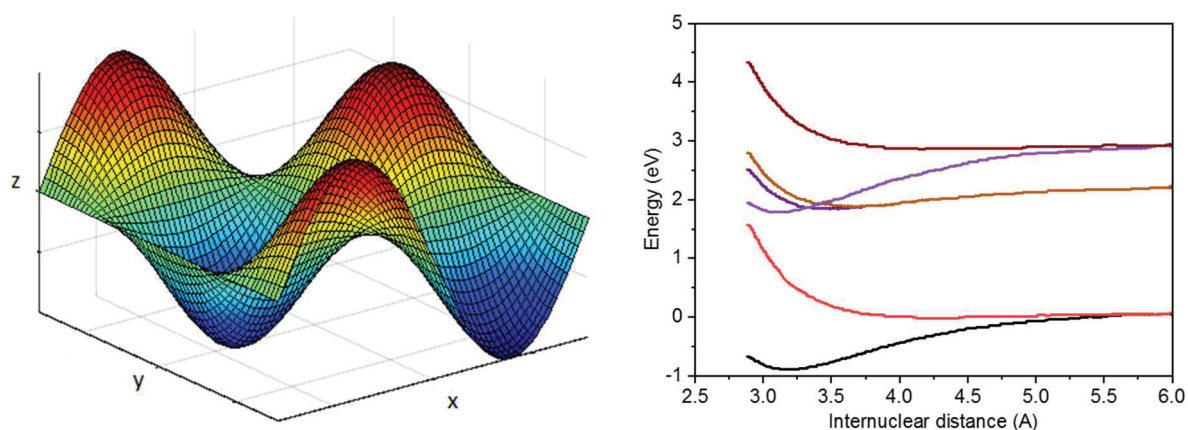


Figure 2-4: (left) schematic diagram of two dimensional PES (right) PEC for benzene dimer computed based on the Morse functions.

2.2 Theory for dimer cations

2.2.1 The charge resonance (CR) and local excitation (LE) transitions

The interaction between neutral and ionized molecules has an important role in the study of action absorption spectra of PAHs in the range of UV to near IR. The delocalization of the charge in dimers is important in the study of electronic spectroscopy. In the absence of interaction between two identical molecules, M_1 and M_2 where M stands for the monomer molecule, the total wavefunction of neutral dimer can be given by:

$$\Phi_{1,2} = \Phi_1\Phi_2 = \Phi_2\Phi_1 \quad \text{Eq. (2-23)}$$

In the dimer cations, the charge can be set on M_1 or M_2 leading to two possible configurations:

THEORETICAL BACKGROUND

$$M_1^+ - M_2 \text{ and } M_1 - M_2^+ \quad \text{Eq. (2-24)}$$

Once a charge is localized on one molecule, an induced dipole occurs on the other one. This leads to a long-range attractive force due to the polarization of the neutral. As a result of that, a splitting of the energy level into two states, namely bonding state and antibonding state, is taking place. The Hamiltonian is given by:

$$H = \begin{pmatrix} E_0 & V \\ V & E_0 \end{pmatrix} \quad \text{Eq. (2-25)}$$

where the diagonal E_0 is the sum of the energies of the neutral and cationic monomers and V is the non-diagonal interaction matrix elements.

$$E_0 = E(S_0) + E(D_0) \quad \text{Eq. (2-26)}$$

where S_0 is the ground state of the neutral and D_0 is the ground state of the cation.

Therefore, the solution of the Hamiltonian can take this form:

$$\psi_{\pm} = \frac{1}{\sqrt{2}} [\Phi_{1,2}(M_1^+, M_2) \pm \Phi_{1,2}(M_1, M_2^+)] \quad \text{Eq. (2-27)}$$

The interaction matrix elements can be given by:

$$V = \langle \Phi_{1,2}(M_1^+, M_2) | H | \Phi_{1,2}(M_1, M_2^+) \rangle \quad \text{Eq. (2-28)}$$

The new eigenvalues are then given by

$$E_{\pm} = E_0 \pm V \quad \text{Eq. (2-29)}$$

The transition between those states is allowed and the energy gap is given by:

$$E_+ - E_- = 2V \quad \text{Eq. (2-30)}$$

This transition between those states is called the charge resonance transition (CR).

Other excited states of the dimer can be formed from the excited states of the monomers and the transitions between the ground state and these excited states are called local excitation (LE) transitions [202,203]. These CR and LE level splittings are illustrated in Figure 2-5.

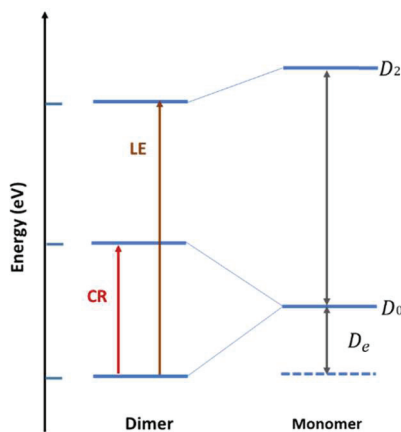


Figure 2-5: Energy level diagram illustrating the level splitting for the CR transition. The second excited state of the dimer is also formed from the excited states of the monomers by such a kind of level splitting.

2.2.2 DFTB calculations to account for charge resonance

Dontot et al. [204] have calculated PECs along the inter-molecular dissociation coordinates and oscillator strengths, using density functional based tight binding with the extended configuration interaction DFTB-CI and Complete Active Space Perturbation Theory CASPTS, for the three PAH dimer cations (benzene, naphthalene, and pyrene) which we have investigated experimentally in the present thesis work (chapter 6). In ref. [204], a few selected frozen geometries such as Sandwich, T-shaped, and rotation of the neutral molecules were discussed.

For the naphthalene dimer, Dontot et al. found the T-shaped geometry leads to a smaller level splitting than the sandwich geometry [204]. Therefore, the most stable structure should be the sandwich geometry. They have calculated the stabilization energies and the equilibrium distances along the sandwich geometry dissociation path in order to compare the two theoretical methods (DFTB-CI and CASPTS). In this paper, they also demonstrate that the PECs of pyrene dimers strongly depend on the twist angle between the two monomers around the intermolecular axis. This dependency is expected to affect strongly the dissociation pathway (see Fig. 6 of ref. [204])

The obtained PECs in ref. [204] for these three dimer cations along their dissociation pathway are very similar to Morse potentials often used for diatomic molecules. Consequently, as a first attempt for interpreting our photo-dissociation spectra discussed in chapter 6, we tentatively utilized one-dimensional ‘effective Morse PECs’ in the cases where no other more sophisticated multidimensional PESs were available.

2.2.3 Morse PECs and photo-dissociation spectra of PAH dimer cations

As mentioned in the previous section, in Chapter 6, we will use ‘effective Morse PEC’ to calculate model photo-dissociation spectra for benzene, naphthalene, and pyrene dimer cations. Using directly the PECs of ref. [204] did not allow us to reproduce the experimental results because the problem cannot be reduced in a single dimension. It would be most probably necessary to account for possible angular motion between the two monomers, adding thus at least two more dimensions to the problem. To overcome this problem, we will parametrize single dimension Morse PECs to calculate photodissociation spectra and, finally, adjust the parameters such that the model spectrum fits with the experimental one. With this procedure, we expect to obtain PECs in the inter-molecular dissociation coordinates that average effects due to the angular motions. In this section, we will shortly introduce basic concepts used to derive the PECs and the model photo-dissociation spectra. The results will be discussed in chapter 6.

2.2.3.1 Harmonic/Anharmonic PEC

Let us consider a diatomic molecule AB, where the atoms A and B are separated by the distance r and interact via the potential $V(r)$. In the harmonic oscillator approximation, the molecular vibrational motion is given by the following Hamiltonian:

$$H = -\frac{\hbar}{2\mu} \frac{d^2}{dx^2} + \frac{1}{2} \mu \omega_e^2 (r - r_0)^2 \quad \text{Eq. (2-31)}$$

where μ is the reduced mass $\mu = \frac{m_A m_B}{m_A + m_B}$ and r is the distance from equilibrium.

The potential energy of the harmonic oscillator can be written as:

$$V(r) = \frac{1}{2} K (r - r_0)^2 \quad \text{Eq. (2-32)}$$

THEORETICAL BACKGROUND

where r_0 is the equilibrium distance and K is a constant. This potential has a parabolic shape with no upper limit to it (Figure 2-6). The allowed vibrational energies are quantized and given by:

$$E_v = \left(v + \frac{1}{2}\right) h\omega_e \quad \text{Eq. (2-33)}$$

where the vibrational frequency is $\nu_e = \omega_e/2\pi = (1/2\pi)\sqrt{K/\mu}$. $h\nu_e$ also corresponds to the energy gap between equally spaced energy levels.

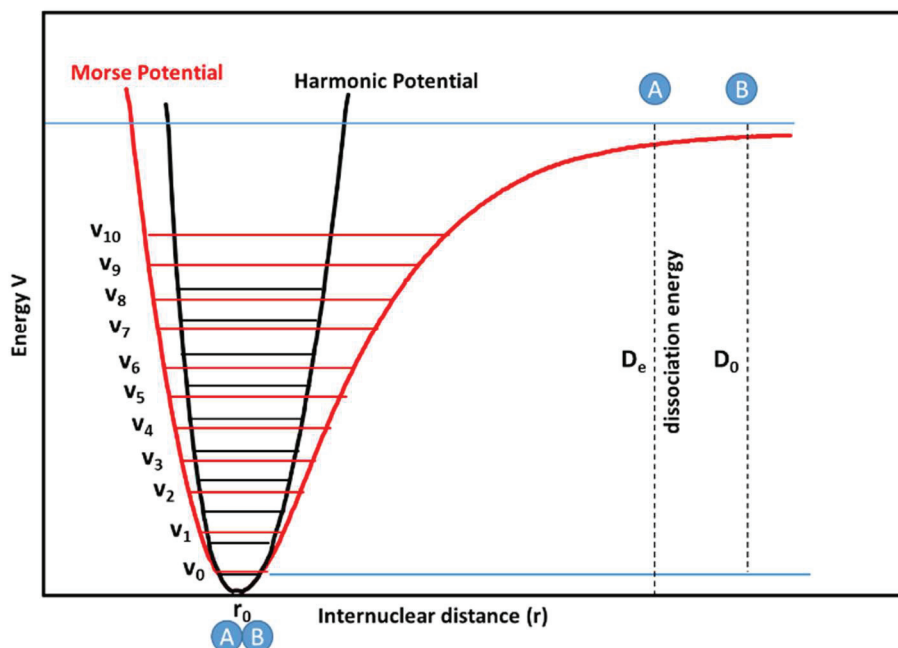


Figure 2-6: Harmonic and anharmonic Morse potentials.

The harmonic oscillator is utilized for molecular vibration at very low vibrational energies. However, the dissociation of the molecule at high energies cannot be explained by this model. The anharmonic Morse Potential is one of the commonly used models of PECs to account for dissociation at high vibrational energy.

In Morse potential, the difference between adjacent levels decreases with increasing vibrational energy. The oscillation period increases when the vibrational energy approaches the dissociation energy, the restoring force decreasing sharply when the molecule is very stretched. The number of vibration levels is finite. The Morse potential is described as:

$$V(r) = D_e \{1 - e^{-a(r-r_0)}\}^2 + V_e \quad \text{Eq. (2-34)}$$

where r_0 is the equilibrium distance, D_e is the dissociation energy of the molecule that is slightly larger than the bond energy D_0 due to the zero-point energy, a is a parameter that can be expressed as $a = \sqrt{\frac{k_e}{2D_e}}$, and V_e is the potential energy at r_0 .

The Schrödinger equation for the vibrational motion of nuclei can be analytically solved and gives rise to a series of energy levels that are given by:

$$E_v = -D_e + \left(v + \frac{1}{2}\right) h\omega_e - \left(v + \frac{1}{2}\right)^2 \frac{(\hbar^2 \omega_e^2)}{4D_e} \quad \text{Eq. (2-35)}$$

$$E_v = -D_e + \left(v + \frac{1}{2}\right)\omega_e - \left(v + \frac{1}{2}\right)^2 \omega_e x_e \quad \text{Eq. (2-36)}$$

where $\omega_e = \sqrt{\frac{2D_e a^2}{m}}$ is the harmonic frequency, v is the vibrational quantum number ($v = 0, 1, 2, 3 \dots v_{max}$), and x_e is the anharmonicity constant.

The spectral coefficients are related to finite dissociation energy by:

$$D_0 = -E_0 = -D_e - \frac{1}{2}\hbar\omega_e - \frac{\hbar^2 \omega_e^2}{16D_e} \quad \text{Eq. (2-37)}$$

To find the dissociation limit, $\frac{dE_v}{dv} = \omega_e - 2\omega_e x_e \left(v + \frac{1}{2}\right)$ at v_{max} should be equal to zero:

$$\frac{dE_v}{dv} = \omega_e - 2\omega_e x_e \left(v_{max} + \frac{1}{2}\right) = 0 \quad \text{Eq. (2-38)}$$

This leads to $v_{max} = \frac{\omega_e}{2\omega_e x_e} - \frac{1}{2}$ and hence to $E_{v_{max}} = D_e = \frac{\omega_e^2}{4\omega_e x_e}$.

For polyatomic molecules, the number of vibrational degrees of freedom increases. Each vibration should be associate with its anharmonicity constant. Therefore, in the first approximation, the polyatomic vibrational energy is then given as a set of independent normal modes.

$$E_v = -D_e + \sum_i \left(v_i + \frac{1}{2}\right)\omega_i - \sum_i \sum_j \left(v_i + \frac{1}{2}\right)\left(v_j + \frac{1}{2}\right)\omega_e x_{ij} \quad \text{Eq. (2-39)}$$

However, in the second approximation, it should be considered that anharmonicity should induce a coupling between the different modes such that they should not be considered as independent modes.

2.2.3.2 The reflection principle

In direct photo-dissociation processes, the parent molecule breaks up rapidly after photon absorption. It is excited to an unbound state whose lifetime is very short compared to the vibrational periods of the molecule. Oppositely, indirect photo-dissociation processes, due to the potential barrier and other forces delay the direct photo-dissociation of the excited state, the order of magnitude of the lifetime may correspond to several vibrational periods.

The energy dependence of the photo-dissociation spectrum and the final state distribution of the products in the direct photo-dissociation process are related to the initial coordinate distribution of the system in the initial electronic state (ground or excited state) and the shape of the dissociative PEC. This is the reflection principle as illustrated in Figure 2-7 for a diatomic molecule. The absorption spectrum reflects the coordinate distribution of the molecule in the initial electronic state. The line width of the spectrum results mainly from two factors: the initial coordinate distribution and the steepness of the excited state of PEC, i.e., the steeper the potential, the broader the line.

THEORETICAL BACKGROUND

overlaps the oscillatory part of the scattering wavefunction and the cross-section again diminishes because positive and negative contributions mutually cancel [205].

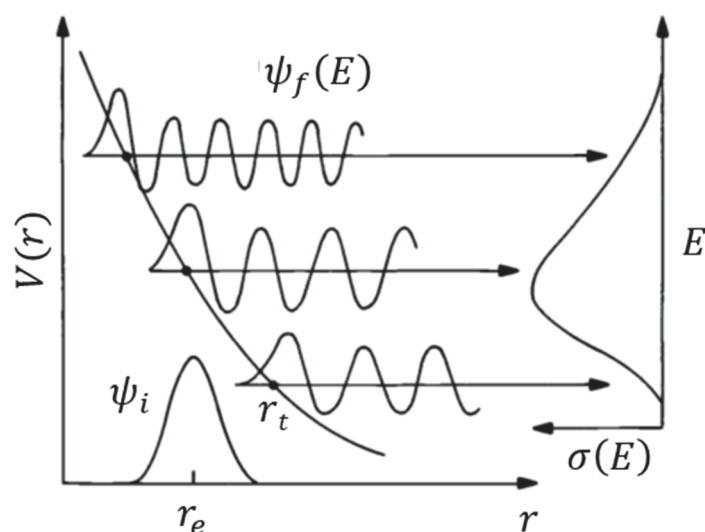


Figure 2-8: Schematic diagram of the overlap of a bound and a continuum wavefunction as a function of energy. r_t is the classical turning point.

2.3 Statistical Models for the relaxation processes of isolated systems

This section is devoted to the statistical models that are useful to derive rate constants that are needed to interpret unimolecular dissociation of ‘hot’ molecules, e.g., PAH cations in the present work, as well as the radiative cooling process, i.e., the recurrent fluorescence and the infrared emission. These concepts apply especially to the interpretation of the experimental results on PAH cations in general and therefore on the phenanthrene cations presented in chapter 5.

2.3.1 RRKM theory

Rice, Ramsperger, and Kassel developed a statistical model (RRK) to quantify the dissociation rates of molecules as a function of their internal energy [206,207]. In this model, the molecule [208] composed of N atoms is assumed to be a set of $s = 3N - 6$ independent coupled harmonic oscillators. The dissociation reaction is assumed to take place if the energy accumulated on one of the harmonic oscillators becomes greater than some critical energy E_0 . All the degrees of freedom are treated with the same probability. The probability of dissociation P is defined as the ratio between the number of ways of distributing the energy E over the oscillators such that the energy in at least one oscillator is higher than E_d , and the number of ways of distributing energy E over all the oscillators. The probability of reaction P can be given by:

$$P = \frac{(E - E_d)^{s-1}/(s-1)!}{E^{s-1}/(s-1)!} = \left(\frac{E - E_d}{E}\right)^{s-1} \quad \text{Eq. (2-44)}$$

Therefore, the dissociation rate can be obtained by multiplying P by the rate A at which the energy is exchanged between the different modes. A is expected to be much larger (by orders of magnitudes) than that of the unimolecular dissociation rate itself.

$$k_d(E) = A \left(\frac{E - E_d}{E}\right)^{s-1} \quad \text{Eq. (2-45)}$$

THEORETICAL BACKGROUND

The RRKM theory was developed by Marcus based upon the concepts of the RRK theory. It is also called quasi-equilibrium theory (QET). In this theory, the transition state, which is at the maximum of the PES along with the coordinate reaction, is used to calculate the dissociation rate. It is relying on two assumptions: (i) all energy states are accessible and have the same probability of population, (ii) dissociation processes occur in a slower timescale than energy redistribution processes such as the intramolecular vibrational energy redistribution (IVR). Under these two assumptions, statistical mechanics can be utilized to calculate the dissociation rate at which trajectories pass through the transition state.

Let ν be the frequency of passage through the transition state. The dissociation rates can be calculated as the ratio between the density of states at the transition state $\rho(E^t)$ and at the stable state $\rho(E_\nu)$:

$$k_d(E) = \frac{\nu \rho(E^t)}{2 \rho(E_\nu)} \quad \text{Eq. (2-46)}$$

During motion through the transition state, one vibrational mode can be treated as an internal translational motion. Therefore, the density of states at the transition state can be written as:

$$\rho(E^t) = \sum N(E_\nu^t) \rho(E_t^t) \quad \text{Eq. (2-47)}$$

where $N(E_\nu^t)$ is the sum of vibrational states at E_ν^t , $\rho(E_t^t)$ is the density of transitional state at $E_t^t = E^t - E_\nu^t$. The rate of dissociation with internal energy can be then given by:

$$k_d(E) = \frac{N(E^t)}{h \rho(E_\nu)} \quad \text{Eq. (2-48)}$$

where $N(E^t)$ is the sum of vibrational levels at E^t . This equation is called RRKM expression for the dissociation rate [209].

2.3.2 The microcanonical temperature for small isolated systems

For an isolated system, the energy is conserved and the system with a specific energy E can be treated as a microcanonical ensemble. The microcanonical temperature T_m can be defined in terms of the level density of the system, which gives the number of states between the energy E and $E + dE$:

$$\frac{1}{k_B T_m} = \frac{d}{dE} \ln \rho(E) \equiv \frac{1}{\rho(E)} \frac{d\rho(E)}{dE} \quad \text{Eq. (2-49)}$$

where k_B is Boltzmann's constant and $\rho(E)$ is given by differentiating the total number of states with respect to energy.

For the emission of small fragments from a cluster, the probability per unit time and unit energy for emission of a particle with energy ϵ can be given by:

$$k(E, \epsilon) = A(\epsilon) \frac{\rho_d(E - E_b - \epsilon)}{\rho_p(E)} \quad \text{Eq. (2-50)}$$

where E is the initial excitation energy of the system, E_b is the binding energy of the particle, ρ_p , ρ_d are the density of states of parent and daughter clusters, $A(\epsilon)$ is proportional to the cross-section for the reverse process.

THEORETICAL BACKGROUND

The decay rate can be obtained by approximating the logarithm of the density states of the daughter ion using a first-order Taylor expansion:

$$\frac{1}{k_B T_d} = \frac{d}{dE} \ln \rho_d(E - E_b) \quad \text{Eq. (2-51)}$$

$$k(E, \epsilon) d\epsilon = A(\epsilon) \frac{\rho_d(E - E_b)}{\rho_p(E)} e^{-\frac{\epsilon}{k_B T_d}} \quad \text{Eq. (2-52)}$$

where T_d is the microcanonical daughter temperature

$$k(E, \epsilon) \propto e^{-\frac{\epsilon}{k_B T_d}} \quad \text{Eq. (2-53)}$$

The total decay rate is given then by integration of $k(E, \epsilon)$ over:

$$k(E) = v(T_d) \frac{\rho_d(E - E_b)}{\rho_p(E)} \quad \text{Eq. (2-54)}$$

By integrating energies between $E - E_b$ and E , the decay rate can be written in Arrhenius form

$$k(E) = v e^{-\frac{E_b}{k_B T_e}} \quad \text{Eq. (2-55)}$$

To find the relationship between the microcanonical temperature and the emission temperature T_e , the density of the state is expanded in the Taylor series considering the heat capacity is constant [210]

$$\ln \frac{\rho(E - E_b)}{\rho(E)} = \frac{-E_b}{k_B (T_m - \frac{E_b}{2C_m})} \times \left(1 + \frac{-E_b^2}{12 C_m^2 (T_m - \frac{E_b}{2C_m})^2} \right) \quad \text{Eq. (2-56)}$$

Using the heat capacity, the emission temperature T_e is given by

$$T_e = T_m - \frac{E_b}{2C_m} \quad \text{Eq. (2-57)}$$

Leger et al. [211] calculated the specific heat capacity of several PAH molecules relative to their maximum value $C_{max} = (3N - 6)k$, where N is the number of atoms. The ratio provided identical curves for different PAHs are given by:

$$\frac{C}{C_{max}} = (1 - e^{-\beta T + \theta}) \quad \text{Eq. (2-58)}$$

where β and θ are fitting parameters, which have been found, for anthracene cation, to be 0.00186 K^{-1} and 0.1327 , respectively [212].

2.3.3 Relaxation of internal energy

For gas-phase systems under high isolation conditions, e.g., atomic or molecular beams stored in electrostatic ion storage devices, when sufficient energy has been gained to exceed at least the lowest activation energy, processes will take place to let the system relax towards its

THEORETICAL BACKGROUND

ground state. Such relaxation processes by eventually emitting particles will irreversibly reduce the internal energy of the system. They are generally denoted as cooling processes. When several relaxation processes are energetically possible, they are often competing depending on their relative rates. In molecular physics, the most common relaxation processes are electron emission (ionization), emission of atoms or small molecules (unimolecular dissociation or fragmentation), and emission of photons [91]:

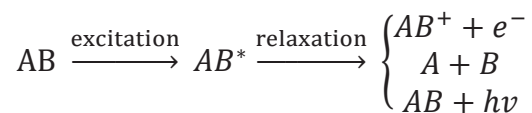


Figure 2-9 illustrates the competition between all these decay channels for anthracene cations and the dependence of the decay rate constants of each channel on the internal energy of ions. The frequency factor and the activation energy are essential data to determine the rate of the relaxation processes. As they are often not known, they can be used as adjustable parameters in models.

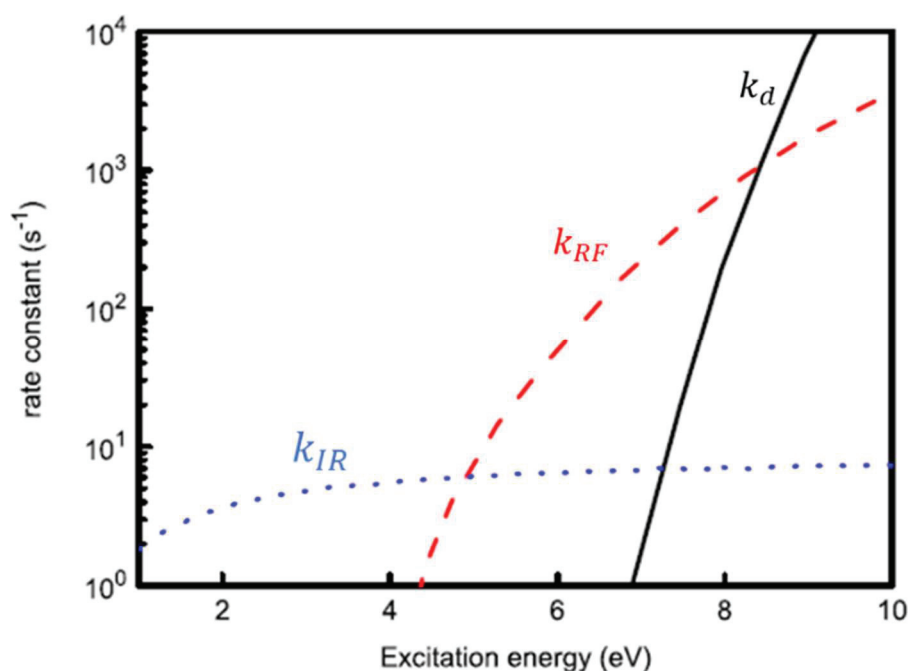


Figure 2-9: Rates of dissociation (k_d), IR vibrational emission (k_{IR}), and recurrence fluorescence (k_{RF}) as a function of the internal energy of singly charged anthracene cation [134].

For isolated molecular cations, IR emission, fluorescence, and dissociation are the main relaxation routes for energy decay after photon absorption. For PAH cations, after absorption of a visible or UV photon, an electronic transition initially takes place from the electronic ground state denoted as doublet D_0 to higher excited states like $D_1 \dots D_n$. In several cases, e.g., naphthalene, anthracene, phenanthrene, etc., the transition to D_1 is forbidden by symmetry in small PAH cations. Then, different processes may occur; some of them can be radiative (IR emission, fluorescence, phosphorescence) (section 2.3.3.2) or non-radiative processes (internal vibrational redistribution IVR, internal conversion IC, inverse internal conversion IIC, and intersystem crossing ISC) (section 2.3.3.1). Additionally, dissociation processes may occur when the internal energy of the molecular ion is higher than the dissociation limit. All these processes are illustrated in Figure 2-10. The photo-dissociation rate is highly dependent upon the initial absorption rate and the competition with other competing processes. These relaxation mechanisms will be explained in more detail in the following, and the typical corresponding lifetimes are given in Table 2-1.

THEORETICAL BACKGROUND

- **Inverse internal conversion (IIC):** This process occurs reversely between vibrationally lower electronic states to higher electronic states ($D_0 \rightarrow D_n$) and its transition rate is much slower than the IC process.

2.3.3.2 Radiative transition processes

The excited molecules can emit photons by several main processes: Fluorescence (F), phosphorescence (P), infrared (IR), and also recurrent fluorescence (RF) as studied in this work. These processes are symbolized in Figure 2-10 by corresponding arrows between involved initial and final states. RF and IR emissions will be discussed in the next sections (2.3.4 and 2.3.5, respectively).

After photon absorption, fluorescence results from the spontaneous re-emission of a photon, often at a longer wavelength, between two electronic states of the same multiplicity with a dipole-allowed electronic transition, as illustrated in Figure 2-11(a). It involves a ‘vertical’ transition from the lowest energy vibrational levels of a higher electronic excited state to a lower electronically excited state or to the electronic ground state. Therefore, fluorescence leads to the re-emission of a fraction of the energy of the initially absorbed radiation. However, for PAH cations, the direct fluorescence rate is in general much smaller than the rates for IVR and IC (Table 2-1). Therefore, it is expected to be a negligible process in the following discussions.

Moreover, some molecular systems can sometimes go through inter-system crossing to an electronic state with a different spin multiplicity. Then, phosphorescence can occur from an excited electronic state to down to the ground state in a spin-forbidden transition, as shown in Figure 2-11(b). Therefore, phosphorescence is a delayed emission of a fraction of the energy of the initially absorbed radiation. Phosphorescence is a much slower process than fluorescence and can take place over a timescale of the order of the second or even longer after the absorption of photon [181].

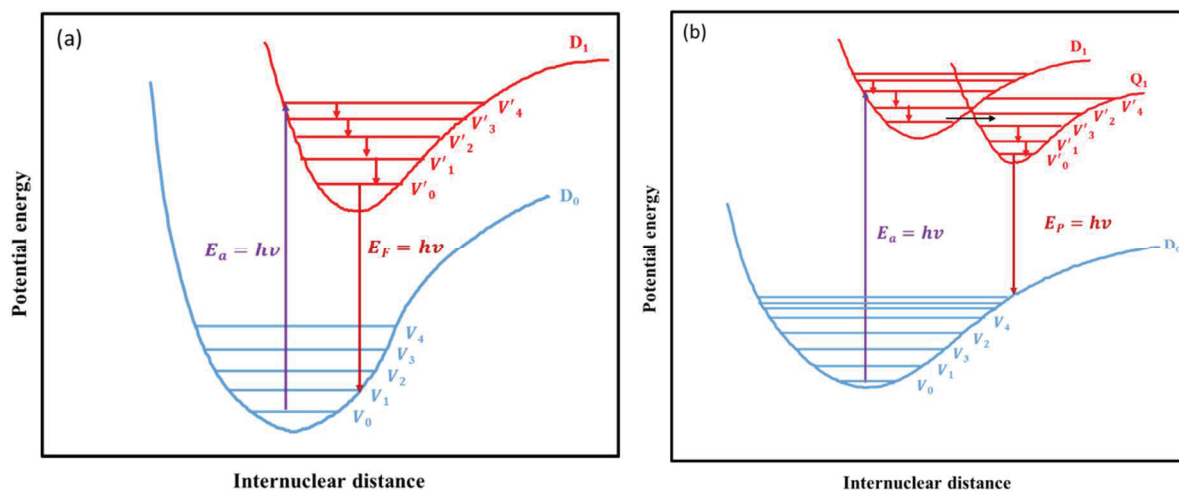


Figure 2-11: Schematic illustration for (a) fluorescence and (b) phosphorescence [181].

The relaxation processes considered in this work take place on the timescales range of μs to several of ms . Fluorescence processes are not taken into consideration in the Mini-Ring experiment because it would be much faster than the observation time window of the experiments. However, when photon absorption is immediately followed by fluorescence, i.e., the emission of a photon of possibly smaller energy than the absorbed one could be expected to contribute to a very small reheating of the stored PAH cations. The coupling between doublet and quadruplet states is also a very unlikely process and the corresponding lifetimes are expected to be much larger than the typical time of other discussed processes. Consequently, phosphorescence is regarded as a negligible process in this work.

2.3.4 Recurrent/Poincaré fluorescence

Léger et al. [8] proposed in 1988 the existence of a statistical electronic fluorescence process known as recurrent fluorescence (most commonly used name nowadays) or Poincaré fluorescence (initial name). In this process, for highly isolated PAH cations, since energy can remain in the vibrational modes of the ground electronic state for a long time, energy transfer from the lower energy electronic state D_0 to a higher energy electronic state D_n may occur via the IIC processes described in section 2.3.3.1 [8]. The IIC process is an intermediate step that can be followed by the emission of a visible or near IR photon to return to the ground electronic state but in a much lower vibrational state. The whole process removes at once a rather high amount of energy (compared to a single vibrational IR emission) and contributes to efficiently cool down PAH cations. This process is symbolized in Figure 2-10 by arrows with ‘RF’ labels.

If all electronic and vibrational states are equiprobable, the time spent in an electronic state i , t_i with a vibrational energy U_i is proportional to its density of states $\rho(U_i)$. Therefore, we can write the following ratio between the times spent in state i and the ground state ($i = 0$) with vibrational energy U_0

$$\frac{t_i}{t_0} = \frac{\rho(U_i)}{\rho(U_0)} \quad \text{Eq. (2-59)}$$

The density of states $\rho(U)$ increases very quickly with the vibrational energy U of the electronic state. It can be calculated, when the vibrational modes are known, by either exact state counting (Bayer-Swinehart algorithm [216,217]) or by the use of an analytic approximation in the harmonic approximation using the Rabinovitch-Whitten formula [218,219].

$$\rho(U) = \frac{(U + aE_z)^{s-1}}{(s-1)! \prod_i h\nu_i} \quad \text{Eq. (2-60)}$$

where $h\nu_i$ are the energy of vibrational modes, s is the number of modes, E_z is the total zero-point energy and a is a correction factor $0 < a < 1$.

For the first excited state, we can expect that the vibrational energy U_1 is downshifted from U_0 by $\Delta E = E(D_1, 0) - E(D_0, 0)$. Therefore, the ratio between the times spent in the (D_1, U_1) and (D_0, U_0) states is given by:

$$\frac{t_1}{t_0} = \frac{\rho(U_1)}{\rho(U_0)} = \frac{\rho(U_0 - \Delta E)}{\rho(U_0)} \quad \text{Eq. (2-61)}$$

The density of states ratio $\rho(U_1), \rho(U_0)$ for $N=18$ atoms was estimated to be in the range 10^{-16} to 10^{-3} and for $N=36$ atoms was estimated to be in the range 10^{-22} to 10^{-5} for the internal energy range of 2-14 eV. These ratios are small yet high enough to induce the RF process [8].

The probability of finding the system in the state (D_1, U_1) is given by:

$$p_1 = \frac{t_1}{t_0 + t_1} = \frac{\rho(U_1)}{\rho(U_0) + \rho(U_1)} = \frac{\rho(U_0 - \Delta E)}{\rho(U_0) + \rho(U_0 - \Delta E)} \quad \text{Eq. (2-62)}$$

When the system is in the (D_1, U_1) , there is a certain probability for a spontaneous fluorescence photon emission which is related to the Einstein rate coefficient A_e of the transition. Therefore, the RF rate can be defined as:

$$k_e(U) = A_e \times p_1 = A_e \frac{\rho(U_0 - \Delta E)}{\rho(U_0) + \rho(U_0 - \Delta E)} \quad \text{Eq. (2-63)}$$

The energy of the emitted photon is expected to be $h\nu_e \approx \Delta E$ for transitions between vibrational levels of similar ν quantum numbers.

It is also expected that the density of vibrational states is much higher in the ground electronic state than in the excited state, i.e., $\rho(U_0) \gg \rho(U_0 - \Delta E)$. Therefore, the electronic transition rate can be approximated by [9]

$$k_e(U) \approx A_e \frac{\rho(U_0 - h\nu_e)}{\rho(U_0)} \quad \text{Eq. (2-64)}$$

The above expressions have been derived for RF processes involving the first electronic excited state. It can be generalized easily to any of the electronically excited states. For small PAH cations, like anthracene or naphthalene, it has been shown that the first excited state, labeled D_1 , cannot contribute to this process since the fluorescence is forbidden by symmetry. For these cations, it was shown that the RF could occur through the D_2 state. Other electronic excited states of higher energy could also contribute but not very significantly because their density of vibrational states become too small.

2.3.5 IR vibrational emission - IR cooling

For an isolated ion composed of N atoms with an internal energy U , the IR emission is treated as a statistical process. The internal energy U is redistributed over the $3N - 6$ modes and decreases gradually among vibrational levels when photons are emitted. The IR photon emission process is characterized by a transition between two vibrational states of one of the modes of the molecule. For the vibrational mode ν_i , the rate of IR emission of the transition $\nu \rightarrow \nu - 1$ is given by:

$$k_{i,\nu} = \nu A_i \frac{\rho^*(U - \nu h\nu_i)}{\rho(U)} \quad \text{Eq. (2-65)}$$

where ρ^* is the density of states of the system without ν quanta in the i mode, A_i is the Einstein coefficient of spontaneous emission of the $1 \rightarrow 0$ transition.

For an ensemble of ions with a large number of vibrational modes, it is hard to determine the emission mode and transition levels at a particular time. Boissel et al. defined an average IR cooling rate, i.e., an energy shift rate, η_{IR} , as the total energy per second (unit in eV/s) emitted in an ion ensemble. It can be expressed by [9]:

$$\eta_{IR}(U) = \left(\frac{dU}{dt} \right)_{IR} = \sum_i \sum_{\nu} k_{i,\nu} h \nu_i \quad \text{Eq. (2-66)}$$

The average rate, expressed in s^{-1} , of the radiative cooling processes can be given:

$$k_{IR} = \frac{1}{\Delta U} \left(\frac{dU}{dt} \right)_{IR} \quad \text{Eq. (2-67)}$$

As an example, Boissel et al. has estimated the IR emission rate for anthracene cations, to be about $k_{IR} = 2 s^{-1}$ in the energy range of 2-10 eV.

2.3.6 Power-law decay

In the present work, the quantification of radiative cooling will be performed by its influence on measured unimolecular decay rates without direct measurement of the photon emission. The photon emission and unimolecular dissociation are competing processes and are assumed to be both statistical. It implies that the population $P(E, t)$ of a state with specific energy E decays with an exponential time profile:

$$P(E, t) = P(E, t = 0) e^{-(k_d(E)+k_p(E))t} \quad \text{Eq. (2-68)}$$

where $k_d(E)$ is the unimolecular dissociation rate constant, $k_p(E)$ is the photon emission rate constant. It is noteworthy, as discussed in the previous sections, that the rates are highly dependent on E . For an ensemble of N_0 isolated systems having different internal energies, we can define the internal energy distribution (IED) as:

$$g(E, t) = \frac{P(E, t)}{N_0} \quad \text{Eq. (2-69)}$$

Our goal in the study of radiative cooling is to quantify the time evolution of $g(E, t)$, which is governed by the following rate equation:

$$\frac{\partial g(E, t)}{\partial t} = -k(E)g(E, t) \quad \text{Eq. (2-70)}$$

where $k(E) = k_d(E) + k_p(E)$ is the total decay rate.

The decay law, i.e., the number of dissociation events at time t is given by:

$$I(t) = \int_0^\infty k_d(E)g(E, 0)e^{-k(E)t} dE \quad \text{Eq. (2-71)}$$

where the initial distribution at time t decrease by a factor $e^{-k(E)t}$.

The decay rate can be obtained for either a single exponential decay when the excitation energy is considered as a narrow energy distribution at E_0 , i.e., $g(E, 0) \propto \delta(E - E_0)$, or for a system in thermal equilibrium with a heat bath. For narrow internal energy distribution, $I(t)$ is expressed as:

$$I(t) = \int_0^\infty \delta(E - E_0) e^{-k(E)t} k_d(E) dE = e^{-k(E_0)t} k_d(E_0) \quad \text{Eq. (2-72)}$$

Let us now consider an isolated ensemble, with a broad IED that extends to energies at which dissociation is dominant, i.e., $k_d(E) \approx k(E)$. The decay rate function becomes much faster varying function of E than $g(E)$; therefore $g(E)$ can be evaluated at energy E_m at which $e^{-k(E)t} k(E)$ peaks. Substituting $dE = \frac{dE}{dk} dk \equiv \frac{dk}{k'}$, where k' denotes the derivative of the function k , we have:

$$I(t) \cong g(E_m) \int_0^\infty e^{-k(E)t} k(E) dE = g(E_m) \int_0^\infty \frac{k(E)}{k'(E)} e^{-kt} dk \quad \text{Eq. (2-73)}$$

Since the factor $\frac{k}{k'}$ varies much less in the integral compared to the exponential, it can also be approximated at energy E_m . Multiplying Eq. (2-73) by t , we obtain:

$$\int dE k(E)t e^{-k(E)t} = \int d(kt) \frac{k}{k'} e^{-kt} \approx \frac{k(E_m)}{k'(E_m)} \quad \text{Eq. (2-74)}$$

Therefore, the decay law is given by:

$$I(t) = g(E_m) \left(\frac{k(E_m)}{k'(E_m)} \right) \frac{1}{t} \quad \text{Eq. (2-75)}$$

Under this assumption, t^{-1} varies much faster than the two first factors and the rate of neutral fragment emission with time become close to a t^{-1} function.

Alongside that the internal energy distribution is needed to be broad, the power-law decay differs from the exponential decay law in other aspects: a characteristic time does not exist; it is not dependent on the kind of emitted particle, i.e., it can be utilized for dissociation, photon and electron emission; it is not invariant under the time displacement [115].

For the photon emission with sufficient energy to quench dissociation, the decay rate can be given by:

$$I(t) = g(E_m) \left(\frac{k(E_m)}{k'(E_m)} \right) \frac{e^{-k_p t}}{t} \quad \text{Eq. (2-76)}$$

where k_p is the photon emission rate.

Power-law decays, with an exponent close to -1 , are observed in various experimental studies performed with ESDs, including the Mini-Ring, as well as the time of flight mass spectrometer experiments. In such a case, the only conclusion that can be obtained about the IED is that it is very broad. However, when a deviation from this law is observed, some conclusions may be drawn about the shape or the time evolution of the IED.

Another expression has been proposed and used in refs. [85,91,115] to account for the quenching by photon emission over broad ranges of time and internal energy:

$$I(t) = I_0 \left(\frac{t}{\tau} \right)^\delta \frac{1}{\exp\left(\frac{t}{\tau}\right) - 1} \quad \text{Eq. (2-77)}$$

where I_0 is an amplitude factor and τ is the typical quenching time. The latter equation will be used in chapter 5 to model the natural decays recorded for phenanthrene cations. It is noteworthy that at short times, $t \ll \tau$, Eq. (2-77) tends to:

$$I(t \ll \tau) = I_0 \left(\frac{t}{\tau} \right)^{-(1-\delta)} \quad \text{Eq. (2-78)}$$

Therefore, δ is interpreted as a quantification of (an expectedly small) deviation from the t^{-1} decay law.

2.3.7 Time evolution of the shape of the IED

The relaxation processes affect the evolution of the IED. The evolution of the IED can be calculated from the rate equation (Eq. (2-70)). After integration, the energy distribution is given by:

$$g(E, t) = g(E, 0)e^{-k(E)t} \quad \text{Eq. (2-79)}$$

where $g(E, t)$ is the IED of the ions at time t , $g(E, 0)$ is the initial IED at time $t = 0$.

Figure 2-12 displays the time evolution of the IED from an infinitely broad (flat) $g(E, 0)$ for phenanthrene cations (dashed horizontal line). It shows that the ions of high internal energy decay first, leading to a depletion of the high-energy side of the IED. Figure 2-12 also shows the IED at two different times, i.e., $g(E, t_1 = 0.1 \text{ ms})$ and $g(E, t_2 = 1.1 \text{ ms})$. The area between these two curves, multiplied by N_0 , the number of ions in the ensemble provides the number of dissociation of recurrent fluorescence photon events between t_1 and t_2 .

Consequently, after some given storage time in the Mini-Ring, the IED will present a rather sharp high energy edge (HEE) that leads to an observable deviation of the decay from the power-law. The energy at the HEE, E_{edge} is generally evaluated at $1/e$ of the maximum of $g(e, 0)$:

$$g(E_{edge}, t) = \frac{1}{e} g(E, 0) \quad \text{Eq. (2-80)}$$

In the experiment, the HEE is probed by photon absorption, whose role is to shift the IED such that the HEE corresponds to internal energies for which the dissociation process is dominant and corresponds to lifetimes that can be easily observed in the Mini-Ring.

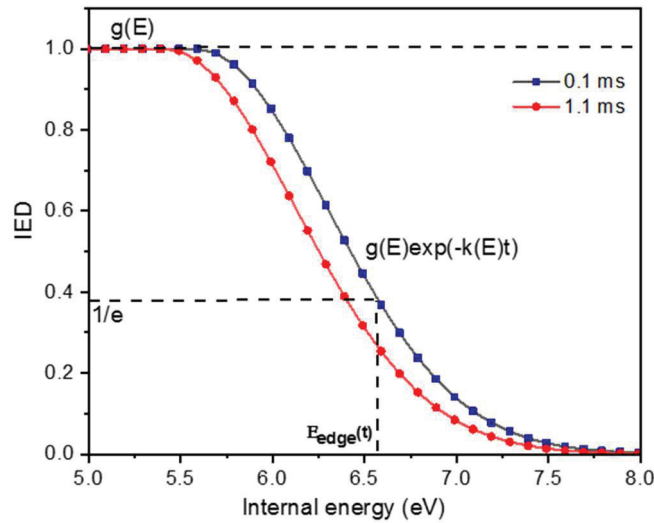


Figure 2-12: Time evolution of the IED illustrating depletion due to dissociation and radiative cooling for phenanthrene. The area between the two curves indicates the additional depletion during a small time interval of 1 ms.

It is possible to estimate how much time t_e is needed to reach a given E_{edge} by solving the following equation:

$$g(E_{edge}, t) = g(E, 0)e^{-k(E_{edge})t_e} = \frac{1}{e} g(E, 0) \quad \text{Eq. (2-81)}$$

We come to the following simple relation:

$$k(E_{edge}) = \frac{1}{t_e} \quad \text{Eq. (2-82)}$$

THEORETICAL BACKGROUND

Moreover, the dissociation rate is given by the Arrhenius law (Eq. (2-55)). Therefore, we can derive that the HEE at the time t_e is given by:

$$E_{edge}(t) = \frac{1}{K_B T_e} \times \frac{1}{\ln vt} + \frac{E_d}{2} = \frac{E_d C}{K_B} \times \frac{1}{\ln vt} + \frac{E_d}{2} \quad Eq. (2-83)$$

where T_e is the emission temperature that can be estimated from caloric curves that give relations between temperature and internal energy.

As can be noted from Eq. (2-83), depletion due to dissociation implies that the HEE is decreasing with time t when the dissociation is occurring, as can be shown in Figure 2-13.

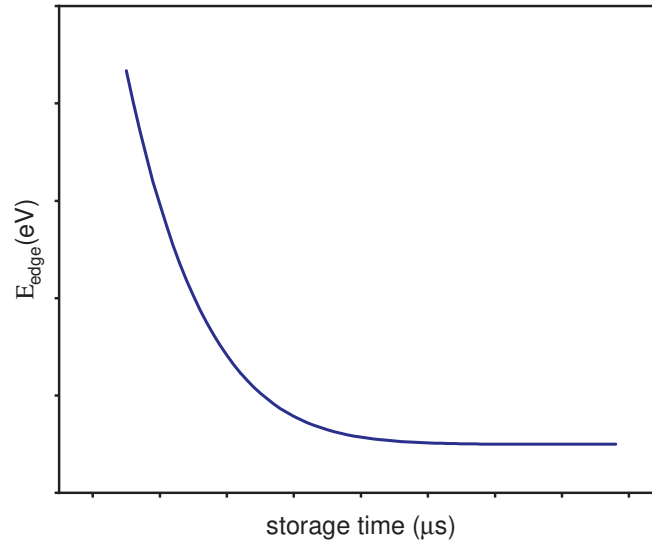


Figure 2-13: Schematic view of the decreasing function of the HEE energy E_{edge} vs time.

2.4 Decay rates for collision-induced dissociation of stored ions

In ESDs, stored ions may be dissociated by collisions with residual gas atoms. For N_0 initially stored ions, the number of remaining ions after a given trajectory length L is given by:

$$N(L) = N_0 e^{-\sigma(E_k)\rho L} \quad Eq. (2-84)$$

where ρ is the density of residual gas in the vacuum chamber, σ is the average collision cross-section and E_k is the kinetic energy.

In the case of constant kinetic energy, therefore constant velocity, v , the decay can be directly given as a function of time, t :

$$N(t) = N_0 e^{-\sigma_0 \rho v t} = N_0 e^{-t/\tau} \quad Eq. (2-85)$$

where σ_0 is the cross-section at given energy E_k and τ is the lifetime.

However, in the Mini-Ring, the stored ions are decelerated and accelerated by conical electrodes. Consequently, the integration of the rate equation is a bit more complex. Nevertheless, the decay curve remains exponential since the cross-section and the velocity are rather smooth functions of the kinetic energy and periodic functions of time:

$$N(t) = N_0 e^{-\rho \int \sigma_0 v dt} \approx N_0 e^{-t/\tau_{av}} \quad Eq. (2-86)$$

where τ_{av} is the lifetime averaged lifetime over one period of the ion trajectory.

2.5 Conclusion

This chapter presented a brief framework of theoretical background and concepts useful for the present thesis work. It was shown how the electronic structure of a molecular system and its properties could be determined using quantum theory in which the Born-Oppenheimer approximation is often used. For polyatomic molecules like PAHs, the Schrödinger equation cannot be solved exactly, emphasizing the importance of the different computational approaches. The density functional theory is effectively utilized to determine many features of the system of interest. Such techniques can provide results and then qualitative explanations of the properties of the system, which can help the experimentalists to interpret the experimental findings. Additionally, the potential energy surfaces were discussed to show how complex they can be due to the large number of degrees of freedom in the case of PAHs.

Photon absorption by PAHs and their dimers, which promotes electrons to electronically excited states was discussed. The corresponding electronic transitions occur on shorter timescales than the atomic vibrations. Thus, the Frank-Condon principle considers that the electronic transitions are instantaneous compared with nuclear motions, i.e., absorption is essentially a vertical transition while the nuclear coordinates remain unchanged.

When excited, for instance, by photon absorption, PAH ions lose their internal energy by different relaxation pathways. After the photon absorption, the molecule is promoted to a higher excited state, and the excess energy can be redistributed, converted between the electronic states and vibrational levels on different timescales by different processes. These are fluorescence emission via electronic states, IR emission via vibrational states, and the dissociation of molecular ions having internal energy higher than the threshold level of the dissociation. Besides, the RF mechanism was also introduced. In this mechanism, the vibrationally hot molecules in the electronic ground state are transferred back to an electronically excited state by the IIC process.

The time dependence of the dissociation events on the IED was also investigated. It was shown that this time-dependence follows a t^{-1} power-law decay for the unimolecular dissociation of an isolated and highly excited molecular ensemble of ions with infinitely broad IED. However, any deviation to this law may be giving information on the shape of the IED and, also, on the cooling dynamics of such an ensemble of hot molecular ions.

3 THE EXPERIMENTAL SET-UP

3	THE EXPERIMENTAL SET-UP	55
3.1	Principles of magnetic and electric deflection of charged particles.....	56
3.1.1	Deflection via magnetic field.....	56
3.1.2	Deflection via electric field.....	57
3.1.3	Comparison between electrostatic and magnetic rings.....	58
3.2	The Mini-Ring experiment and the beam-line.....	59
3.2.1	General overview of the experimental set-up.....	59
3.2.2	ECR ion sources.....	60
3.2.3	Transport beam line.....	66
3.2.4	The Mini-Ring.....	69
3.3	Laser Equipment.....	77
3.3.1	General description of the laser system.....	78
3.3.2	Setting the overlap between the laser beam and stored ions.....	81
3.4	Timing of the experiment.....	84
3.4.1	Storage sequence.....	84
3.4.2	Time structure of recorded neutral fragments.....	84
3.5	Computer control and Data acquisition.....	85
3.5.1	The National Instruments PCI (NI-6229).....	85
3.5.2	Time to digital converter (TDC V4).....	87
3.6	The experimental set up in DESIREE at Stockholm.....	88
3.6.1	The Double ElectroStatic Ion Ring ExpEriment, DESIREE.....	88
3.7	Conclusion.....	91

The main experimental component of the present studies on PAH dimer cations is an electrostatic ion storage ring, so-called the Mini-Ring because of its reduced dimensions compared to other existing rings at the time it was built. The prime purpose of the Mini-Ring is to enable in-flight studies on slow atomic and molecular processes such as radiative cooling, delayed dissociation, and photo-dissociation spectroscopy of large molecular ions on timescale range from milliseconds up to one second. The commissioning of the Mini-Ring was reported in a technical paper in 2008 [109]. One of the purposes of this chapter is to describe in detail this apparatus in its latest developments. In addition, the dedicated electron cyclotron resonance (ECR) ion source and ion transport beam line that has been used to produce ion beams and inject them into the Mini-Ring will be presented. The laser apparatus and its aspects used in the present work to excite ions, and hence to investigate their relaxation processes is also presented. The computer control and data acquisition system will be discussed as well.

THE EXPERIMENTAL SET-UP

Additionally, a one-week beam time at the cryogenic storage ring DESIREE in Stockholm, Sweden, has been dedicated to carry out specific spectroscopic studies on naphthalene dimer cations. Therefore, a concise description of the DESIREE experiment is presented in the last part of this chapter.

Before starting explaining the experimental set-ups individually in detail, it was found rather useful to introduce the basic concepts and principles of magnetic and electric deflection of ions briefly in order to give a short overview of respective essential differences in terms of application to ion storage rings.

3.1 Principles of magnetic and electric deflection of charged particles

A charged particle can undergo either magnetic or electric deflection depending on what kind of study is wanted. In most of the experiments with ESRs, ions of interest are mass-selected with a magnetic sector and are deflected by the electric field. This is the case in the present work at both the Mini-Ring and DESIREE experiments. In the following section, a brief explanation is presented.

3.1.1 Deflection via magnetic field

It is well known that when a charged particle of given kinetic energy enters a region of space where there is a uniform magnetic field perpendicular to the direction of motion, it will follow a circular trajectory due to a central magnetic force, as shown in Figure 3-1. This force is driven by the Lorentz equation:

$$\vec{F} = \frac{d\vec{P}}{dt} = m\vec{a} = q\vec{v} \times \vec{B} \quad \text{Eq. (3-1)}$$

where $\vec{B} = B_z \vec{k}$ is the magnetic field, $\vec{v} = v_x \vec{i} + v_y \vec{j} + v_z \vec{k}$ is the ion's velocity, m and q are the ion mass and charge, respectively.

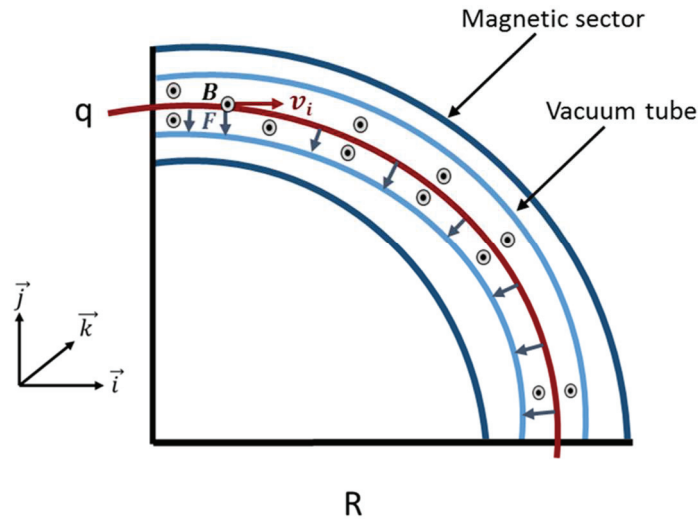


Figure 3-1: Schematic view of magnetic deflection of charged particle.

From second Newton's law, it is easily shown that the ion momentum P and the magnetic field are related by the following equation:

$$P = mv = \sqrt{2mE_k} = BRq \quad \text{Eq. (3-2)}$$

where E_k is the ion kinetic energy and R is the constant radius of curvature given by:

$$R = \frac{mv}{qB} = \frac{v}{\omega} \quad \text{Eq. (3-3)}$$

where ω is the constant angular velocity, expressed as:

$$\omega = \frac{qB}{m} \quad \text{Eq. (3-4)}$$

Often, one defines the magnetic rigidity as the product of the magnetic field by the radius of curvature:

$$BR = \frac{mv}{q} = \frac{P}{q} \quad \text{Eq. (3-5)}$$

In practice, for keV ion accelerators, the ion source is, in general, placed on a high voltage platform at an electric potential V . Hence, the velocity can be derived from the following equation:

$$E_k = qV = \frac{1}{2}mv^2 \quad \text{Eq. (3-6)}$$

For a mass selection magnet, since the radius R is constant and the ion momentum is fixed, the magnetic field is the only changeable parameter. Therefore, for a given bending radius R and a given acceleration voltage V , the mass to charge ratio m/q value of the selected ions can be selected by tuning the magnetic field B . The mass to charge ratio is finally given by:

$$\frac{m}{q} = \frac{B^2 R^2}{2V} \quad \text{Eq. (3-7)}$$

Conversely, the value of the selecting magnetic field B to select an ion of a specific mass m and charge q read as:

$$B = \left(\text{constant} \times \frac{1}{R} \right) \sqrt{\frac{Vm}{q}} \quad \text{Eq. (3-8)}$$

In this expression, which is generally used to calibrate mass spectra, it is clearly seen that the magnetic field scales with the square root of the mass.

Moreover, the maximum magnetic field is generally limited to a given B_{max} (due to the current limit of the power supply or to maximum heat dissipation...), which restricts the accessible masses to an upper limit m_{max} , which is inversely proportional to acceleration voltage:

$$m_{max} = \frac{B_{max}^2 R^2 q}{2V} \quad \text{Eq. (3-9)}$$

3.1.2 Deflection via electric field

A charged particle entering a region of space where there is a uniform electric field $\vec{E} = -E \vec{e}_y$ will be deflected by an angle α , as shown in Figure 3-2.

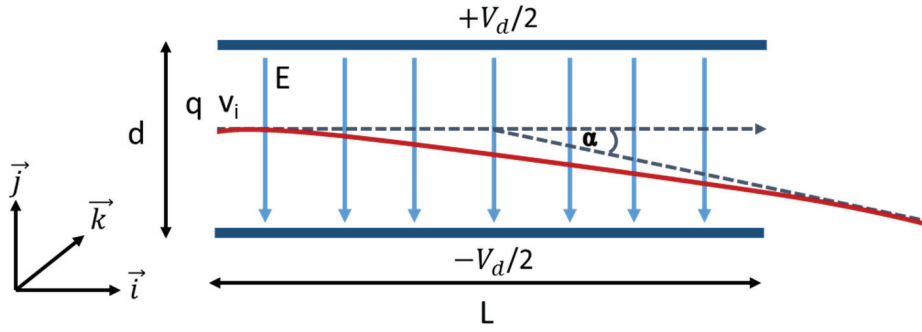


Figure 3-2: Schematic view of electrostatic deflection of positively charged particle.

Neglecting fringe field effects, this angle α , can be easily derived from the second Newton's equation:

$$\frac{d\vec{P}}{dt} = m \frac{d\vec{v}}{dt} = q\vec{E} = q \frac{V_d}{d} \quad \text{Eq. (3-10)}$$

$$R = \frac{2E_k}{qE} \quad \text{Eq. (3-11)}$$

The angle of deflection is given by

$$\tan \alpha = \frac{v_y}{v_x} = V_d L \frac{2q}{E_k} \quad \text{Eq. (3-12)}$$

with $E_k = qv$,

$$\tan \alpha = -\frac{2V_d L}{v d} \quad \text{Eq. (3-13)}$$

The angle of deflection of the charged particle is hence independent of the charge and mass of the particle. This has been lead to the development of the ESDs depending on this main idea. The angle of deflection hence depends on the kinetic energy of the charged particle.

3.1.3 Comparison between electrostatic and magnetic rings

As demonstrated in the two previous sections, the bending force is the key difference between the electrostatic and magnetic storage rings. In electrostatic rings, the rigidity would be proportional to E_k/q , which virtually allows for the storage of particles of any mass as long as the kinetic energy and charge are fixed values. It is also noteworthy that storage conditions, i.e., voltages to be applied on the electrostatic ring electrodes, are mass independent. This turns to be an advantage since, experimentally, storage conditions can be optimized using intense beams (e.g., atomic ion beams like Ar^+) and kept identical for much less intense beams. Nonetheless, it may also be an inconvenience since ions mass selection has to be performed externally before injection. In contrast, in magnetic rings, the rigidity is proportional to $\sqrt{m E}/q$, which limits possible studies to low masses or high charges.

They are other advantages of the electrostatic rings, e.g., compactness, ease of construction (and therefore cost), linearity of voltages with the kinetic energy of stored ions, ion trajectory reproducibility due to the absence of magnetic hysteresis. However, the linearity of voltages limits the usage of electrostatic rings up to low beam energies in the 1-100 keV range, whereas the magnetic rings allow for the storage of high-energy beams since the bending field strength increase less strongly, i.e., proportionally to the square root of the kinetic energy [220].

3.2 The Mini-Ring experiment and the beam-line

3.2.1 General overview of the experimental set-up

As already mentioned in the introductory paragraph of this chapter, the overall experimental setup is comprised of three parts. These are the ion source, the transport beam line (selection magnet, focusing, and deflection), and the Mini-Ring (Figure 3-3). Ions are produced almost at rest inside an ECR ion source located on a high voltage platform biased at 12 kV. Therefore, 12 keV ion beams are extracted out from the source, mass over charge selected by a 90° magnetic sector, and transported to the Mini-Ring.

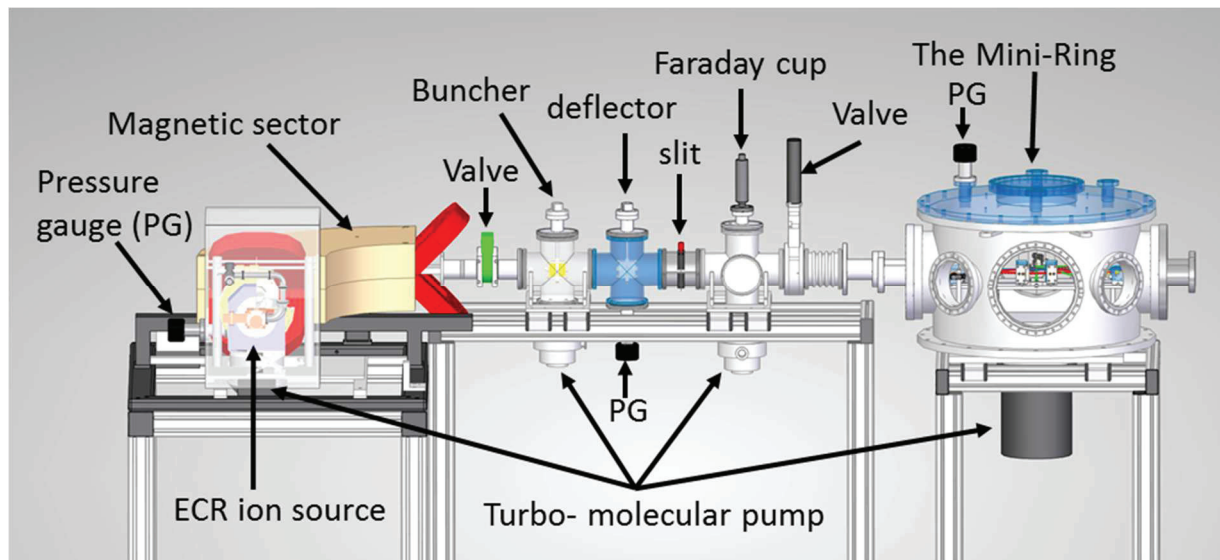


Figure 3-3: Schematic illustration of the entire experiment set-up.

In the transport beam line, the continuous ion beam is chopped by a parallel plate deflector to form ions bunches of typically 2 to 5 μs that can be stored in the Mini-Ring. Horizontal and vertical corrections of the ion trajectory can be done with parallel plate deflectors and ion beam intensity can be finely controlled by a slit whose opening can be adjusted from the outside of the transport beam-line vacuum chamber.

Ions are injected into the Mini-Ring via suitable injection optics composed of an electrostatic lens and a deflector, useful for fine ion-trajectory corrections. The ion bunches are stored for several milliseconds in the Mini-Ring, typically 2 to 100 ms. During storage, the ions can be excited via absorption of photons from either crossed or merged nanosecond pulsed laser beam (not shown in Figure 3-3). Finally, the neutral fragment yields resulting from the dissociation of the stored ions are detected by microchannel plates (MCP) on the opposite side of the injection section of the Mini-Ring and/or by a channeltron electron multiplier (CEM) located behind one of the conic electrodes of the Mini-Ring. A suitable data acquisition electronics allows for data recording and for plotting the neutral fragment counts as a function of the storage time.

The Mini-Ring based-experimental setup is equipped with a set of four turbomolecular pumps connected to three primary pumps to guarantee differential pumping from the ion source to the Mini-Ring. Pressure is estimated to be about 10^{-2} mbar of the ion source, measured in the range $10^{-6} - 10^{-5}$ mbar in the Einzel lens chamber between the ions source and the selection magnet, 10^{-8} mbar in the transport beam line and $1 - 2 \times 10^{-9}$ mbar in the Mini-Ring chamber.

As shown in Figure 3-3, the repartition of the four turbo-molecular pumps is as follows:

- One is located below the chamber of the Einzel lens between the ion source and the selection magnet. It helps also pumping in the ions source and the magnet chambers

- Two pumps are located in the transport beam line
- A 1000 l/s pump is located under the Mini-Ring chamber.

The turbo-molecular pumps are connected to three oil-free primary pumps. One of which is shared by the two turbo-molecular pumps of the transport beam line.

For ion storage rings, vacuum is an important matter because collisions with residual gas are the main limitation of the lifetime. During the commissioning phase of the Mini-Ring, it has been shown that the lifetime of Ar^+ beams were about 300 ms at a pressure of 4×10^{-9} mbar.

In the following sections, each part of the entire experimental set-up will be individually discussed in detail, starting with the ECR ion source, the Mini-Ring, the detectors, and the external relevant equipment, such as the laser and the data acquisition electronics.

3.2.2 ECR ion sources

An ECR ion source is a plasma device, which is commonly utilized to generate high-intensity ion beams of singly to multiply charged ions. They are common ion sources in accelerator facilities for atomic and nuclear physics studies and industrial applications. Various kinds of designs of ECR sources have been developed over the past decades to generate atomic or molecular ion beams [221,222], depending on their specific properties and the desired charge state. The charge state, beam intensity, energy, angular and velocity dispersion, stability, etc., are important features that can determine the choice of an ion source. Among others, Cesium sputter ion sources [140], laser ablation ion sources [223] are widely employed to produce anionic ion beams. Nier-type electron impact [137], Penning [153], Electrospray [224] ion sources are widely used to produce cationic or anionic beams to be stored in electrostatic storage devices. Plasma-type ion sources such as radio-frequency plasmas [153] or ECR ion sources are also commonly used to deliver high-intensity ion beams with rather good stability for several hours. Since ECR ion sources satisfy most of the requirements needed for the production of molecular ion beams in general and PAHs ion beams in particular, a “Nanogan I” ECR ion source, from the company Pantechnik, was used in previous works [76,133,212,225] to generate the cationic ion beams of monomers of PAHs. In the present work, we used this source to produce beams of phenanthrene cations, dimer cations of benzene, and two PAH dimer cations (naphthalene dimer, pyrene dimer) by using rather special tuning conditions.

Ion beams produced by ECR ion sources have several interesting features in the context of electrostatic ion beam storage, e.g., high-intensity ion beams in a range of from pA up to μA , long time beam stability in the order of hours to days, low divergence, and versatility. Indeed ECR sources can be used to produce a wide variety of atomic and molecular ions in different charge states. They are also rather easy to operate, to maintain, and the day-to-day reproducibility is rather good.

The following sub-sections are dedicated to a brief description of the historical context of the developments of ECR ion sources, their operation principle, and the characteristics of the Nanogan I used in the present work.

3.2.2.1 Brief historic view about ECR ion sources

The emergence of the ECR ion source is dated from the late 1960s when the ECR principle was used in plasma fusion reactors [221]. R. Geller et al. [226] have built the first ECR ion source called MAFIOS in Grenoble, France, using a solenoid magnet mirror in order to produce high charge state ions. MAFIOS had several advantages, such as no electrode corrosion due to arcs, the electrical power supplies of H.V. platforms were not needed, and the cathodes and anodes in the discharges were unnecessary [226]. Soon later, a very large SUPERMAFIOS ion source was built using a combination of a hexapole and a solenoid magnet. As a result, a minimum B magnetic field configuration could be generated to stabilize the plasma against magneto hydrodynamic instabilities and to create a closed resonance surface inside the plasma

THE EXPERIMENTAL SET-UP

chamber. In addition, the formation of the beam was using an axial extraction system. This design has inspired the conception of most of the modern ECR ion sources, which still have the same aspects [226,227].

The evolution of the design of ECR ion sources in terms of performance can be nearly classified into four-generation depending on the high-frequency electromagnetic waves. The first generation was operated in between 5-10 GHz. The second generation, such as GTS [228], ECR4 [229], AECR [230], and Caprice [231], was operated 10-20 GHz, commonly used in heavy-ion accelerators and atomic physics research. The third generation, such as VENUS [232], SECRAL [233], SCECRIS [234], and SUSI [235], was operated at 28 GHz with full superconducting magnets to provide higher intensity beams and higher charge states such as more than one mA U^{35+} , $1 \mu A Fe^{26+}$, and $0.1 \mu A U^{60+}$ for material irradiation. The fourth generation is emerged and operated at more than 40 GHz, such as LEAF at the Institute of Modern Physics (Lanzhou, China) [236].

In addition to the previous classification, in some kinds of ECR ion sources, the solenoid magnets used for the generation of the axial magnetic field could be replaced by permanent magnets, leading to all-permanent magnet ECR ion sources. Such ion sources could be made more compact and the consumption of electrical power is much reduced. The Nanogan I ECR ion source from PANTECHNIK Company used in this study belongs to the second generation (10 GHz) and is all comprised of permanent magnets.

3.2.2.2 The components of ECR ion sources

An ECR ion source can be divided into different main components, as shown in Figure 3-4 in the case of the Nanogan I. These are a plasma chamber (often a cylindrical tube), a minimum B-field configuration generated by a solenoid and permanent magnets, the microwave antenna, a plasma electrode, and an extraction electrode. The material to be ionized may be a gas or in the case of a solid material at ambient temperature, a vapor is provided from an oven. Depending on the model of ECR ion sources, different ways are used for the gas injection or for integrating an oven to feed the plasma.

In order to minimize collisions between ions and electrons and charge exchange with neutral species, the pressure should be low in the range of 10^{-7} mbar or less. Turbo-molecular pumps are generally used to obtain the necessary vacuum in the plasma chamber.

The ion source, including the plasma electrode, is set to a high voltage (acceleration voltage V in sections 3.1.1 and 3.1.2) and the extraction electrode remains grounded ($0 V$) in order to extract ions from the plasma and to accelerate them towards the transport beam line.

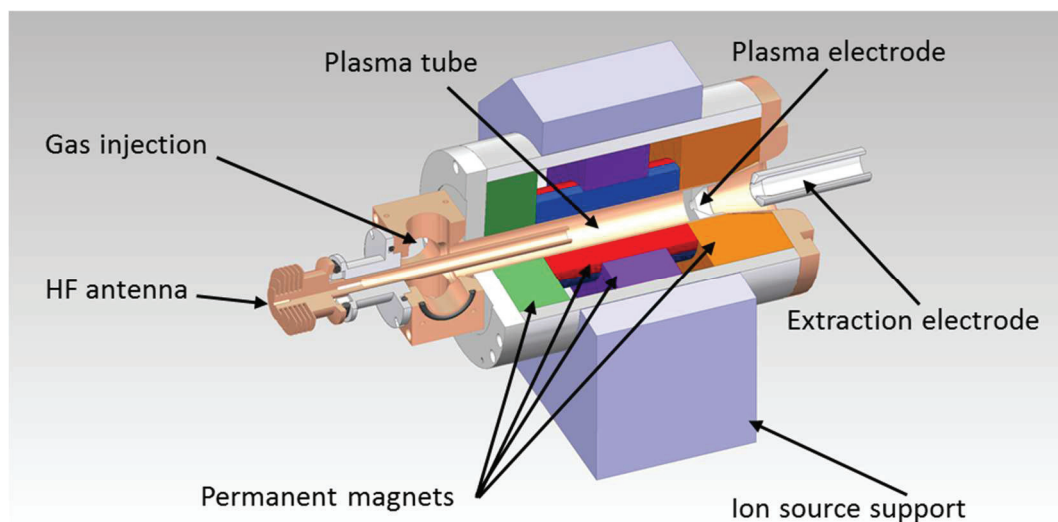


Figure 3-4: Schematic illustration of the main parts of ECR ion source Nanogan I.

3.2.2.3 General operating principle of ECR ion sources

In the plasma of an ECR ion source, electrons gyrate around the magnetic field lines due to the Lorentz force. The gyration frequency is referred to as the cyclotron frequency $\nu_g = \omega_g/2\pi$. When the HF microwave frequency, f_{HF} , is the same as f_g , the plasma electron is then either accelerated or decelerated. This is called the ECR condition (more detail will be given in section 3.2.2.5 below). A two-component plasma, comprised of energetic electrons and rather cold ions, is formed by electron impact ionization on the injected gas or vapor. In order to maintain the plasma, the electron and the ions are confined by a minimum-B magnetic structure. This structure also provides a closed surface, called the ECR surface, at which the ECR condition is realized. It is also worth noting that the electrons and ions are not in thermal equilibrium. They are in dynamic equilibrium by ambipolar diffusion, which maintains the neutrality of the plasma in ECR ion sources.

3.2.2.4 The minimum B-magnetic field

An axial magnetic field mirror in the plasma chamber is usually generated by using solenoids or permanent magnets while the radial field is produced by using a set of multipole permanent magnets. Anyhow, a minimum-B magnetic field inside the plasma chamber is produced by superimposing these axial and radial fields, as illustrated in Figure 3-5. In the center of the plasma chamber, the magnetic field is at the minimum and increases in all directions away from the center. Close to the wall of the plasma chamber, the magnetic field is constant with closed surfaces at which electrons are expected to gain energy through the ECR resonance [221].

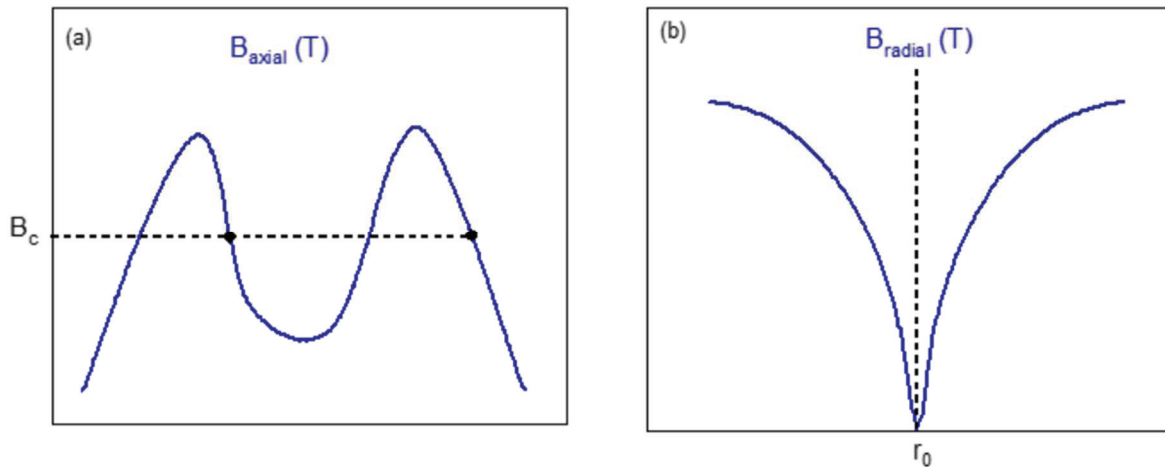


Figure 3-5: (a) Axial magnetic field, (b) Radial magnetic field of an ECR ion source. r_0 refers to the center of the source. B_c refers to cyclotron resonance condition.

3.2.2.5 Electron cyclotron resonance condition

Resonant interaction between the microwave field and the electron motion around the magnetic field can produce and sustain a plasma. The cyclotron resonance condition is:

$$\omega_g = \frac{eB}{m_e} = \omega_{HF} = 2\pi f_{HF} \tag{Eq. (3-14)}$$

where B is the magnetic field, e and m_e are the electron charge and mass. Therefore the magnetic field (in Tesla) at the resonance condition simply scales as (with f_{HF} in GHz) [221]:

$$B = 2\pi \frac{m_e}{e} f_{HF} = \frac{f_{HF}}{28} \tag{Eq. (3-15)}$$

Because of the minimum-B field configuration, the electron cyclotron condition can be fulfilled on a closed surface surrounding this minimum, referred to as the surface of resonance. The free electrons in the plasma can spiral back and forth between different magnetic isosurfaces (surface of constant magnetic field intensity). They can also change trajectory because of electron-electron, electron-ion, or electron-neutral gas collisions. When they reach the resonance surface, they accelerate (or decelerate) resonantly and gain (or lose) kinetic energy. Electrons are accelerated when they are in phase with the HF electric field and decelerated when they are out of phase. The maximum energy gain is then realized at the resonance condition. Due to the long confinement time, electrons may often pass through the resonance surfaces. Therefore, they may acquire high kinetic energies, possibly up to several keV. Such energetic electrons may collide with atoms or molecules, leading to ionization into high charge states, either by successive single impact ionization or by single impact ionization. Since the ions have heavy mass, they are not accelerated and can be confined by the space charge of electrons of plasma. Electron cyclotron resonance parameters such as magnetic field intensity, HF frequency and amplitude, and gas pressure can affect considerably the charge state distribution of produced ions [221].

3.2.2.6 Collision parameters

Collision processes are usually expressed in terms of collision cross-section σ . In a plasma, it is related to the mean free path, λ , and the collision frequency, ν_c . The mean free path is simply given by:

$$\lambda = \frac{l}{n\sigma} \quad \text{Eq. (3-16)}$$

where n is the density of the target particle (neutral gas, ions, or electrons).

The Collision frequency ν_c is defined as the reciprocal of the average time interval between two collisions, i.e., the traveling time corresponding to one mean free path. Since the value of collision frequency is in general somewhat comparable with the typical plasma frequencies such as the cyclotron frequency, it is a convenient collision parameter to determine. It is given by [221]

$$\nu_c = \frac{1}{\tau_c} = n\sigma v \quad \text{Eq. (3-17)}$$

where v is the electron (or ion) velocity.

The frequency of plasma oscillations, as defined in Eq. (3-18), is the characteristic frequency of the free electron motion around the positively charged ions. It has to be greater than the electron-neutral collision frequency ν_{en} :

$$f_p = \frac{\omega_p}{2\pi} = \frac{1}{2\pi} \sqrt{\frac{e^2 n_e}{\epsilon_0 m_e}} > \nu_{en} \quad \text{Eq. (3-18)}$$

In the present work, since we want to produce beams of molecular cations and even more fragile molecular dimer cations, electrons should not gain too much kinetic energy to prevent dissociation processes. Consequently, the neutral gas density and the HF amplitude have to be finely adjusted. On the one hand, the electron collision frequency should be of the same order of magnitude as the HF frequency to prevent electrons from gaining too much energy between two collisions with neutral molecular gas. On the other hand, the collision frequency ν_{en} must remain smaller than f_p to prevent plasma extinguishment.

3.2.2.7 Ionization

Highly charged ions may be produced mainly by sequential electron impact ionization. In order to achieve sequential electron impact ionization, the ions and electrons should be confined for sufficient time. Confinement times of ions, τ_i , need to be about $10^{-2}s$ in a typical ECR ion source [237]. A sufficiently high electron temperature and density are necessary for the electron-ion collision rate to remain sufficiently high in comparison with the confinement time. Furthermore, the microwave frequency, which is generally fixed to define the size of ECR is another important parameter that affects the electron density, n_e , the electron temperature, T_e and the product ($n_e\tau_i$), which in turn could be increased by the plasma confinement and by injecting cold electrons to the plasma. τ_i is related to τ_e , which, in turn, is related to the entire electron population. It can be approximated by [221,238]:

$$\langle\tau_e\rangle\approx\left(1+\frac{n_{eh}}{n_{ec}}\right)\tau_{ec}\quad Eq.(3-19)$$

where n_{eh} is the density of hot electrons, n_{ec} and τ_{ec} are the density and the average confinement time of cold electrons, respectively.

The product ($n_e\tau_i$) relates directly to the ion beam current of the ECR ion source. The higher the electron density and ion confinement time, the higher the beam current [221]:

$$I_i\propto n_eV/\tau_i\quad Eq.(3-20)$$

where V is the plasma volume.

Although ECR ion sources have originally been designed to produce multiply charged ion beams, they also proved to be efficient in producing stable and intense singly charged ion beams. Moreover, they have recently been successfully used to produce molecular ion beams. In the present work, in order to produce ion beams of PAH cations and PAH cation dimers, the presence of too energetic electrons is not desired. To prevent a too high acceleration of the electrons, rather high pressure of naphthalene has been injected as a support gas to reduce the mean free path of electrons. In this case, indeed, single impact ionization of the monomers is sufficient for the subsequent formation of dimers.

3.2.2.8 The Nanogan I ECR ion source features

As already mentioned, the ion source used in the present work to prepare the beams that were injected in the Mini-Ring is the Nanogan I from the company Pantechnik (Figure 3-6). It is a compact ECR ion source placed on insulated support for an extraction voltage of 12 kV and includes a ceramic insulator for the extraction exit. The fully permeant magnet design can provide a magnetic field for the confinement of the plasma. The magnetic intensity is in order of 1 T. It works with a power of 10 W. A 10 GHz of high frequency traveling wave tube amplifier is introduced into the ion source through a rectangular waveguide and coupled to plasma co-axial coupling. An oven inside which different kinds of solid state samples are heated is situated at the opposite side of the extraction electrode.

3.2.2.9 Extraction of the beam from the source

In the Mini-Ring experimental set-up, ion beams are produced using a Nanogan I ECR ion source, extracted via extraction electrode, and accelerated into kinetic energy of 12 keV, which corresponds to the potential of high-voltage (H.V.)-platform, which in turn is sustained by isolation. Figure 3-6 shows a photograph of the ECR ion source on the H.V.-platform used in this work. The ion beam is then leaving the ion source at the kinetic energy given by:

$$E = q(V_{ion\ source} - V_{extraction\ electrode}) = \frac{1}{2}mv^2 \quad Eq. (3-21)$$

where $V_{ion\ source}$ is the acceleration voltage, $V_{extraction\ electrode} = 0\ V$ since the extraction electrode is connected to the rest of the beam line, which is connected to the ground, m is the mass, and q is the charge state of the ions.

The extracted ion beam current can be estimated as:

$$I = \frac{1}{4}Aqnv \quad Eq. (3-22)$$

where A is the size (area) of the plasma electrode aperture, n is the ion density in the plasma and v is the mean velocity of extracted ion and q charge of ions.

Despite that ECR ion sources can be used in both continuous and pulsed modes, the continuous system was always used in the present experiments because it was rather easy to obtain enough beam currents. Although higher currents might be expected in the pulse mode, lower kinetic energy dispersion is expected in the continuous mode. Moreover, in the pulse mode, a high-voltage, high-current a fast transistor switch would be needed leading to an increased cost for an uncertain gain.



Figure 3-6: Photograph of the Nanogan I ECR ion source used in the present work.

3.2.2.10 The Nanogan I ion source operation conditions for dimer formation

The Nanogan I ion source was used to produce ion beams of cationic dimers under special tuning conditions. These conditions are changeable depending on the nature, physical and chemical properties of each species. Naphthalene is sublimated without heating, while bigger species such as anthracene, pyrene are placed in the reservoir (oven), which can be heated at such temperatures that the PAH powder can be sublimated for a long time up to several days with a rather constant and sufficient flow. HF power was in the range of 0.5-3 W. Naphthalene was used as a support gas, which is needed to cool down the plasma to temperatures at which the cationic dimer can be formed. The pressure gas in the plasma chamber was monitored by a valve with a controllable opening located in between the naphthalene powder separate reservoir and the ion source. The pressure in the ion source could not be measured directly; however, a calculation shown in chapter 4 demonstrates that it was in the range of 10^{-1} - 10^{-2} mbar.

3.2.3 Transport beam line

The transport beam-line consists of all ion-optics elements, placed between the ion source and the Mini-Ring, that are needed to focus, select, deflect and bunch the ion beam.

3.2.3.1 Einzel lens

After the extraction of ions from the plasma electrode of the ion source, they were directed into a conic-shaped electrode of a diameter of 5 mm placed at a precise distance of 35 mm from the plasma electrode. In order to focus the ion beam without changing its energy, an electrostatic Einzel lens is placed on the same holder as the extraction electrode to optimize the alignment, as shown in Figure 3-7. The Einzel lens is a symmetric three-cylinder ion-optical electrostatic lens (see Figure 3-8). The two identical extreme ones are grounded and the voltage of the central one is adjustable in the range of 5-7 kV to set the focal length of the lens. It acts as a two-inline, doublet lens to achieve a net strong, short, and adjustable focusing distance. It is important to place the Einzel lens between the source and the selection magnet to bring the ion beam into the focal point of the magnet.

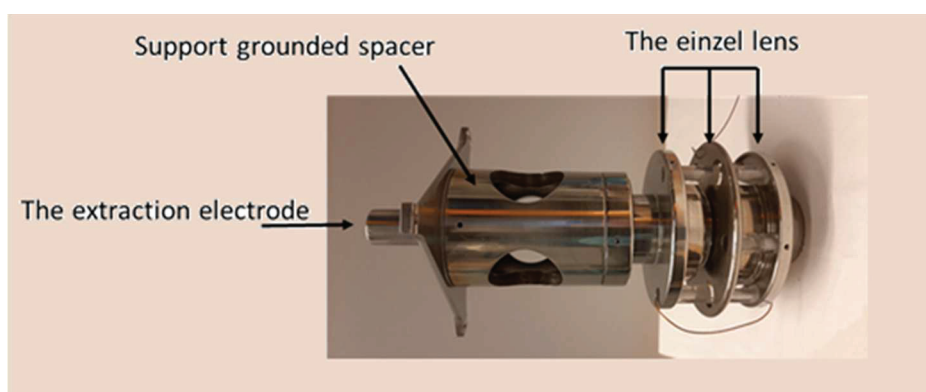


Figure 3-7: A Photograph of an Einzel lens used in this work.

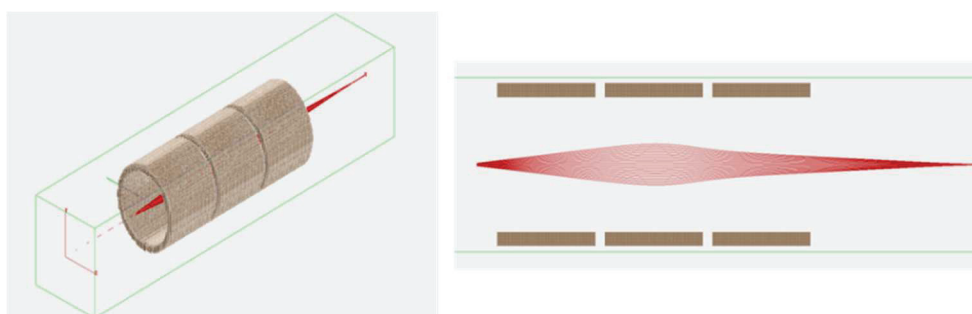


Figure 3-8: Simion 8.1 software schematic illustration of an Einzel lens.

3.2.3.2 The mass-selecting magnet

The ion beam extracted from the ion source is comprised of several species resulting from the ionization and, possibly dissociation of the background gas molecules, the support gas molecules (often naphthalene in this work), and the molecules or their dimers of interest for the present studies. Consequently, a mass selection device is required to select the species of interest. A 90° double-focusing magnet of 50 cm in radius has been chosen. Such devices are commonly used in ion accelerators for ion selection according to the mass-to-charge ratio.

The magnet is supplied by a current through two high current power supplies (52 V, 60 A), from DELTA ELEKTRONIKA company, connected in parallel. The magnetic field is related to the total current delivered by the power supplies, which is controlled by a LabVIEW program via a data acquisition PCI card (NI 6221). Mass spectra can be obtained by scanning the magnet current and by recording the ion beam current on a Faraday cup (FC, see section 3.2.4.3). Two FCs were used in this work: the one is located in the transport beam line right after the slit (see

THE EXPERIMENTAL SET-UP

Figure 3-3), the other one is located in the Mini-Ring chamber and can be reached by the ions after a single revolution without storage.

3.2.3.3 Buncher or beam chopper

As already mentioned, the Mini-Ring stores bunches of ions with a time width, Δt_b , of a few microseconds (typically 1 to 10 μs). Since the ion source provides a continuous beam, it is necessary to prepare these bunches in the transport beam-line. To this purpose, we use a beam chopper composed of two sets of two parallel-plate electrodes separated by a 10 mm distance. By choosing which of the two sets, vertical or horizontal plates, is connected to the power supplies, it can be decided whether the chopped beam is deflected horizontally or vertically, respectively. In this work, it has been decided to deflect horizontally because the downstream slit is vertically oriented. Figure 3-9 shows a 3D representation of the design of the Buncher.

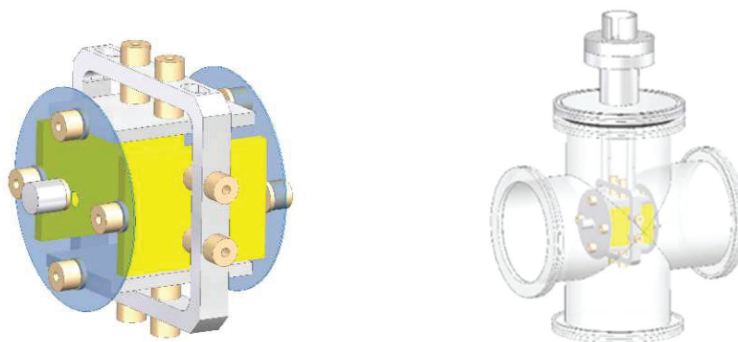


Figure 3-9: Schematic illustrations of the buncher.

The typical voltage used to deflect the ion beam is typically of $\pm 130\text{ V}$, one of the plates being connected to the positive voltage and the other to the negative voltage. Fast high voltage switches (Belke HTS 61-03-GSM) are used to ground the buncher electrodes to let ion bunches enter into the Mini-Ring. Therefore, the buncher acts as an alternate beam injection by chopping off the continuous beam for a duration Δt_b to fill the ring with ion bunches, and subsequently chopping it on to deflect the ion during the storage time T_s .

The rise and fall times of the buncher have to be short in comparison to the bunch duration in order to avoid disturbing the injection of ions into the storage ring. With the aforementioned fast high voltage switches, the minimum rise and fall times of the voltage can be intrinsically in the tens of ns range much shorter than our requirement; however, we added suitable resistors to increase these values slightly to about 100 ns to reduce electronic noise occurring at the rise and fall times.

Figure 3-10 displays a scheme of the switch. For the positively polarized plate of the buncher, the $-HV\text{ IN}$ input is connected to the ground, whereas the $+HV\text{ IN}$ is connected to a high voltage power supply (Model FUG HCP 14-2000: $\pm 2000\text{ V}$, 60 mA). The HV out is connected to the electrode of the buncher. The timing of the fast switches is controlled by a TTL (0-5 V) signal that is generated by a function generator. At the low level of the TTL IN, (0 V), the HV OUT outputs is set to $+HV\text{ IN}$, which bends the ion beam trajectory. At the high level of the TTL IN (5 V), the HV OUT outputs 0 V and, therefore, the ion beam can pass through the buncher. Consequently, the width of the ion bunch is defined by the width of the TTL pulse.

It is noticeable that if the ion beam was not bunched, it would enter into the Mini-Ring chamber, be deflected by the first deflector of the Mini-Ring, and hit some electrode on the wall of the chamber, producing secondary ions and electrons that would contribute to the noise on the detectors.

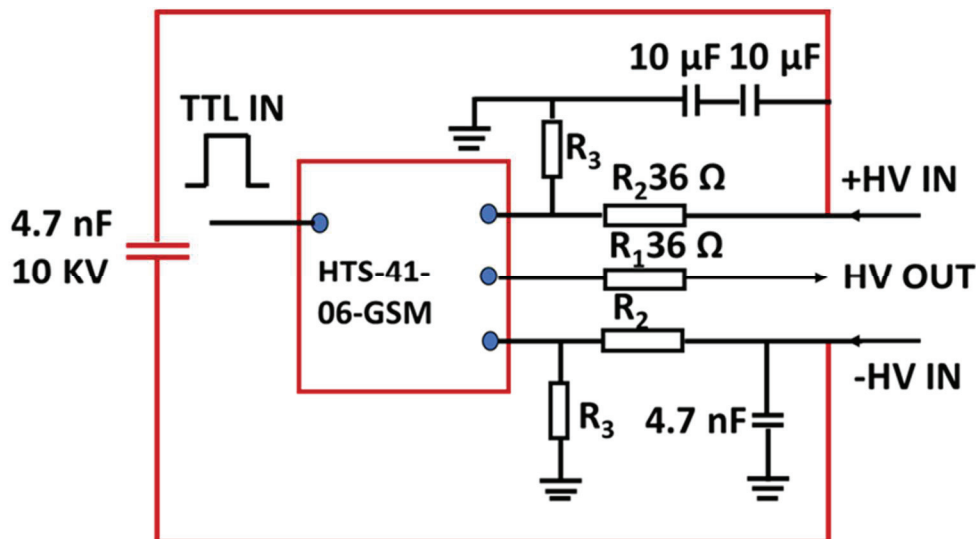


Figure 3-10: Circuit of the fast switch.

3.2.3.4 Ion-optics of the beam injection

A set of injection ion-optics, including a two-unipotential lens and a deflector, is located at the entrance of the Mini-Ring, on the same support plate. It is used to adjust finely the angle of the injection, the position, and the focus of the ion beam. A photograph and a sketch of these injection optics are shown in Figure 3-11.

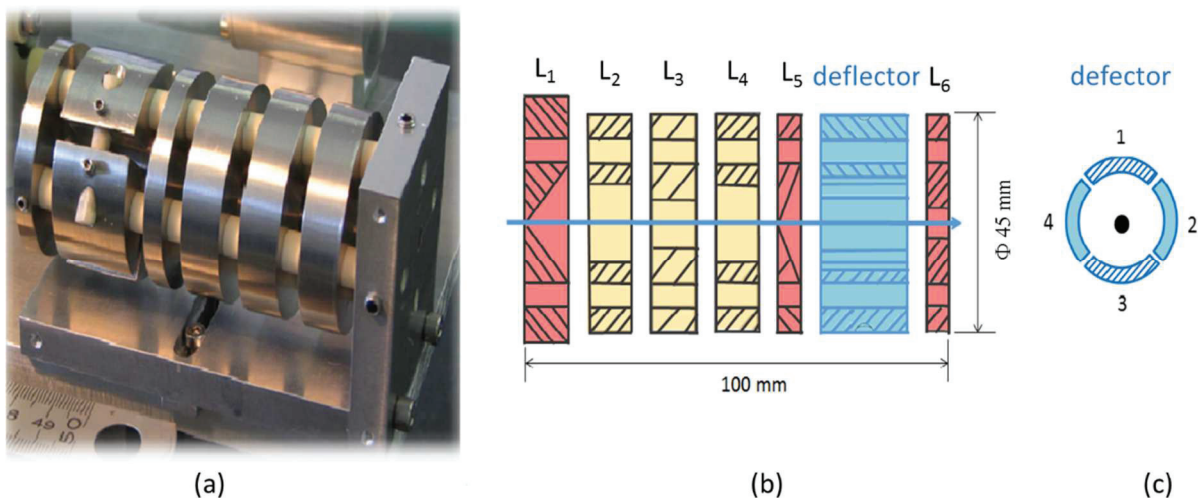


Figure 3-11: Illustration of the ion- optics injection system. (a) Photograph of the lens and deflectors (steerers) and their dimensions, cylindrical-shaped electrodes. (b) Scheme of the injection optics. Grounded electrodes are red-colored. L_2 and L_4 are set to the same high voltage to focus the beam. The deflector electrodes are colored in blue. (c) The deflector is comprised of segmented cylindrical-shaped electrodes to allow for vertical and horizontal deflection.

The lens is comprised of five electrodes herein labeled L_1 to L_5 . L_1 , L_3 , and L_5 are connected to the ground. Electrodes L_2 and L_4 are connected to the same high-voltage power supply. They are used to focus (or defocus, depending on the needs) the incoming ion beam in both horizontal and vertical planes to obtain a parallel ion beam.

The deflector is made of a cylindrical conductor that has been segmented into four parts that can be connected independently to a high voltage. In practice, we use a single power supply to provide a high voltage and potentiometers to dissymmetrize the voltage on each of the opposite vertical and horizontal segments. With this method, the average voltage also contributes to the total focusing effect of the injection optics.

THE EXPERIMENTAL SET-UP

For the 12 keV beams used in the present work, typical voltages of lens and steerer were about 3.8 kV and 0.7 kV, respectively.

The two sets of deflectors are employed for the corrections of injection direction and position of the ion beam in both the horizontal and vertical directions. The L_1 , L_5 , and L_6 elements along with the slit upstream the vacuum chamber of the Mini-Ring are designed along the ion beam transport line for the purpose to be used to restrict the trajectories of ions to match with the emittance of the injected beam.

3.2.4 The Mini-Ring

The original idea of the design of the Mini-Ring was to store ions on closed orbits of a small size electrostatic ring in order to reduce the revolution time by typically a factor of ten in comparison with other existing electrostatic storage rings. The expected gain due to this short revolution time was a much better sampling of the decays of the excited stored molecular ions.

In order to achieve this goal, the Mini-Ring was designed with a small number of ion-optical electrodes allowing for building a very compact instrument. Thereby, the ring makes use of solely eleven electrodes, including grounded electrodes, forming four electrostatic parallel deflecting plates and two conical mirrors. The Mini-Ring was originally inspired by the Conetrap developed firstly at Stockholm University [176] and its replica was built in Lyon before the Mini-Ring project started. The basic conceptual idea of the Mini-Ring can be viewed as a Conetrap with an off-axis injection.

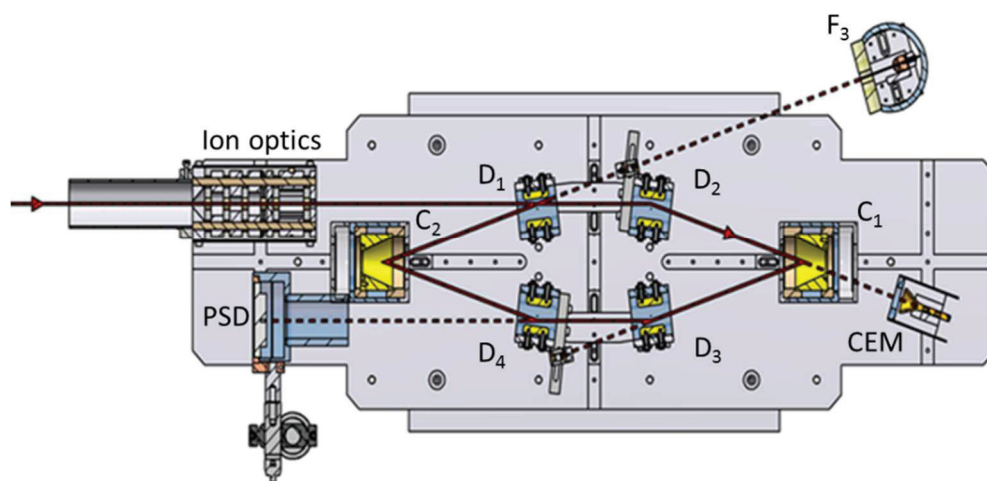


Figure 3-12: Scheme of the Mini-Ring.

3.2.4.1 The mechanical design and ion-optical elements

As an electrostatic ring, the Mini-Ring relies solely on the use of electrostatic ion-optics. It is of the length of 40 cm and width of 20 cm. A scheme of the Mini-Ring is given in Figure 3-12. It is comprised of two kinds of ion optical elements: Parallel-plate deflector (PPD) and Conical shaped electrode (CSE). There are four PPD mounted in good parallelism, labeled D_1 to D_4 in the order they are crossed by the stored ions, and each of them is supported by a separate rectangular grounded shield. In addition, two conical-shaped electrodes herein on the same axis labeled C_1 - C_2 are supported by a grounded shield as well. All the optical elements are mounted on the same support plate to ensure precise alignment in the horizontal plane and define their position accurately. The precision of the positioning on the support plate is expected to be better than 0.5 mm. The grounded housing is mainly used to reduce fringing fields in the direction of ion beams. Figure 3-13 is a photograph of the Mini-Ring mounted inside its vacuum chamber.

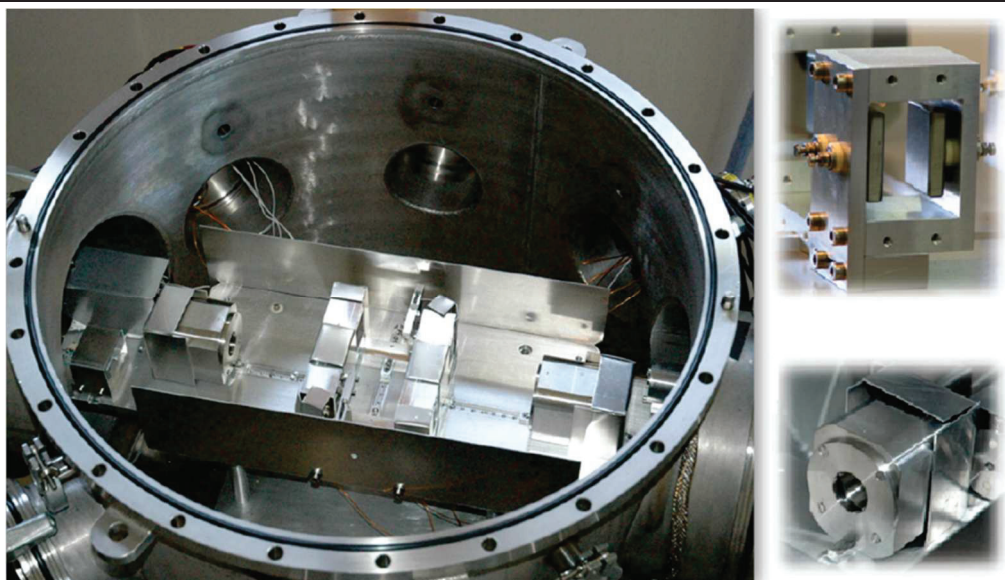


Figure 3-13: Photographs of the Mini-Ring inside its vacuum chamber, of one of its deflectors and one of its conical mirrors.

Detailed sketches of the deflectors and the conical mirrors are displayed in Figure 3-14. In this figure, the yellow-colored parts are set to high voltages while the gray and blue parts are grounded housing and supports.

The conical-shaped electrodes and their surrounding housing have the same axis of cylindrical symmetry. The conical electrode has an opening angle of 44° . The distance between the cone electrode and the front grounded electrode, which is 10 mm, affects the shape of the equipotential surfaces. Once a high voltage is set to the cone electrode, the electrostatic potential surface curves inside the Cone while the flat potential surfaces are produced nearly to the front grounded electrode. These equipotential surfaces given by such geometry give reflection and focusing effect much like an optical spherical mirror. Therefore, the conical electrode is referred to as an ‘electrostatic mirror’ as well.

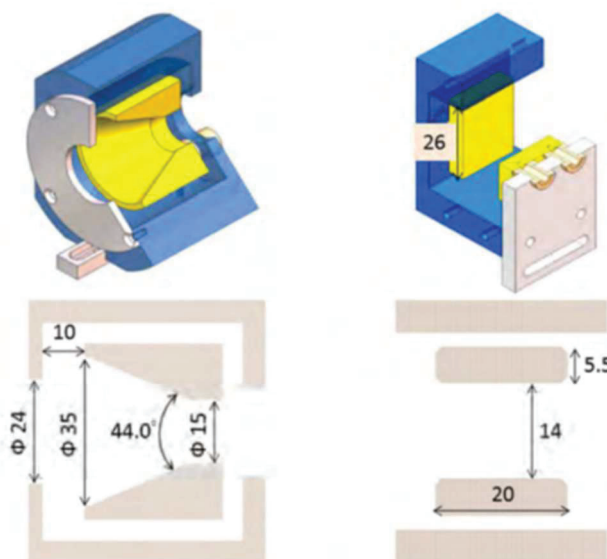


Figure 3-14: Design of conical mirror (left side) and the deflector (the right side), the dimensions are given in mm. The yellow-colored parts are the high-voltage electrodes, and the gray and blue-colored parts are the grounded housing and support.

3.2.4.2 The trajectory of the stored ions and typical voltages

The ideal ion trajectory displayed in Figure 3-12 has a quasi-hexagonal shape. Six straight line sections can be seen in between the different bending elements. The deflection angle

THE EXPERIMENTAL SET-UP

induced by the PPDs is about 18° . For a 12 keV ion beam, the positive and negative voltages on the PPD electrodes are set to be about 1.98 kV. The electrostatic potential in the center of the deflectors is almost zero when applying the voltages on the plates, making the charged particles pass through the deflector without changing kinetic energy. PPDs are tilted by an angle of 7° in order to optimize the trajectory of ions so that they remain far enough from the electrode edges.

The conical mirrors have two purposes: one is obviously to reflect the ions with the same exit angle as the entrance angle; the second is to refocus slightly the beam to maintain its parallelism. The voltage required on the conical electrode for a 12 keV ion beam is about 16 kV.

It is noteworthy that storage is still maintained if the voltages are changed by about ± 10 V on the PPDs and ± 50 V on the conical mirrors.

3.2.4.3 Faraday cups

Faraday cups (FC) are commonly employed to characterize ion beam currents. It is simply composed of a shielded electrode connected to a pico-ampere meter that can be moved into or be placed at the end of the beam trajectory. In the Mini-Ring experiment, two FCs are employed to measure the intensity of the ion beam along the beam trajectories. The first one is a movable FC located at an appropriate position between the buncher and the Mini-Ring, i.e., right behind the slit of the transport beam line. It is used for beam preparation purposes, i.e., check of mass selection, optimization of the source conditions, optimization of selection magnet current, optimization of Einzel lens voltage. This FC is suitable for measuring ion-beam current intensity in the range of pA to μ A. The second FC, which is mounted inside the Mini-Ring chamber, is used to collect reflected ions by C_2 after a single turn in the Mini-Ring when the D_1 is set to be 0 V. It is located in the straight-line continuity of the $C_2 - D_1$ axis. The latter FC is used to perform mass spectrometry with a better resolution than with the transport beam line FC. This Faraday cup is used in chapter 6 to perform mass spectrometry of the dimer cations.

3.2.4.4 Optimization of the storage

Obviously, in order to store ions on stable trajectories, the voltages on the ion optical elements of the Mini-Ring should be set properly. The injection angle towards the conical mirrors, the trajectory of the ion beam between the deflectors and conical mirrors, or between two deflectors should be rather finely adjusted. Direct visualization of an intense ion beam proved to be an effective method for pre-setting the electrode voltages. Final adjustments were later performed using stored ion beam and data acquisition, especially imaging the neutral fragments on the PSD.

The first optimization of the Mini-Ring voltages was performed with a 12 keV continuous intense Ar^+ ion beam. The measured beam current was about 4μ A. The Mini-Ring was filled with N_2 gas at pressure $P(N_2) = 2 \times 10^{-4}$ mbar to induce collisions with the ion beam along the storage trajectory that produces visible light. A digital camera with a high sensitivity CMOS was placed either on the top window or the side window of the Mini-Ring in order to record the position of the ion beam in the horizontal and vertical planes, respectively. The photographs were taken with a 30 s exposure time. The blue light resulting from collisions between N_2 and Ar^+ ions is a direct visualization of the trajectory of Ar^+ ions in the Mini-Ring for its first revolution of storage. Figure 3-15(a) shows the ion beam in the horizontal plane taken from the top window of the Mini-Ring as well as the neutral fragments on the surface of MCP as a blue spot that has more or less the same size as the ion beam. Figure 3-15(b) shows the position of the ion beam in the vertical plane taken from the side window of the Mini-Ring.

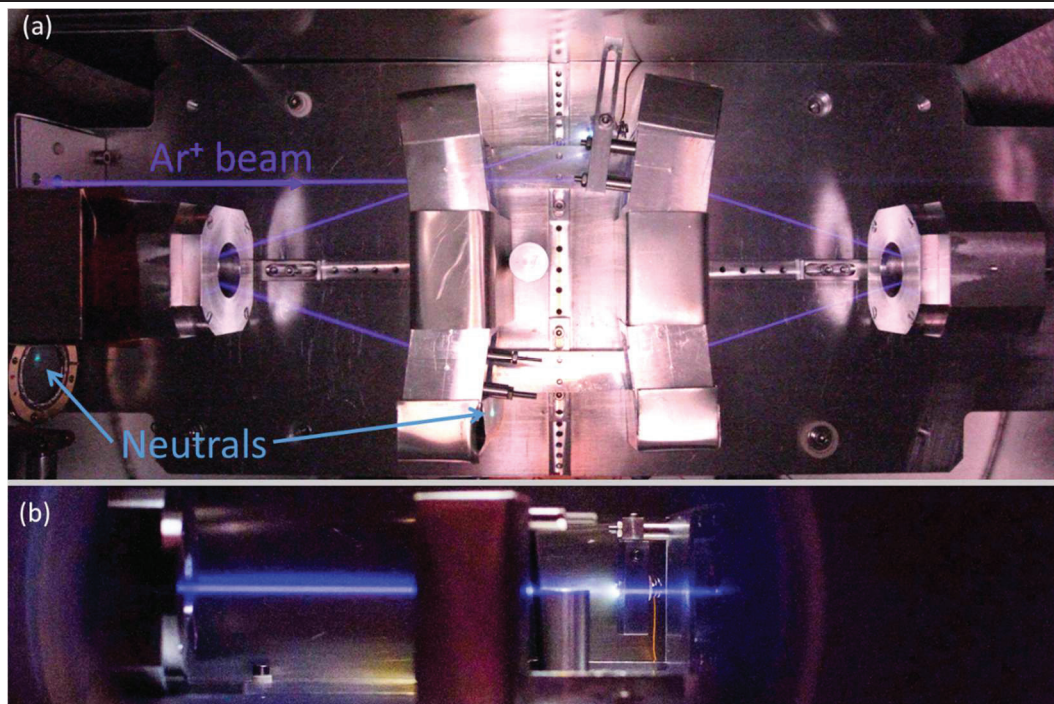


Figure 3-15: Photograph of a stored ion beam of singly cationic Ar at 12 keV for a single evolution in the Mini-Ring, the chamber was filled with N₂. (a) The horizontal plane of the ion beam trajectory is taken from the top window of the Mini-Ring, (b) The vertical plane of the ion beam trajectory.

From the photographs of the beam, via the known precise distance between the ion optical elements, it was possible to estimate that the diameter of the ion beam to be about $\varphi = (2 \pm 1)$ mm. The corresponding beam profile is shown in Figure 3-16 [225], where the measured profile is fitted with the Gaussian function.

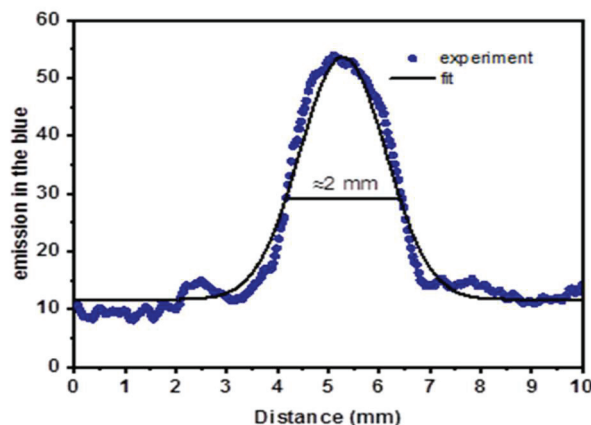


Figure 3-16: The diameter of the ion beam as a function of emission.

3.2.4.5 Kinetic energy acceptance and consequences for daughter ion storage

The Mini-Ring has been optimized to store ions within a narrow kinetic energy acceptance window $\Delta E_k = \pm 40$ eV around $E_k = 12$ keV. By the loss of a small neutral fragment of mass ΔM from the parent molecules of mass M , the kinetic energy of the residual daughter charged fragment is decreased by $(\Delta M)_{max}/M E_k$. When it is smaller than 40 eV, the daughter ion will still be stored in the Mini-Ring together with parent ions; otherwise, it will be fastly ejected. Hence, kinetic energy acceptance window results in a fragment mass acceptance window, $M \pm (\Delta M)_{max}$, where $(\Delta M)_{max} = M(|\Delta E_k|/E_k) = M(40/12\,000) = M/300$. The daughter ions of mass, which is smaller than $M - (\Delta M)_{max}$ would not be stored in the Mini-Ring. Concretely, the daughter ions resulting from the loss of one H atom will be rapidly lost for parent ions whose mass is below 300 a.m.u.

3.2.4.6 Detectors

In the Mini-Ring experiment, the stored molecular ions may dissociate into neutral and charged fragments, either spontaneously if their internal energy is high enough, or due to laser excitation. In addition, ions collisions with residual gas may result in dissociation events. In storage ring experiments, neutral fragments are detected easily because their trajectory out of the ring is easy to predict since, obviously, they are not deflected by electric fields. Oppositely, the trajectories of the charged fragments would be very difficult to predict because they are highly dependent on the fragment charge and mass, and on the position at the time of the fragmentation event.

The Mini-Ring is equipped with two complementary detectors: a position-sensitive detector (PSD), which is composed of a MCP and a resistive anode, and a CEM. Both are dedicated to the detection of neutrals. However, in the coincidence measurement (Section 6.3), the MCP is used to detect ions and the channeltron is for the detection of neutrals. These detectors could have been positioned at six different places because the Mini-Ring has six straight sections where neutral fragments could be collected. It has been chosen to locate the MCP at the end of the straight section of $D_3 - D_4$ to detect neutral formed in between D_3 and D_4 and the channeltron was positioned behind C_1 to detect neutrals coming out from the straight line between D_2 and C_1 and passing through the hole drilled at the backside of C_1 and its surrounding housing. With this configuration, the number of neutral fragments collected by each of the detectors is estimated to be approximately one-sixth of the neutral fragments created by the ion bunch during the storage. In the following subsections, the detectors are presented individually in more detail.

3.2.4.6.1 Position sensitive detector

The PSD is composed of two identical MCPs of 25 mm in diameter equipped with a resistive anode. This system combined with its dedicated electronic equipment constitutes a time and position-sensitive detector. The time information of this PSD is provided by electronic TTL pulses giving, with a short constant delay, the times at which detected particles hit the MCP surface. Besides, the resistive anode allows for measuring the position of the particle impact on the MCP. The PSD is useful in the Mini-Ring for two specific purposes. Firstly, the optimization of storage parameters can be done with a test beam (often Ar^+) by reducing the spot size and the deviation of the center of the spot from turn to turn (betatron oscillations). Secondly, kinetic energy release (KER) can be estimated from the comparison of the spot size of the stored molecular ion beam with one of the test beams. A photograph of PSD is presented in Figure 3-17.

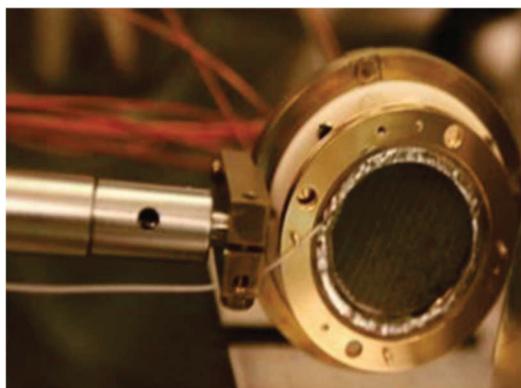


Figure 3-17: A photograph of MCP detector and resistive anode (PSD).

The output analogic signals of the PSD that provide the (x, y, t) position and time information are connected to a dedicated electronic device, model 2401B, from the Quantar Technology INC, Santa Cruz, California, USA, which is a time and position computer that delivers three signals (more explanations about the generation of these signals will be given in

THE EXPERIMENTAL SET-UP

section 3.2.4.6.1.2) that can be used as inputs in an oscilloscope or digitized by a data acquisition electronics:

- The strobe signal corresponds to the time information of a detected particle.
- The X-signal is a square signal whose amplitude is in proportion to the horizontal position of the detected particle
- The Y-signal is a square signal whose amplitude is in proportion to the vertical position of the detected particle

Both X and Y signals are synchronized with the strobe signal. The amplitudes of these signals are digitized with a NI-6221 data acquisition card (National Instruments) and the image is computed and displayed by a LabVIEW program. As an example, a typical record of such an image is given in Figure 3-18.

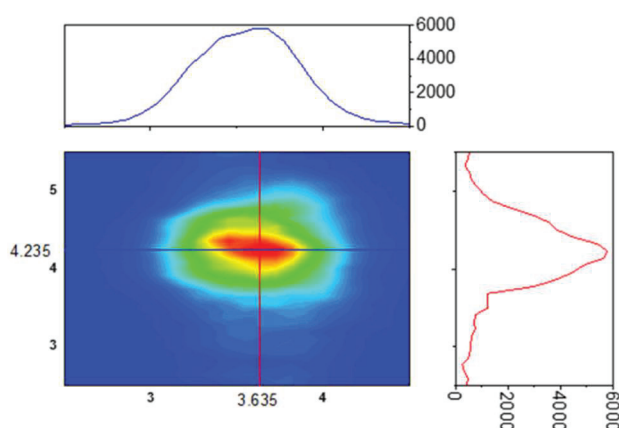


Figure 3-18: Typical images of the neutral profile of cationic dimer of benzene.

3.2.4.6.1.1 The microchannel plates (MCP)

The MCPs used in the present PSD were purchased from HAMAMATSU photonics. They are planar disks with a regular packed array of tiny lead silicate glass tubes, the so-called microchannels. Each tube acts as a charge amplifier by turning each single particle impact on the input side into a charge pulse by releasing electrons from the tube wall by secondary emission. An incident particle enters a single channel through a tiny orifice to strike its inner wall, emitting at least one or several secondary electrons. By applying a voltage between the input and output side of the wall, the secondary electrons are accelerated and collide with the channel wall to emit further electrons. By repeating this process, it creates a cascade giving, in fine, a cloud of electrons that can be extracted from the output side of the channel. The first MCP of the present PSD was covered with magnesium fluoride (MgF_2) in order to improve the efficiency of producing the first electron at the impact of the particle. The MCP gain is determined by the ratio of the channel length to the channel diameter and secondary emission factor. Two MCP are stacked together in V- shape, referred to as chevron stack configuration, to provide a sufficient amplification (10^6 to 10^7 gain). The structure of MCP, single-channel, and the secondary electron emission is shown in Figure 3-19.

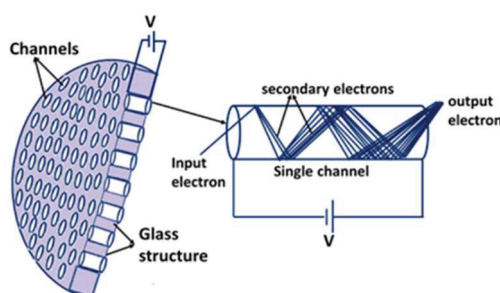


Figure 3-19: Schematic drawing of structure MCP detector and secondary electron emission.

THE EXPERIMENTAL SET-UP

The grid that can be seen in the photograph of MCP (Figure 3-17) is an electron repeller that is polarized to a negative voltage to push back the emitted electron in the direction of the MCP, leading to an improvement of the detection efficiency. To avoid the saturation of the MCP detector, the count of neutrals produced by the stored ions should be small enough. To do so, a vertical slit between the buncher and the Mini-Ring is used to control the number of neutrals hitting the MCP detector.

3.2.4.6.1.2 Resistive anode and position computer

The resistive anode is positioned behind the microchannel plates and its electrical potential guarantees that the electron pulses coming out of the second MCP impact the resistive anode. It divides this charge pulse into four outputs at each corner of the anode. Preamplifiers and amplifiers turn the four low-level charge pulses into higher-level pulses and shape them. Then, the shaped pulses, referred to as *A*, *B*, *C*, and *D*, are sent to the inputs of the position analyzer. The position analyzer generates two analog square signals whose amplitude is proportional to the pulse position *X*, *Y* according to the formulae $X = (B \times C)/(A + B + C + D)$ and $Y = (A \times C)/(A + B + C + D)$. The four edge gating controls enable us to choose wanted parts of images and to delete unwanted parts. Figure 3-20 summarizes the operational functioning of the PSD electronics.

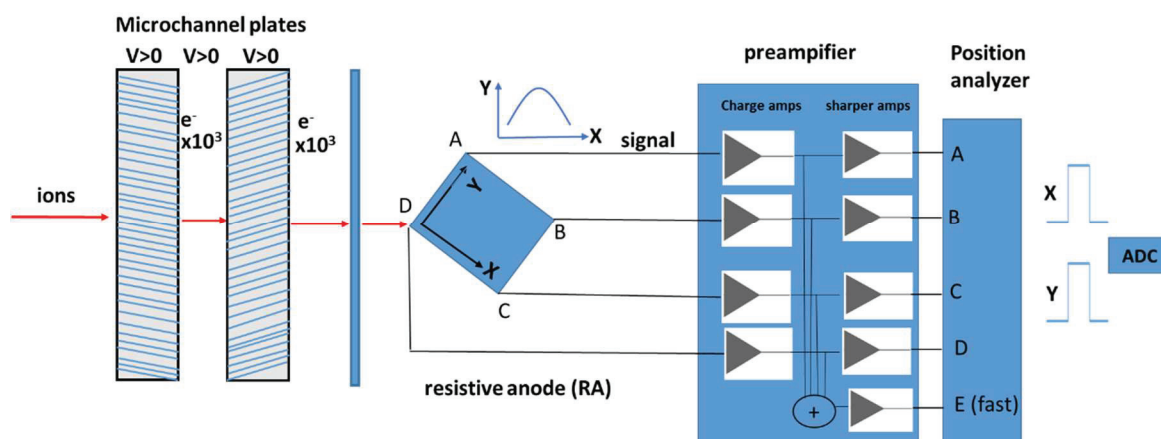


Figure 3-20: Schematic drawing of the processes of detection.

Originally, the *X* and *Y* signals could be observed using the *X* and *Y* channels of an oscilloscope (*XY*-mode), using the strobe signal as the trigger. As already mentioned, nowadays, we rather use a data acquisition card (NI 6229, discussed in subsection 3.5.1) to record the amplitude of the signal and to display the image on a computer screen.

3.2.4.6.1.3 Time measurements

The strobe output of the QUANTAR 2401B device provides a TTL pulse that can be used for time measurements of the detecting particles. This signal is used as a “Stop” input in a time-to-digital converter (TDC), TDC-V4 purchased from the “Institut des Sciences Moléculaires d’Orsay”. The START input of the TDC-V4 is provided by the TTL signal used for the buncher. Consequently, the buncher is the time reference ($t = 0$) for the experiment. There is intrinsically a delay between the real arrival time of particles on the PSD and the corresponding TTL pulse employed as the time signal. This delay is considered to be identical for all the particles and does not affect the time measurements. A typical time spectrum is displayed in Figure 3-21. It shows the time evolution of neutral fragments of dimer benzene hitting the MCP detector (more details are given in Chapter 6). The observed neutral resulting from unimolecular dissociation from the highest internal energy molecules decay first and contribute to the high intensity in a short time. The inset shows the periodic structure of the time spectrum. In this case, short bunches (in comparison with the revolution period) were injected in the Mini-Ring, and neutrals were detected at each passage of the bunch between D_3 and D_4 .

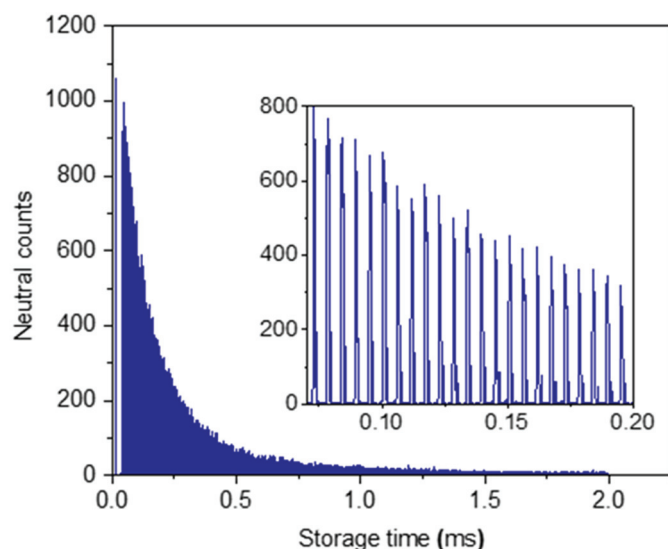


Figure 3-21: An example of the evolution of neutrals detected by the MCP as a function of storage time.

3.2.4.6.2 Detection and collection efficiencies

The detection efficiency, i.e., the probability of detection of the particles impacting the detector, is obviously an important feature. It depends on several factors such as the kinetic energy and the charge of the particles. The most probable neutral fragments resulting from the unimolecular dissociation of PAH cations are H and C₂H₂. In the case of PAH dimer cations, the dissociation is expected to separate the system into two monomers (one charged and one neutral). Therefore, depending on the stored ions species and their dissociation pathway, the neutral fragments to be detected may have different masses, velocities, and kinetic energies. Hence, the detection efficiency is not expected to be the same in all cases and is mostly dependent on the kinetic energy.

For a parent ion of mass M and kinetic energy E_M , the kinetic energy E_m of the daughter of mass m (that is expected to have approximately the same velocity as the parent ion if kinetic energy release is neglected) is given by the simple relation:

$$E_m = \frac{m}{M} E_M \quad \text{Eq. (3-23)}$$

Consequently, for 12 keV phenanthrene parent ions, the detection efficiency is less than 5% for emission of H ($m=1$) fragments which have a rather small kinetic energy of about 70 eV [239]; whereas it is of about 40% for the C₂H₂ ($m=26$) fragments, which have a higher kinetic energy of 1.753 keV [240]. We remark here the importance of working at the highest possible kinetic energy to improve the detection efficiencies.

The collection efficiency is another important factor of the detection system. It depends on the diameter of the detector and the kinetic energy release (KER) of the dissociation process. It is possible to relate the maximum diameter of the spot ϕ to the KER via the following relation [225]:

$$\phi = \frac{2D}{\sqrt{\frac{m E_M}{m' KER} - 1}} \quad \text{Eq. (3-24)}$$

where D is the distance between the emission and detection of neutral, m and m' are the masses of the neutral and charged fragments, respectively, and E_M is the kinetic energy of the parent ion.

THE EXPERIMENTAL SET-UP

In the case of phenanthrene, the trajectory of H fragments is found to be much more sensitive on the KER. For anthracene, the KER of emission of H was measured to be about 0.35 eV. Since the phenanthrene is its isomer, it can be expected that the order of magnitude of the KER is the same. Consequently, KER causes a significant deviation of the trajectories of H fragments. This results in a larger spot size than the PSD diameter, leading to poor collection efficiency. Therefore, considering the poor detection-collection efficiency of the H fragment, it can be stated that most of the detected neutrals are C₂H₂ fragments [77]. For the dimer cations, the collection of the neutral fragments is expected to be with maximum efficiency, i.e., 100 % because the neutral fragment mass is half of the parent mass and the KER is expected to be rather small.

3.2.4.6.3 Channeltron electron multiplier (CEM)

The Mini-Ring has been equipped with a CEM with a collecting surface of 1 cm² located at the extension of the straight line between D₂ and C₁ in order to detect the neutral fragments that could go through the backside hole of C₁. It has the same principle of amplification as that of MCPs, but with a higher gain (typically about 10⁸). However, the CEM cannot perform position measurements. It is used to improve the resolution of the decay time measurements, to access very short decay times after laser shooting (shorter than half of a period), and for coincidence experiments. Figure 3-22 shows a photograph of the CEM.

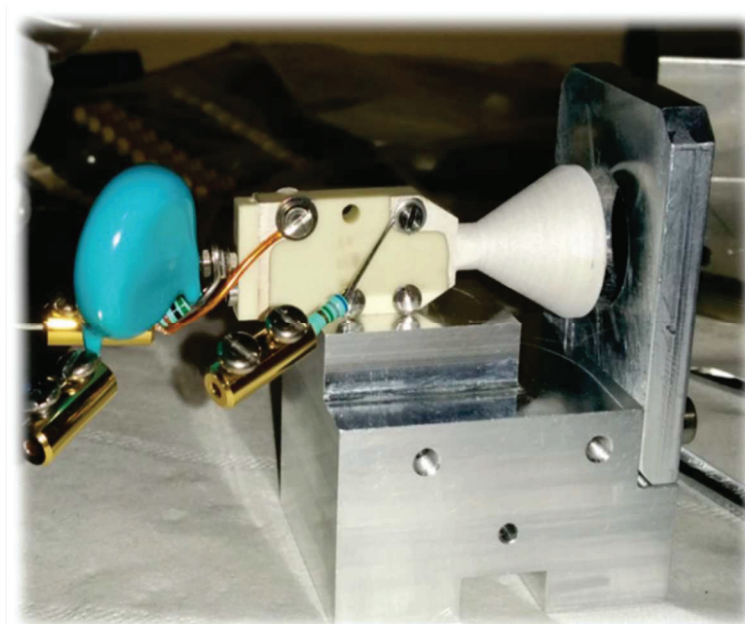


Figure 3-22: Photograph of the CEM.

The output analogic signal of the CEM is sent to a constant fraction discriminator, transformed to a TTL pulse, and sent into a second input of the TDC-V4 card. Therefore, time measurements of neutrals detected by the CEM can be performed in parallel with those detected by the MCP.

3.3 Laser Equipment

In most experiments described in the next chapters, stored ions have been excited using nanosecond laser pulses in order to induce dissociation either to probe the internal energy distribution (in the case of phenanthrene cations) or to record the photodissociation spectra (in the case of PAH dimer cations). The following sections are dedicated to the laser system, the optical arrangement to align the laser beam with the trajectory of the stored ion, and the synchronization of the laser pulses with the stored ions.

3.3.1 General description of the laser system

A tunable Nd:YAG laser system model NT242 from the EKSPLA company is utilized in this experiment. A scheme of this laser is given in Figure 3-23, and Table 3-1 compiles the main characteristics of this laser. This laser device is comprised of five main components:

- i. The Q-switched pump laser Nd:YAG laser NL220
- ii. Second Harmonic Generator (SHG)
- iii. Third Harmonic Generators (THG)
- iv. Optical Parametric Oscillator (OPO)
- v. Sum Frequency Generation (SFG)

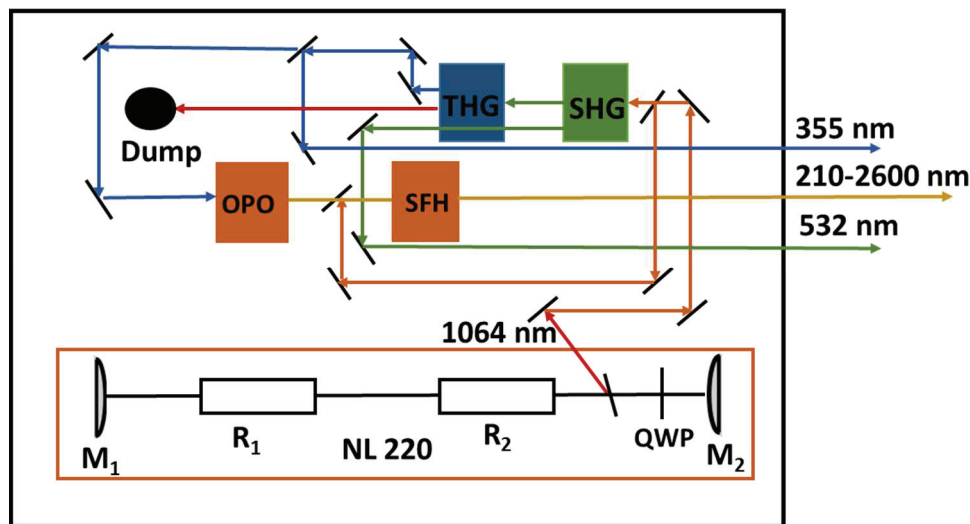


Figure 3-23: A simplified schematic drawing of the tunable Nd: YAG laser system.

This laser provides access almost continuously to wavelengths in the range from 200 nm to 2400 nm via the OPO and the SFG, to the second harmonic (SH) wavelength of 532 nm, and to third harmonic (TH) wavelength of 355 nm via three separate outputs.

Table 3-1: Main characteristics of the EKSPLA NT242 laser.

Pulse energy	450 μ J (POP), 40 mJ (UV), 60 mJ (visible)
Pulse repetition rate	1000 Hz
Linewidth	$< 5 \text{ cm}^{-1} \approx 6 \text{ meV}$
Pulse duration	3-6 ns
Typical beam diameter	$3 \times 6 \text{ mm}$
Pump wavelength	355 nm, 355/1064
Typical pump pulse energy	3 mJ, 3/1mJ
Pulse duration	4-8 ns at 1064
Cooling temperature	18-27 $^{\circ}\text{C}$
Tuning resolution	$1-2 \text{ cm}^{-1}$

THE EXPERIMENTAL SET-UP

The NL220 laser is composed of two Nd:YAG rods pumped with diodes. The diode pump technology allows for the high cadence of 1 kHz reached by this laser device. This NL220 provides a high intensity of the first harmonics at 1064 nm with an average power of about 8W. This first harmonics laser beam pumps the SHG and THG crystals in order to provide about 1.8 W and 2.7 W average power of SH and TH, respectively. These values are the maximum powers measured at the corresponding output of the laser device. They strongly depend on the temperature setting of the crystals. The TH and SH are used to pump the OPO and SFH crystals. The average power measured at the OPO output is strongly dependent on the selected wavelength. There are several branches in the spectrum depending on the use of the OPO and/or SFG.

3.3.1.1 Time structure Laser pulse

The repetition rate of 1000 Hz is an important feature of the laser system for fast data collection. By using a Q-switch divider, the repetition rate can be changed to smaller values when needed starting from 1000, 500, 333 Hz. The maximum repetition rate of the laser is well adapted to the timing of Mini-Ring experiments. For experiments with dimer cations, we stored for 2 ms only and we used a repetition rate of 500 Hz to excite the stored ions only once in the storage sequence. For experiments with phenanthrene cations, we stored for 10 ms and used the maximum repetition rate to record 10 laser-induced decays per storage sequence.

The laser pulse duration is about 3 ns. This value has been checked with a photodiode connected to an oscilloscope.

3.3.1.2 Laser power and energy per pulse

The laser average output power (P_{ave}) was directly measured using a power meter. Two models of power meters have been used. Powermeter Vector H310, equipped with a head that can measure up to 10 W was used to measure the highest powers of the harmonic outputs of the laser. The Nova II /Ophir Photonics power meter whose head is limited to a maximum power of 2 W and was employed to measure the lower powers from the OPO output, in the visible and IR range up to 2200 nm.

Since the average power of the laser can be measured while the laser is Q-switching at a rate f_{Qs} (often corresponding to a maximum of 1 kHz), the energy per pulse in joules, E_p , is simply calculated by dividing the average power by the repetition rate:

$$E_p (J) = \frac{P_{ave}}{f_{Qs}} \quad Eq. (3-25)$$

The fluence $F(J/m^2)$ can be defined by dividing the pulse energy by focal spot area:

$$F(J/m^2) = E_p / A \quad Eq. (3-26)$$

For the third harmonics, the pulse energy at 1 kHz had a maximum value of $E_p(355 \text{ nm}) = 2.7 \text{ mJ}$ corresponding to a fluence of $F(355 \text{ nm}) = 5.4 \times 10^{17} \text{ eV/cm}^2$, whereas, for the second harmonic these values were $E_p(532 \text{ nm}) = 1.8 \text{ mJ}$ and $F(532 \text{ nm}) = 3.7 \times 10^{17} \text{ eV/cm}^2$. The OPO output energy is, by nature, strongly dependent on the wavelength. The OPO pulse energy is given as a function of wavelength in Figure 3-24. It has a maximum output energy of about 140 μJ per pulse at about 460 nm.

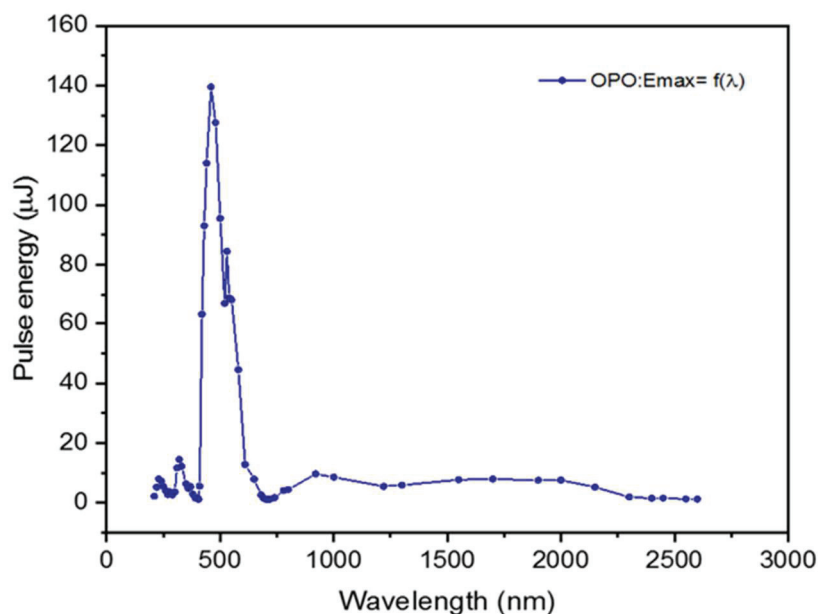


Figure 3-24: Output pulse energy as a function of the wavelength of the OPO output of the EKSPLA NT242 laser.

The typical output pulse energy is 3H, SSH, SFC, and PG as well as the IDLER (Figure 3-25). The UV part, 3H/SSH/SFG was not used in this work. The IDLER was used for the photodissociation spectra of the dimers due to a rather flat maximum intensity between 1500 and 2000 nm corresponding to a pulse energy of 8 μJ/pulse.

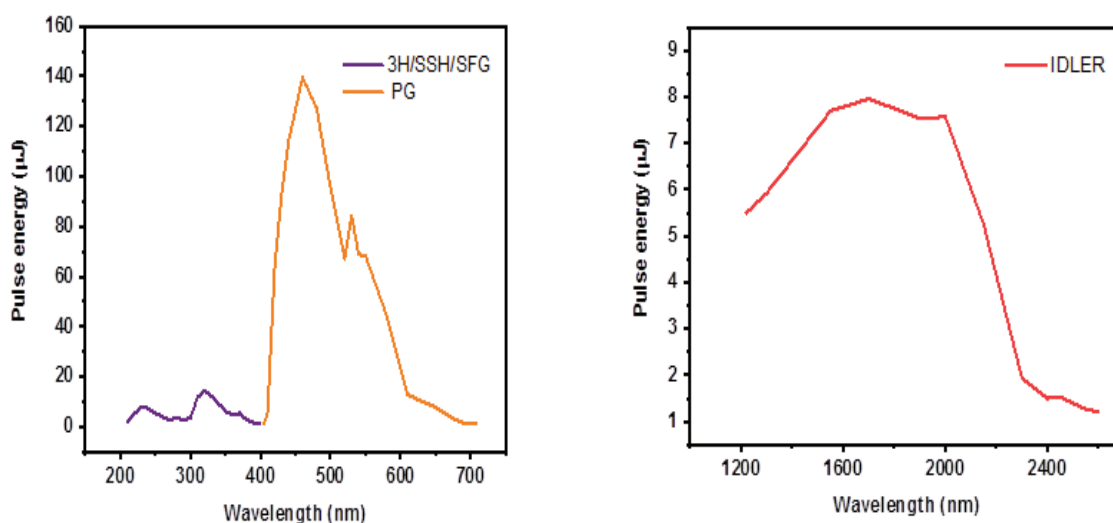


Figure 3-25: 3H/SSH/SFG and PG output pulse energy of the EKSPLA NT242 laser shown on the left side and Idler output pulse on the right side.

For the sake of corrections of the photodissociation spectra, the photodissociation intensity has been normalized with the number of photons per laser pulse. Indeed, to provide photodissociation spectra that are proportional to the photo-dissociation absorption cross-section, the correct normalization parameter is not the pulse energy, but the number of photons per pulse, N_{ph} , which is, in turn, proportional to the wavelength:

$$N_{ph} = \frac{E_p}{h\nu} \propto \lambda E_p \quad \text{Eq. (3-27)}$$

where $h\nu$ and λ and the photon energy and wavelength, respectively.

THE EXPERIMENTAL SET-UP

In the preparation of experimental runs, especially in the alignment phase, it is important to vary the laser intensity. Most importantly, performing absorption spectra with different laser intensities allows for estimating the possible contribution of the two (or several) photon absorption processes. The laser intensity is controlled by the Q-switch delay of the pump laser. The Q-switch delay is set at 196 μs to deliver the maximum intensity. Smaller pulse energies can be obtained by changing (increasing or decreasing) the Q-switch delay. The variation of pulse energy as a function of Q-switch delay is displayed in Figure 3-26.

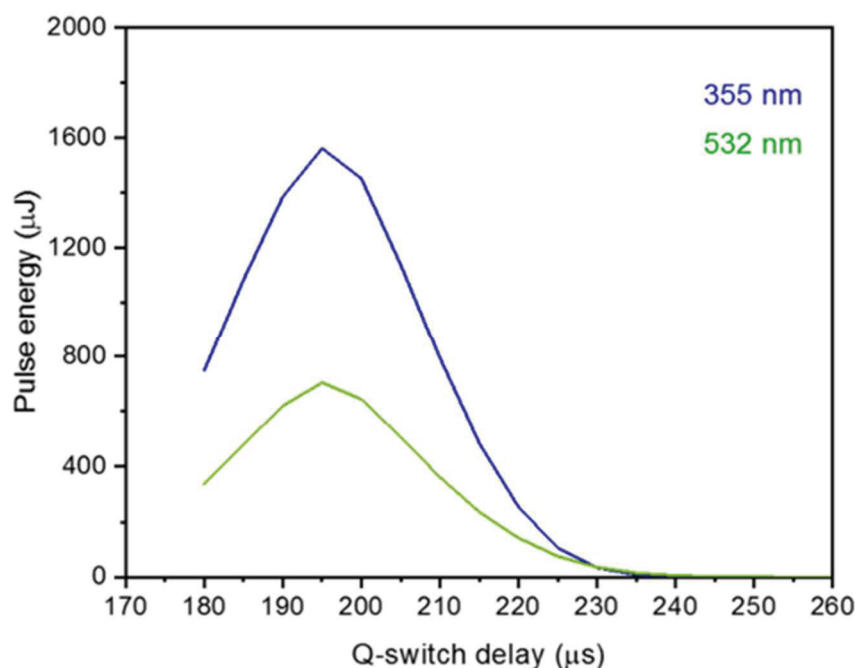


Figure 3-26: Laser pulse energy as a function of Q-switch delay for the second and third harmonic.

3.3.2 Setting the overlap between the laser beam and stored ions

When the laser beam overlaps with the stored ions, the internal energy of the latter is increased depending on the number and energy of the absorbed photons. If they reach sufficient excitation energy, they can decay eventually after some delay time. The laser-induced delayed dissociation of some PAHs cations (naphthalene, anthracene, pyrene,...) has been investigated in previous works with the Mini-Ring [76,77,133,135,212,225,241–243]. The case of naphthalene is presently routinely used to verify and adjust the laser-ion time and spatial overlap in the merged beam configuration.

3.3.2.1 Laser injection configurations

For the photo-dissociation experiments, the laser beam has to be driven to interact with the molecular ion beam circulating in the Mini-Ring. A set of suitably chosen mirrors and lenses have been placed on optical tables, as shown in Figure 3-27. The OPO output has a dedicated set of driving broadband metallic mirrors whose reflection coefficient is rather constant in the visible and infrared range, i.e., in the 400-2000 nm range. It is noteworthy that several mirrors are needed in order to provide fine vertical and horizontal positioning of the laser beam to optimize the alignment or to cross with the ion beam.

One of the advantages of the very open design of the Mini-Ring is that several options are possible for injecting the laser beam into the Mini-Ring. The three main options that have been used in this work are (see Figure 3-28):

- i. The merged beam configuration between D_1 and D_2 , where the laser pulse and the stored ion trajectory overlap parallelly. Detection of the laser-induced fragments in the

THE EXPERIMENTAL SET-UP

- two next sections is performed by the CEM and the MCP. This option has been used for delayed dissociation of the phenanthrene cations (Chapter 5).
- ii. The crossed beam between D_3 and D_3 configuration, where the laser pulse shots the ion beam at a right angle. This configuration allows for the detection of prompt dissociation. In cases where no delayed dissociation exists (e.g., for PAH dimer cations), this is the only option for action spectroscopy using the MCPs (Chapter 6).
 - iii. The crossed beam between D_2 and C_1 configuration. This configuration has been employed with PAH dimer cations to perform a coincidence detection of the neutral fragment by the CEM and the charged fragment by the MCPs (Chapter 6).

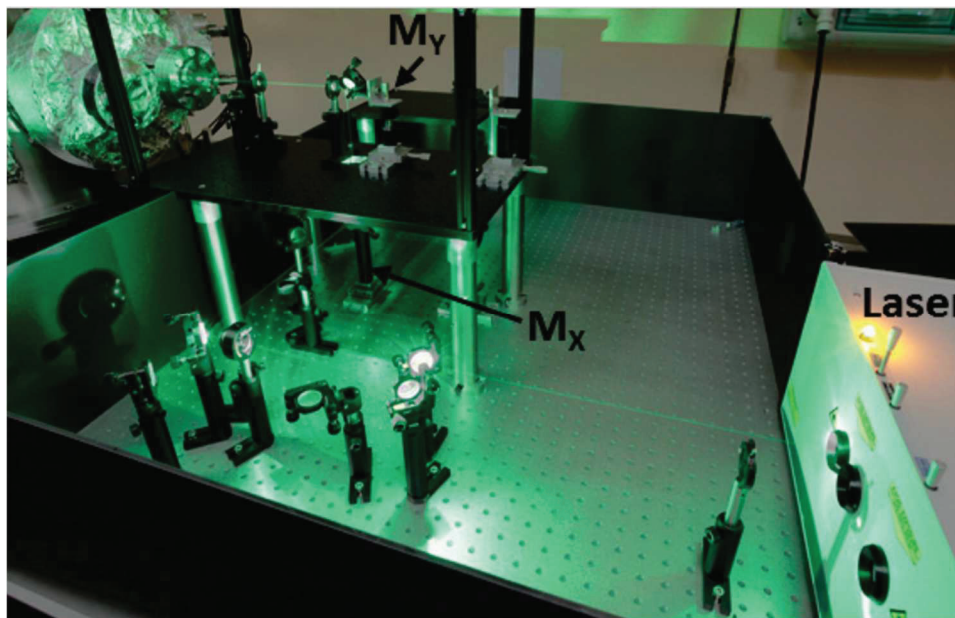


Figure 3-27: Photograph of the tunable Nd:YAG laser system.

It is noteworthy that with configuration (ii), the laser beam was injected with a small vertical angle to avoid crossing with ions that would be in between D_1 and D_2 . Moreover, the beam could exit the Mini-Ring vacuum chamber through a glass window. Therefore, it was possible to measure the laser power at the end of the laser path, which was useful for laser intensity corrections of photodissociation spectra.

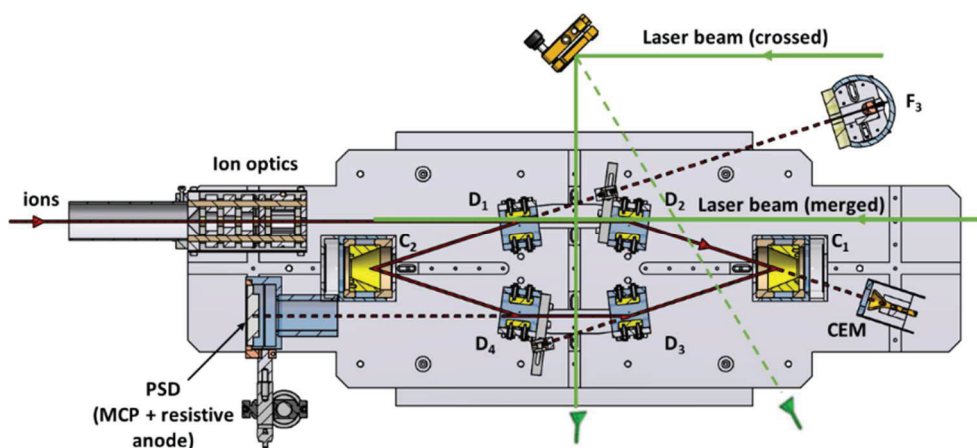


Figure 3-28: Scheme of the Mini-Ring with different laser injection configurations.

3.3.2.2 Time overlap

Time overlap is an issue when short ion bunches are injected into the Mini-Ring. Then, laser pulses have to be synchronized with the ion bunch even after hundreds of revolutions. The laser control device provides a TTL signal that is synchronized with the emission of the laser

light pulse. Therefore, the time overlap can be obtained by adjusting finely the delay between the buncher and laser TLL signals.

In addition, the phase synchronization between the laser pulses and the ion revolution is of great importance when multiple laser pulses are used for the excitation of the stored ions at different storage times over a single storage cycle. In order to manage this, the laser electronics offer the possibility to change the laser pulse frequency, f_L , to fulfill the following synchronization condition

$$f_{ion} \approx n f_L \quad \text{Eq. (3-28)}$$

where f_{ion} is the ion revolution frequency and n integer number. The laser frequency is typically 1 kHz, but it can be changed in steps of 1 Hz to approximately fulfill the condition of Eq. (3-28).

For long storage times, the time overlap issue is less critical because of ion debunching. Indeed due to a slight difference in kinetic energy and trajectory angles, the revolution period (or frequency) slightly varies from one ion to another. Consequently, the bunch structure is lost little by little as long as the ions are performing revolutions around the ring. Due to debunching, the stored ions end by filling the entire ring and behave like a continuous beam ruling out the time overlap issue at the price of decreasing the ion density.

3.3.2.3 Position overlap and laser alignment strategy

In order to optimize the overlap between the two beams, the laser beam should be of the same diameter as the ion beam approximately, i.e., about 1 to 1.5 mm. A lens is used to obtain approximately a parallel laser beam of this size.

The fine positioning of the laser beam has to be tested with Naphthalene cations. Figure 3-29 shows two different cases of good and bad overlaps between the laser and the ion beams, in the merged beam configuration. Figure 3-29(a) shows that the ideal overlap, i.e., ideal horizontal and vertical relative orientations of the laser and ion beams, leads to a huge intensity of laser-induced delayed dissociation peaks and the width of these peaks correspond to the travel time between D_1 and D_2 , i.e., about 0.8 s for 12 keV for phenanthrene cation.

Figure 3-29b shows non-ideal overlap when the laser points towards the inner part of the ion trajectory. The laser beam crosses the ion beam at two different points inside D_1 and D_2 . At the first point, ions have not been completely deflected by D_1 and at the second ions have been already deflected by D_2 . Each of the two crossing points gives rise to a corresponding peak in Figure 3-29(b) of neutrals with possibly a different intensity. This laser beam configuration can be intentionally set because it provides an opportunity to adjust finely the laser direction. Indeed a difference in the peak intensity is interpreted as a non-ideal vertical alignment. In this case, the laser beam has to be reoriented in the vertical plane to obtain similar amplitudes for the two peaks. Then, the laser beam is moved back in the horizontal plane such that one peak only is found as in Figure 3-29(a), and such that the peak width should be slightly smaller than the time difference between the two peaks in Figure 3-29(b).

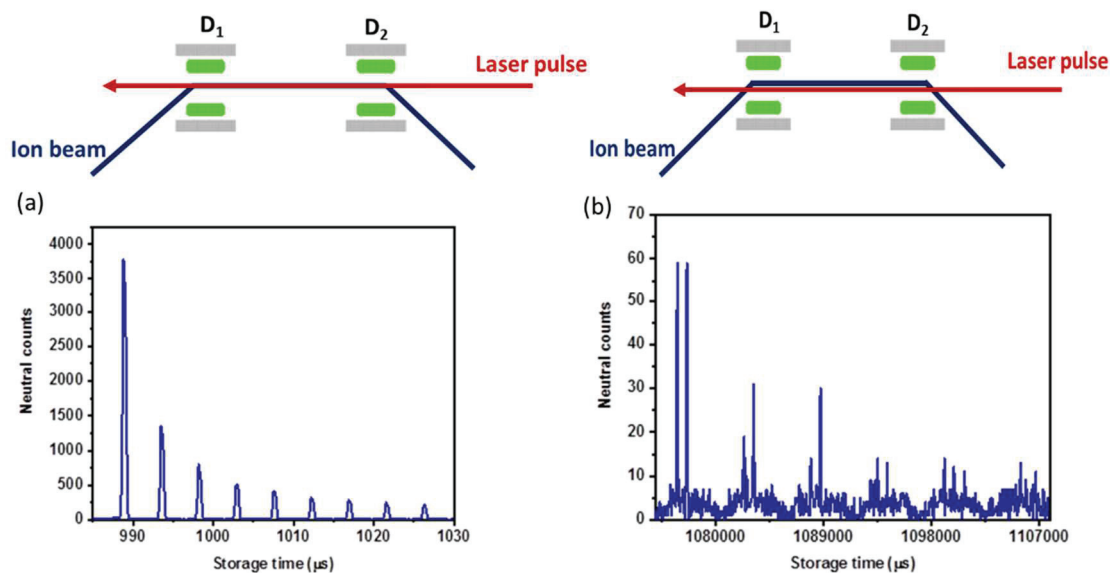


Figure 3-29: (a) Laser-induced decay is obtained when the laser beam overlaps with the stored ions with almost the same diameter as the ion beam; this is the ideal overlap condition that is expected in typical experimental conditions. (b) Laser-induced decay is obtained in non-ideal overlap conditions when the laser beam is pointed towards the “inner” part of the ion trajectory; two peaks per ion revolution are observed corresponding to sharp crossing points between the laser and ion beams.

3.4 Timing of the experiment

3.4.1 Storage sequence

Most of the time, the buncher deflects the ion beam away from the Mini-Ring entrance, preventing thereby ions to enter the ring during the storage time. For a short time, typically in the 1-5 μs range, the voltage on the buncher is switched to 0 V, letting an ion bunch enters into the Mini-Ring. At the first passage of the ion bunch through D_1 , the D_1 voltage is off to let it go through without deflection towards D_2 , which deflects the trajectory towards C_1 . While the ion bunch is far from D_1 , it is safe to switch it on so that the ion bunch is deflected at the next passages through D_1 to remain stored on stable trajectories in the ring. After a pre-defined storage time, T_S , the D_1 voltage is switched off to let the remaining ions exiting the Mini-Ring towards the faraday cup F_3 .

3.4.2 Time structure of recorded neutral fragments

As already mentioned, during storage, neutral fragments (due to spontaneous unimolecular dissociation, laser photo-dissociation, or collision with rest gas) can be detected by the MCPs or the CEM according to their emission location (between D_3 and D_4 or D_2 and C_1 , respectively). The first passage between D_3 and D_4 corresponds to the first peak at a short storage time. The ions are then stored on the same trajectory as the initial one, to complete a sequence and go for a second turn, which gives a second peak, as presented in Figure 3-30. At every single turn, there is a probability for detecting a neutral fragment, which yields the periodic time structure. After well-controlled storage time T_L , the laser pulse is sent to excite the ion beam with precise synchronization with the buncher as already discussed 3.3.2. Thus, fractions of the ions in the bunch are re-excited by laser absorption. The first neutral signal is obtained at half a revolution period, T , after laser pulse. For the next turns after laser excitation we observe a huge increase of the neutral yield, providing a laser-induced decay. This laser-induced decay will be the probe of the internal energy distribution at the time of the laser shot. Such delayed peaks due to laser-induced decay are observed at each $(n + 1/2)T$ after the laser irradiation are shown in Figure 3-30. It is worth mentioning that this is true even if the periodic structure of the beam is lost due to debunching. Such a record as the one of Figure 3-30 is the accumulation of thousands of storage sequences.

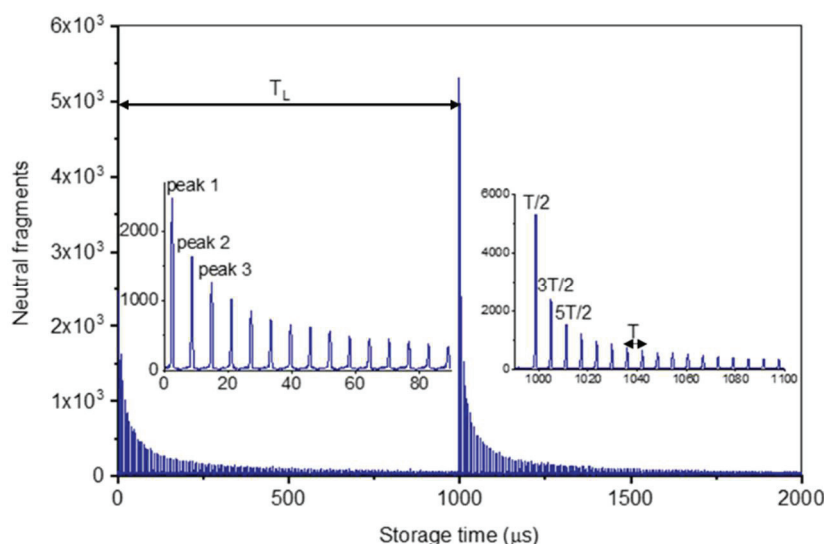


Figure 3-30: Neutral count spectrum detected over a storage time of 2 ms, the laser pulse for excitation the ions at 1 ms.

The timing of the storage sequence, of the laser pulses, and data acquisition is synchronized with TTL (0 to 5 V) or NIM (0 to -0.8 V) logical signals. The timing of the logical signals used for the storage, laser excitation of the ions, and detection measurements are displayed in Figure 3-31(a) for phenanthrene cation and (b) for PAHs dimer cation. For some of those signals, the delay and width need to be precisely controlled. Three function generators (Tektronix AFG 3022C) are used to prepare these logical signals with appropriate amplitudes (TTL or NIM), delays, and widths.

The storage cycle starts with the ‘buncher signal’. This TTL signal is used to switch the buncher high voltage. It should be noted that the leading edge of this signal is employed as the time reference for each cycle, i.e., it is used to trigger the other function generators and time measurements. For instance, it also provides the ‘START signal’ input of time measurements in the TDC V4 data acquisition card. A ‘STOP signal’ input is also generated with a suitable delay (corresponding approximately to the end of the storage cycle) to end the time measurement of the TDC V4 acquisition card.

The buncher signal also triggers the TTL ‘storage signal’ that is used to switch the high voltage of D_1 . The delay and width of this storage signal must be correctly set according to the ion flight time from the buncher, Δt_s , and the storage time, T_S , respectively.

Since the laser cannot be triggered by an external source, the laser output TTL signal (‘laser signal’) is employed as the overall trigger of the whole experiment. However, as the present description of the timing considers the buncher signal as time zero, the delay between the buncher and laser signals is finely adjusted, such that the next laser pulse is synchronized with a given ion revolution number. The delay time between this ‘next laser pulse’ and the buncher signal is referred hereafter as the ‘delay laser’, t_L .

3.5 Computer control and Data acquisition

As mentioned in previous sections, in order to control the beamline and the data acquisition of the MCP detector, two data acquisition cards are employed in this experiment: the NI-6229 and the TDC V4. This section is dedicated to a short description of the computer control of the experiment and the data acquisition.

3.5.1 The National Instruments PCI (NI-6229)

The NI-6229 is comprised of 16 analog inputs and 4 analog outputs. All have timing accuracy and resolution of 50 ppm of sample rate and 50 nm, respectively.

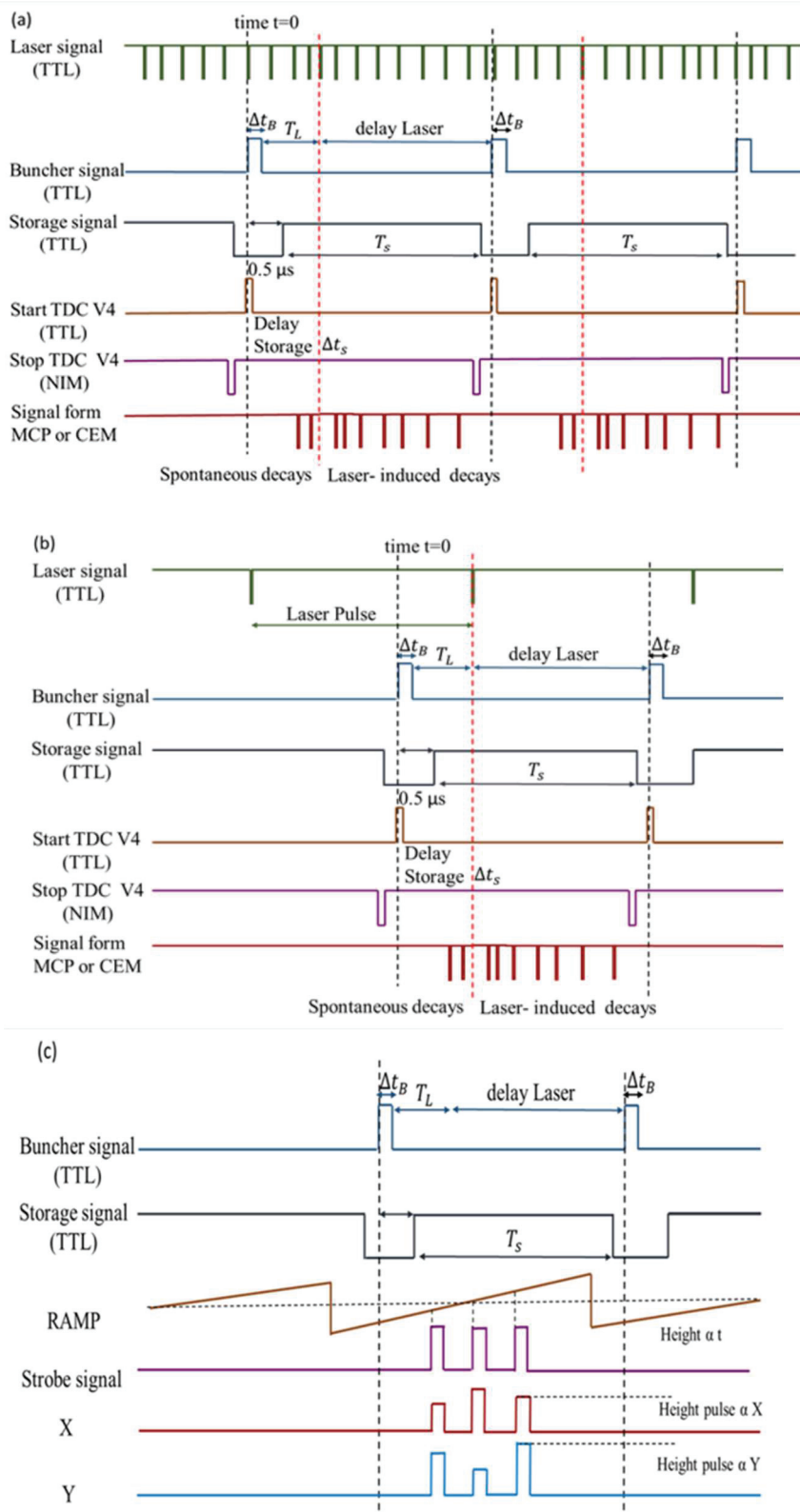


Figure 3-31: Schematic drawing of the acquisition and control systems, (a) timing diagram for phenanthrene experiment (chapter 5), (b) Diagram for PAH dimers experiment (chapter 6), (c) Timing position and time measurement with the NI- 6229.

3.5.1.1 Analog inputs and outputs

The 16 analog inputs are differential channels with ADC resolution of 16 bits with a maximum voltage of ± 10 V. In this work, Channel 0 is connected to 0-10 V output of the pico-ammeter used to measure the currents of faraday cups, F_{line} and F_3 . It is useful for ion beam control, optimization, and for recording mass spectra. Channels 1 and 2 are connected to the X

THE EXPERIMENTAL SET-UP

and Y outputs of the Qantar electronic device that is used to measure the position. This way we measure the amplitudes of the X and Y signals that are proportional to the X and Y positions. Channel 3 is connected to the ramp signal that is generated by a wavefunction generator. It provides the time information related to the position measurement of a detected particle on the PSD.

The analog outputs are 4 channels with DAC resolution of 16 bits with an output range of ± 10 V. In this work, channel 0 is connected to 0-10 V input of the current power supply of the magnet. This is useful to scan the magnet current to perform mass spectra. Channel 1 is connected to the 0-10 V input of the high voltage power supply of the ions source. Channel 2 is connected to the 0-10 V input of the high voltage power supply of the Einzel lens located between the source and the magnet. Channel 3 is connected to the 0-10 V input of the voltage power supply of Cone 2.

The NI-6229 is controlled by LabVIEW programs. Different and independent programs are used:

- i. To control some of the beamline electrode voltages (ions source, Einzel lens) and the Mini-Ring C_1 and C_2 voltages.
- ii. To monitor the selection magnet current, record Faraday cup currents and perform mass spectra.
- iii. To record the amplitude of the PSD X and Y signals to perform the imaging of the detected neutral fragment by the PSD. In the same program, rough time information (with approximately 1 μ s resolution) associated with the detection of a neutral fragment is performed by generating a ramp voltage with a function generator and by recording this ramp voltage simultaneously with the X and Y signals, illustrated in Figure 3-31(c). This method allows for getting images associated with each ion revolution of the storage sequence.

3.5.2 Time to digital converter (TDC V4)

Time to digital converters (TDC) are commonly used devices to measure digital time events in time of flight mass spectrometry, for instance. They measure and digitize the time interval between a 'START signal' pulse and one or several 'STOP signals' in single or multi-stop modes, respectively.

The TDC V4 is composed of 16 TDC input channels that can be used in multi-stop mode. It has also a 'START signal' and an 'END' input channel (the latter acknowledges the end of time measurement sequence and makes the device ready for the next start signal).

The TDC V4 can perform precise time spectra with an intrinsic resolution of 120 ps and a maximum time range of 8 ms. In practice, the time range can be extended to a maximum of 1 s by using the 'range extension mode' and, recorded neutral fragment counts are stored in time bins of 120 ns for storage time below 20 ms. The time bins were increased for longer storage time for reasons of data management and screen display. However, the original data are recorded on the disk in 64 bits hexadecimal numbers with an intrinsic resolution of 120 ps.

In this work, Channel 0 was used for the precise of the timing of the PSD signal output from the Qantar device. Channel 1 was used for precise timing channeltron signal via a constant fraction discriminator that was used for transforming the analog channeltron signals to TTL pulses. Channel 2 is employed for time-selected counts. It is used for two purposes. Firstly, when set to select broad time ranges at the end of the storage sequence, it was used for refining the optimization of the storage conditions, i.e., the Mini-Ring voltages and injection of the beam. Secondly, when it was set to select a short time range right after the laser beam pulse to finely optimize the overlap between the laser and the stored ions by maximizing the count rate of the laser-induced neutral fragments.

3.6 The experimental set up in DESIREE at Stockholm

A part of the experimental work presented in this thesis was performed at Stockholm University with the cryogenic ESR, DESIREE. The present experiments with DESIREE aimed to access very long storage times and very low temperatures, such that the infrared radiative cooling and photodissociation spectroscopy of PAH dimers could be investigated. This section is thus dedicated to a brief description of the DESIREE facility. More detailed information can be found in ref. [244].

3.6.1 The Double ElectroStatic Ion Ring ExpEriment, DESIREE

DESIREE stands for the Double ElectroStatic Ion Ring ExpEriment. It is composed of two electrostatic storage rings, S-ring (symmetric ring) and A-ring (asymmetric ring), whose design is based on the ELISA storage ring [79,245]. The two rings are interconnected with a common straight section, as can be seen in the photograph of Figure 3-32 and the technical scheme of Figure 3-33. The main steering components of each ring are two 160° cylindrical deflectors (CD), four quadruple doublets (QD), four 10° parallel plate deflectors, and eight symmetric or six asymmetric ring correction elements (CC, CV). The circumference of each ring is about 8.6 m and each ring has a straight section at the injection side and a common straight section called merging region (MR) in between. Pickup electrodes are mounted at both ends of the merging region to control the intensity and position of the ion beam.

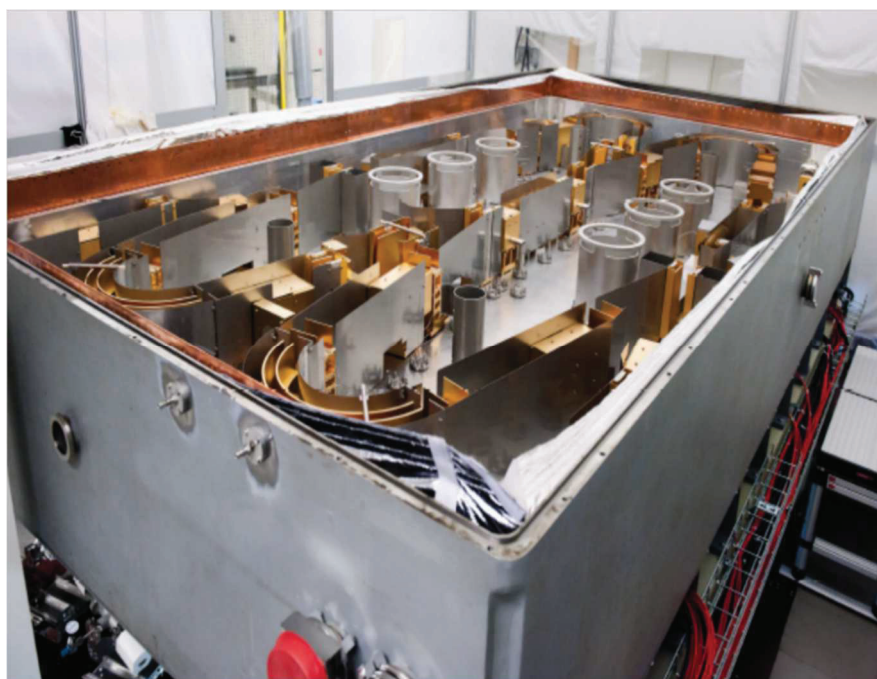


Figure 3-32: Photograph of DESIREE.

The entire double storage ring DESIREE is mounted on a single platform and placed inside a double-walled chamber, i.e., an outside copper wall and an inner aluminum wall separated by thermal screening (see Figure 3-32). This design allows keeping the inside temperature down to about 13 K and the inside pressure below 10^{-14} mbar. Under Such temperature and pressure conditions, DESIREE enables the storage of ions for long periods up to hours. Thereby, the atomic, molecular ions can be stored for storage times that are longer than the decay times of vibrationally excited states. It is, therefore, possible to study the cooling dynamics of initially hot molecules and to prepare molecules in their vibrational and, possibly, rotational ground states [138,139,244,245].

DESIREE was designed to perform experiments with merged ion beams, e.g., neutralization between positive and negative ions at small relative velocities and the measurement of lifetimes of metastable state for both anions and cations atomic ions. Since in the present work, we

THE EXPERIMENTAL SET-UP

performed only a single ring experiment, i.e., A-ring because it allows for using the charged fragment detector, no further description of double-ring experiments will be presented here. More information can be found in refs. [138,139,244,245].

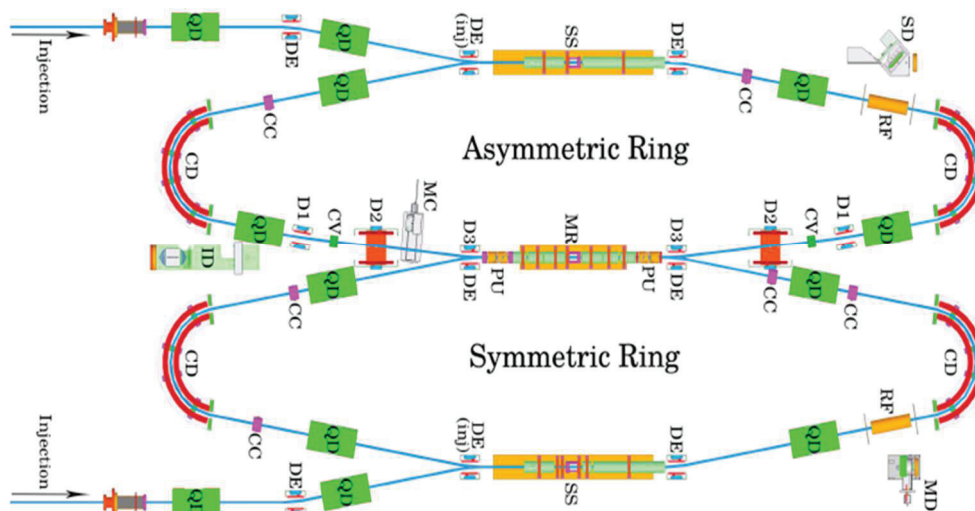


Figure 3-33: Schematic illustration of DESIREE and respective ion optical elements [139].

The ion beam can be injected into DESIREE from different ion source platforms at maximum voltages of 100 and 25 kV via two 90° deflectors (Figure 3-34). In the present work, the latter platform at 20 kV was equipped with a full permanent magnet ECR ion source Monogan M100 from Panteknick Company. Its HF frequency, provided by a solid-state generator, can be adjusted from 2 to 2.45 GHz with a power of at least 30 W. In both of the injection ion beams of the transport line, a 90° selection magnet is used to select a specific ion mass/charge ratio. The ion beam is hence steered and guided through a set of electrostatic ion-optical elements and injected into the corresponding ring. Moreover, a set of Faraday cups are placed along the injection lines to monitor the beam current.

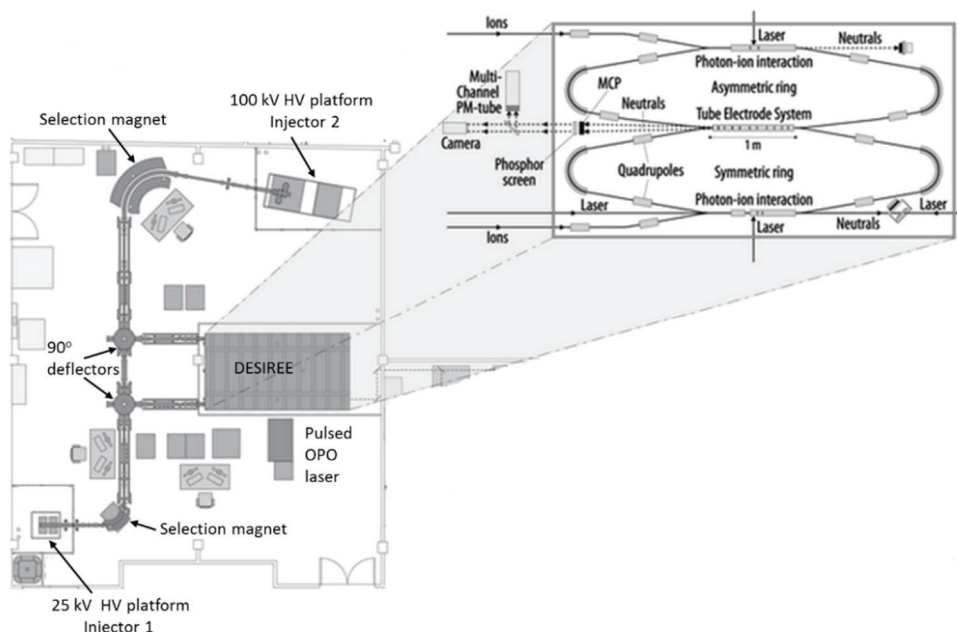


Figure 3-34: A schematic illustration of the DESIREE facility, showing the ion source platforms and selection magnets [246].

THE EXPERIMENTAL SET-UP

In order to detect neutrals and charged ions, several detectors are mounted in line with each of the straight sections of the rings. These are, imaging detectors (ID) at the end of the merging region, optically transparent secondary electron emission detector (SD), movable position-sensitive detectors (MD, MC) equipped with electronic devices called resistive anode encoder symmetric ring (RAES), and resistive anode encoder asymmetric ring (RAEA) at the end of each ring. A fragment detector (FD) can be moved by a stepper motor to a position where charged fragments can be detected. All detectors have a z-configuration, triple stack of MCPs. The MCP sizes are 40 mm for the RAES, RAEA, SD, and FD, and 80 mm for the ID. The ID uses a phosphor screen with a CCD camera to determine the position of the impact of the neutral fragments on the MCPs (Figure 3-35).

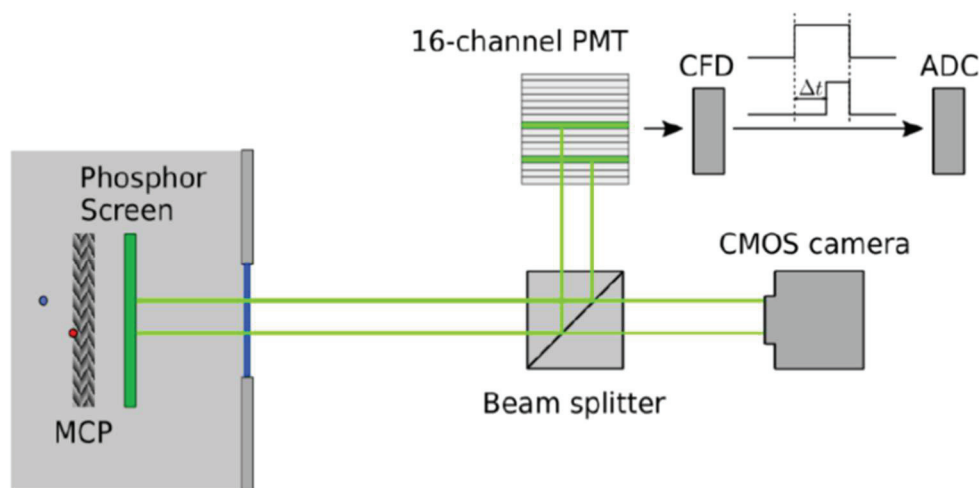


Figure 3-35: Schematic illustration of the imaging detector [247]

Laser beam overlap or crossing with the stored ion on the straight sections of the rings (MR, SS) is accessible by several glass windows.

In the present work, we used the ID and FD detectors for detection in coincidence of the neutral and charged fragments of naphthalene dimer cations. The measurement cycle was in three steps: inject, store, dump. The voltage of the DE injection deflector is changed to storage mode after the ion bunch enters the ring and remains at this value until the end of the measurement window. When the storage is changed to dump mode, the remaining ion beam is removed and the next ion beam is injected. Data is accumulated over many measurement cycles. The A-ring was almost filled by injecting ions bunches of $69 \mu\text{s}$ time width. In the present work, the storage time was limited to 30 s. This was found to be a good compromise between the necessary repetition rate needed to acquire enough statistics and the time needed to ensure that the vibrational cooling process would be approximately completed.

During storage, dissociation events of naphthalene dimer cations were characterized by the coincidence detection of a neutral and a charged monomer by ID and FD detectors, respectively.

A 10Hz, wavelength-tunable, pulsed OPO laser was shot perpendicularly to the ions beam in the merging region (MR) to perform photo-dissociation spectroscopy at different storage times, i.e., every millisecond. The maximum pulse energy was 12 mJ. Wavelength was scanned from 750 to 1750 nm with a step of 40 nm.

A one-week beam -time has been dedicated to studying the cooling dynamics of naphthalene dimer cations at DESIREE in which longer storage time and cryogenic temperature of stored ions is achievable.

3.7 Conclusion

This chapter has been devoted to discussing the experimental set-ups used in the present thesis work. Most of the work has been performed with the Mini-Ring, except a one-week experimental run at DESIREE.

We have shown that in ERS storage conditions, i.e., voltages on the ESR electrodes, are independent of the mass of the stored particles. Therefore, in our case, PAH cations and dimer cations of different masses can be stored without changing any voltage of the Mini-Ring (or DESIREE) as long as the kinetic energy is kept constant. However, these ions have different velocities, so the timing of the experiment is to be adapted from one molecule to another.

In this chapter, the details of the Mini-Ring experiment have been presented. In brief, molecular ion beams, produced by the ECR ion source, which is placed on a high voltage platform at 12 kV, are selected by a 90° bending magnet sector depending on their charge to mass ratio. Then the continuous ion beam is chopped to obtain ion bunches of the desired width of several μs , which are finally guided and injected by a set of ion-optics into the Mini-Ring. The compact Mini-Ring, storage conditions, timing sequence have also been described. The laser equipment used to excite the stored ions has also been described, and we have shown how it can be used to probe the internal energy distribution of the stored PAH monomer cations and how photodissociation spectra of PAH dimer cations can be recorded. The resulting neutral fragments are detected by a set of MCPs combined with a resistive anode to form a PSD and a CEM. Two data acquisition systems are used in the present work to record the time and position measurements of the neutrals emitted in each turn in the Mini-Ring.

Finally, the DESIREE facility has been briefly described. During a one-week beam-time, we could record the near-IR photo-dissociation spectrum of naphthalene dimer cations, benefiting from the cryogenic environment to study the evolution of this spectrum as a function of the internal temperature of the naphthalene cations.

In the three next chapters, we will discuss the experimental results concerning the production of PAH monomer and dimer cations (Chapter 4), the recurrent fluorescence process for phenanthrene cations (Chapter 5), and the photo-dissociation spectroscopy of PAH dimer cations (Chapter 6).

4 PRODUCTION OF ION BEAM OF PAHs

4	PRODUCTION OF ION BEAM OF PAHs	92
4.1	Short review of different ion sources for the production of PAH and PAH dimer cations in the gas phase	92
4.2	General source conditions inside the ion source	93
4.2.1	Roles of HF power and pressure	93
4.2.2	Estimation of the pressure inside the ion source	94
4.3	Production of ion beams of phenanthrene monomer cations	95
4.4	Production of ion beams of dimer cations	97
4.4.1	Dimer of naphthalene	98
4.4.2	Dimer of pyrene	99
4.4.3	Dimer of benzene	100
4.5	Possible mechanism of formation of dimer cations of PAHs	101
4.6	Conclusion	102

The success of the experiments that will be described in the next chapters is highly dependent on the ability to produce the desired molecular ions with sufficient intensities. As already mentioned in the previous chapter, ECR ion sources have not been developed for the production of molecular ion beams. Therefore, it is interesting to study the specific conditions that permit the production of PAH cations and PAH dimers cations beams. In this chapter, the study is performed by analyzing mass spectra for different source conditions.

After a short review of different methods of production of PAH cations and PAH dimer cations, we present the general conditions used with the Nanogan I ECR source. The next section is dedicated to the specific production conditions of the ion beam of monomer cations of phenanthrene, the study of radiative cooling of which will be presented in Chapter 5. The last section is devoted to the production of dimer cations of benzene, naphthalene, and pyrene, the three-dimer cations that have been investigated in this work (see Chapter 6) using both the Mini-Ring and DESIREE (only for naphthalene).

4.1 Short review of different ion sources for the production of PAH and PAH dimer cations in the gas phase

Since PAH cations and their dimers have been studied for several decades in the gas phase, various techniques have been used to produce small PAH ion beams in the past depending on the needs of each specific study and, also, on the know-how of the research groups. A short, non-exhaustive review of several techniques is presented in this subsection.

Supersonic jets, laser-induced plasma, synchrotron VUV, electron impact, and ion impact techniques have been used to form PAH cations and their dimers. Boissel et al. [9] used an ion trap experimental set-up where the PAH cations were generated by laser impact on a solid pellet, placed on the trap axis. Neutral and ionized PAHs were also produced by irradiation in order to perform the Matrix Isolation Spectroscopy (MIS) where studied species are isolated at low temperatures in the low polarizability Ne matrices [7].

Dimer cations of PAHs were firstly created in glassy solutions by gamma-ray irradiation [248–251]. Resonant two-photon ionization (R2PI) was used to form PAHs in the gas phase [252]. Inokuchi et al. [10,253] have developed a laser-induced plasma technique combined with an argon gas expansion to produce cold dimer cations of naphthalene cations [10,253]. They suggest that the dimers are formed by the accretion of neutral molecules to the ionized ones and are subsequently cooled in the gas expansion. For benzene dimer cations and clusters, the same group has used an electron-impact ionizer placed next to a pulsed nozzle where a mixture of benzene, deuterated benzene-d₆, and argon was expanded into a vacuum chamber through the pulsed nozzle [254]. Ohashi and Nishi used a pulsed ionization laser to ionize neutral benzene clusters, which were formed in a supersonic beam [255].

Joblin et al. [256] used imaging photoelectron-photoion coincidence spectrometry (iPEPICO) with VUV synchrotron radiation to study PAH clusters of pyrene and coronene produced in a molecular jet. An in-vacuum steel oven is used to reach high temperatures up to 500 °C. The PAH vapor was mixed and driven by an argon flow, which was expanded through a 50-micrometer nozzle. The backing pressure was adjusted to maximize the production of PAH clusters, such as the dimer of pyrene. The free jet was skimmed through a 2 mm ID orifice and passed through the ionization zone while crossing the VUV synchrotron beam at a right angle at the center of the iPEPICO spectrometer [256]. In addition, PAHs such as pyrene clusters were studied by using the threshold collision-induced dissociation (TCID). The ions were produced in a gas aggregation source and then thermalized at 25 K through thousands of collisions with helium. The temperature of the oven was set to 40 °C, and the flow of helium gas was entered into the source through the oven. The source pressure was about 1 mbar, and ionization occurs by electron impact. A tungsten filament heated by a current of about 2.4 A is used to emit electrons [257,258].

4.2 General source conditions inside the ion source

In the Nanogan I ECR ion source, the conditions can be changed mainly by adjusting two parameters: the HF power and the pressure of the injected gas (es). The relevant HF power range to produce intact monomer cations of PAHs was 0.5–2 W. Since it is not possible to directly measure the pressure in the source, the pressures given in the following have been measured in the chamber next to the ion source. The relevant range for the measured pressure was 2×10^{-7} to 1×10^{-5} mbar.

4.2.1 Roles of HF power and pressure

Both HF power and the pressure inside the source play a vital role in the production of PAHs and their dimers. On the one hand, when HF power is increased, the electrons are accelerated in the plasma to higher kinetic energies. Therefore, electron impacts on PAHs deposit higher amounts of energy while ionizing. This may lead to unwanted dissociation of the ionized species. Consequently, HF power should be reduced nearly to the minimum possible value that still maintains the plasma. On the other hand, an increase of pressure results in a reduction of the electron mean free path, leading to a shortening of the time for electron acceleration between two collisions. As a consequence, on average, electron kinetic energies are reduced when pressure is increased, leading to less energy deposition on molecules during electron impact ionization processes. Moreover, when the pressure is increased and neutral gas at room temperature is added, the plasma globally is cooled down.

For heavier PAHs such as pyrene, even though they are heated in an oven, the attainable vapor pressure is not sufficient to reduce sufficiently the plasma temperature. In this case, naphthalene is used as a support gas to reach the necessary pressure to cool the plasma sufficiently.

In summary, the low HF power and the high pressure in ranges that still maintain plasma are needed to operate the ion source for producing beams of small PAHs cations under stable conditions. This becomes very critical for the preparation of ion beams of PAH dimer cations since the required conditions are often at the limit of extinction of the plasma. Moreover, the internal energy distributions of the PAH cations or PAH dimer cations can be intentionally modified by varying the plasma conditions.

4.2.2 Estimation of the pressure inside the ion source

As mentioned above, the precise pressure inside the ion source could not be directly measured. Yet, it could be determined from the pressure measured using the vacuum gauge in the pipe located in the next vacuum chamber of the beamline. The measured pressure was in the range of 0.2 to 30×10^{-6} mbar depending on the source conditions. It can be expected to be proportional to the ion source pressure. In this section, we tentatively derive a calculation that was used to estimate that the ion source pressure that is expected to be in the range of 10^{-2} to 10^{-1} mbar. The estimated pressure has been calculated by using two quantities: one is the pumping speed and the other is the conductance determined by the tube sizes and holes between the ion source and the next chamber.

The dynamics of gas at low pressure can be described by the Knudsen number (Eq. (4-1):

$$K_n = \frac{\lambda}{L} \quad \text{Eq. (4-1)}$$

where L is the characteristic linear dimension of the vacuum chamber and λ is the mean free path of neutral gas molecules that can be estimated by using Eq. (4-2).

$$\lambda = \frac{k_B T}{\sqrt{2} d^2 p} \quad \text{Eq. (4-2)}$$

where d is the diameter of the molecule, T is the gas temperature, k_B is the Boltzmann constant and p is the pressure.

Different regimes are possible depending on the Knudsen number, including continuum flow (turbulent and laminar flow) and molecular flow. There are also different ways to calculate the pressure. We assumed that the regime is either laminar or molecular flow:

- Free molecular flow: in this regime, molecular collisions with the walls of the vacuum chamber control the gas dynamics and the molecular flow Q is proportional to the pressure difference $\Delta P = P_1 - P_2$:

$$Q = C(P_1 - P_2) \quad \text{Eq. 4-3)}$$

where C , the conductance between the two chambers, depends on the molecular speed and geometry, i.e., the tube diameter, D , and the length, L :

$$C = \frac{Q}{\Delta P} = \frac{1}{6} \frac{D^3}{L} \sqrt{\frac{2\pi k_B T}{m}} \quad \text{Eq. (4-4)}$$

- laminar flow: intermolecular collisions control the gas dynamics, and the gas conductance is given by:

$$C = \frac{Q}{\Delta P} = \frac{\pi}{128} \frac{D^4}{L\eta} P_m \quad \text{Eq. (4-5)}$$

PRODUCTION OF ION BEAM OF PAHs

where $P_m = \frac{P_1+P_2}{2}$ is the average pressure and η is the dynamical viscosity.

The pump speed is given by:

$$S = \frac{Q}{P} \quad \text{Eq. (4-6)}$$

By using the equations above and numerical values shown in Table 4-1, the average pressure inside the ion source is estimated to be in the order of $10^{-1} - 10$ mbar using the free molecular flow and in the range $10 - 100$ mbar using the laminar flow. Knowing that the vapor pressure of naphthalene is 0.11 mbar, the above ranges overestimate the actual source pressure, most probably because the above equations are not accurate enough to estimate the gas flow through the small hole between the plasma chamber and the next tube. In practice, we may consider that the valve between the naphthalene reservoir and the plasma chamber is almost fully open to reach the measured value of 1×10^{-5} mbar, therefore this situation should correspond to a pressure of about 10^{-1} mbar in the plasma chamber.

Table 4-1 : numerical values used for estimating the pressure in the ion source.

D (m)	L (m)	T (k)	m (kg)	η^1 (SI)	C (m ³ /s)	S (l/s)	P (mbar)	Q (mbar.l/s)
2×10^{-3}	5×10^{-4}	293	2.125×10^{-25}	2.45×10^{-3}	4.22×10^{-7}	345	1×10^{-6}	3.45×10^{-4}

4.3 Production of ion beams of phenanthrene monomer cations

In order to prepare ion beams of phenanthrene monomer cations, phenanthrene powder from SIGMA ALDRICH with a purity of 98% has been placed in the small reservoir at the end of the HF antenna of the ion source. This reservoir can be heated from the outside, thanks to the high thermal conductivity of the copper rod used to hold the HF antenna and the reservoir. Plasma conditions were optimized by performing mass spectra: the intensity of the desired intact PAH cation was maximized while the intensities of the fragments were minimized.

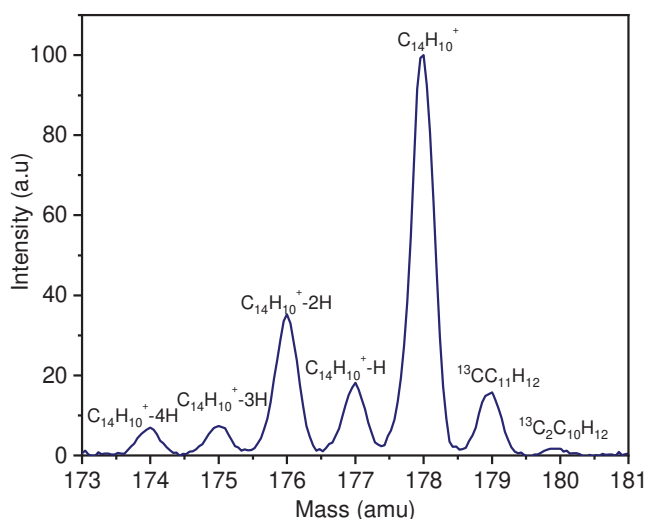


Figure 4-1: A typical mass spectrum recorded during the preparation of phenanthrene cation beams (plasma conditions optimized for maximizing the phenanthrene ion current intensity).

¹ A measure of this value for naphthalene was found at the following web address:
http://www.ddbst.com/en/EED/PCP/VIS_C123.php.

PRODUCTION OF ION BEAM OF PAHs

A typical mass spectrum recorded for phenanthrene cations was obtained with 0.2 W of HF power and a measured pressure of 2.2×10^{-7} mbar. Several peaks are presented in Figure 4-1. The highest peak at mass 178 a.m.u. is attributed to the monomer cation of phenanthrene. The next two peaks at masses 179 and 180 a.m.u. are due to the ^{13}C isotope. Peaks at smaller masses in the range of 173-177 a.m.u. are attributed to fragments with one and more missing hydrogen atoms. The highest intensity of phenanthrene cations was obtained in these conditions. Their presence indicates that the plasma temperature was high enough to induce the dissociation of some of the produced phenanthrene cations. In other words, the internal energy conferred to the phenanthrene cations was rather high, at least in the same order of magnitude of the dissociation energy of phenanthrene. The plasma could not be sufficiently cooled by the addition of naphthalene as support gas to prevent dissociation. However, the high internal energy turns out to be an advantage to study the cooling processes as will be discussed in chapter 5.

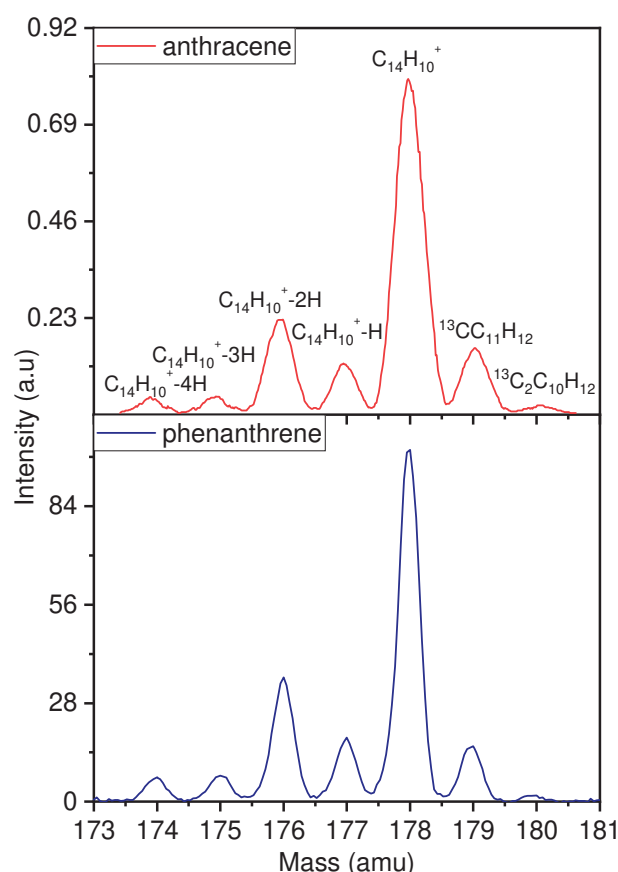


Figure 4-2: Comparison of the main spectra obtained for the anthracene and phenanthrene cations in similar operating conditions.

It is worth mentioning that phenanthrene and anthracene cation have the same atomic mass. They are isomeric forms of $\text{C}_{14}\text{H}_{10}^+$. A very pure phenanthrene powder for plasma was used and the ion source had been cleaned before use. Therefore, we exclude possible direct contamination by anthracene even though experiments have been performed with this molecule in the past. By comparing the mass spectra of the monomer of phenanthrene and monomer of anthracene, as in Figure 4-2, it can be noted that they are very similar. They show the same set of fragments from 1 H to 5 H losses. The presence of these fragments is the indication of a broad internal energy distribution that extends above the dissociation limit of the intact PAHs and the fragments.

As seen for previously studied naphthalene and anthracene cations, the relative intensities of the phenanthrene cations and their fragments are highly dependent on the source conditions. Former Ph.D. students working with the Mini-Ring have produced monomer cations of naphthalene and anthracene cations. The monomers of naphthalene were produced at three

PRODUCTION OF ION BEAM OF PAHs

different source conditions, with HF powers of 1, 2.2, 0.7 W and measured pressures of 1.2×10^{-6} , 4.7×10^{-7} , 4.6×10^{-7} mbar, respectively [136,225]. The typical mass spectra of naphthalene cations are illustrated in Figure 4-3, showing parent naphthalene peaks and the fragments (-H, -2H, -2H, and $-C_2H_2$). It was observed that for the highest value of microwave power (2.2 W, Figure 4-3(b)), the high intensities on the fragment peaks indicate that the produced naphthalene cations had high internal energy and could be fragmented in the ion source. It is also noteworthy that doubly charged naphthalene is observed in this case. The optimal source conditions were achieved to study naphthalene cations in the case of Figure 4-3(c), where the intensities on the fragment peaks are very small.

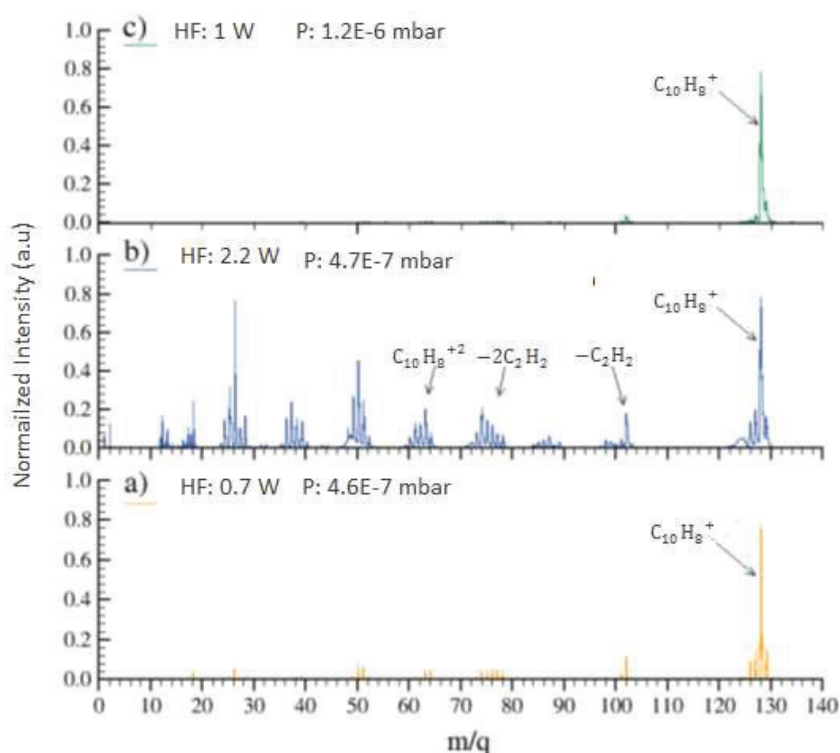


Figure 4-3: Mass spectra recorded for naphthalene cations for three different power and pressure conditions.

As for phenanthrene, the anthracene cations were produced with the help of naphthalene support gas in order to cool down the plasma as much as possible [76,134,212]. The pressure in the ion source was 3×10^{-7} mbar and the microwave power varied from 2 and 0.91 W. The obtained mass spectrum contains the main peak of singly charged anthracene and two sets of peaks attributed to fragments resulting from H and C_2H_2 losses. These are the two main dissociation pathways of anthracene. Once the microwave power changed from 2 to 0.91 W, the intensity of fragmented anthracene decreased. Therefore, anthracene cations can have different internal distributions.

4.4 Production of ion beams of dimer cations

In the present work about dimer cations, it was necessary to achieve the production of ion beams of the following dimer cations: naphthalene $(C_{10}H_8)_2^+$, pyrene $(C_{16}H_{10})_2^+$, and benzene $(C_6H_6)_2^+$. At ambient temperature, liquid benzene and naphthalene powder have sufficiently high vapor pressures to reach the necessary pressure conditions (i.e., the highest values of the aforementioned pressure ranges) for dimer production. For bigger PAHs, the oven situated at the very end of the HF antenna of the ion source was used to increase the vapor pressure, which, however, was insufficient for the production of dimers. By cooling the plasma with high pressure of naphthalene as support gas, it became possible to produce ion beams of dimer cations with sufficient intensities to perform the photodissociation experiments presented in chapter 6. Indeed, especially in the case of the dimers, it is important to be able to ionize the

monomer molecules while minimizing the chances of dissociation, the plasma should be kept as cold as possible. As shown in the previous section about monomers and the next sections about dimers, mass spectra can change drastically by changing the support gas pressure. The HF power is also maintained as low as possible but slightly above the plasma extinction critical value. It is also noteworthy that when source conditions are optimized to maximize the dimer cation intensities, the monomer cation intensities are not maximum, and secondly, the ratio of intact over fragmented dimers is close to its maximum.

4.4.1 Dimers of naphthalene

Figure 4-4 displays examples of mass spectra recorded with Faraday F₃ in the case of naphthalene dimer cations at two different naphthalene gas pressures in the ion source. The naphthalene powder has been purchased from Fluka chemicals with a purity of 99%. At high-pressure 1×10^{-5} mbar, as shown in Figure 4-4(a), intact dimer naphthalene cations only are observed in the 250-258 a.m.u. mass range together with peaks attributed to isotopic dimers. Oppositely, at a lower pressure of 5×10^{-6} mbar, the mass spectrum is dominated by fragmented dimers corresponding to the loss of one or several hydrogen atoms (Figure 4-4(b)).

Figure 4-4 shows that fragmented monomer cations can easily form a bond with a neutral monomer (or possibly with fragmented neutral) to form a fragmented dimer. In contrast, a lower pressure results in a higher electronic temperature of plasma, leading to fragmentation of the dimers with one or more missing hydrogen atoms. These two observations are in line with the expectations since, as explained in section 4.2.1, at the higher pressure, the kinetic energy of electrons in the plasma is not high enough to deposit sufficient internal energy during an ionizing collision to dissociate the resulting naphthalene cations.

During experiments described in chapter 6, it has been decided to work in the “cold” plasma conditions, i.e., in the conditions of Figure 4-4(a), because it was corresponding to the highest beam intensities. The typical beam intensities obtained on the beamline faraday cup (F_L) were in the range of 70 to 100 nA for naphthalene dimer cations.

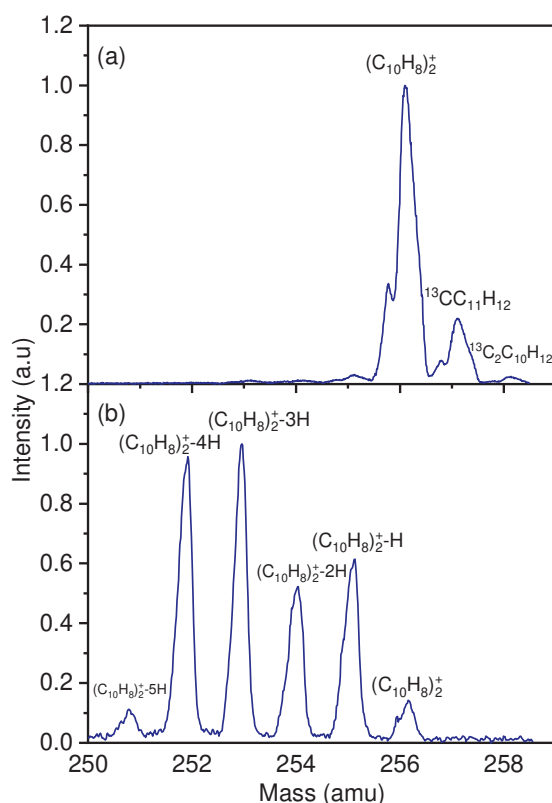


Figure 4-4: Mass spectra recorded for naphthalene dimer cations at two different ion source pressures. (a) $P_s = 2 \times 10^{-5}$ mbar and (b) $P_s = 5 \times 10^{-6}$ mbar.

4.4.2 Dimers of pyrene

Figure 4-5 shows a typical mass spectrum recorded for the production of pyrene dimers $(C_{16}H_{10})_2^+$. Dominating peaks are from monomers of naphthalene $(C_{10}H_8^+)$, pyrene $(C_{16}H_{10}^+)$, and anthracene $(C_{14}H_{10}^+)$. The existence of anthracene was caused by contamination of the source from a previous experiment performed with this molecule. However, the presence of $C_{14}H_{10}^+$ was helpful for mass calibration. The dimers of naphthalene, pyrene, and anthracene were observed in the high mass range above 250 a.m.u. The trimer of naphthalene $(C_{10}H_8)_3^+$ was also observed in the mass spectrum at 384 a.m.u.

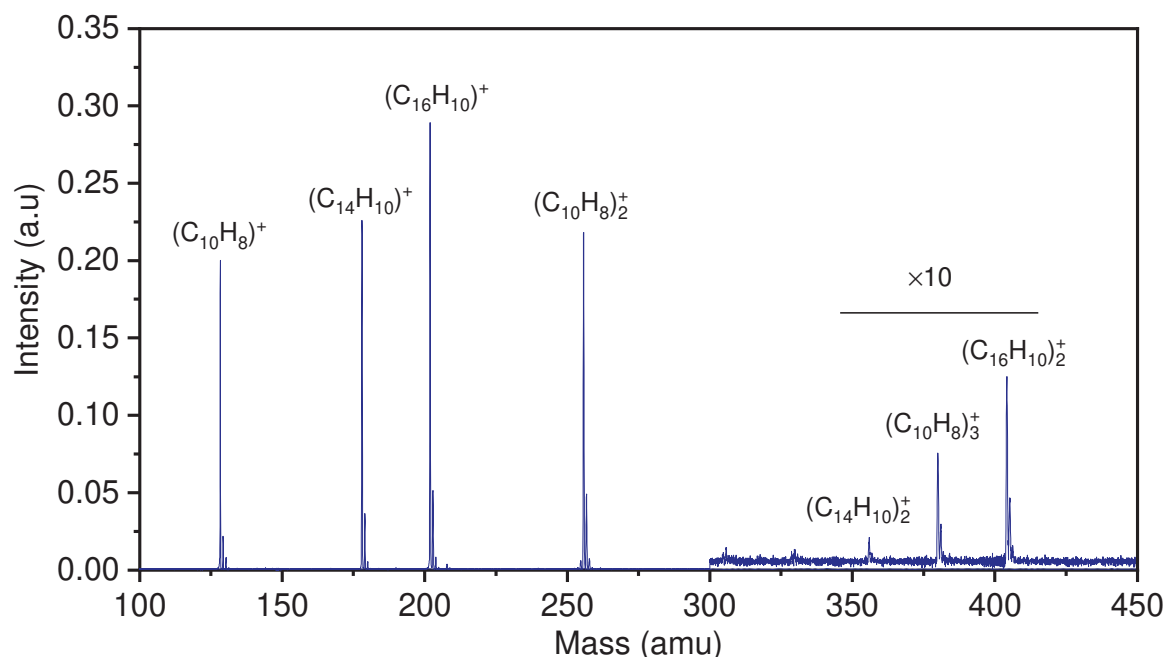


Figure 4-5: Typical mass spectra recorded for dimer cations of pyrene.

The mass spectrum of dimer pyrene is also obtained by optimizing source conditions, as shown in Figure 4-6. This spectrum is obtained at HF power of 0.9 W and the pressure of 6×10^{-6} mbar. To evaporate the pyrene powder, the oven was heated in voltage and current conditions of 11.5 V and 2.8 A, respectively, which correspond to a power of about 35 W. Unfortunately, this setup does not provide any possibility for direct measurement of the temperature inside the oven. Three peaks at masses in the range of 400-480 a.m.u. corresponding to $(^{12}C_{16}H_{10})_2^+$, $[(^{13}CC_{15}H_{10})(C_{16}H_{10})]^+$, $[(^{13}C_2C_{14}H_{10})(C_{16}H_{10})]^+$ or $[(^{13}C_2C_{15}H_{10})(^{13}CC_{15}H_{10})]^+$ were observed. The high-intensity peak at 404 a.m.u. in the displayed mass spectrum represents intact dimer pyrene, and the two next peaks at 405 and 406 a.m.u. are attributed to the ^{13}C isotopic pyrene dimers. It has been checked that the intensity ratios between these three peaks correspond to the natural abundance of ^{13}C . Therefore, we exclude the possibility of interpreting these three peaks due to fragmented dimers that could have lost one or two H atoms. It is noticeable that fragmentation of monomers and dimers is not observed in the mass spectrum of Figure 4-5. It reveals that the plasma is much colder than in the case of the monomers.

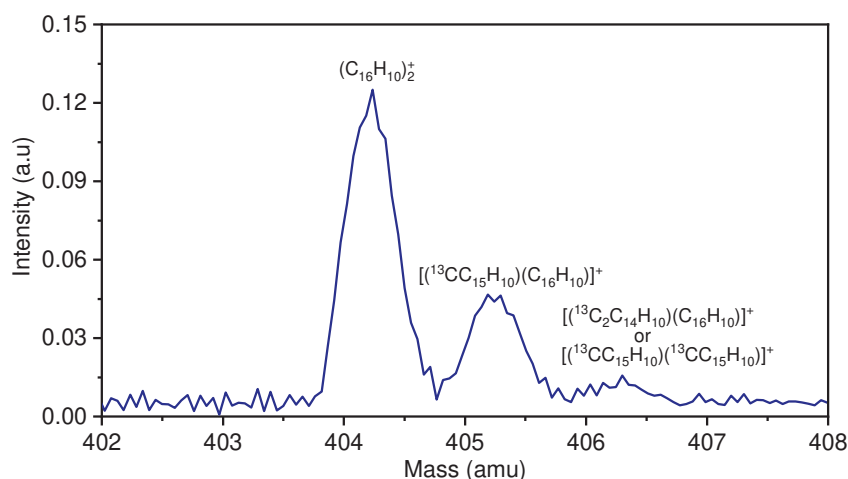


Figure 4-6: Mass spectra recorded for pyrene dimer cations.

4.4.3 Dimers of benzene

A typical mass spectra, shown in Figure 4-7, were recorded for benzene dimers. This spectrum was obtained at an HF power of 2.8 W and a pressure of 2.1×10^{-6} mbar (Figure 4-7(a)) of benzene gas only (no addition of naphthalene in this case) and 4×10^{-7} mbar (Figure 4-7(b)). The peak at mass 156 a.m.u. is attributed to the benzene dimer cation and the other peaks are fragments corresponding to the loss of hydrogen atoms from dimers of benzene-H to dimers of benzene-5H. It is noteworthy that despite our efforts to cool down the plasma, it was not possible to get rid of the fragment peaks as in the cases of naphthalene and pyrene while keeping a sufficiently high intensity of intact benzene dimer cations to perform experiments with the Mini-Ring. As shown in Figure 4-7(a), the intact dimer cation corresponds to the peak of highest intensity, whereas in Figure 4-7(b), the spectrum is dominated by fragment peaks.

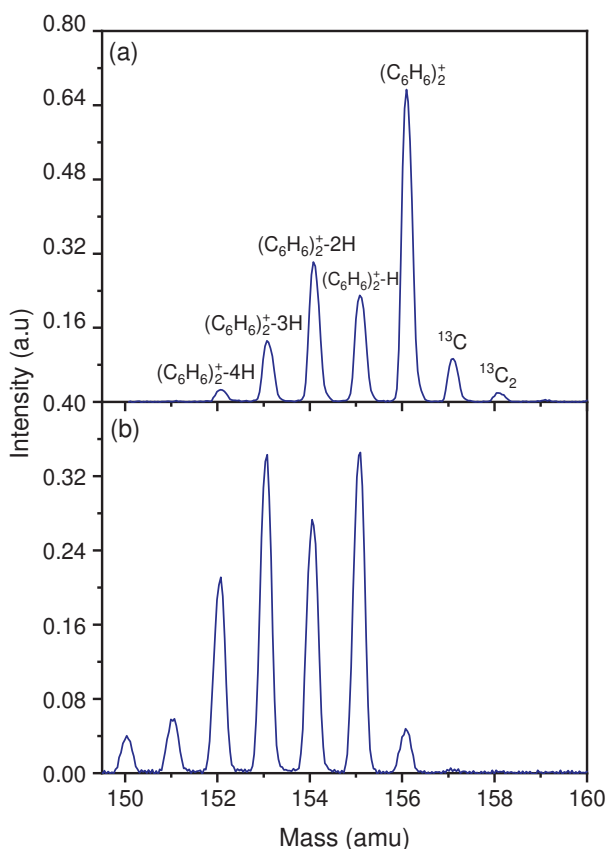


Figure 4-7: Mass spectra recorded for benzene dimer cations.

In order to study the effect of the pressure of the production on dimer cation beams and their fragments, a systematic study was performed to study the variation of the intensity as a function of the benzene pressure in the ion source, as presented in Figure 4-8. The intensities of the fragments, as expected, were found to decrease at high pressure, but the remaining intensity of benzene was not sufficient for performing photo-dissociation experiments in the coldest situation for which the dimers of benzene are obtained.

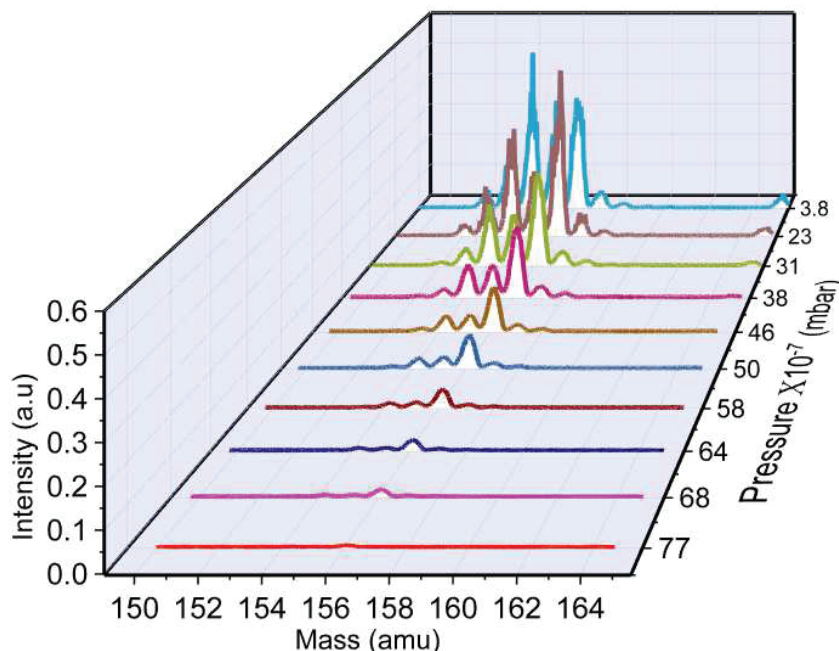


Figure 4-8: The effect of increasing pressure on the dimer cations of benzene.

4.5 Possible mechanism of formation of dimer cations of PAHs

Different formation mechanisms of PAH dimer cations inside the ion source can be envisaged. A possible mechanism would be that neutral monomers are ionized by electron impact, which also implies energy deposition. If the deposited energy is small enough, the PAH cation remains intact and has a chance to collide at low relative kinetic energy with a neutral PAH. In the approach phase, the polarization creates an attractive potential. If some of the relative kinetic energy is lost possibly by photon emission (the inverse process of photo-dissociation) or by the transfer to the vibrational motions of the monomers (a kind of IVR process leading to the energy transfer from intermolecular to intramolecular vibration modes), then the two monomers would remain 'trapped' in the potential well of the dimer cation. Another option is probably to be excluded: formation of the neutral dimer first followed by electron impact ionization. In this case, the deposited energy would most probably result in the dissociation of the dimer into two monomers.

Since the splitting into two monomers is by far the most favorable dissociation pathway, as it will be demonstrated experimentally in Chapter 6, the observation of fragmented dimers supports the mechanism proposed at first. Indeed, in this case, the H loss of the monomer has to occur before the formation of the dimer. The proposed formation mechanism is illustrated in Figure 4-9. In the case of the -H, it should be considered that the story is probably not finished, as shown in Figure 4-9. A molecular rearrangement should occur to form a stronger bond between the two monomers. Experimental evidence of this stronger bond will be discussed in Chapter 6.

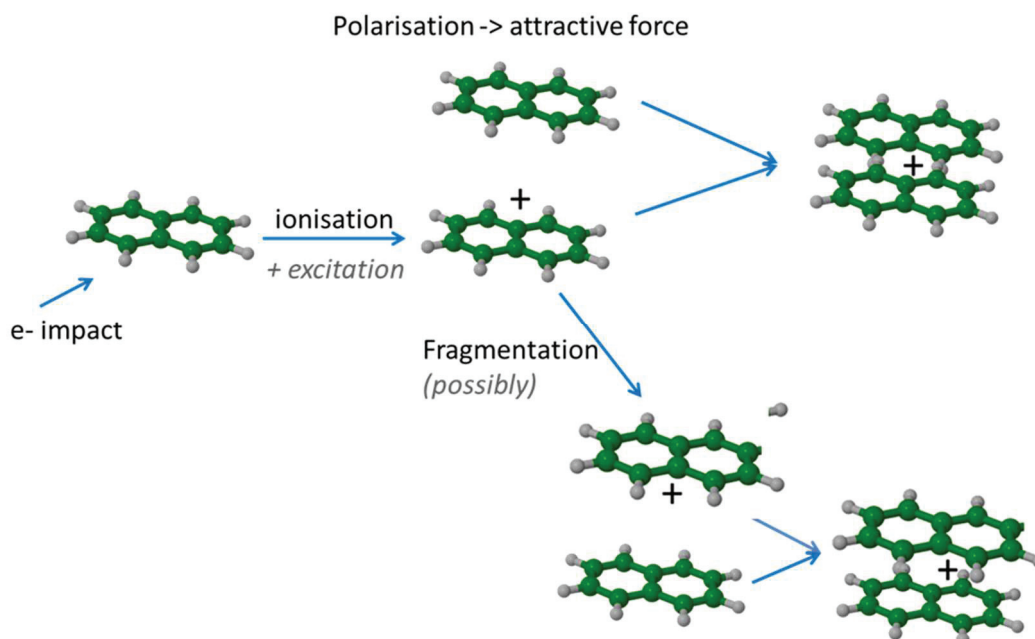


Figure 4-9: Schematic illustration of the mechanism of production of dimer cation.

4.6 Conclusion

In this chapter, the special source conditions used to generate monomers, particularly phenanthrene, and dimer cations of PAHs have been discussed. Low HF power and high pressure are required to operate the ion source to produce stable ion beams of small PAHs and to keep the plasma as cold as possible. The plasma parameters, e.g., temperature, were found to be hard to determine; therefore, the production of ion beams of PAHs and their dimer has been controlled by such source conditions. The pressure inside the ion source has been estimated to be in the order of 10^{-1} - 10^{-2} mbar.

For monomer phenanthrene cations, the ion source conditions were obtained with 0.2 W of HF power and a measured pressure of 2.2×10^{-7} mbar. The situation becomes very critical for the preparation of ion beams of PAH dimer cations since the required conditions are often at the limit of extinction of the plasma. Moreover, the internal energy distributions of the PAH cations or PAH dimer cations can be intentionally modified by varying the plasma conditions. The benzene and naphthalene dimer cations have been produced without a support gas. Benzene dimers are found to be hard to be obtained in cold conditions that prevent dissociation. For heavier PAHs such as anthracene, phenanthrene, pyrene, etc., the attainable vapor pressure obtained by heating the species in the oven is not sufficient to prevent too high plasma temperatures. Naphthalene is then added as a support gas to get to the necessary pressure to cool sufficiently the plasma.

The cooling of plasma in the ion source with naphthalene as a support gas will be employed in future experiments to produce other PAHs and possibly other kinds of molecular ion beams. Future experiments are planned with the methyl-pyrene cation. This is an example of such kinds of molecular ion beams that will benefit from the presently accumulated knowledge on the operation conditions of ECR ion sources.

5 EXPERIMENTAL RESULTS OF PHENANTHRENE MONOMER CATIONS

5	EXPERIMENTAL RESULTS OF PHENANTHRENE MONOMER CATIONS	103
5.1	The natural decay of monomer phenanthrene cations	103
5.2	Laser-induced dissociation.....	105
5.3	Time evolution of the internal energy distribution	107
5.3.1	Energy Distribution of ions.....	107
5.3.2	Time and energy window.....	108
5.3.3	Modeling the neutral yield	112
5.3.4	Experimental Laser-induced decay curves	114
5.3.5	Determination of the energy shift rate using photon energies	116
5.3.6	Time evolution of HEE of the IED	118
5.3.7	The measured population decay rate.....	120
5.4	Conclusion	123

The relaxation dynamics of small cations of PAHs such as naphthalene, anthracene, and pyrene produced with a given internal energy distribution (IED) were performed in several previous studies in our lab [76,77,133,135,136,259]. The studies clearly demonstrated that these cations could cool down by a fast radiative process called recurrent fluorescence (RF) in the millisecond time range and later on by infrared vibrational transitions (IR) in the second time range. Such processes have been explained in detail in chapter 2.

This chapter presents a quantitative experimental study of the cooling process of phenanthrene cations. The present results will be compared with the aforementioned study about anthracene cations, an isomer of phenanthrene. Spontaneous dissociation, also referred to as natural decay in the following, has been investigated as well as laser-induced dissociation that is used to probe the time evolution of the internal energy distribution (IED) at different storage times. Cooling rates are estimated from the time evolution of the IED, which is calculated by two methods: the decay factor obtained from power-law fits of the decay and simulated decays using Gaussian IEDs.

During each storage cycle, some of the stored phenanthrene cations dissociate spontaneously due to unimolecular dissociation and neutral fragments yields can be detected as a function of the storage time. In the first section, this natural decay is analyzed to discuss the competition between unimolecular dissociation and radiative cooling processes.

5.1 The natural decay of monomer phenanthrene cations

In order to investigate the natural decay of monomer phenanthrene cations, i.e., spontaneous dissociation without laser irradiation, phenanthrene cations have been stored for a storage time up to 10 ms, which is relevant for the RF cooling process. The ions are introduced into the Mini-Ring after a flying time t_0 of about 28 μs through the transport beamline. The

EXPERIMENTAL RESULTS OF PHENANTHRENE MONOMER CATIONS

production time of the ion bunches, i.e., $t = 0$ is considered the start time of each storage cycle. The revolution period of the stored phenanthrene cations is $6.57 \mu\text{s}$. The number of neutral fragments integrated over each turn is plotted as a function of the storage time. Figure 5-1 shows the natural decay curve for phenanthrene cations recorded up to 10 ms. The neutral fragment yield results from two contributions, namely, spontaneous unimolecular dissociation of hot phenanthrene cations and collisions of phenanthrene cations with the residual gas. As already mentioned in chapter 2, the neutral fragment yield resulting from spontaneous unimolecular dissociation obtained can be modeled by Eq. (5-1) [105]:

$$I(t) = \int g(E) k_d(E) e^{-k_d(E)t} \quad \text{Eq. (5-1)}$$

The neutral fragment yield presents three regimes, as displayed in Figure 5-1. In regime I, the decay follows a power-law attributed to the delayed dissociation of hot phenanthrene cations in the ECR ion source. As mentioned in chapter 2, an ensemble of ions with a broad IED is expected to follow such a power-law decay. In regime II, the neutral yield deviates clearly from the power-law decay, indicating the existence of a non-dissociative cooling process that quenches the dissociation process. In the present case, it is attributed to fast radiative cooling by recurrent fluorescence. In regime III, spontaneous unimolecular dissociation is completely quenched, i.e., the internal energy of the stored phenanthrene cations is insufficient for inducing dissociation processes. Therefore, the remaining neutral yield results from collisions with the residual gas. Indeed, such collisions can increase sufficiently the internal energy to induce dissociation processes.

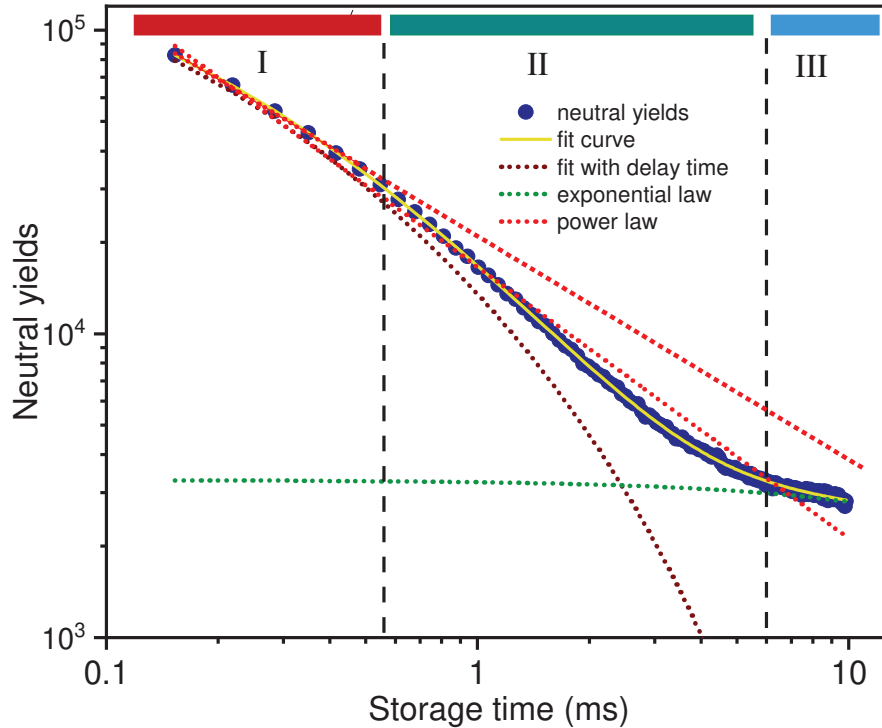


Figure 5-1: Natural decay curve of phenanthrene cations, the blue curve is the integrated neutral fragment yields, the red dashed lines are attributed to the power-law decay distribution with decay factor 1.04 and 0.85, the orange curve is the contribution of power-law and exponential law, the green dashed line shows the contribution of collisions with residual gas.

Consequently, the total neutral yield, I_T , is given by the sum of the natural decay, I_d , and the collision-induced dissociation, I_c :

$$I_T(t) = I_d(t) + I_c(t) \quad \text{Eq. (5-2)}$$

For $I_d(t)$, we use Eq. (2-77) (see section 2.3.6) to account for the quenched natural decay. In addition, at longer storage times, in regime III, the neutral fragment yield follows the exponential decay given by Eq. (2-85) (see section 2.4). Therefore, the neutral fragment yield of Figure 5-1 has been fitted using the following function:

$$I_t(t) = I_0 \left(\frac{t}{\tau_d} \right)^\delta \frac{1}{\exp\left(\frac{t}{\tau_d}\right) - 1} + N_0 e^{-t/\tau_c} \quad \text{Eq. (5-3)}$$

where I_0 , τ_d , δ , N_0 , τ_c are adjustable parameters.

As a first try, we attempt to fit with power-law on the whole time range. The obtained value of the exponent is $\alpha = 1.04$. However, the fit is not satisfactory in region II of the natural decay. In a second attempt, the fit with power-law is restricted to few first turns. It gives $\alpha = 0.86$. The fit is good in the region I and represents the natural decay that would be expected in the absence of radiative cooling.

The third fitting attempt uses Eq. (5-3) that includes the radiative cooling effect and the collisions with the rest gas; the obtained fit is in very good agreement with the experimental data. The value of the exponent δ is found to be very close to zero, indicating that the initial decay at short times ($t \ll \tau_d$) is very close to t^{-1} . The quenching characteristic time is found to be $\tau_d = 1.2$ ms. The collision induced decay time is found to be $\tau_c = 100$ ms. Previous studies with the Mini-Ring on anthracene cations have shown a similar behavior with a quenching time by radiative cooling τ_d of about 1 ms and τ_c of about 300 ms, which corresponds to a slightly longer storage lifetime of anthracene cations due to probably smaller background gas pressure [76]. The analysis of the natural decay shows that the quenching times are approximately the same for phenanthrene and anthracene cations.

To summarize, the analysis of the evolution of phenanthrene cations shows three different regimes: the hottest ions dissociate first at a very short time, then dissociation is quenched by radiative cooling, leading to a rapid drop of the neutral fragment yields, and, finally, at longer storage time, only collisions with residual gas can dissociate the stored ions. It means that in regime III, radiative cooling has become the dominant process and further time evolution of the IED is essentially controlled by this process. Therefore, a probe is needed to quantify the time evolution of the IED in regime III. Laser absorption is an ideal probe, especially in single-photon absorption conditions, since a known, fixed quantity of energy is added to the internal energy of the targeted molecules. The results of such experiments are discussed in the following sections.

5.2 Laser-induced dissociation

In order to probe the time evolution of the IED, third harmonic (355 nm) and OPO laser pulses were shot every millisecond, at precise times, so-called laser-firing time t_{laser} , between D₁ and D₂ in the merged beam configuration. Laser wavelength and power have been varied to change the probe photon energy and test the single or double photon absorption conditions, respectively. Figure 5-2 displays a typical time spectrum, i.e., the neutral fragment yield as a function of storage time recorded with the wavelength of 440 nm for singly charged phenanthrene. A photon absorption resulted in a substantial increase of the internal energy such that a huge enhancement of the neutral fragment yield was observed after the laser firing times. The intensity of the laser power was kept in the range of 50-90 mW to have a negligible contribution of multiple photon absorption. Figure 5-2 shows the raw data for 10 laser shots per

EXPERIMENTAL RESULTS OF PHENANTHRENE MONOMER CATIONS

storage sequence at a wavelength of 440 nm. As all the data acquired in the present series of experiments, this spectrum was obtained after integration over about 10^6 storage cycles to gain sufficient statistics for subsequent data analysis. The total neutral fragment count rate was kept between 800 and 1000 counts per second. This rate is a compromise to avoid double counts in the same turn while achieving good statistics with a reasonable number of ion injections.

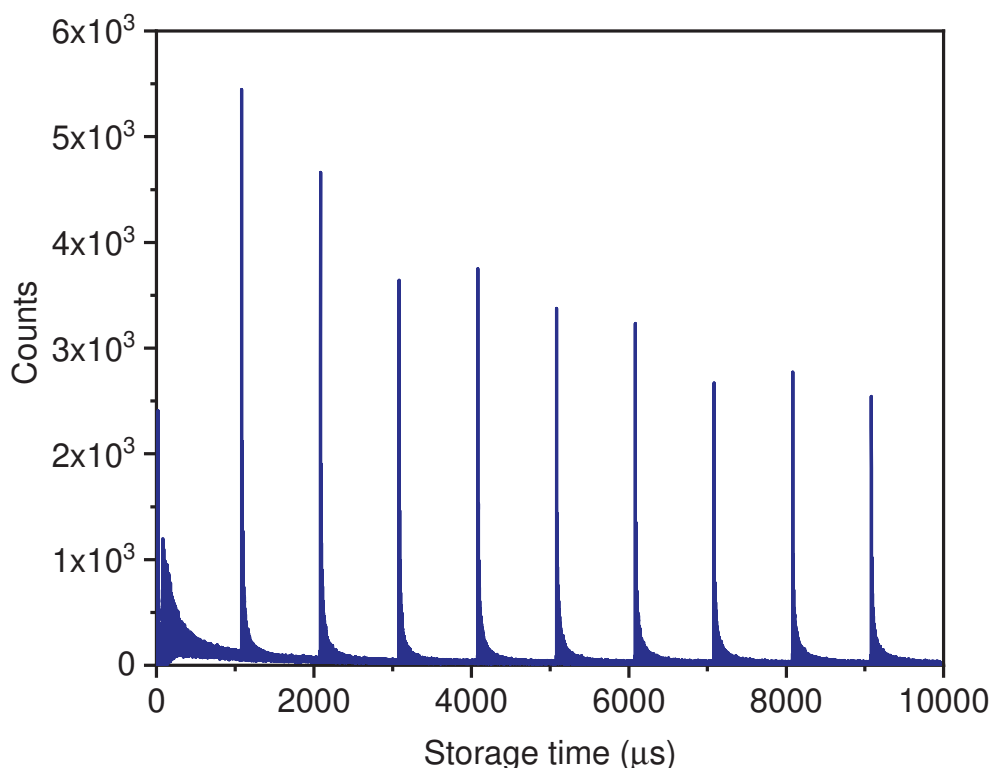


Figure 5-2: Laser-induced decays for cations of phenanthrene with laser power of 95 mW at wavelength 440 nm. The laser was shot every ms during the storage time of 10 ms

The natural decay that has been discussed in the previous section is also observed in Figure 5-2 in the first ms of storage time. Nonetheless, the laser-induced decay surpasses the natural decay intensity by a factor greater than 4. The decay of long-lived ions (those that have lower internal energy) spreads over a rather long timescale. For instance, the natural decay after 1 ms, at first laser shot time, is still present and corresponds to a background that has to be subtracted to account for the laser-induced decays only. The neutral counts due to collisions with the residual gas also contribute to the background and have to be subtracted too.

A zoom-in of the first laser-induced decay for the first-millisecond laser shot is shown in Figure 5-3. The time-space between two consecutive sharp peaks corresponds to the revolution time for ions in the Mini-Ring, and the width of each peak is about one microsecond. In this case, phenanthrene of 12 keV kinetic energy is found to be $6.57 \mu\text{s}$. Consequently, the first peak was detected at about $3.285 \mu\text{s}$ after the laser shot, which is about half of the revolution time from the excitation region and detection region. This time is the minimum time to detect the neutral fragment yields on the PSD after laser irradiation. An expanded view of the recorded neutral yield over each turn as a function of storage time for 1 ms is illustrated in the inset of Figure 5-3 as well.

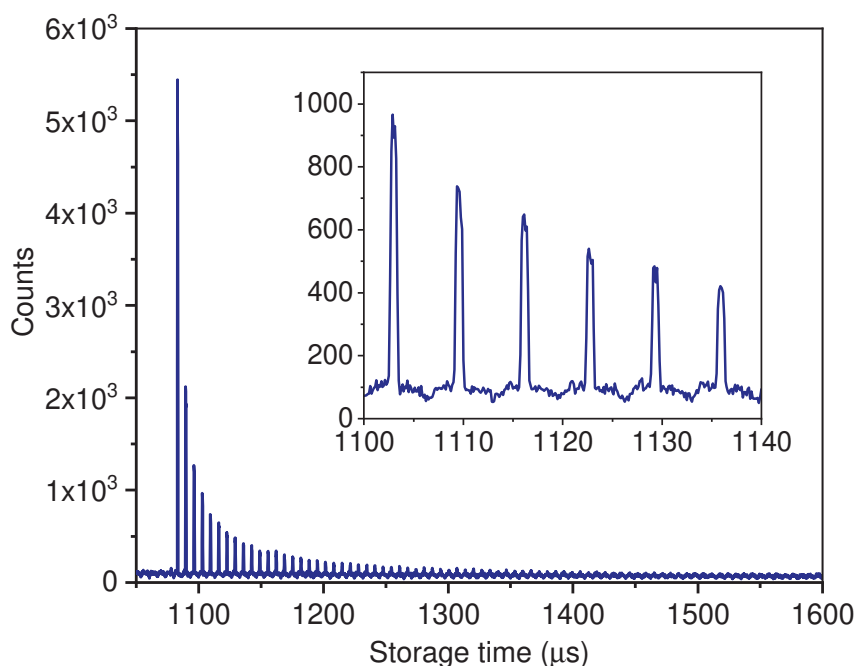


Figure 5-3: First laser-induced decay at about 1 ms. The inset is an expanded view of the 6 first turns after the laser shot.

5.3 Time evolution of the internal energy distribution

5.3.1 Energy Distribution of ions

The internal energy distribution $g(E, t)$ is defined as the number $N(E, t)$ of phenanthrene cations whose internal is E at time t , divided by the total number of $N(t)$ phenanthrene cations at time t :

$$g(E, t) = \frac{N(E, t)}{N(t)} \quad \text{Eq. (5-4)}$$

After the absorption of the photon, it is expected that dissociation dominates over all other relaxation processes, namely, recurrent fluorescence and vibrational IR emission cooling. Therefore, the decay law is given by:

$$\frac{\partial g(E + hv, t)}{\partial t} = -k_d(E + hv) g(E + hv, t) \quad \text{Eq. (5-5)}$$

where $k_d(E + hv)$ is the dissociation rate of the internal energy of $E + hv$ after photon absorption.

After integration, the energy distribution is given by:

$$g(E + hv, t) = g_0(E) e^{-k_d t} \quad \text{Eq. (5-6)}$$

where, $g_0(E)$ is the initial energy distribution at the laser firing time before photon absorption.

The initial shape of the IED is given in the ion source. During the ionization process by electron impact, the distribution of the deposited energy should present a bell-shaped curve. During ion transport and storage, dissociation and radiative cooling processes induce modifications of the IED shape. Dissociation of ions of the highest internal energy leads to a depletion of the IED on its high-energy side. The high-energy side of the IED of the stored

phenanthrene ions presents hence an edge, called hereafter the high-energy edge (HEE), whose shape is weakly dependent on the initial shape of the IED after few milliseconds of storage. Radiative cooling may also have some influence on the shape of the HEE. On the low-energy side, the shape of the IED is expected to be changed since RF repopulates the IED. Then, on this low energy side, dissociation and RF would have very low probabilities to occur, and the IR cooling lifetime would be much longer than the transport time from the source to the Mini-Ring and also much longer than the storage times used in this work. There may be an edge also, i.e., a low-energy edge (LEE) with an extension to 0 eV, but it is not expected to be as sharp as the HEE. In previous studies [76,77,133–136,259], the HEE only has been investigated using different shapes for the HEE, power function, or Gaussian function. These previous works were not sensitive to the LEE shape, i.e., flat or Gaussian shapes gave the same results. Accordingly, in this present work, the HEE only will be discussed.

5.3.2 Time and energy window

In order to be able to observe and quantify a process, such as dissociation, the corresponding lifetime should not be too short (at least 3 or 4 times the revolution period would be a limit $\rightarrow \tau_d^{min} \rightarrow E^{High}$) and not too long (it is more difficult to determine a precise limit there but let's say something like 100 revolution periods $\rightarrow \tau_d^{max} \rightarrow E^{Low}$). This is defining the 'time window' of the experiment.

The time window can be related to the internal energy window, via the dependence of the dissociation rate, $k_d(E)$ and therefore, of the lifetime $\tau_d(E) = \frac{1}{k_d(E)}$, on internal energy. As stated in paragraph 2.3.2, the dependence of the dissociation rate may be estimated by the Arrhenius law (Eq. (2-55)). Figure 5-4 gives the dissociation lifetime as a function of the internal energy for phenanthrene cations.

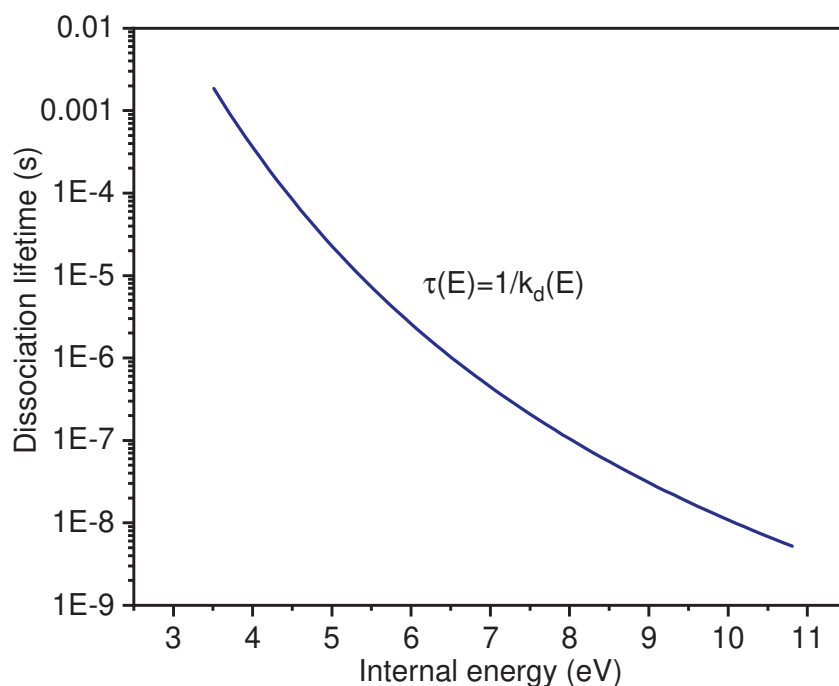


Figure 5-4: The lifetime of phenanthrene cations.

The contributions to the total neutral fragment yield from phenanthrene can be calculated as a function of internal energy and, conversely, as a function of storage time. Figure 5-5 shows the center energy of the main contribution as a function of the storage time. It illustrates the relation between the energy window and detection time (time window) in the Mini-Ring. The neutral fragments are collected after the half revolution in the ring, showing they are only sensitive to the ion population with internal energy less than 9.5 eV.

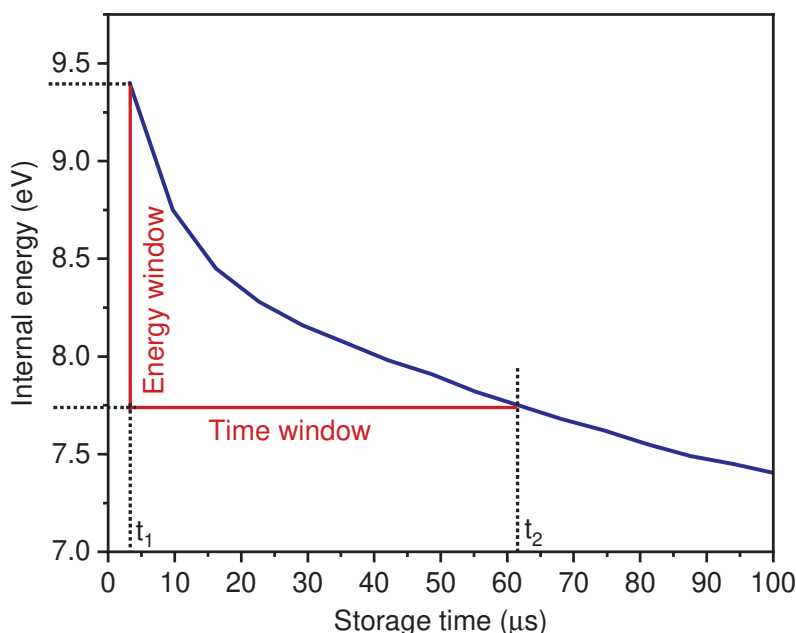


Figure 5-5: Center value of the main contribution energy region as a function of storage time and the time window and corresponding energy window for phenanthrene cations.

The time window has an important influence on the collection of neutral counts after laser excitation, in particular, at the short time limit. The shorter the characteristic time window, the higher the collected neutral counts. For a given ion velocity, each electrostatic ion storage ring has its own characteristic time window and hence energy window. The Mini-Ring time window is shorter than that of ELISA [79], DESIREE [139], and $\mu\text{E} - \text{ring}$ [158], which have a much longer orbit length than the Mini-Ring. For the Mini-Ring, the time window is in the order of tens of microseconds, whereas for the other mentioned rings, it is in the hundreds of microseconds. Consequently, the Mini-Ring allows for investigations on higher internal energies compared to the other larger rings. This feature makes it very sensitive to the recurrent fluorescence process.

In order to probe the IED of the stored ions, the internal energy of the probed ions that have absorbed a photon should have a lifetime compatible with the time window. The IED edges, i.e., the LEE of the HEE, or both of them if the distribution is sharp enough after laser excitation, should be inside the energy window. In the present case, single-photon absorption is used to bring the HEE of the IED in the correct energy range, i.e., inside the energy window, such that the lifetimes are inside the time window. Hence, different positions of the HEE inside the energy window lead to different decays.

Due to the laser absorption that shifts the internal energy of the excited ions by $h\nu$, the IED is modified according to the following equation:

$$g'(E, t) = g(E, t) \times (1 - P_1) + g(E - h\nu) \times P_1 \quad \text{Eq. (5-7)}$$

where $g'(E, t)$ is the IED after photon absorption, P_1 is the probability of single-photon absorption. The first term of Eq. (5-7) is the unchanged IED of ions that have not been absorbed, and the second term corresponds to the shifted IED. Therefore, the IED of the excited ion population is given by:

$$g'_{ex}(E, t) = g(E - h\nu) \times P_1 \quad \text{Eq. (5-8)}$$

EXPERIMENTAL RESULTS OF PHENANTHRENE MONOMER CATIONS

$g'_{ex}(E, t)$ is expected to have the same shape as $g'(E, t)$ since P_1 is supposed to be constant in Eq. (5-7) and Eq. (5-8). It may be a crude approximation since it can be expected that the Franck-Condon factor of the corresponding electronic transition and, therefore, the absorption cross-section may depend on the internal energy.

Figure 5-6 illustrates the expectations on the decay schematically depending on the position of the HEE of g'_{ex} with respect to the energy window. In Figure 5-6, a rectangle shape has been given to g'_{ex} to simplify the discussion. In case the HEE is above E_{high} in the energy window, the IED can be considered as infinitely broad; therefore, the induced decay is expected to follow a t^{-1} decay law. Oppositely, in case the HEE is lower than E_{low} , ions can barely dissociate in the time window, giving very low-intensity flat decay that is generally not exploitable.

On the other hand, when the HEE of g'_{ex} is inside the energy window between E_{low} and E_{high} at different positions, the decay deviates from the t^{-1} decay law, especially for the first turns after photon absorption. Although the decay does not follow exactly a power-law (detailed explanation in section 5.3.3), a fit with a $t^{-\alpha}$ law allows for getting information of the position of the HEE inside the energy window: the higher the HEE position, the greater the value of the decay factor α . This case is suitable to collect exploitable neutral counts that are sensitive to any changes of the IED.

Figure 5-7 illustrates that when probing the IED using two different photon energies at different storage times, it may happen that the HEE of both g'_{ex} arrive at the same position inside the energy window and therefore lead to the same decay factor. This trick is used in the following to determine the internal energy shift rate of the HEE, $\Delta E/\Delta t$, where ΔE and Δt correspond to the photon energy and shooting time differences, respectively.

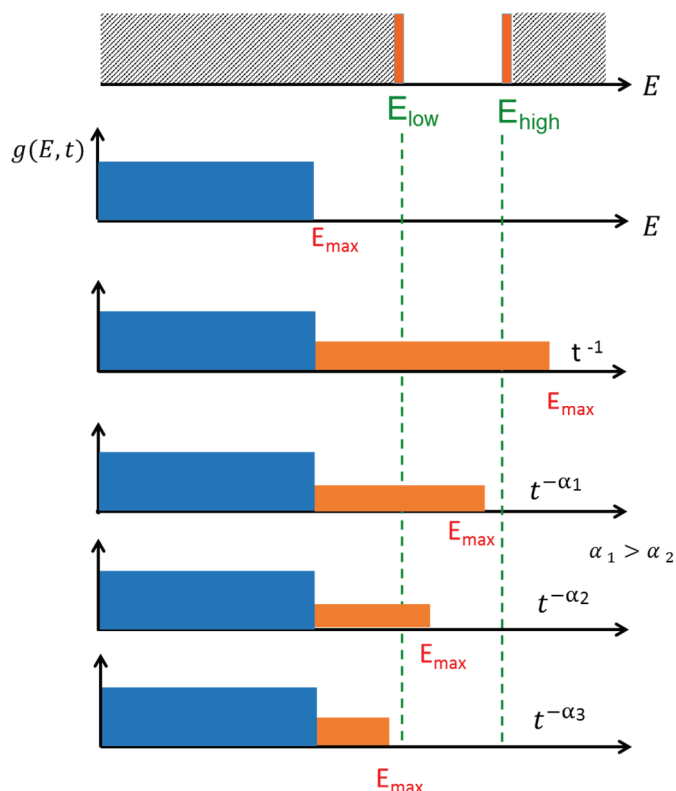


Figure 5-6: Illustration of high-energy edges of stored ions before (blue rectangle) and after absorption of the photon energy (orange rectangle).

Figure 5-8 shows the time evolution of the population of phenanthrene cations during the cooling process, where E_0 represent the the energy window and $E_0 - h\nu$ is the energy before absorption of the photon energy of the laser. Two-photon absorption $E_0 - 2h\nu$ may be observed depending on the photon energy and storage time. This provides information on the time

EXPERIMENTAL RESULTS OF PHENANTHRENE MONOMER CATIONS

evolution of the IED from t_{laser} dependence. The laser-induced neutrals detected in a specific delay after the laser excitation will come from cations with a specific internal energy E_0 . The observed neutral fragment yields are proportional to the population of ions at E_0 and hence the population of ions at $E_0 - hv$ and $E_0 - 2hv$ just before to photon absorption. For the observation of the decay yield of phenanthrene at a specific time after laser irradiation, the internal energy of the decaying ions is fixed. As the photon energy is constant, if the cross-section of the absorbing ions is constant as well and is independent of the storage time before the laser pulse, the neutral fragment yields are proportional to the population of ions before laser excitation at the specific probed excitation energy. This leads to the sampling of the population at $E_0 - 2hv$ as a function of time.

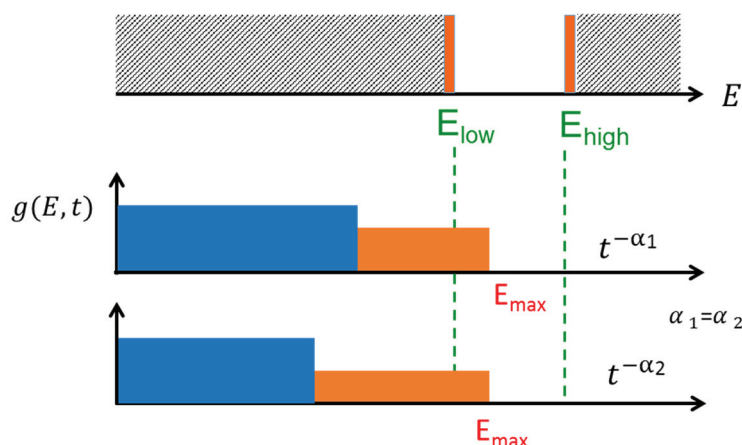


Figure 5-7: High-energy edge inside the energy window after absorption of different photon energies.

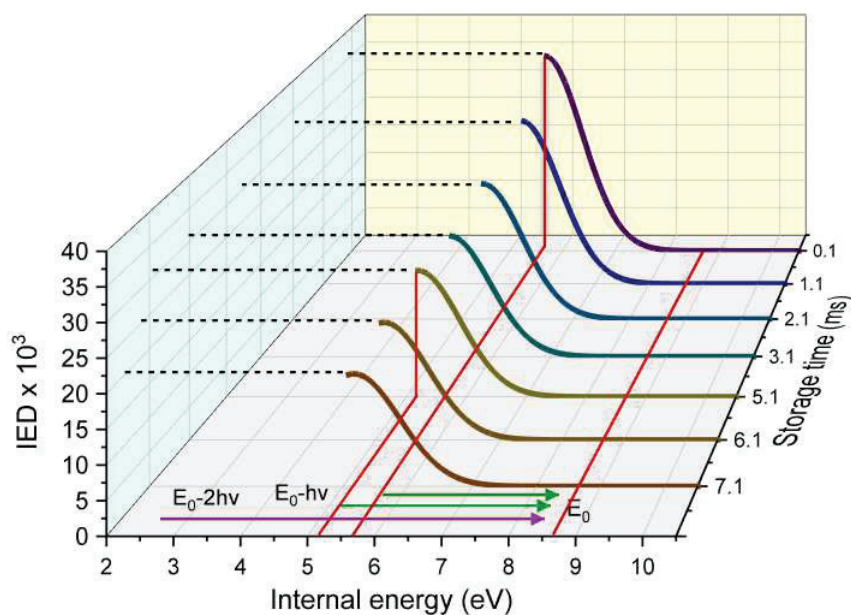


Figure 5-8: Time evolution of phenanthrene cations during the cooling process, where E_0 is the energy window, hv is the photon energy of the laser.

As the ECR ion source used in this work provides hot ions with broad internal energy, single visible photon absorption is sufficient for the excitation process of ions at short storage times. The choice of photon energy is crucial to ensure that the HEE goes inside the sensitive energy window after absorption. If the ions were produced at a much lower temperature, multiphoton absorption (in the visible range) would be required to excite the ions. Similarly, for long storage times, as the ions become colder with time, single photons absorption may not be sufficient, and two-photon absorption may become necessary to bring the HEE of the IED into the energy window.

5.3.3 Modeling the neutral yield

After laser absorption, the IED is such that the dissociation rate is expected to be much higher than the radiative cooling rates due to recurrent fluorescence and IR vibrational emissions. The modeling neglects these cooling rates. We consider a new ion ensemble whose internal energy has been shifted by the photon energy. We also consider that this new ion ensemble does not interact with the remaining ions that have not absorbed any photon. For a given internal energy, the time evolution of the number of ions $N(E, t)$ remaining in the ring follows the rate equation:

$$\frac{\partial N(E, t)}{\partial t} = -k_d(E)N(E, t) \quad \text{Eq. (5-9)}$$

The solution of this equation is an exponential decay:

$$N(E, t) = N(E, 0) \exp(-k_d(E)t) \quad \text{Eq. (5-10)}$$

The detector only collects neutrals emitted in between deflectors D₃ and D₄. In the following, the corresponding flight time between deflectors D₃ and D₄ and the revolution period are denoted Δt_{34} and T , respectively. At the n^{th} revolution after laser shot, the number of emitted neutrals is given by:

$$S_n(E) = N\left(E, \left(n + \frac{1}{2}\right)T - \frac{\Delta t_{34}}{2}\right) - N\left(E, \left(n + \frac{1}{2}\right)T + \frac{\Delta t_{34}}{2}\right) \quad \text{Eq. (5-11)}$$

$$S_n(E) = N(E, 0) \exp(-k_d(E) \left(\left(n + \frac{1}{2}\right)T \right)) \left(\exp\left(k_d(E) \frac{\Delta t_{34}}{2}\right) - \exp\left(-k_d(E) \frac{\Delta t_{34}}{2}\right) \right) \quad \text{Eq. (5-12)}$$

$$S_n(E) = 2N_0 g'_{ex}(E, t' = 0) \exp\left(-k_d(E) \left(n + \frac{1}{2}\right)T\right) \sinh\left(k_d(E) \frac{\Delta t_{34}}{2}\right) \quad \text{Eq. (5-13)}$$

where N_0 is the number of ions that have absorbed a photon and $g'_{ex}(E, t' = 0)$ is the IED of these ions at the photon absorption time.

In Eq. (5-13), the argument of the hyperbolic sine function is constant; therefore, for an infinitely narrow IED, i.e., a Dirac delta function at a given energy E , one would obtain an exponential decay.

An infinitely broad, flat, IED can be simulated by summing the contributions of the decays resulting from the set of energies covering a broad range compared to the energy window as shown in Figure 5-9. There is a close correspondence between energy and the time at which it contributes the most. Low energies contribute for a long time and high energies at short times. To obtain a broad internal energy distribution, all the contributions can be summed up, and a perfect line in the log-log scale with a slope of about -1 is obtained. Therefore, the decay follows t^{-1} for broad internal energy distribution. These decays have been computed using $S_n(E)$ for a set of 51 internal energies in the energy range 6-11 eV. Few of such decays are displayed for clarity in Figure 5-9. Each of the individual exponential decay curves is plotted with the log-log scale in Figure 5-9. The correspondence between time and energy can be clearly seen in this figure. For instance, the maximum contribution of the decay at $E = 8.5$ eV is about 200 μs . The

EXPERIMENTAL RESULTS OF PHENANTHRENE MONOMER CATIONS

sum of the contributions of all individual decays is plotted in Figure 5-9 (black straight line). This is demonstrating that the decay corresponding to a flat distribution is a power-law. A fit to this curve shows that the power is more precisely -1.06.

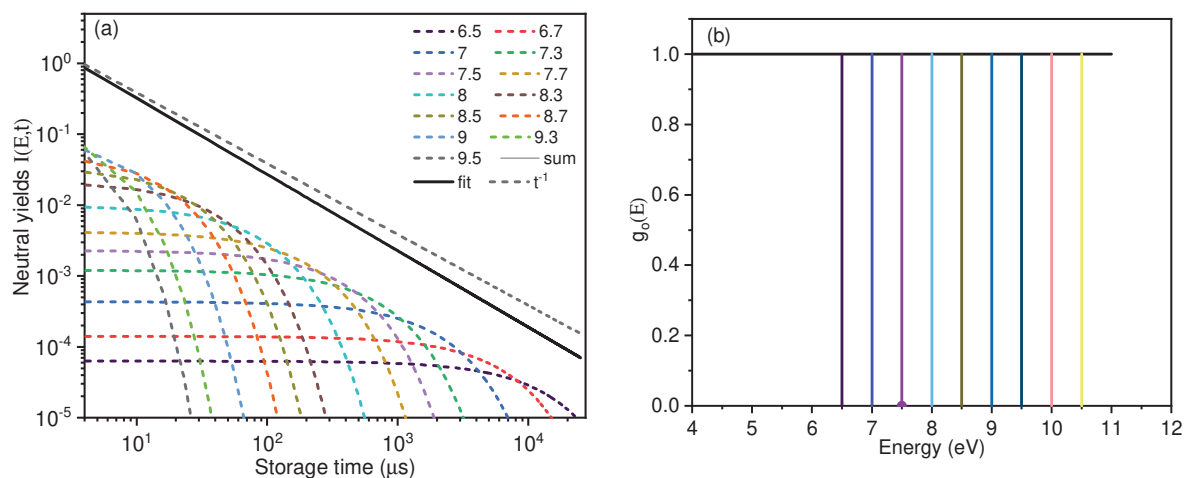


Figure 5-9 : (a) The contributions to neutral fragment yields from phenanthrene cations with different energy (dashed colored lines) as a function of time, the total neutral fragment yields (black line), and power law (dashed line). (b) Flat IED.

In Figure 5-10, we consider an IED that presents an HEE. In this case, the contributions at a short time will be lowered; therefore, the decay can be separated into two parts with two different power-laws with an exponent smaller than one at a short time and approximately of -1 at a long time. This case corresponds to the present experimental result that will be discussed in the next sections.

For completeness, we consider in Figure 5-11 the case of an IED with a low-energy edge where contributions at long times would be lowered. The decay would then be separated into two parts with two different power-law as well, with an exponent close to -1 at short times and greater than 1 at long times.

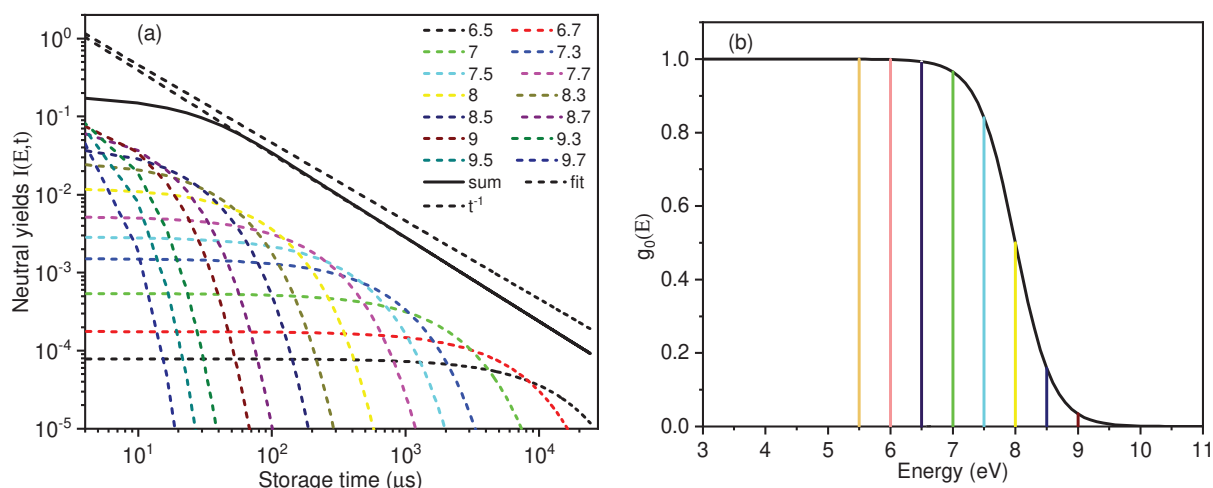


Figure 5-10 : (a) The contributions to neutral fragment yields from phenanthrene cations with different energy (dashed colored lines) as a function of time, the total neutral fragment yields (black line) with decay factor less than 1, and power law (dashed line). (b) IED with a high energy edge.

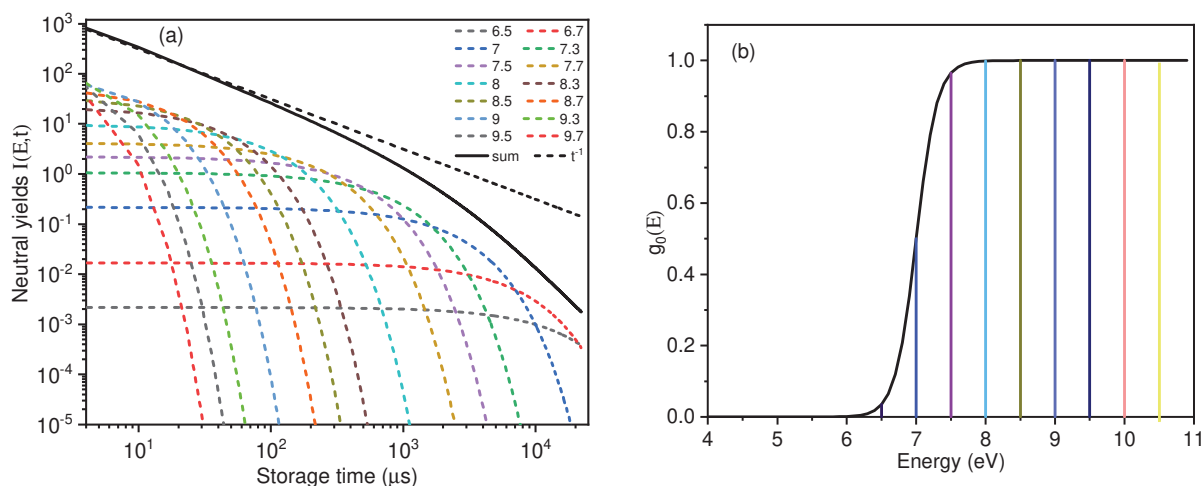


Figure 5-11 : (a) Contributions to neutral fragment yields from phenanthrene cations with different energy (dashed colored lines) as a function of time, the total neutral fragment yields (black line, and power law (dashed black line)). (b) IED with a low energy edge.

5.3.4 Experimental Laser-induced decay curves

In the present experimental results, the IED of the stored phenanthrene cations has been probed with nanosecond laser pulses at different wavelengths of 355 nm, 420 nm, and 440 nm with intensities in the range of 50-90 $\mu\text{J}/\text{pulse}$. Laser-induced decay curves have been recorded every ms from 0.1 to 9.1 ms. They are plotted in Figure 5-12 and analyzed as a function of t' , the time from each laser firing time, i.e., $t' = t - t_{laser}$, where t is the reference time of the whole experiment, i.e., the $t = 0$ corresponds to the buncher trigger signal.

As an example, the decay curve at $t_{laser} = 1 \text{ ms}$ is displayed on log-linear scales in Figure 5-13(a) and log-log scale Figure 5-13(b). It demonstrates clearly that the decay is not exponential as could be expected for a narrow (Dirac-like) IED but much closer to a power-law typical of a broad IED. The obtained decay factor of $\alpha = 0.92$, close to but slightly below 1, shows that the HEE of the IED after laser absorption is inside the energy window, slightly below E_{max} which is estimated to be about 10 eV.

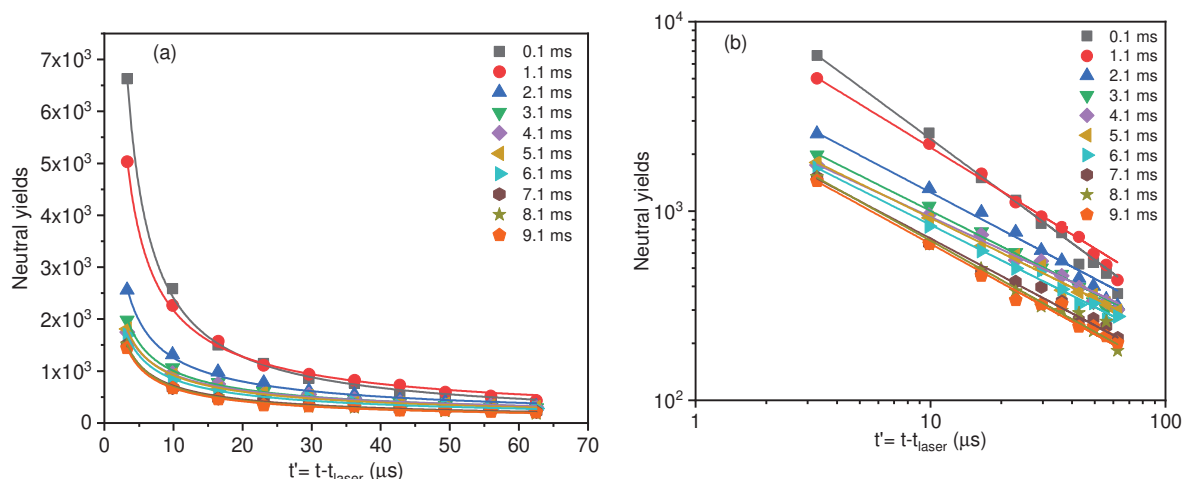


Figure 5-12: Laser-induced decay curves for the first ten turns after the laser shots at times from 0.1 ms to 9.1 ms for a laser wavelength of 440 nm, (a) Linear scale (b) Log-log scale.

All recorded laser-induced decay curves of Figure 5-12 have been fitted by power-laws. The fits are, in general, in rather good agreement with the experimental decays. The decay factor was found to decrease from $\alpha = 0.92$ for $t_{laser} = 0.1 \text{ ms}$ to $\alpha = 0.48$ for $t_{laser} = 5.1 \text{ ms}$ and, unexpectedly, to increase again up to $\alpha = 0.6$ for $t_{laser} = 9.1 \text{ ms}$.

EXPERIMENTAL RESULTS OF PHENANTHRENE MONOMER CATIONS

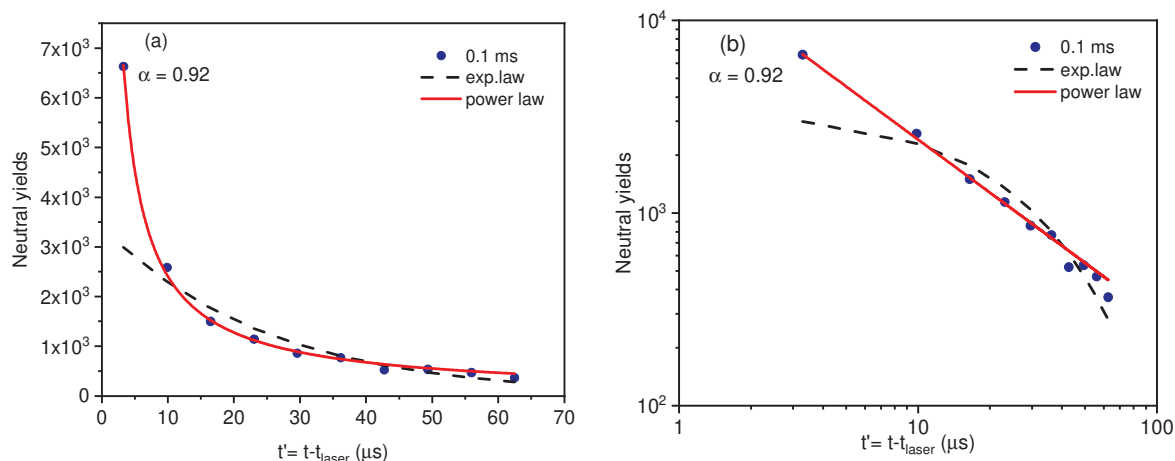


Figure 5-13 : (a) Neutral fragment yields induced at the laser shot 0.1 ms in linear scale with power law and exponential law fit, (b) Neutral fragment yields induced at the laser shot 0.1 ms in log scale.

The decay factors obtained for the different storage times and the wavelengths of 355, 420, 440 nm are plotted in Figure 5-14. For 420 and 440 nm, the values of the decay factor are divided into two regions. In the region I, the expected decrease with storage time corresponds to one-photon absorption. In region II, the increase of the decay factor with the storage time is interpreted as due to two-photon absorption. Indeed, when alpha comes down to about 0.5, the HEE of the IED is probably too close to E_{min} after single photon absorption to induce a significant decay. For 420 and 440 nm, the absorbed energy in the case of two-photon absorption brings the HEE inside the energy window. Then, the observed decay is dominated by two-photon absorption. For 355 nm, the two-photon absorption brings the whole IED to too high internal energies leading to too short decays to be observed. Therefore, only single-photon absorption is observed with 355 nm.

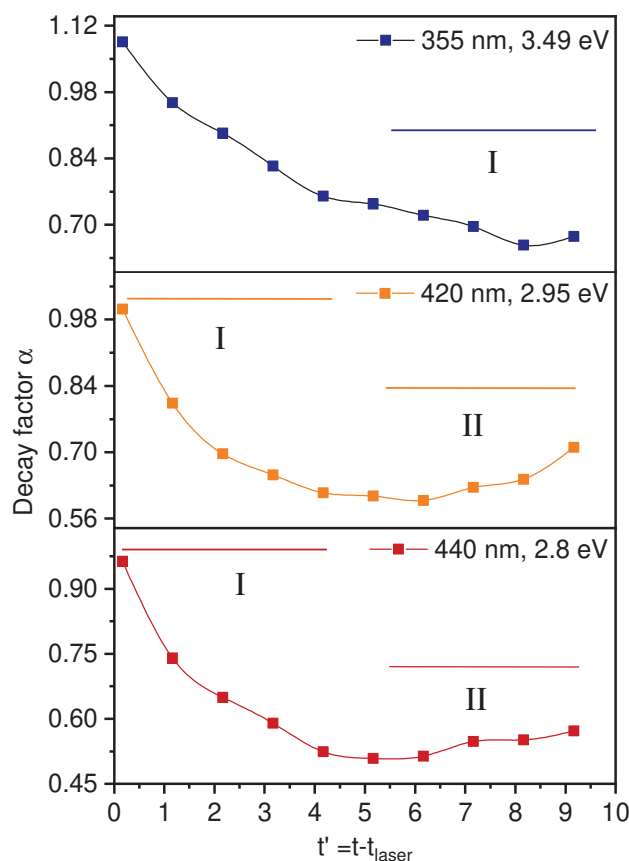


Figure 5-14: Decay factors for different wavelengths, showing one-photon and two-photon absorption.

EXPERIMENTAL RESULTS OF PHENANTHRENE MONOMER CATIONS

Figure 5-15(a) displays the first five fitted curves from 0.1 ms to 4 ms. The decrease of decay factor α as a function of the storage time is presented in Figure 5-15(b) for single-photon absorption at the wavelength of 355 nm. The decay factor is applied to describe the decay tendency of the neutral fragment yields with increasing storage time. This indicates that the IED after laser excitation shifts towards lower energy with increasing storage time. Therefore, the energy shift rate of the HEE of the IED can be obtained as discussed in the following.

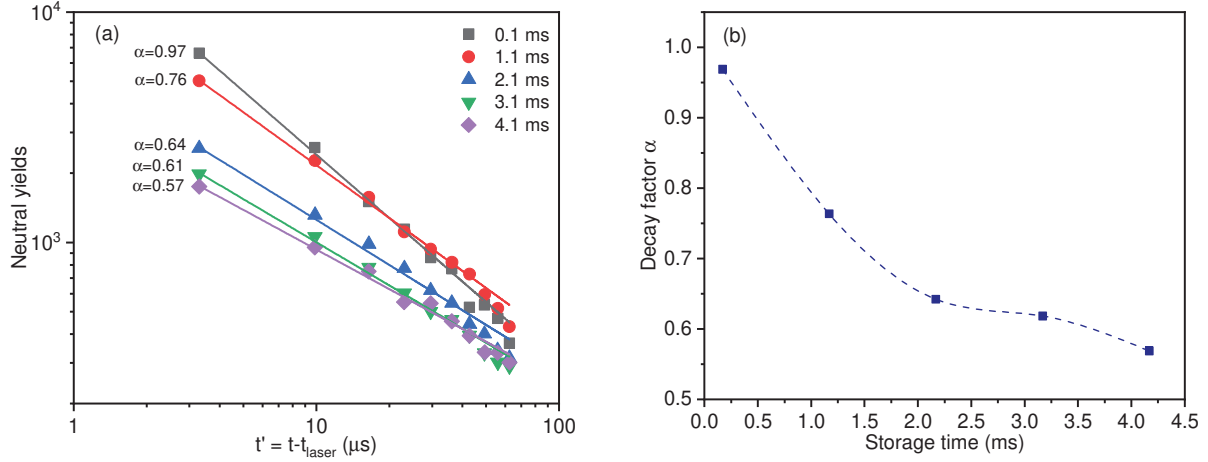


Figure 5-15: (a) Laser-induced decay curves for the first ten turns after laser excitation at 0.1, 1.1, 2.1, 3.1, 4.1 ms. (b) Time evolution of the decay factor for the storage time 0.1, 1.1, 2.1, 3.1, 4.1 ms.

5.3.5 Determination of the energy shift rate using photon energies

The energy shift rate $\Delta E/\Delta t$ of the HEE, as defined in Eq. (5-14) can be obtained by comparing the decay factors α obtained with different photon energies. As stated in section 5.3.2, the basic idea relies on the hypothesis that a given value of α is related to a given value of the HEE. In this case, three different photon energies, $E_1 = 3.49$, $E_2 = 2.95$ and $E_3 = 2.82$ eV, have been used to excite the stored ions. The variation of the resulting decay factors as a function of the storage time is displayed in Figure 5-16 for each photon energy. The times t_i and t_j at which identical values of α were obtained for the corresponding photon energies E_i and E_j , respectively, can be graphically determined from Figure 5-16.

$$\frac{\Delta E}{\Delta t} (\langle t \rangle) = \frac{E_i - E_j}{t_i(\alpha) - t_j(\alpha)} \quad \text{Eq. (5-14)}$$

The resulting energy shift rates are plotted as a function of mean storage time, $\langle t \rangle = (t_i + t_j)/2$ in Figure 5-17. Table 5-1 compiles energy shift rates at several different mean storage times. The energy shift rate shows a strong decreasing tendency with storage time. As mentioned in section 5.1, the delayed dissociation of stored ions is the prevailing relaxation process at the very short storage time, i.e., less than 0.6 ms. The radiative cooling becomes competitive with the dissociation process at about 0.6 ms and hinders the dissociation process after 6 ms. Therefore, the fast energy shift rate in the short storage time range, i.e., less than 6 ms, could be resulting from both dissociation and the radiative cooling, whereas the shift rate in the longer storage time, longer than 6 ms, could be ascribed mainly to the radiative decay. The energy shift rate demonstrates a sensitive dependency on the storage time, hence, the IED of an ensemble of stored ions.

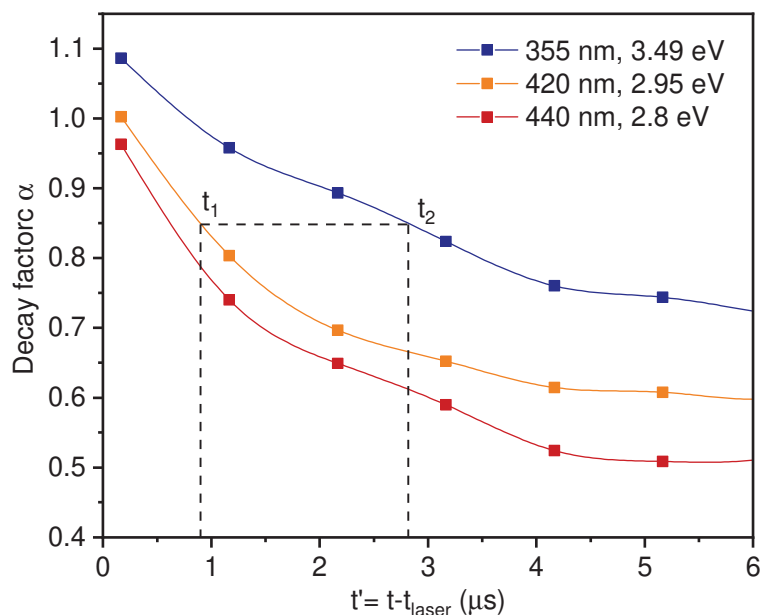


Figure 5-16: Decay factor as a function of storage times for different wavelengths.

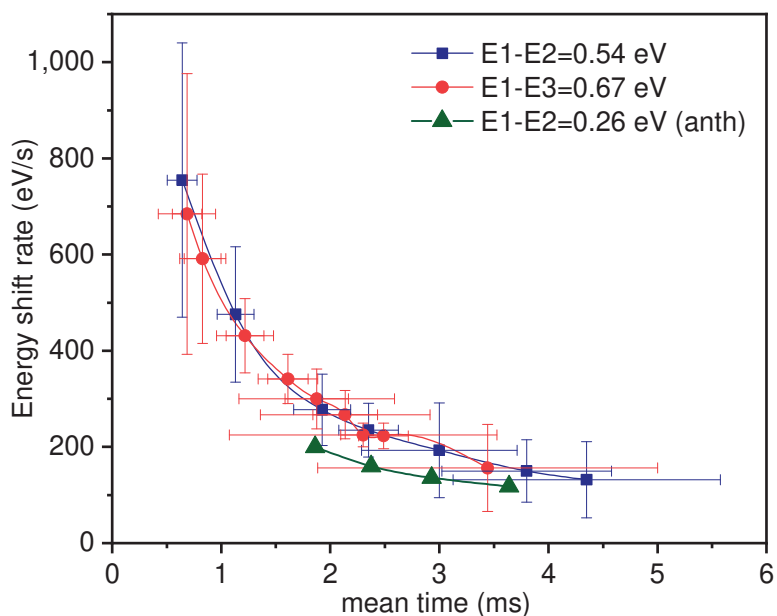


Figure 5-17: Energy shift rate at different storage times for different energy photons for phenanthrene cations (red dots and blue squares). Error bars account for statistical uncertainties. Green triangles are results previously obtained for anthracene cations [134].

Table 5-1: Energy shift rate at different photon energies

$E1 - E2 = 0.54$		$E1 - E2 = 0.67$	
Energy shift	Mean time	Energy shift	Meantime
447.3	0.65	688.5	0.69
450.4	1.1	443.9	1.2
277.2	1.92	299.9	1.87
235	2.35	240.9	2.4

EXPERIMENTAL RESULTS OF PHENANTHRENE MONOMER CATIONS

The energy shift rate of phenanthrene cations is compared with the previously studied isomer, anthracene, as presented in Figure 5-17. It is noted that the energy shift rate has a similar decreasing trend with increasing storage time. However, it is found slightly higher for phenanthrene than anthracene cations. At a mean time of 2 ms, it is estimated to be about 300 eV/s for phenanthrene cations and to be 200 eV/s for anthracene cations.

It can be concluded that the method of decay factor is relevant to determine the time evolution of the HEE of IED. This evolution is quantified by the energy shift rate, which is found slightly larger for phenanthrene than anthracene. This method enables a quantitative discussion on the energy lost due to relaxation processes with time; however, it cannot provide any correspondence with internal energy. Moreover, at short storage time, the contribution of the depletion due to spontaneous dissociation cannot be excluded. It can be considered negligible at about 6 ms. Furthermore, the decay factor method relies solely on one parameter α , which may not be precise enough to describe the neutral yield decays and may have uncertainties as well. It has been used without involving any IED simulation. In the following section, the neutral yield decay curves are modeled using such a function, giving rise to a realistic estimation of IED.

5.3.6 Time evolution of HEE of the IED

In this section, the energy shift rate will be determined via a more sophisticated method where the IED after laser absorption at different storage times will be determined from a fit of model decay curves to experimental ones. The energy shift rate will be evaluated from the shift of the HEE of the IED in between the different laser shot times. In order to limit the number of fitting parameters in the model, we used Gaussian functions for the IED, although the IED shape may be more complex, especially on its low energy side. On the high energy side, the depletion due to dissociation at a short time and to RF in the millisecond time range may be rather well fitted by a Gaussian function. Therefore, in the following the IED, $g'_{ex}(E, t' = 0)$ is given by the Gaussian distribution:

$$N'_{ex} = A \times g'_{ex}(E) = \frac{A}{\sqrt{2\pi}\sigma} e^{-(E-E_0)^2/(2\sigma^2)} \quad \text{Eq. (5-15)}$$

where E_0 , and σ are the center and standard deviation of the IED and A in an amplitude corresponding to the number of laser-excited ions.

The neutral counts at different storage times of photon wavelength of 355 nm have been simulated as a function of internal energy of IEDs described by a Gaussian function at each laser shot. The experimental and simulated decay curves are presented in Figure 5-18 for $t_{laser} = 0.1$ to $t_{laser} = 9.1$ ms. The dissociation decay curve is calculated for each value of the internal energies. Global model decay curves have been calculated from the weighted sum of these individual decays where the weights are given by Eq. (5-15) by discretizing the internal energy in steps of 0.1 eV. Finally, the obtained modeled neutral yield decay curves are fitted to the experimental decay curves by adjusting the parameters A , E_0 and σ of Eq. (5-15).

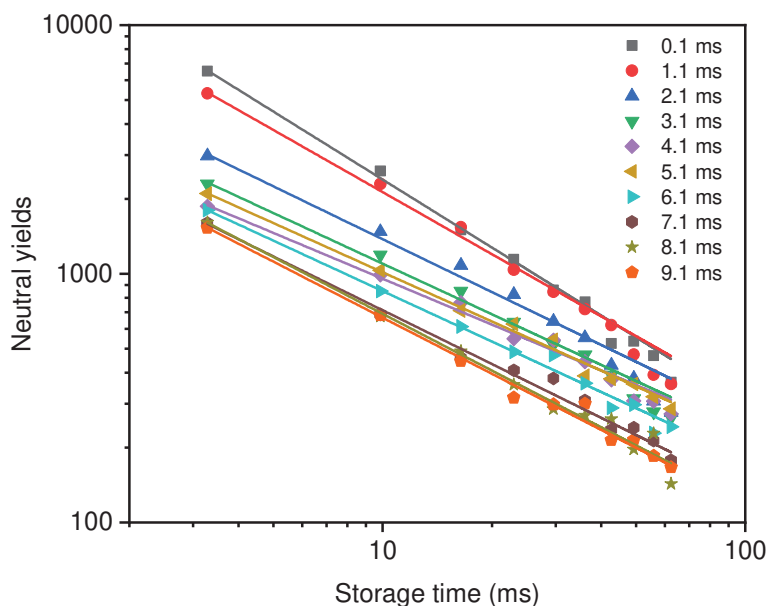


Figure 5-18: Experimental and simulated decay curves for $t_{laser} = 0.1$ to $t_{laser} = 9.1$ ms.

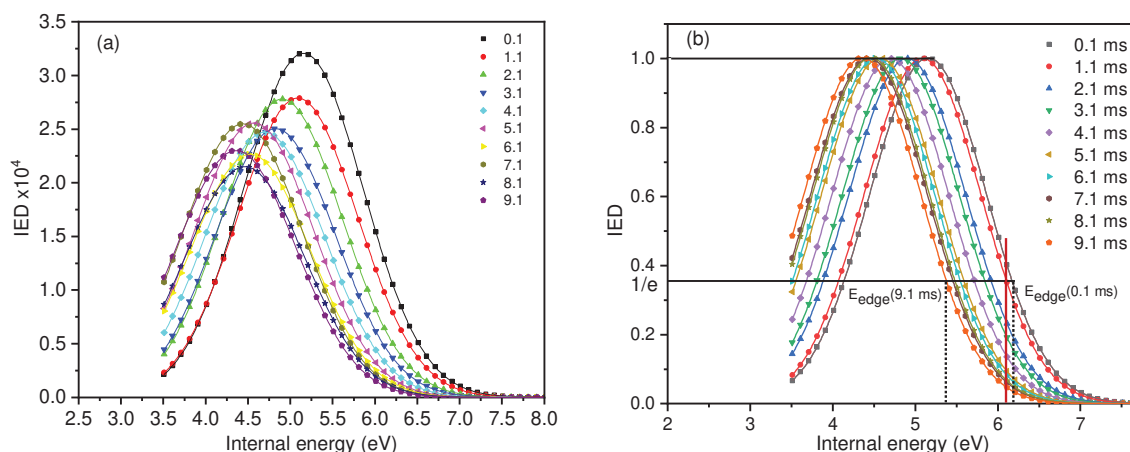


Figure 5-19: (a) IED of stored phenanthrene ions at different storage times from 0.1 to 9.1 ms, (b) Normalized IED of stored ions at the considered storage time.

Using this fitting procedure, IEDs have been obtained independently for all laser-induced decays. The HEEs of the obtained distributions are determined from the population at HEE according to the relation $N(E_{edge}) = A/e$. The resulting HEEs, E'_{edge} , are those for ions that have absorbed a photon. Therefore, the HEE, E_{edge} , of ions that have not absorbed any photon at the time t_{laser} is simply given by:

$$E_{edge}(t_{laser}) = E'_{edge}(t_{laser}) - h\nu \quad Eq. (5-16)$$

In the energy shift rate, the value of ΔE can be extracted from the difference between the high energy edge of the distributions on the high energy side for each curve at a specific storage time. On average, over the whole 1-10 ms time range of the experiment, the energy shift rate is found to be:

$$\frac{\Delta E}{\Delta t} = \frac{E_{edge}(0.1 \text{ ms}) - E_{edge}(9.1 \text{ ms})}{9 \times 10^{-3}} = 95 \text{ eV/s} \quad Eq. (5-17)$$

EXPERIMENTAL RESULTS OF PHENANTHRENE MONOMER CATIONS

We plotted in Figure 5-20 the energy shift rate calculated using the IEDs of two consecutive laser shot times as a function of storage time from 0.1 to 9.1 ms. Although the results present some fluctuations due to experimental and fitting uncertainties, the energy shift shows a clear decreasing tendency from about 150 eV/s at 0.1 s down to about 50 eV/s at 8 ms.

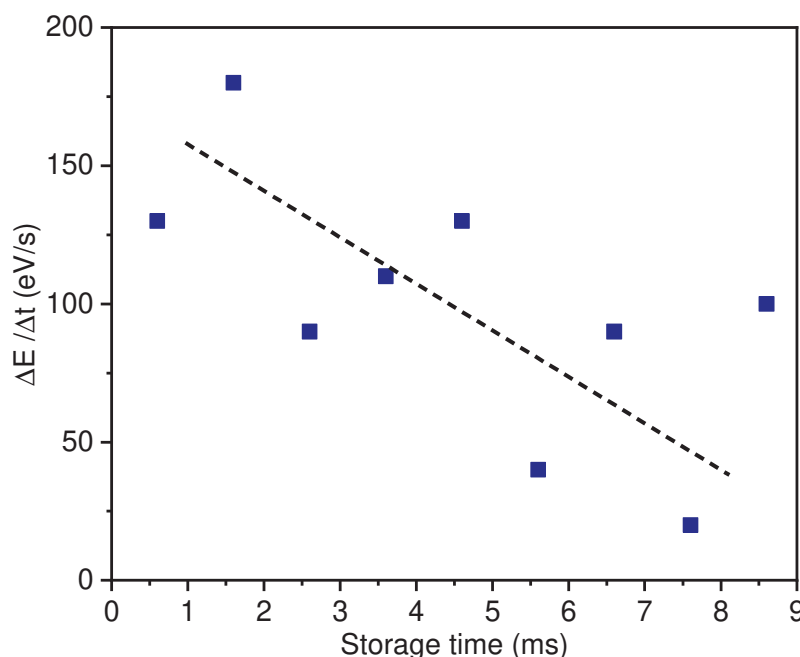


Figure 5-20: Energy shift rate as a function of storage time.

As also discussed in section 5.1, both radiative and dissociation processes are competitive in the storage time range of 0.6-6 ms and the radiative cooling process is predominant after 6 ms. The estimated $\Delta E/\Delta t$ value is therefore attributed to the radiative cooling process of the stored ensemble of ions after 6 ms storage times.

5.3.7 The measured population decay rate

We define the population decay rate, $k_{measured}$, as the rate at which ions of a given internal energy E_0 disappear by any process, i.e., dissociation, recurrent fluorescence, or vibrational transition. It can be extracted from the observed IED for a given internal energy E_0 as a function of the storage time. As an example, in Figure 5-19(b), a vertical line at internal energy $E = 6.1$ eV can be drawn to cross all the IED curves at different storage times. The population at the crossing points is then plotted as a function of the storage time in Figure 5-21, in a semi-log scale. The time-dependent population decay of ions is clearly found to be exponential. This procedure has been repeated with a step of 0.2 eV in the internal energy (E) range from 5.1 to 6.7 eV and the corresponding curves are plotted in Figure 5-21. Exponential fits provide the characteristic rates $k_{measured}(E_0)$, which can be mathematically defined by:

$$k_{measured}(E) = -\frac{1}{g(E, t)} \frac{\partial g(E, t)}{\partial t} = \frac{1}{g(E, t)} \frac{\partial g(E, t)}{\partial E} \left[\frac{\Delta E}{\Delta t} \right]_{measured} \quad Eq. (5-18)$$

It can be noted that a fast energy shift of the IED gives rise to fast population decay, and subsequently, fast population decay gives rise to a fast energy shift rate.

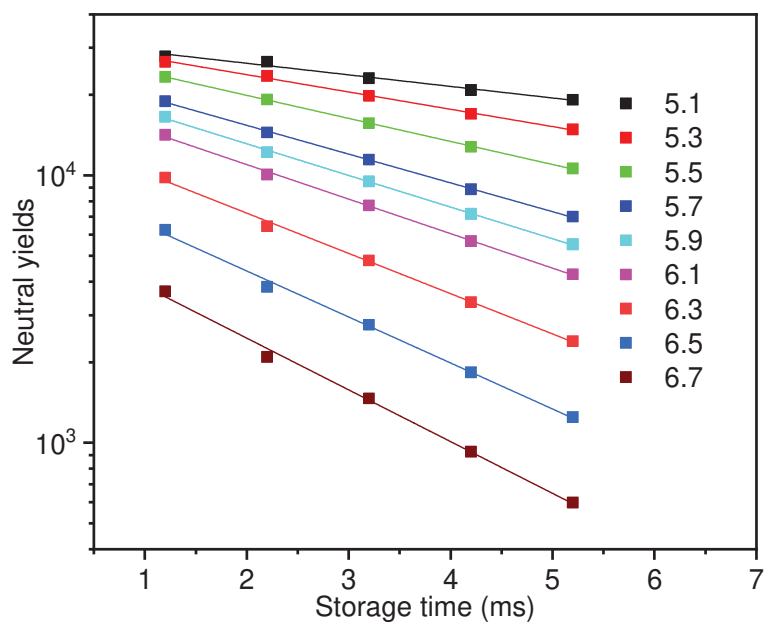


Figure 5-21: The evolution of ion population of phenanthrene as a function of storage time at different internal energies from 5.1 to 6.7 eV. For each internal energy, the population decay is fitted with the exponential function.

Table 5-2: calculated dissociation rate k_d and measured population decay rate k_m as a function of internal energy.

1.7 eV				1.5 eV		
anthracene				phenanthrene		
E(eV)	$k_d(s^{-1})$	$k_m(s^{-1})$	$\eta_{cool,el}(s^{-1})$	$k_d(s^{-1})$	$k_m(s^{-1})$	$\eta_{cool,el}(s^{-1})$
5.05				0.05	100	30
5.25				0.2	149	43
5.45	0.03	110	34	0.6	198	54
5.65	0.12	184	55	1.9	248	66
5.85	0.39	257	75	5.3	297	76
6.05	1.2	330	93	14.1	347	86
6.25	3.44	404	110	34.9	396	95
6.45	9.2	477	126	82	445	103
6.65	23.2	550	141	182	495	112
6.85	55.4	624	155	389.7		

Table 5-2 presents the values of $k_{measured}$ for phenanthrene cations together with new values for anthracene cations obtained in this work using the method employed in [77]. It should be noted that $k_{measured}$ is the sum of the individual rates of all the possible energy relaxation processes, namely, dissociation, recurrent fluorescence, and vibrational cooling:

$$k_{measured} = k_d + k_{RF} + k_{IR} \quad \text{Eq. (5-19)}$$

The dissociation rate k_d for anthracene have been calculated from the activation energy and entropy of activation in [57] and recently reanalyzed [260]. The new values of k_d are higher than ones calculated in [57] and used in [5]. Similarly, for phenanthrene k_d values were

EXPERIMENTAL RESULTS OF PHENANTHRENE MONOMER CATIONS

obtained from the Arrhenius law (Eq. (2-22)). It is found that these values are much smaller than $k_{measured}$ in the energy range from 5 to 6.45 eV, leading to consider the dissociation process as negligible. This statement agrees with the results of section 5.1 about the natural decay for which the dissociation process was found negligible at long storage time. Therefore, the observed population decay is dominantly due to the radiative cooling process in the 5 to 6.45 eV energy range.

The IR and RF emissions have very different relative contributions in the radiative cooling mechanism. However, let us consider, at first, the total population decay rate due to radiative cooling processes, k_{rad} , as the sum of the population decay rates due to IR emission, k_{IR} , and RF emission, k_{RF} :

$$\frac{dg(E, t)}{dt} = -k_{rad}g(E, t) = -(k_{IR} + k_{RF})g(E, t) \quad Eq. (5-20)$$

The IR cooling rate $\eta_{cool,IR} = -1/E[dE/dt]$ of PAHs are found to be small comparing to fluorescence emission rate. For anthracene, it was estimated to be 2 s^{-1} in the energy range from 2 to 10 eV and nearly independent of energy [9]. At internal energy of 6.65 eV, the shift due to IR emission of the HEE is estimated to be at a rate of $(\Delta E/\Delta t)_{IR} = -\eta_{cool,IR} \times E = 13.3 \text{ eV/s}$. This value is much smaller than the measured energy shift rate, $(\Delta E/\Delta t)_{measured}$, which are 95 and 100 eV/s for phenanthrene and anthracene, respectively. At a given energy E , the shift of the HEE due to IR induce a population decrease characterized $k_{IR}(E)$ given, from the fitted Gaussian distribution, by:

$$k_{IR}(E) = \frac{1}{g(E, t)} \frac{\partial g(E, t)}{\partial E} \left[\frac{\Delta E}{\Delta t} \right]_{IR} = \frac{(E - E_0)E}{\sigma^2} \eta_{cool,IR} \quad Eq. (5-21)$$

The energy shift rate due to the RF rate is characterized by the electronic transition rate $k_{RF}(E)$. The fluorescence emission from the ion ensemble at higher energy can lead to the increase of the ion population at a given energy. The time evaluation of the ion population at a given internal energy E can be given by:

$$\frac{dg(E, t)}{dt} = -k_{RF}g(E, t) + k_{RF}(E + h\nu_{RF})g(E + h\nu_{RF}, t) \quad Eq. (5-22)$$

Where $h\nu_{RF} = 1.5 \text{ eV}$ and $h\nu_{RF} = 1.7 \text{ eV}$ are the D_2 - D_0 electronic transition energy of the phenanthrene [261] and anthracene cations [9], respectively. The fluorescence rate is statistical and depends on the probability of occurrence of fluorescence, which in turn depends on the transition energy. The recurrent fluorescence rate via the $D_2 - D_0$ transition can be calculated using the Fermi's golden rule:

$$F_{D_2 \rightarrow D_0} \propto \frac{\rho_{D_2}(E - h\nu_{D_2 \rightarrow D_0})}{\rho_{D_0}(E)} P_{D_2 \rightarrow D_0} \quad Eq. (5-23)$$

Where $\rho(D_2)$ is the density of states of D_2 , $\rho(D_0)$ is the density state of D_0 , and $P_{D_2 \rightarrow D_0}$ is the probability of the $D_2 \rightarrow D_0$ transition.

At a given internal energy, at which dissociation and IR cooling are negligible, the RF cooling rate, $\eta_{cool,RF}$, can be obtained from the D_2 - D_0 electronic transition energy and the measured population decay rate:

$$\eta_{cool,RF} = \frac{k_{measured} h\nu_{RF}}{E} \approx \frac{k_{RF} h\nu_{RF}}{E} \quad Eq. (5-24)$$

EXPERIMENTAL RESULTS OF PHENANTHRENE MONOMER CATIONS

For internal energy of, e.g., 6.05 eV, for phenanthrene and anthracene cations, one obtains very similar values of 86 and 93 s⁻¹, respectively. Since the electronic transition energies D_2-D_0 of anthracene is slightly smaller for phenanthrene than anthracene, it could be expected that the density of states is more favorable for IIC. However, this effect is probably compensated by the fact that the emitted photon takes out more energy at one in the case of anthracene. Therefore, the net effect of the rate of RF is found similar in both cases.

In summary, it can be concluded that the fluorescence rate of the monomer cations of phenanthrene and anthracene is in the same order of magnitude. However, for the internal energy higher than 5.9 eV, it is possibly a bit smaller than the monomer cations of anthracene, as illustrated in Figure 5-22.

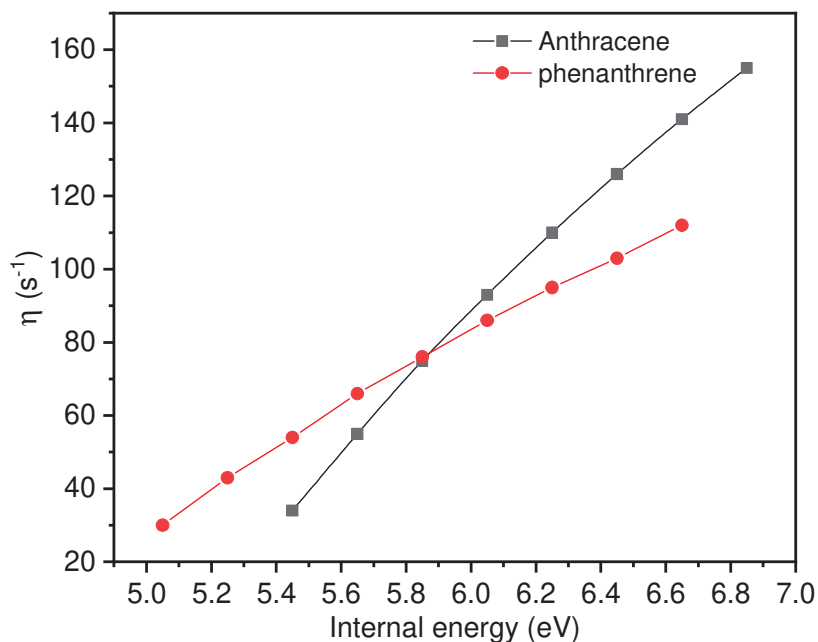


Figure 5-22: Fluorescence emission rate as a function of internal energy for phenanthrene and anthracene cations.

5.4 Conclusion

In this chapter, we investigated the cooling dynamics of phenanthrene cations stored in the Mini-Ring for times up to 10 ms. Neutral fragment yields induced by laser excitation at different wavelengths and storage times were used to probe the time evolution of the IED of stored ions. The high value of the radiative cooling rate of such cations could not be explained by IR vibrational transition only. However, the RF cooling rate is found to be consistent with the measured cooling rates. We have used three different methods to quantify the effect of the RF process on the cooling of phenanthrene cations: the quenching of the natural decay, fits of laser-induced at different wavelengths by a power-law, and time evolution of the IED by modeling of the laser-induced decay. The three methods were consistent when comparing the results of phenanthrene and anthracene cations: for both cases, the cooling rate and the energy shift rate are found in the same order of magnitude in the presented time and internal energy ranges.

Up to now, all the studied monomer cations (naphthalene, anthracene, pyrene, etc., and others are on the way) have demonstrated a fast radiative cooling rate. In the next chapter, we will discuss the case of PAH dimer cations and we show that the situation regarding dissociation and radiative is very different.

6 EXPERIMENTAL RESULTS FOR DIMER CATIONS

6	EXPERIMENTAL RESULTS FOR DIMER CATIONS	124
6.1	The natural decay of cationic dimers	125
6.2	Prompt dissociation.....	128
6.3	Dissociation pathway - Coincidence experiments	130
6.4	Experimental photodissociation spectra of cationic dimers.....	131
6.4.1	Method	131
6.4.2	Cationic dimers of Naphthalene.....	132
6.4.3	Cationic dimers of benzene.....	134
6.4.4	Cationic dimers of pyrene	137
6.5	Semi-empirical Modelling	138
6.5.1	Cationic dimers of naphthalene.....	138
6.5.2	Cationic dimers of benzene.....	141
6.6	Results of DFTB-EXCI Modelling for pyrene dimer cations.....	143
6.6.1	The photo-absorption spectrum	143
6.6.2	Photo-absorption spectra dependence on temperature.....	144
6.6.3	The potential energy surfaces in reduced dimensionality.....	145
6.6.4	Comparison of the theoretical absorption spectrum with the experimental photodissociation spectrum	146
6.7	IR radiative cooling of the dimer of naphthalene at DESIREE	147
6.8	Fragmented dimer cations.....	149
6.9	Conclusion	151

This chapter is devoted to the experimental investigation of the relaxation processes of cationic dimers of small PAH. The studies focus on cationic dimers of benzene (C_6H_6) $_2^+$, naphthalene ($C_{10}H_8$) $_2^+$, and pyrene ($C_{16}H_{10}$) $_2^+$. Although benzene is not considered to belong to the PAH family, we found it useful to include this molecule in the present study as it is the elementary brick of this family.

After the formation of these dimer cations in the ECR ion source and storage in the Mini-Ring, several studies have been performed, such as spontaneous decay, photo-dissociation spectroscopy, and coincidence experiments to identify the neutral fragment yields. The modeling of experimental results has been carried out using different approaches, namely, semi-empirical and DFT calculations which have been performed in collaboration with LCPQ Toulouse. A section of this chapter is dedicated to experiments carried out at the DESIREE facility about the study of the evolution of naphthalene dimer cations with long storage times

EXPERIMENTAL RESULTS FOR DIMER CATIONS

up to several seconds in a cryogenic environment. The final section of this chapter is dedicated to fragmented dimer cations that have quite different behaviors compared to the intact ones.

6.1 The natural decay of cationic dimers

As demonstrated in the previous chapter dedicated to monomer cations of phenanthrene and in several earlier works, the examination of the natural decay is in itself very informative. Therefore, the different cationic dimers investigated in the present chapter, $(C_6H_6)_2^+$, $(C_{10}H_8)_2^+$, and $(C_{16}H_{10})_2^+$ have been stored in the Mini-Ring, without using laser excitation, for storage times up to 100 ms. As for the monomer cation of phenanthrene, the natural decay of dimer cations results from spontaneous statistical dissociation due to high vibrational energy that has been distributed onto the systems in the ion source. The raw data of typical records for these three cationic dimers are displayed in Figure 6-1. The inserts of these figures show the bunch structure of the injected ion beam in the Mini-Ring. However, after several milliseconds of storage time, typically 10 ms, this structure is lost due to kinetic energy and angular dispersions of the stored ion beam. Further detail can be found in ref. [109]. This issue has to be taken into account in the data analysis, especially when the counts are binned in time bins corresponding to a single revolution period. In principle, longer storage time would be possible; however, the present storage time of 100 ms was sufficient to demonstrate that the storage time is limited by collision with residual gas.

The natural decays of the three aforementioned cationic dimers were obtained as a function of the storage time by integration over each time bin, which has been selected to the corresponding revolution period. They are displayed in log-log scale in Figure 6-2. The natural

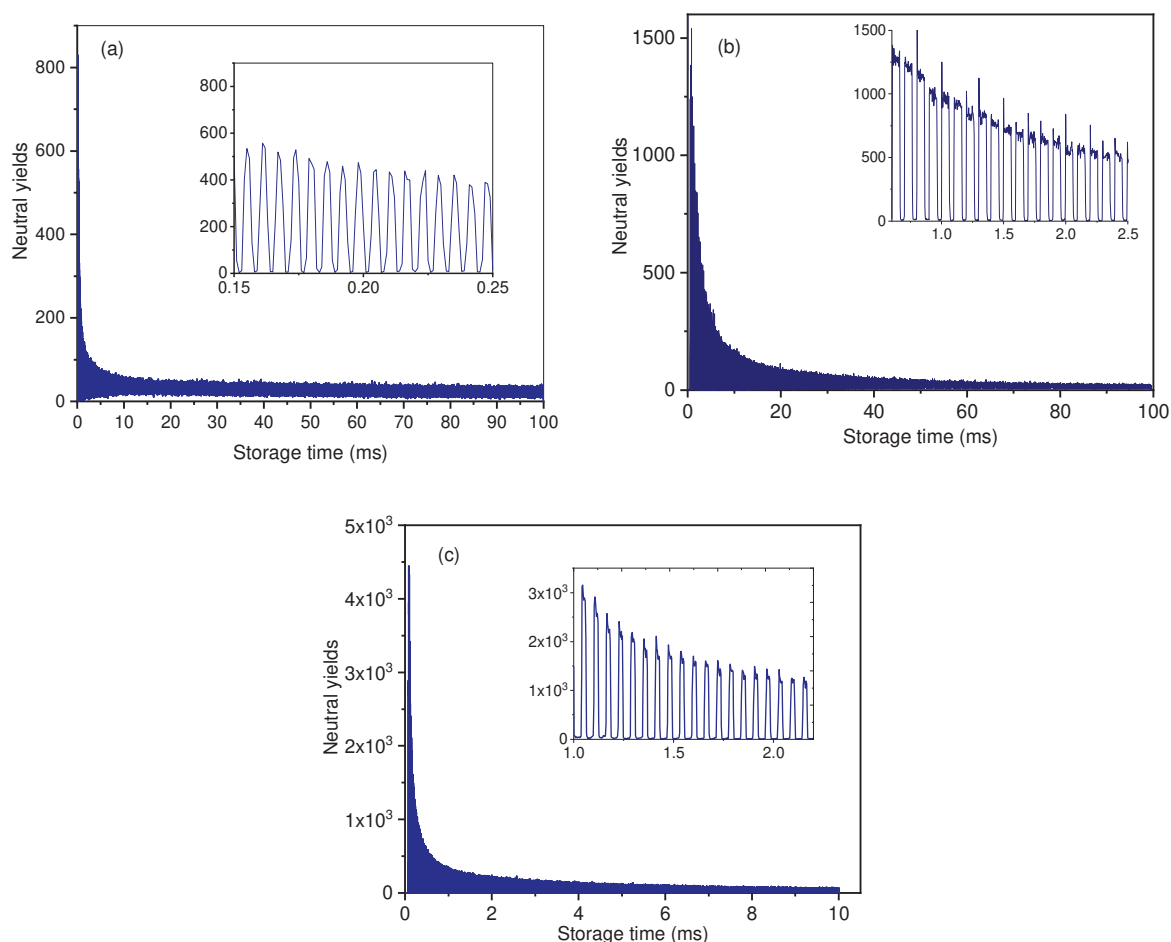


Figure 6-1: Neutral counts recorded on the PSD detector for different cationic dimers of PAH. (a) Cationic dimers of naphthalene, (b) Cationic dimers of benzene, (c) Cationic dimers of pyrene up to 10 ms.

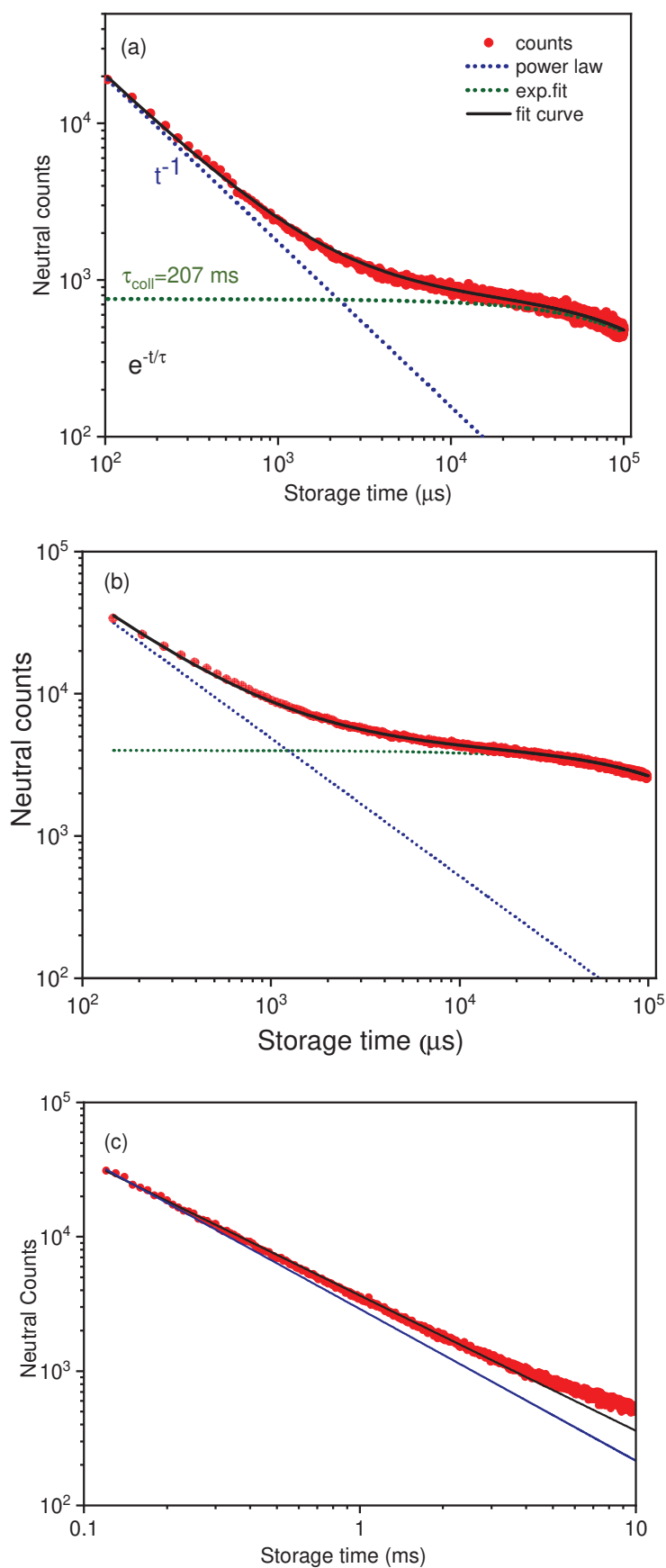


Figure 6-2 : (a) Natural decay of cationic dimers of naphthalene, (b) Natural decay of cationic dimers of benzene, (c) Natural decay of cationic dimers of pyrene. The red dot refers to neutral counts on the PDS, and the green dotted line refers to an exponential fit to neutral counts at long storage time, the blue dotted line refers to power-law fit with a decay factor of 1.

EXPERIMENTAL RESULTS FOR DIMER CATIONS

decays clearly show the presence of two contributions attributed to spontaneous dissociation and collisions with the residual gas. The total neutral fragment count, $N_t(t)$, is then given by:

$$N_t(t) = N_{sp}(t) + N_{coll}(t) \quad \text{Eq. (6-1)}$$

where the neutral counts due to spontaneous decay, $N_{sp}(t)$, is a power-law decay observed at short storage times (straight line shape in log-log scale). The contribution of the collisions with the residual gas, $N_{coll}(t)$, is an exponential decay law whose lifetime is proportional to the pressure (about 2×10^{-9} mbar) and collision cross-sections. Therefore, the expressions of $N_{sp}(t)$ and $N_{coll}(t)$ used to fit the natural decay are:

$$N_{sp}(t) = A_1 t^\alpha \quad \text{Eq. (6-2)}$$

$$N_{coll}(t) = A_2 e^{-t/\tau} \quad \text{Eq. (6-3)}$$

where A_1 and A_2 are amplitudes that depend on the total number of stored ions, α is the power-law decay factor, and τ is the lifetime due to collisions with the rest gas.

In the three cases of Figure 6-2, the power-laws found from the fits are very close to $\alpha = -1$, which is typical of a broad IED of the dimer cations produced in the ion source. The decays do not present any other shape that could be attributed to the quenching of the dissociation by a non-dissociative cooling process. We conclude that the fast radiative cooling process due to recurrent fluorescence is not an effective cooling process for these cationic dimers. This result is in contrast with the case of monomer cation of phenanthrene investigated in chapter 5 and with all other monomer cations previously studied in our lab, e.g., anthracene [76] and naphthalene [135]. On the other hand, radiative cooling remains possible by vibrational infrared cooling but on a much longer timescale than that of recurrent fluorescence. The absence of recurrence fluorescence is likely due to inadequate configurations of the electronic states and the much smaller dissociation energies of cationic dimers. For instance, in the case of naphthalene, the dissociation energy of the cationic dimer is about 0.5 eV, a much smaller value than the dissociation energy of the monomer cation, which is about 4.5 eV. This low dissociation energy does not allow any possibility for a match between high vibrationally excited states of the electronic ground state and any non-dissociative electronic excited state by which the inverse internal conversion and, therefore, the recurrent fluorescence could occur. In addition, the first excited state is a dissociative state, which leads to prompt dissociation only. Similar reasoning is likely to apply for cationic dimers of benzene and pyrene.

In the case of pyrene, we attempt to constrain the IED by simulating decays at fixed internal energies and testing different IEDs. Decays are calculated from the weighted sum of the individual decays obtained at given internal energy using a flat IED including energies up to 1.8 eV (Figure 6-3(a)) or IEDs presenting high-energy cut-offs at 1.4 eV and 1.5 eV (Figure 6-3(b)). A power-law fit to the simulated decay in the case of the flat IED provided an exponent decay factor, $\alpha = -1.13$. This value is in reasonable agreement with the measured value of decay factor $\alpha = -1.06$. Figure 6-3(a) also demonstrate that most of the ions carrying more than about 1.4 eV are dissociated during the first 1.8 ms of storage, the time at which OPO laser pulses are sent to perform the photo-dissociation spectra.

Moreover, Figure 6-3(b) displays the natural decays that would be obtained if the initial IED had a high-energy cut-off, at half-maximum of 1.4 and 1.5 eV. They would give decays that would deviate from the power-law at times shorter than about 1 ms and 0.1 ms, respectively. Since, in the experiment, the storage started about 120 μ s after the ions were extracted from the source, we conclude that the internal energy distribution had an extension up to at least 1.5 eV.

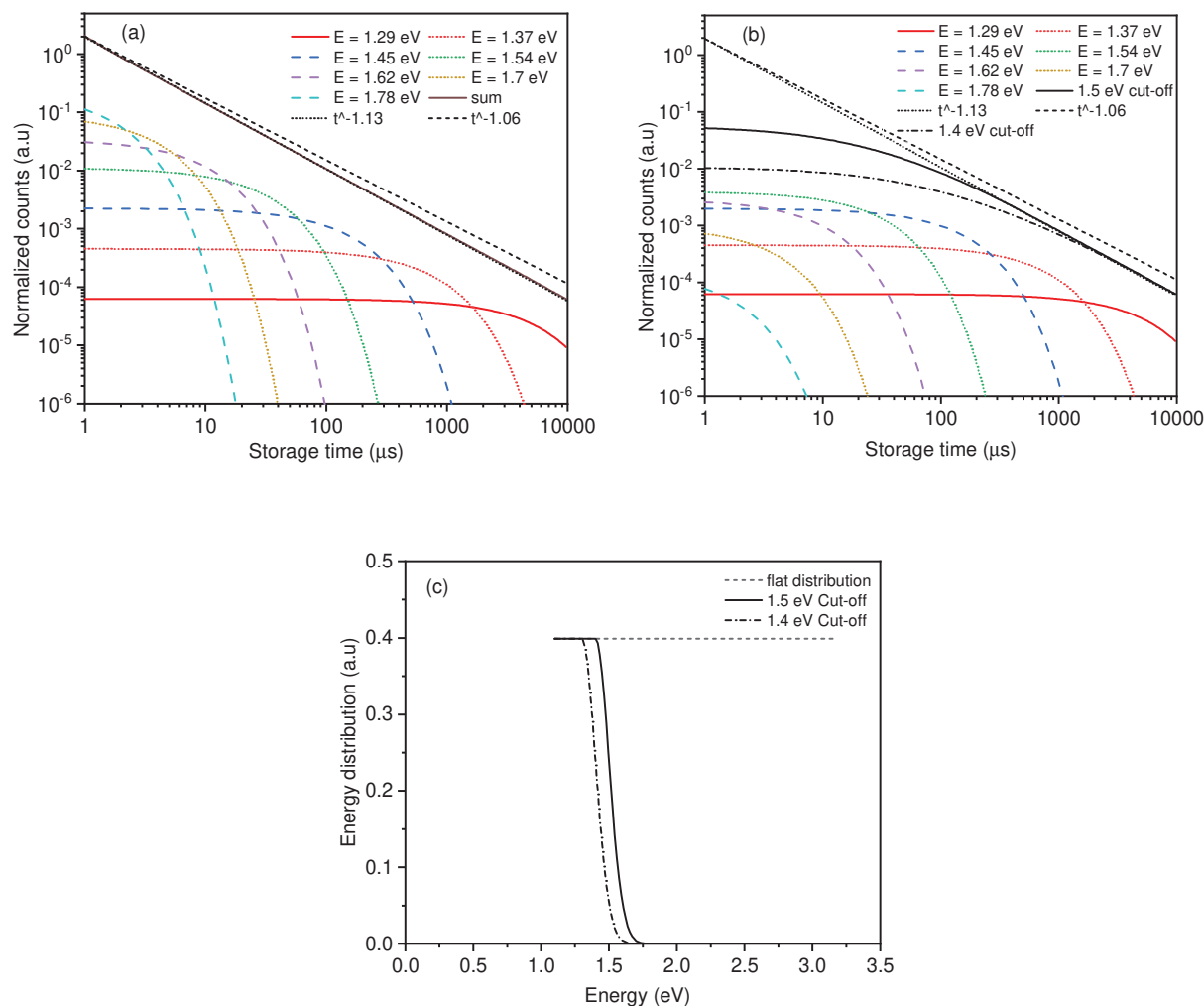


Figure 6-3: (a) and (b) Simulated natural decays calculated at given internal energies. (c) Different internal energy distributions, flat IED, IED with high energy cut-off at 1.5 eV at half maximum, and IED with high energy cut-off at 1.4 eV at half maximum.

As a conclusion about this investigation of the natural decay, we can state that the absence of quenching implies the absence of fast radiative cooling by recurrent fluorescence for the three investigated dimer cations. Although it was not shown in the previous discussions, it is noteworthy to mention that fragmented dimer cations such as cationic dimers of benzene- H presents the same behavior as intact dimer cations concerning the quenching, and consequently, the recurrent fluorescence. Simulations for pyrene dimers allowed us to state that their initial IED extends at least above 1.5 eV. Similar IED extensions are expected for the other investigated dimers.

6.2 Prompt dissociation

During the very first experiments with dimer cations, we have remarked that no delayed dissociation could be observed after visible photon absorption. To record action spectra of dimer cations, we had to send the laser in the cross-beam configuration as shown in Figure 6-4 to excite the stored ions between D_3 and D_4 and to collect on the PSD neutral fragments resulting from prompt dissociation.

A typical laser-induced time spectrum recorded with benzene dimers and excited with the second harmonics at 532 nm is displayed in Figure 6-5. The laser pulse energy was about 80 μJ/pulse, small enough to prevent multiphoton absorption. The storage time of about 2 ms before laser excitation was chosen as a compromise between a reduced contribution of the

EXPERIMENTAL RESULTS FOR DIMER CATIONS

background due to the natural decay and high repetition rate to acquire data with reasonable statistics.

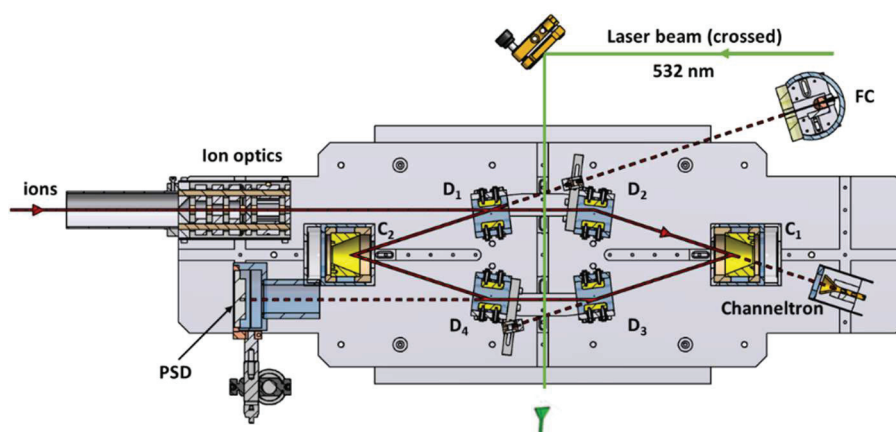


Figure 6-4: Schematic view of ion beam and second harmonic laser in a cross beam configuration.

The narrow peak at about 1.8 ms corresponds to the huge enhancements of the neutral fragment yields due to photo-dissociation. Delayed dissociation was not observed, showing that the lifetime of cationic dimers after absorption of the laser photon is much smaller than one revolution period. This is in contrast with monomer cations of phenanthrene investigated in chapter 6, for which delayed dissociation for several turns was observed as for all other PAHs monomer cations studied so far. Moreover, prompt dissociation only was observed for all laser wavelengths in the visible and near-IR regions. The prompt dissociation can be attributed to a non-statistical process for which the laser absorption in the CR (Figure 6-6(a)) or LE bands populates dissociative excited states, as schematized by the red curve in Figure 6-6(b). Similar results have been found for the other cationic dimers studied in the present work (naphthalene and benzene). Another example of such a photo-absorption time spectrum of pyrene dimer cations is displayed in Figure 6-7. It was recorded during a wavelength scan in the range of 400 to 700 nm. In both cases (benzene and pyrene), the comfortable signal-to-noise ratio of nearly 50 is remarkable.

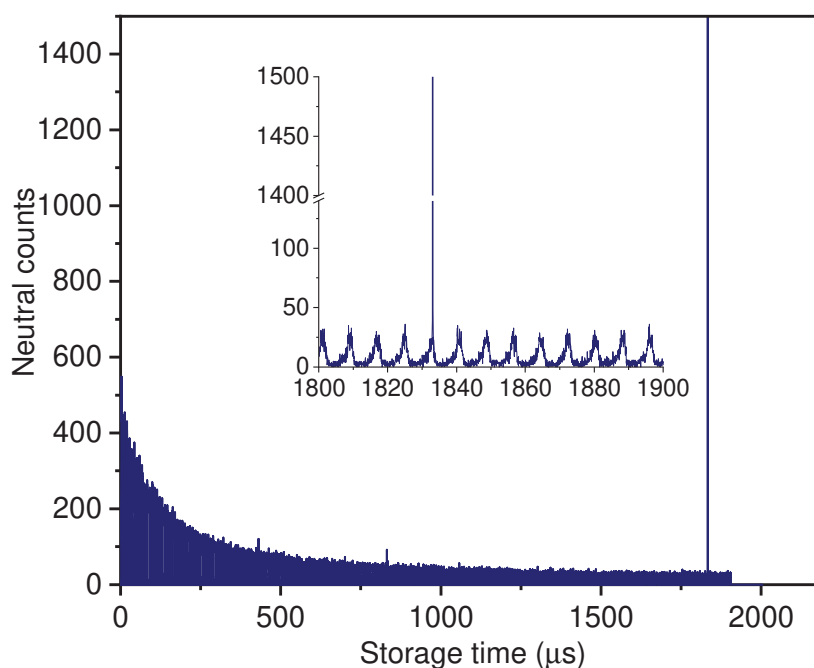


Figure 6-5: Typical time of flight spectrum of the dimers of benzene with second harmonics (532 nm) laser shot at 1.8 ms. The inset displays a zoom-in of a typical spectrum of the neutral fragments counts as a function of storage time in a time close to the laser shooting time.

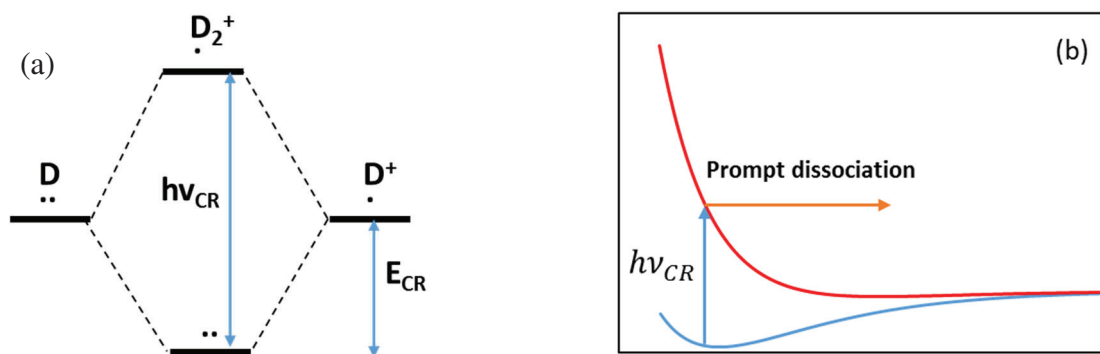


Figure 6-6 : (a) Schematic diagram of the two energy levels for dimers cations formed by charge resonance (approximation of diatomic-like molecule). (b) Schematic potential energy curves showing prompt dissociation due to the population of a dissociative state after laser absorption.

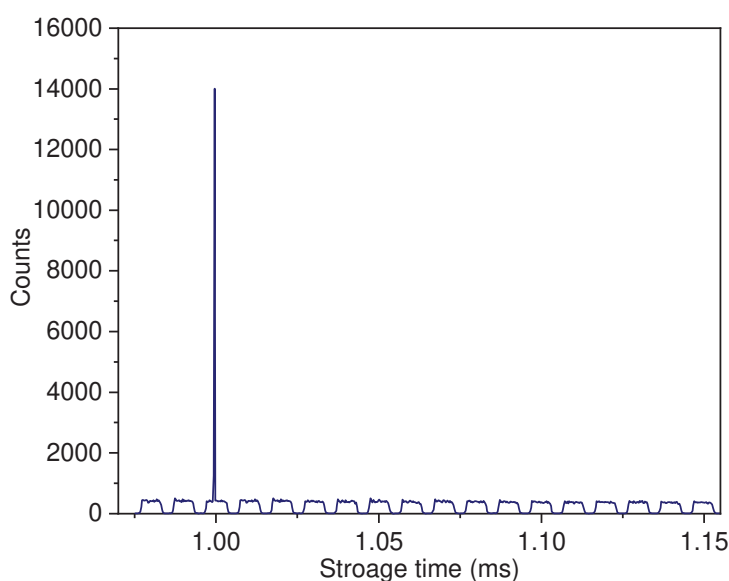


Figure 6-7: Integrated neutral fragment counts recorded at storage time of about 1 ms during wavelength scans of the laser from 400-700 nm. The sharp peak is due to laser-induced dissociation. The absence of delayed dissociation is remarkable.

6.3 Dissociation pathway - Coincidence experiments

In order to identify the dissociation products, we attempted to perform a coincidence experiment between the neutral and charged fragments. The second harmonic laser (532 nm) was shot between D_2 and C_1 to enhance the number of dissociation events, as shown in Figure 6-8. In this experiment, we used a continuous beam of pyrene dimer cations that performed a single turn in the Mini-Ring (the fast switches of the buncher and D_1 were not used and the voltage was constantly set to 0 V on the corresponding electrodes).

The neutral fragments resulting from photo-dissociation could go through the cone C_1 and could be detected by the channeltron behind it. For driving to the PSD, the cationic fragments whose kinetic energy is half of the kinetic energy of its parent ion, the voltages of C_1 and D_3 have been set to half of their nominal values and the voltage of D_4 has been set to 0 V. The electronic signal from the channeltron has been used as a start of a time-to-digital converter and the PSD as a stop. With these settings, it has been confirmed, as expected, that cationic dimers dissociate into two fragments of equal masses. By scanning the voltages of C_1 and D_3 , from zero V to their nominal value (2 kV and 16 kV, respectively), no other dissociation scheme could be observed for pyrene dimer cations. It is expected but not verified in the present work

EXPERIMENTAL RESULTS FOR DIMER CATIONS

that naphthalene and benzene dimer cations have the same fragmentation scheme, i.e., splitting in two fragments of equal mass.

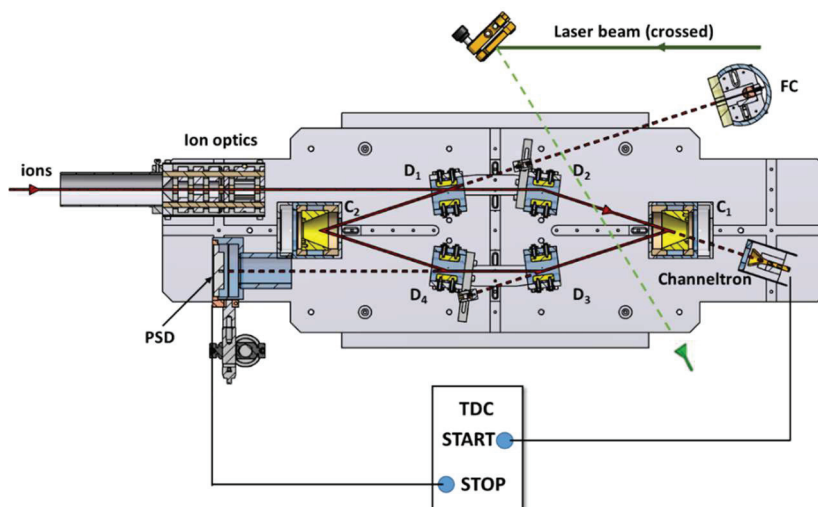


Figure 6-8: Scheme of the coincidence experiment in which the second harmonic laser (532 nm) was shot between D_2 and C_1 to enhance the number of dissociation events.

6.4 Experimental photodissociation spectra of cationic dimers

6.4.1 Method

In order to record the photo-dissociation spectrum of the cationic dimers in the Mini-Ring, the laser wavelength has been scanned in the range of 400-2000 nm. To reduce the contribution of background counts resulting from the natural decay and collisions with the rest gas, we used a proper time gate to select the laser-induced neutral counts, as illustrated in Figure 6-9.

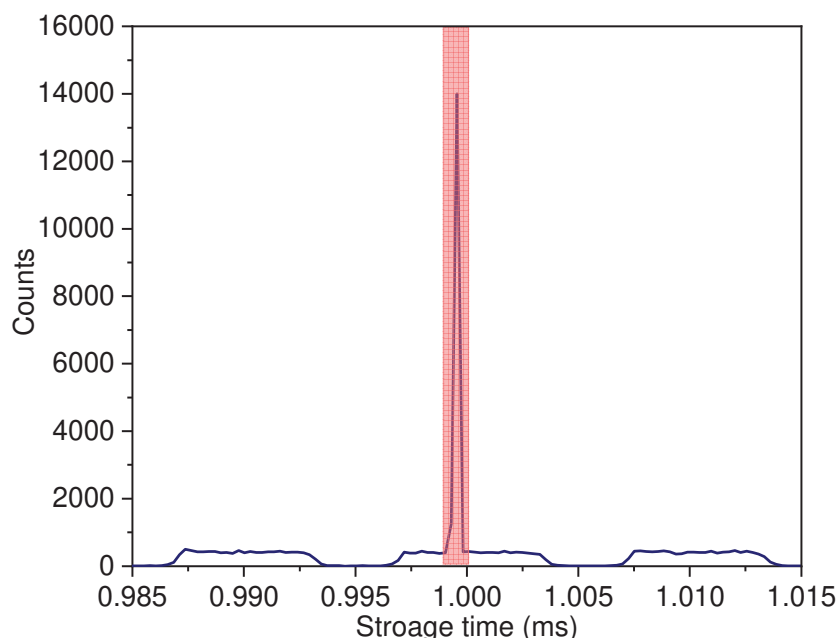


Figure 6-9: The pink area symbolizes the time gate used to properly select the laser-induced neutral counts.

The accumulated count is the sum of the counts of the neutral fragments produced by the laser pulse, N_L , and the background counts, N_b , inside the selected time window. The background counts are measured in the absence of the laser pulse. Thereby, the signal is obtained by subtracting the background counts from the counts of the neutral fragments, N_{raw} , i.e., $N_L = N_{raw} - N_b$. As the counts due to the natural decay and the collisions with the residual gas, N_N , are expected to be linearly dependent on the number of ions in the stored ion bunch. It

EXPERIMENTAL RESULTS FOR DIMER CATIONS

can be used to correct for slight fluctuations of the ion beam intensity. For this correction, the total counts per second, $N_T = N_N + N_L$, is recorded to normalize neutral fragment yield spectra. Moreover, as discussed in chapter 4, the energy per pulse, E_{pp} , varies as a function of the wavelength. To obtain a spectrum that is proportional to the photo-dissociation cross-section, we normalize by the number of photons pulse, which is proportional to E_{pp}/λ (where λ is the laser wavelength). To summarize, N_{raw} , N_T , and E_{pp} are recorded while varying λ ; therefore, the photo-dissociation cross-section, $\sigma_{PD}(\lambda)$ is proportional to the corrected counts, N_{corr} , given by:

$$\sigma_{PD}(\lambda) \propto N_{corr} = \frac{N_{raw} - N_b}{E_{pp} \times (N_T - (N_{raw} - N_b))} \times \lambda \quad \text{Eq. (6-4)}$$

6.4.2 Cationic dimers of Naphthalene

The Photo-dissociation spectra of cationic dimers of naphthalene were previously performed in the solution and the gas phase. Badger and Brocklehurst calculated the energy levels of the cationic dimers of benzene and cationic dimers of naphthalene [262]. Inokuchi et al. [10] obtained the photo-dissociation spectrum of cationic dimers of naphthalene by laser-induced plasma in the range of wavelength 400-1400 nm. Two bands were obtained in this range. The lowest energy band at 1180 nm (1.05 eV) is attributed to the charge resonance (CR) effect. It corresponds to the electronic transition between the ground state and the first excited state of the dimer. In a simplified scheme, assimilating the dimer to a diatomic molecule, these authors stated that the first electronic states could be constructed from the monomer ground states as following (see Figure 6-10):

$$\psi_{\pm} = \frac{1}{\sqrt{2}} (\psi_1^+ \psi_2 \pm \psi_1 \psi_2^+) \quad \text{Eq. (6-5)}$$

Where ψ^+ and ψ are the electronic wavefunctions of charged and neutral monomers [10]. The dissociation energy (D_e) resulting from the separation into a neutral monomer and a charged monomer was estimated to be half of the CR band energy ($D_e = 0.53$ eV). The second band is a local excitation band (LE) at 580 nm (2.14 eV) resulting from the electronic transition between the ground state and second excited state that is formed from at the second excited state of the monomers (the first one leads to a forbidden transition).

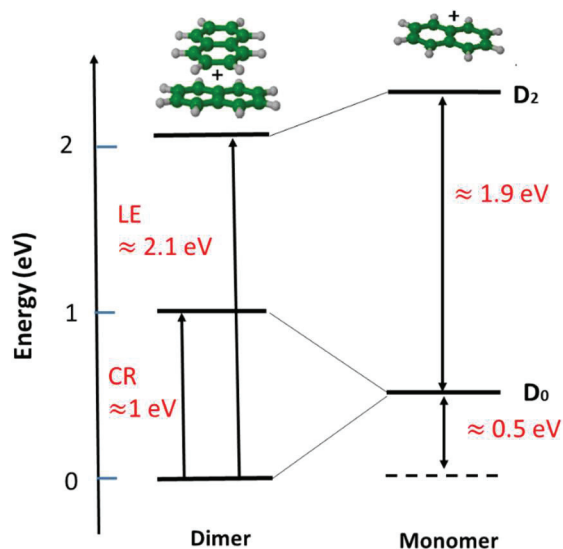


Figure 6-10: Schematic diagram of the electronic energy levels of cationic monomer and dimer of naphthalene, showing CR and LE lines and the estimation of the dissociation energy.

EXPERIMENTAL RESULTS FOR DIMER CATIONS

Other studies also determined the dissociation energy of the cationic dimers of naphthalene such as thermodynamic coupled to mass spectrometry ($D_e = 0.77 \text{ eV}$ [263]), two-color two-photon measurements of the ionization potentials (IP) and appearance energies (AP) ($D_e = 0.68 \text{ eV}$ [264]).

Theoretical investigations showed that there are several possible structure configurations for the cationic dimer of naphthalene, such as stacked structures and T-shape structures [265] (Figure 6-13). Theoretical studies [204,265,266] have shown that the favored lowest energy structures for the dimer cations of naphthalene are sandwich structures (stacked SS and SE).

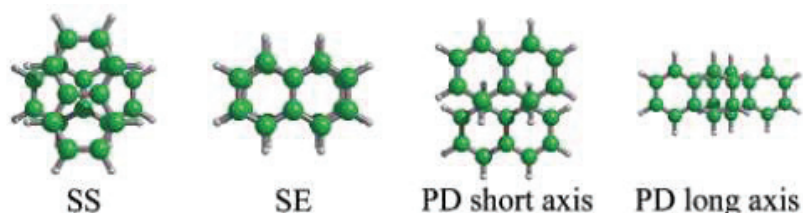


Figure 6-11: Some of the possible structures of the cationic dimers of naphthalene, including the favored low energy structures, i.e., the sandwich structures.

In the present work, the photo-dissociation spectrum presented in Figure 6-12 also shows two broad bands: the CR band at about 1 eV and the LE band at about 2.2 eV. The dissociation energy estimated as half of the CR transition energy, i.e., would be about 0.5 eV, in good agreement with the value obtained by Inokuchi et al. [10]. Their spectrum is also shown in Figure 6-12 for easy comparison with the present work. The CR band obtained in our case is much broader than in the experiment of Inokuchi et al. [10]. There is also a slight shift towards lower energies of about -0.093 eV of the center position of the CR band compared Inokuchi's spectrum. This is most probably due to a much broader IED given in the ion source, hence much higher internal energies of the dimer cations stored in the Mini-Ring. Indeed, the plasma of the ECR ion source is at a much higher temperature than the cold gas jet source employed by Inokuchi et al. [10]. Due to the absence of fast radiative cooling for such cationic dimers, the storage time of 2 ms is not sufficient to obtain a significant change in the IED. We have verified that the width of CR and LE bands was not significantly changed for longer storage time up to 20 ms in the Mini-Ring. However, as will be discussed below, we could observe significant changes when using 30 s storage time in the cryogenic DESIREE ring. Back to the Mini-Ring, it is remarkable that the LE band is much narrower than the CR band. The LE band in Mini-Ring is almost of the same width as in Inokuchi's spectrum.

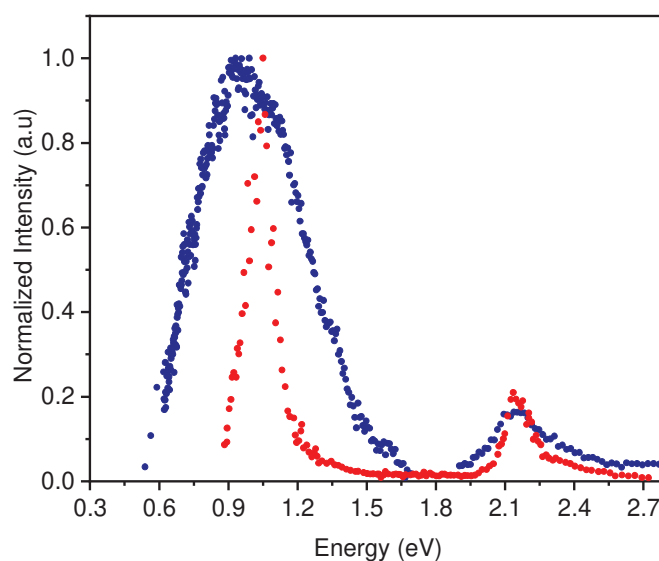


Figure 6-12: Experimental photo-dissociation spectrum of naphthalene dimer cations. Blue circles: this work; red circles: Inokuchi et al. [10].

EXPERIMENTAL RESULTS FOR DIMER CATIONS

Table 6-1: Energies of CR and LE transitions of the cationic dimers of naphthalene.

	CR (eV)	LE (eV)
Gas phase [10]	1.05	2.17
Liquid phase [267]	1.21	
Liquid phase [268]	1.24	
This work	1±0.2	2.15

The dissociation energy of cationic dimers of naphthalene in the gas phase, tentatively estimated to be half of the CR band, about 0.5 eV. This value is close to previous experimental values obtained by different methods (Table 6-2). Theoretical approaches give a double value compared to our work (Table 6-2). The systematic difference between theoretical and experimental dissociation energy cannot be attributed to experimental uncertainties or too strong approximations in the calculations. This discrepancy might, tentatively, be attributed to temperature effects with a possible isomerization. Interestingly, the structural configurations of cationic dimers of Naphthalene are found to be sensitive to the internal energy so that possible isomerization may occur even at low internal energy.

Table 6-2: Experimental and theoretical dissociation energy for the ground state of the cationic dimers of naphthalene.

Experimental method	D _e (eV)	Theoretical method	D _e (eV)
Absorption Spectroscopy (solution) [269]	0.59	DFTB-CI [204]	0.9
IP and AP (gas phase) [270]	0.68	CAS(1/1)PT2/B1 [204]	1.17
Thermochemistry (gas phase) [263]	0.77	Valence-band model potential [265]	0.86
Photo-dissociation (gas phase) this work	0.5	TPSS0/def2-qzvpp/D3BJ this work	1.18

6.4.3 Cationic dimers of benzene

The same procedure is carried out to record the photo-dissociation spectrum of the cationic dimers of benzene, which has a role as a model for studying π - π interactions [271] and is also used as a prototype for studying the processes of ionization-induction in noncovalent aromatic complexes [272]. Examples of possible structural configurations are displayed in Figure 6-13. The configurations of the lowest energies have a parallel (sandwich) shape or a T-shape.

As for the naphthalene dimer cations, the photo-dissociation spectrum recorded for benzene dimer cations, displayed in Figure 6-14, also presents two broad peaks. In the present case, the CR band located in the near-infrared region is centered at about 1.4 eV, and the LE band is centered at about 2.8 eV, in the visible range. In Figure 6-14, we can compare our spectrum with the one previously recorded by Ohashi et al. [273–276]. They recorded the photo-dissociation spectra of dimers of benzene produced from photo-ionization of benzene clusters which undergo successive neutral monomer evaporations. These evaporations lead to $(C_6H_6)_2^+$ cations of relatively low internal energy, which, however, was not determined in their experiment. They observed two CR bands at 920 nm and 1160 nm (1.35 and 1.07 eV) in the near-IR region and, two LE bands ($\pi\pi$) at 440 nm (2.8 eV) and LE($\pi\sigma$) at 580 nm (2.1 eV) in the visible range. The two CR bands were attributed to two different displaced parallel

EXPERIMENTAL RESULTS FOR DIMER CATIONS

structures (sandwich configurations) that slightly shift the dimer cation energy levels. They exclude the possibility of the T-shape configuration that would lead to very different energy levels and would not agree with the observation of the intense CR band. Figure 6-15 illustrates a simplified energy diagram in the case of the sandwich shape and resumes the corresponding transitions on the energy level diagram.

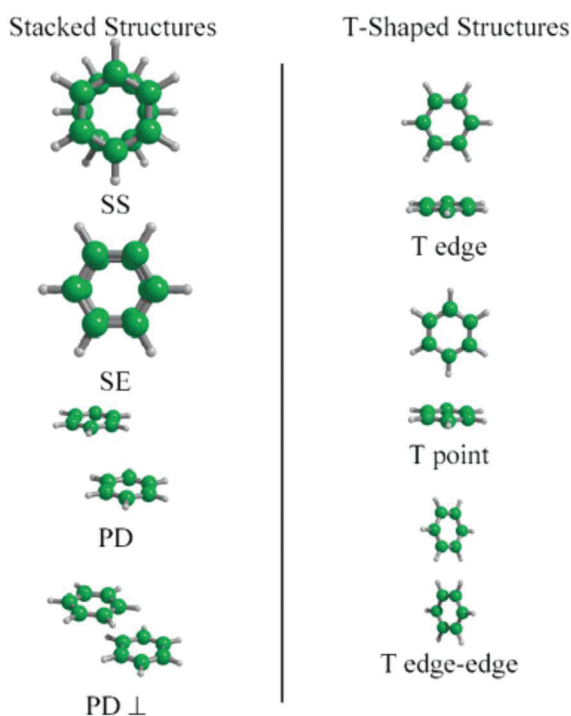


Figure 6-13: Some structural configurations of the cationic dimers of benzene [265].

In the spectrum recorded with the Mini-Ring, the high internal energy of the stored benzene dimer cations prevented us from separating the two CR bands because of a too strong broadening. Globally, when comparing our spectrum with Ohashi's one, the centers of the bands agree rather well, except for the small LE line at 2.1 eV, where we observe a deep in our spectrum. Nonetheless, the relative intensities of the LE and CR line are rather different in the

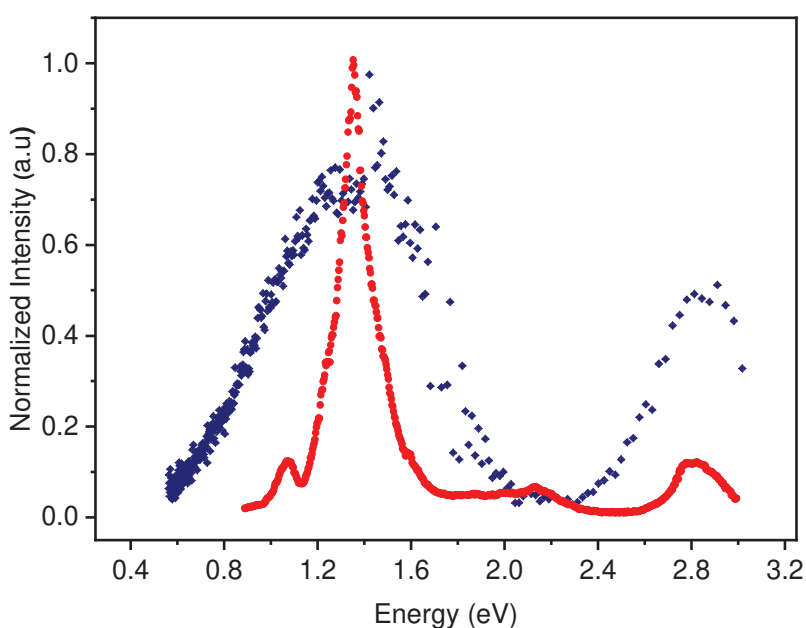


Figure 6-14: Experimental photo-dissociation spectrum of benzene dimer cations. Blue squares: present work; red circles digitized from Ohashi et al. [276].

EXPERIMENTAL RESULTS FOR DIMER CATIONS

two spectra. Whether these discrepancies could be attributed to the high internal energy would need more experimental investigations, especially in a cryogenic environment, to record spectra as a function of the temperature.

In the condensed phase, γ irradiated liquid of benzene has also led to the observation of the two bands at 2.64 (LE) and 1.36 eV [249], while in irradiated paracyclophanes the CR band was assigned to 1.36 eV [277]. CR and LE values for benzene dimer are summarized in Table 6-3.

Table 6-3: Experimental Energies of CR and LE transitions of cationic dimers of benzene

	CR (eV)	LE (eV)
Gas phase [276]	1.35	2.82
Liquid phase [249]	1.36	2.62
This work	1.4	2.85

In ref. [276], Ohashi et al. argued that the dissociation energy, D_e , can be given by half of the CR energy ΔE_{CR} in the case of a negligible overlap integral between the two CR wavefunctions, i.e., $S = \langle \psi_1^+ \psi_2 | \psi_1 \psi_2^+ \rangle \ll 1$:

$$D_e = \frac{\Delta E_{CR}}{2} = |\langle \psi_1^+ \psi_2 | H_{12} | \psi_1 \psi_2^+ \rangle| \quad \text{Eq. (6-6)}$$

where H_{12} is the hamiltonian of CR intermolecular interaction and ψ_i and ψ_i^+ ($i = 1, 2$) are the electronic wavefunctions of C_6H_6 and $C_6H_6^+$. The dissociation energy is determined as half of the center energy of the CR band gives, in our case, $D_e = 0.7$ eV (Figure 6-15). The dissociation energy of benzene dimer was calculated to be $D_e = 0.65$ eV by Miyoshi et al. [278] using ab initio methods (CASSCF and MRSDCI). Different experimental methods have been used to determine the dissociation energy of benzene dimer cations. Meot-Ner et al. [263] measured the association ($C_6H_6^+ + C_6H_6 \rightleftharpoons (C_6H_6)_2^+$) equilibrium rate constant as a function of temperature to build Van't Hoff plots. They found $D_e = 0.74$ eV. Other techniques like Two-color two-photon measurements of the ionization potentials (IP) and appearance energies have led to very similar values: $D_e = 0.66$ eV [279] and $D_e = 0.665$ eV [280], respectively. Hiraoka et al., using an electron beam high-pressure mass spectrometer, found $D_e = 0.89$ eV [281]. Table 6-4 resumes theoretical and experimental values of the dissociation energy for the ground state of benzene dimer.

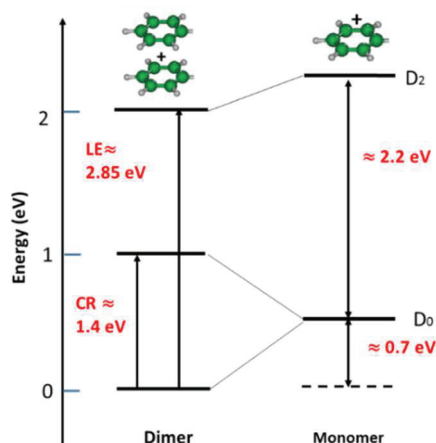


Figure 6-15: Schematic diagram of the electronic energy levels of cationic monomers and dimers of benzene.

EXPERIMENTAL RESULTS FOR DIMER CATIONS

Table 6-4: Experimental and theoretical dissociation energy for the ground state of the cationic dimers of benzene.

Dimer of Benzene			
Experimental method	D_e (eV)	Theoretical method	D_e (eV)
IP and AP (gas phase) [279,280]	0.66 - 0.665	DFTB-CI [204]	0.99
Thermochemistry (gas phase) [263]	0.73	CAS (1/1) PTT2/B1 [204]	0.98
Clustering reaction (gas phase) [282]	0.89	Valence-band model potential [265]	1.13
Photo-dissociation (gas phase) this work	0.7	Ab initio [278]	0.65

6.4.4 Cationic dimers of pyrene

The same experiments, i.e., photo-dissociation spectrum, have been performed for the cationic dimers of pyrene (Figure 6-16(a)). To our knowledge, this is the first time the photo-dissociation has been recorded for dimers of pyrene. Again, two broad bands have been recorded, one centered at about 2.3 eV (550 nm) and the other centered at about 0.8 eV (1560 nm). As for benzene and naphthalene dimer cations, the LE band is found much narrower than the CR band. Following similar reasoning as for the other two cases, we may tentatively attribute the bands to the LE and CR bands, respectively. Therefore, this spectrum would lead to the energy level diagram of Figure 6-16(b). The dissociation energy that would be deduced from half of the CR transition energy would be of $D_e \approx 0.4$ eV. However, as will be discussed in section 6.6 dedicated to results of DFT modeling, the situation is much more complex than this crude simple view when more states of the monomers are considered to build the dimer states and when all the degrees of freedom of the relative movements between the two monomers are included.

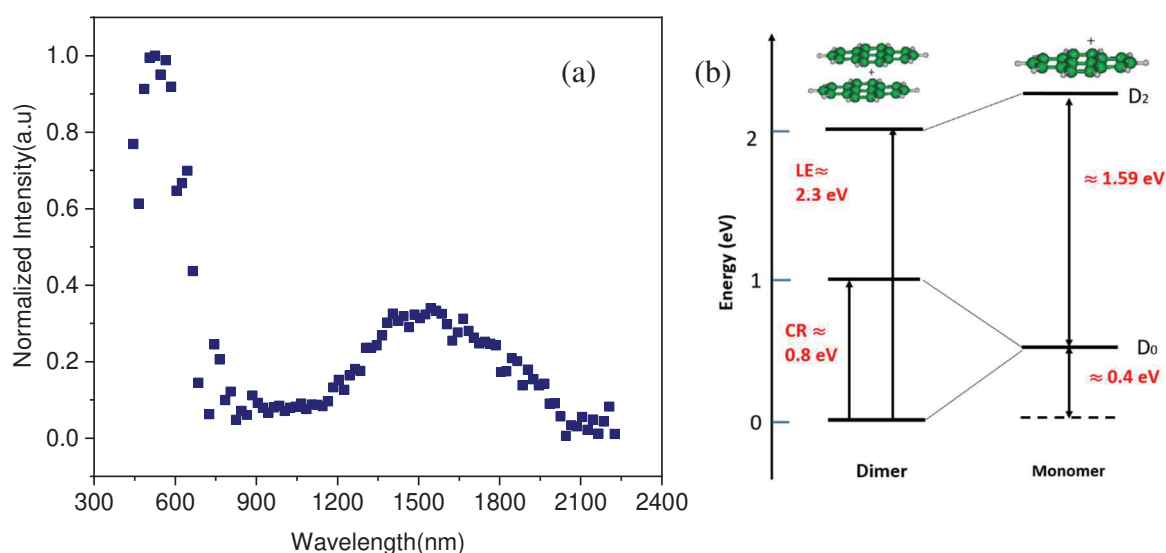


Figure 6-16: (a) Photodissociation spectrum of the cationic dimers of pyrene where intensity recorded as a function of the wavelength. Ion beam fluctuations and background have been subtracted. (b) An approximate schematic electronic energy level of monomer and cationic dimers of pyrene.

6.5 Semi-empirical Modelling

Dontot et al. [204] have studied theoretically cationic dimers of PAHs and calculated the potential energy curves as a function of the distance of the two monomers in the separation coordinate (i.e., in reduced dimensions). They have also shown that the PECs are expected to change significantly with the twisting angle between two monomers. We remarked that the PECs of ref. [204] could be rather well fitted by Morse potentials (see chapter 2). Therefore, in the following sections, we will follow our paper in ref. [283], where we tentatively proposed to use effective Morse PECs to model our recorded experimental photo-dissociation spectra. These effective PECs are expected to average the effects of the set of real isomer-dependent potential energy hypersurfaces.

6.5.1 Cationic dimers of naphthalene

In order to simulate experimental photodissociation spectra, the following procedure has been made. Starting parameters have been taken from the fitted Morse potential with ab initio calculations of Dontot et al. [204]. The PECs of the lowest electronic states of the dimer of naphthalene in the sandwich configuration as a function of the separation between the two monomers of ab initio calculations could be nicely fitted by Morse potentials. The results of these fits for the lowest six electronic states are displayed in Figure 6-17, and the corresponding parameters of the Morse PECs are given in table Table 6-5.

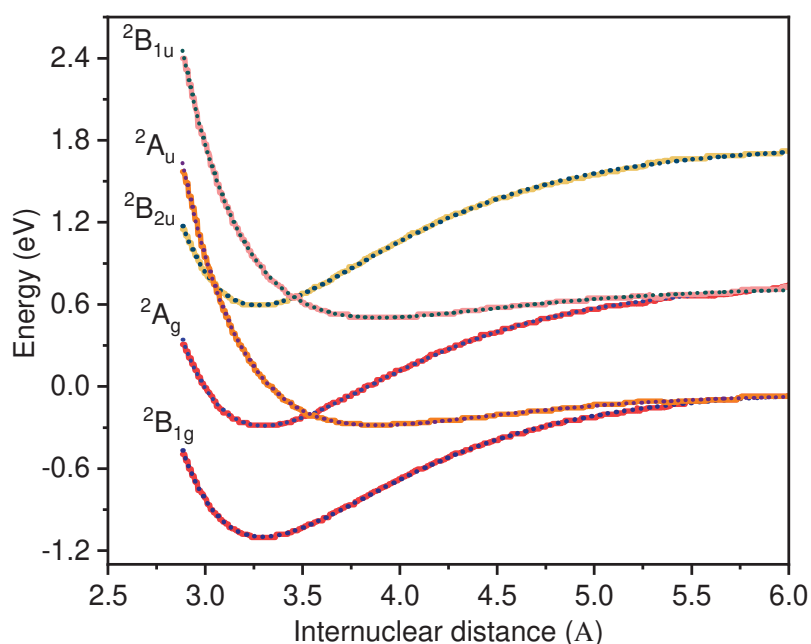


Figure 6-17: Colored plain thick lines: theoretical PECs for the lowest six electronic states digitized of dimer naphthalene from ref. [204]. Blue dots: fits of theoretical PECs with Morse potentials.

The Schrödinger equation with Morse potentials can be solved analytically and, therefore, the vibrational energy levels can be calculated. Consequently, the Frank-Condon factors for the absorption transition to the dissociative excited state 2A_u can be estimated by the overlap of the wavefunctions obtained with parametrized potential energy curves (see chapter 2). Figure 6-18 displays the absorption transition from the ground state ${}^2B_{1g}$ to the first excited state 2A_u and the second excited state ${}^2B_{1u}$. The shape of the vibrational wavefunction for the $v = 0$ and $v = 5$ vibrational levels of the electronic ground state ${}^2B_{1g}$, the shape of the wavefunction in the continuum of the first excited state 2A_g are shown as well. The red and green curves on the left side represent the simulated absorption function for CR and LE transitions from the $v=0$ of the ground state (reflection spectrum). The relative amplitudes of both bands are arbitrary.

EXPERIMENTAL RESULTS FOR DIMER CATIONS

Table 6-5: Parameters of the Morse potential used to simulate Dontot's work of cationic dimers naphthalene: dissociation energy D_e , equilibrium distance r_e , and minimum potential energy V_e .

	$^2B_{1g}$	2A_u	$^2B_{1u}$	2A_g	$^2B_{2u}$
D_e (eV)	1.07	0.21	0.22	1.04	1.17
r_e (Å)	3.29	3.89	3.89	3.298	3.27
V_e (eV)	-1.09	-0.09	0.5	0.286	0.59
a (Å)	1.38	1.33	1.35	1.37	1.36

Boltzmann distributions of internal energy are used to calculate the contribution of the five first vibrational levels from $v = 0$ to $v = 5$ of CR and LE bands. The contribution of higher vibration levels is neglected. Such states may mostly have a contribution to the sides of the bands and may somewhat improve the agreement between theoretical and experimental bandwidths. Figure 6-19 displays the results of the modeling together with the experimental photo-dissociation spectra in 'hot' (this work, Figure 6-19(a)) and 'cold' (Inokuchi et al. [10], Figure 6-19(b)). By using the PECs of Figure 6-17 resulting from the direct fit to the theoretical PECs of ref. [204], we obtained simulated CR bands that do not fit with the experimental results, as clearly evidenced by the dotted brown curves of Figure 6-19.

The parameters of the Morse potentials have then been adjusted to minimize the difference between simulated and experimental results. Table 6-6 gives the resulting parameters of the Morse potentials and the corresponding PECs are displayed in Figure 6-18. A rather good overall agreement has been found between the model and experimental CR lines. A small difference of only 0.18 eV has been found between the centers of the model and experimental CR bands.

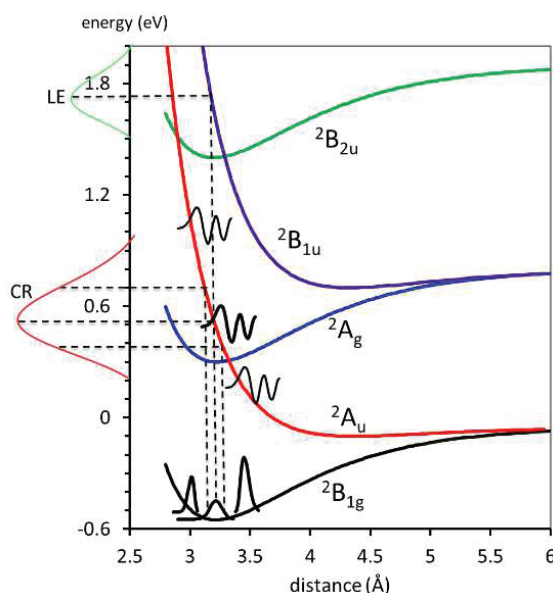


Figure 6-18: Morse Potential curves used in the calculation to simulate the experimental photodissociation spectra. The simulated absorption function for the CR and LE transitions is displayed on the left side of the vertical scale.

Besides, in collaboration with A.-R. Allouche, the energies of all the vibrational modes of the cationic dimers of naphthalene have been calculated using TPSS0 [284] (Tao, Perdew, Staroverov, and Scuseria (TPSS) [285] meta hybrid with 25% of exact exchange) density functional theory (DFT) functional with the def2-qzvpp basis set, including the dispersion via the D3 version of Grimme's approach with Becke-Johnson damping [286]. Based on these

EXPERIMENTAL RESULTS FOR DIMER CATIONS

methods, the vibration energies of the six lowest vibrational modes, which are intermolecular motions between the two monomers, have been calculated to be between 9.7 and 13.2 meV. These values are in the same order of magnitude as the one calculated from the Morse potential used in this work with the parameters for the ground state as shown in Table 6-6.

Table 6-6: Optimized parameters of the Morse potential used in the model of cationic dimers naphthalene: dissociation energy D_e , equilibrium distance r_e , and minimum potential energy V_e .

	${}^2B_{1g}$	2A_u	${}^2B_{1u}$	2A_g	${}^2B_{2u}$
D_e (eV)	0.5	0.05	0.1	0.5	0.5
r_e (Å)	3.21	4.37	4.33	3.22	3.196
V_e (eV)	-0.55	-0.1	0.7	0.3	1.4
a (Å)	1.36	1.28	1.24	1.33	1.30

The discrepancy between the modeled photo-dissociation of CR bands and the theoretical one using PECs from Dontot et al. [204] may question the validity of using one-dimensional PECs. Indeed, Dontot et al. emphasized the effect of the twisting angle. Therefore, the relative motion between the two monomers may be rather complex. It should involve other motions that are not considered in the one coordinate potentials during the photo-dissociation process. Hence, estimating the effect of several intramolecular vibration motions would need the full calculation of the multi-dimensional potential energy surfaces (PES). In the present interpretation, we tentatively consider that using the ‘effective’ Morse potentials resulting from the adjusted parameters of Table 6-6 averages all the temperature and possible isomerization effects on the relative motion of the monomers, such as the twisting rotation.

For the lowest vibrational level $v = 0$ of the ground state ${}^2B_{1g}$, the Morse potential parameters of Table 6-6 lead to a good agreement between the model CR and LE bands and the experimental photo-dissociation spectrum recorded by Inokuchi et al. [10] in cold conditions (Figure 6-19(b)). The center and width of the modeled and experimental bands are in very good agreement. Therefore, this is supporting the validity of the adjusted PECs of the ground state and excited states.

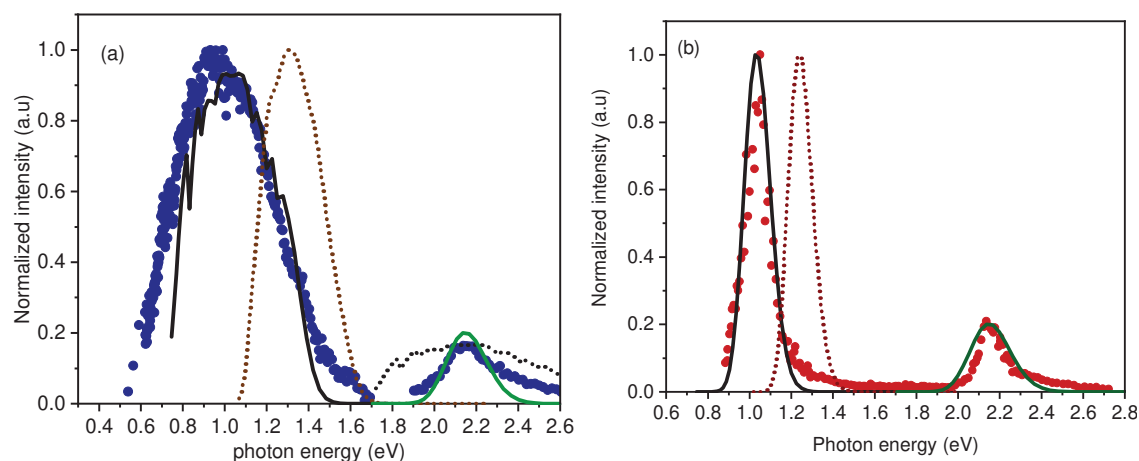


Figure 6-19: (a) Experimental photo-dissociation spectrum recorded with Mini-Ring (blue dots) is recalled here for easy comparison with model curves. Simulated CR (black plain curve) and LE (black dotted line) bands dotted black curve in the hot condition (400 K), including the contributions of the vibrational states from $v = 0$ to $v = 4$ calculated with effective Morse potential. The green curve is the simulated LE line using $v = 0$ only. (b) Experimental photodissociation spectrum in cold condition obtained by Inokuchi et al. (red dots), simulated photodissociation spectral for the CR line as black curve and the LE line as green curve in the cold condition using the $v = 0$ vibrational state only. The dotted brown curves in (a) and (b) are simulated CR lines from the calculation of Dontot et al. [204].

EXPERIMENTAL RESULTS FOR DIMER CATIONS

For the higher vibrational levels, the maximum amplitude of the wavefunction is nearly close to the edge of the potential well. Thus, the probability of presence is maximum at these distances, as shown in Figure 6-18. Therefore, the higher vibrational levels $v > 0$ needed to model the CR band in hot conditions provides more constraints to the shapes of the PECs of the ground state and excited electronic states than the cold spectrum, which, however, fixes more precisely the energy difference between the two states.

Using these effective PECs, we could obtain a good agreement between the modeled and the experimental CR bands of this work at a Boltzmann temperature of about 400 K (Figure 6-19 (a)). The position of the modeled CR band presents a small shift towards lower energy comparing to that of the low-temperature spectrum. This shift is estimated to be about -0.02 eV and is found a bit smaller than the experimental shift of -0.18 eV.

The modeled LE band is found about twice as broad as the experimental LE band measured with Mini-Ring in hot conditions, which, surprisingly, was found only very slightly broader than the LE band in cold conditions in the spectrum of Inokuchi et al. [10]. The diatomic model with averaged Morse potential for one coordinate might also be too simplistic to describe the form of the LE peak absorption correctly. Nevertheless, an unexpected small broadening of the LE band in hot conditions might be interpreted in two possible ways:

- (i) For LE, one of the monomers is expected to absorb the photon, which implies involving the intramolecular C-H and C-C vibrations of this monomer only. Since these intramolecular vibration level spacing have been calculated at much higher energy than intermolecular vibrations, the population of the higher vibrational levels $v > 1$ of the intramolecular vibration is expected to be weak at the temperature of 400 K deduced from the CR broadening.
- (ii) The dissociative state ${}^2B_{1u}$ might not be populated directly by the absorption of a photon. The ${}^2B_{2u}$ bound state could be populated by the internal conversion process. This leads to statistical dissociation giving a thinner peak than the modeled LE band in the figure. The high oscillator strength frequency of transitions at 2.1 and 2.2 eV computed by Dontot et al. [204] may support this interpretation.

6.5.2 Cationic dimers of benzene

We have followed the same procedures for modeling the dimer of benzene. The modeled photo-dissociation spectra are compared with experiments in hot conditions (the Mini-Ring, Figure 6-20(a)) and cold conditions (Ohashi et al. [276], Figure 6-20(b)). As for naphthalene, the PECs of Dontot et al. [204] lead to rather strong discrepancies between the model and experimental photodissociation spectra. Therefore, we used parametrized 'effective' Morse potentials to get a better model-experiment agreement. The corresponding Morse parameters are given in Table 6-7, and Morse PECs for the six lowest electronic states are shown in Figure 6-21. The Boltzmann temperature used in the model for the hot conditions of Figure 6-20(a) is 400 K, as for the naphthalene dimer case.

Concerning the LE band, we remark that at the temperature of 400 K, the low energy edge of the band is rather well reproduced, in contrast with the case of the naphthalene dimer cations. A possible reason would be that the monomers are vibrationally excited in the benzene case. More theoretical investigations would be needed for the benzene dimer cations.

EXPERIMENTAL RESULTS FOR DIMER CATIONS

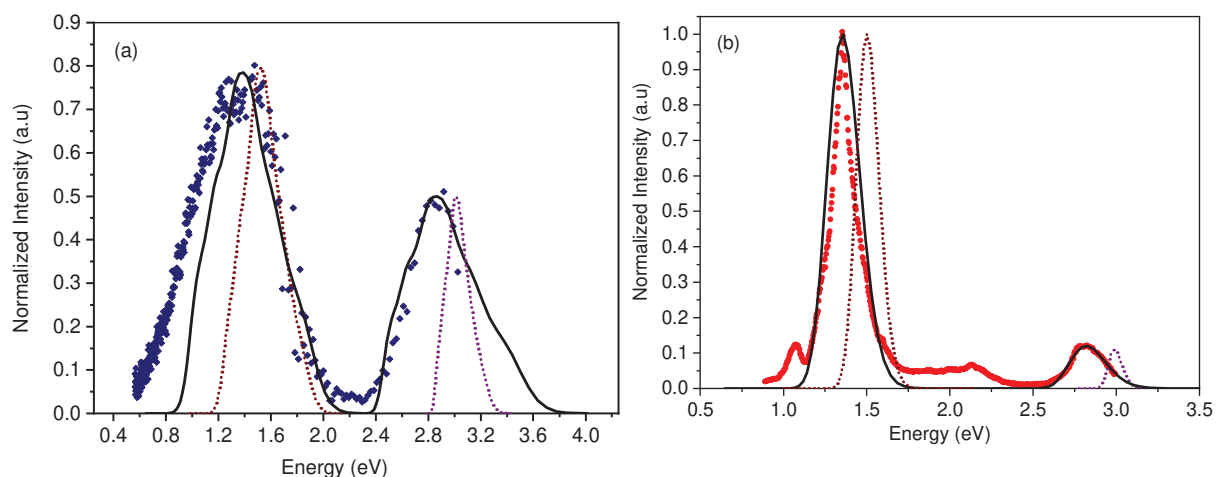


Figure 6-20 : (a) Blue square curve represent experimental photodissociation spectrum obtained in hot condition for this work, the black line represents modeled photodissociation for CR and LE bands calculated with effective Morse potential energy curves, brown and pink dotted curves represent theoretical photodissociation spectrum for CR and LE bands respectively calculated from potential energy curves of Dontot et al. [204]. (b) Red circle curve represent experimental photodissociation spectrum obtained in cold condition for the previous experiment of Ohashi et al. [276], black line represent modeled photodissociation for CR and LE bands calculated with effective Morse potential energy curves, brown and pink dotted curves represent theoretical photodissociation spectrum for CR and LE bands respectively calculated from potential energy curves of Dontot et al. [204]

Table 6-7: Optimized parameters of the Morse potential used in the model of cationic dimers of benzene: dissociation energy D_e , equilibrium distance r_e , and minimum potential energy V_e .

	${}^2B_{1g}$	${}^2E_{1u}$	${}^2A_{2u}$	${}^2A_{1g}$	${}^2E_{1u}$
D_e (eV)	0.98	0.05	0.37	0.55	1.15
r_e (Å)	3.18	4.24	3.50	3.62	3.12
V_e (eV)	-0.88	-0.34	1.84	1.38	1.78
a (Å)	1.35	1.48	1.39	1.54	1.36

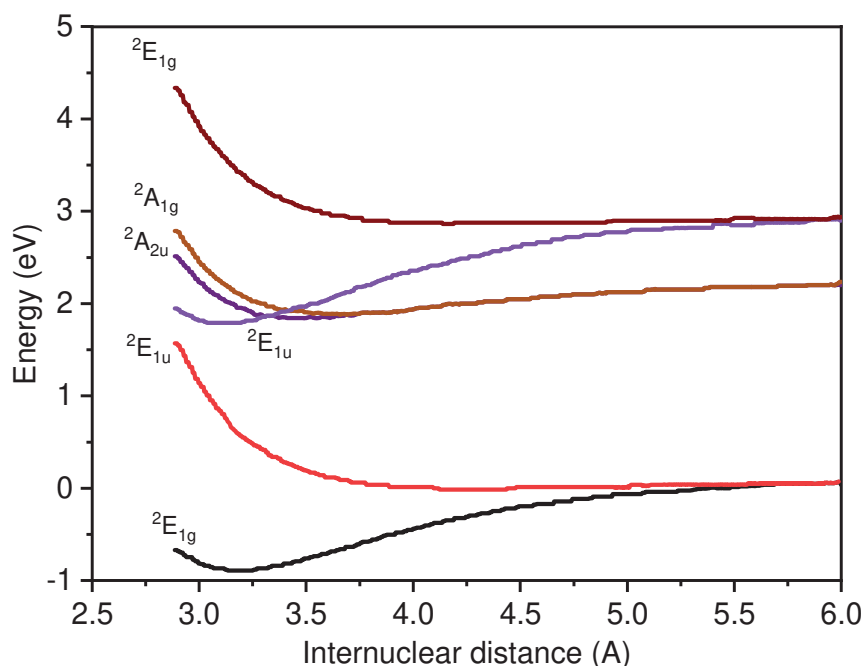


Figure 6-21: Morse potential energy curves of benzene dimer cation used to model CR and LE bands.

6.6 Results of DFTB-EXCI Modelling for pyrene dimer cations

6.6.1 The photo-absorption spectrum

To theoretically simulate the photoabsorption spectrum as a function of temperature for pyrene dimer cations, a density-functional based tight-binding (DFTB) with the extended configuration interaction (EXCI) calculation has been carried out by a theoretician group of the LCPQ from Toulouse University (Mathias Rapacioli et al.). This work about pyrene dimer cations (experiments with Mini-Ring in Lyon and theory in Toulouse) resulted in a collaborative publication between our groups [189]. The calculation included all excited electronic states correlated with the five lowest dipole-allowed excited states of monomer cations and a Monte Carlo exploration of the electronic ground state PES.

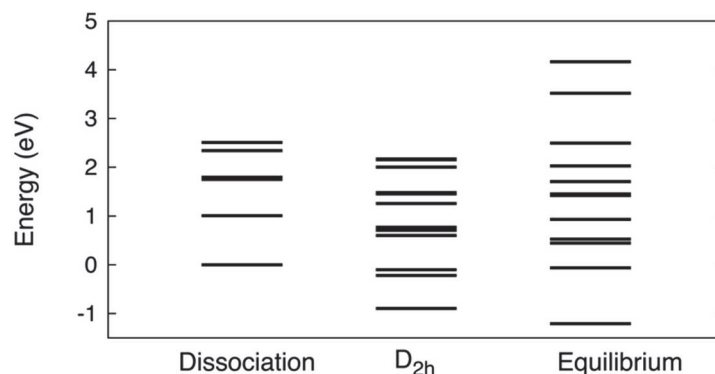


Figure 6-22: Energy level diagram for three geometric configurations of the pyrene cationic dimers (left: dissociation, center: D_{2h} -constrained minimum, at intermolecular distance $R=2.98 \text{ \AA}$; right: equilibrium geometry).

The values of the excitation energies of these first five, dipole-allowed, monomer excited states, D_2 , D_3 , D_4 , D_5 , and D_6 , with respective symmetries ${}^2B_{1u}$, 2A_u , ${}^2B_{1u}$, 2A_u , and ${}^2B_{1u}$ are found at 1.01, 1.75, 1.80, 2.34, and 2.51 eV, respectively. These values are in reasonable agreement with other theoretical [287–289] and experimental [290–292] values.

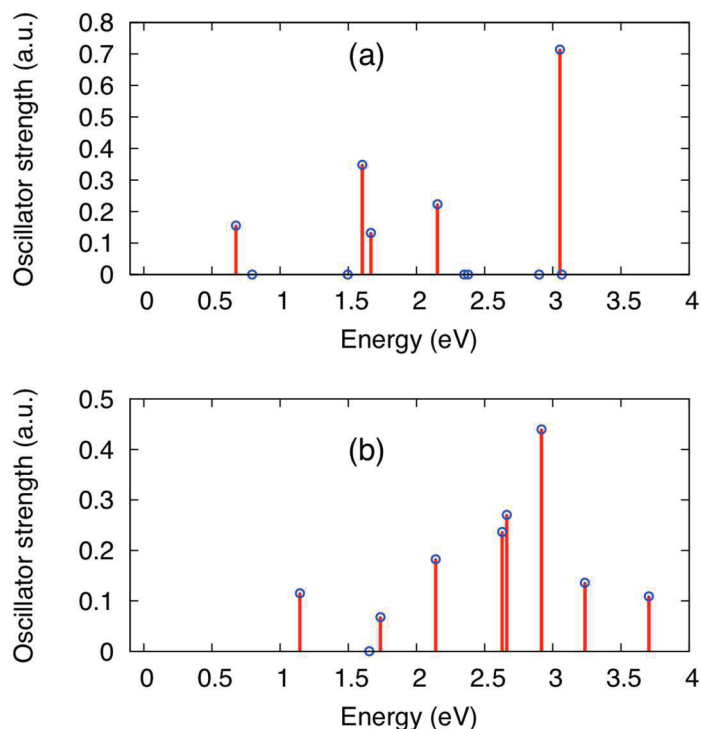


Figure 6-23: Vertical absorption spectra for two geometric configurations of the pyrene cationic dimers. Bottom: equilibrium geometry, top: D_{2h} -constrained minimum at $R=2.98$. The symbols indicate state positions while sticks provide intensities.

EXPERIMENTAL RESULTS FOR DIMER CATIONS

The evolution of the excited state configurations with the geometry of the dimer has been investigated. It can be noticed that depending on the global symmetry and the specific geometry, the various valence bond configurations can mix and CI eigenstates that are asymptotically forbidden, become dipole-allowed at a finite intermolecular distance. This dependence is illustrated by plotting the vertical energy diagram levels in Figure 6-22 and the spectra in Figure 6-23, including all presently calculated excited states for two particular dimer geometries, the equilibrium geometry (C_1 symmetry) and the eclipsed (superposed) parallel geometry (D_{2h} symmetry).

The spectrum at the equilibrium geometry has more absorbing components in the region 2-3 eV due to its lower symmetry vs. the D_{2h} structure. At equilibrium, the vertical transitions with significant intensities lie at 1.14, 1.66/1.73, 2.14, 2.62/2.66, 2.91, 3.23, and 3.70 eV. Another noticeable feature is the shift of the lower transition energy, corresponding to the antibonding CR state, from 1.15 eV in the C_1 geometry to 0.68 eV in the D_{2h} geometry.

6.6.2 Photo-absorption spectra dependence on temperature

Figure 6-24 displays the simulated photo-absorption spectra of the pyrene cationic dimers at various temperatures between 10 and 500 K. At 10 K, the absorption spectrum of the dimer is characterized by peaks around 1.1, 1.7, 2.1, 2.6, 2.9, 3.2, and 3.7 eV, essentially corresponding to the features at the equilibrium geometry, with the maximum intensity at 2.9 eV. The lowest energy peak at 1.1 eV corresponds to the CR excitation, whereas the highest ones all correspond to local excitations. When the temperature is increased, namely above 200 K, several features characterize the evolution of the spectra. First, the CR band strongly broadens, covering energies in the range 0.65-1.25 eV. Second, simultaneously, the CR band center at 1.1 eV at low-temperature shifts to the blue by -0.2 eV at 500 K; third, the bands above 1.5 eV tend to merge with increasing temperature, resulting in two broadened bands around 2.1 and ~2.80 eV. The band at 2.1 eV essentially builds up above 200 K. This is the band that was tentatively attributed to the LE transition at 2.3 eV of the experimental photo-dissociation spectrum (Figure 6-16). The more intense peak also undergoes a temperature shift from 2.9 to 2.8 eV (-0.1 eV), significantly smaller than that of the CR band maximum. This most intense peak could not be recorded in the experiments since the intensity of the OPO laser in this photon energy range is very small.

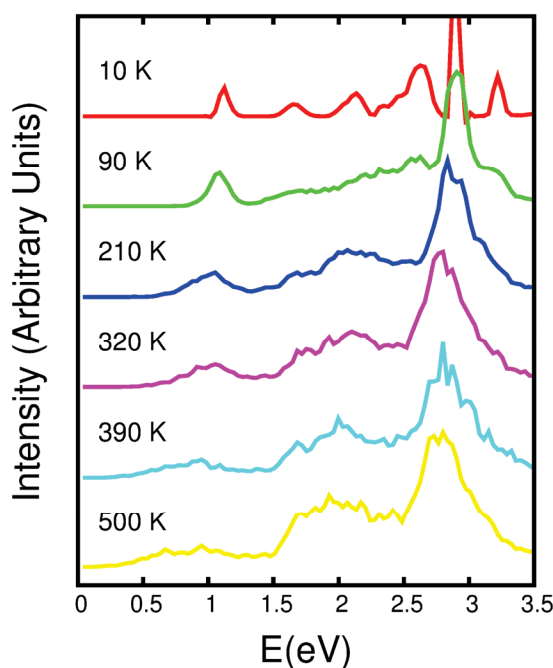


Figure 6-24: Simulated temperature evolution of the total photo-absorption spectrum for the cationic dimers of pyrene between 10 K to 500 K.

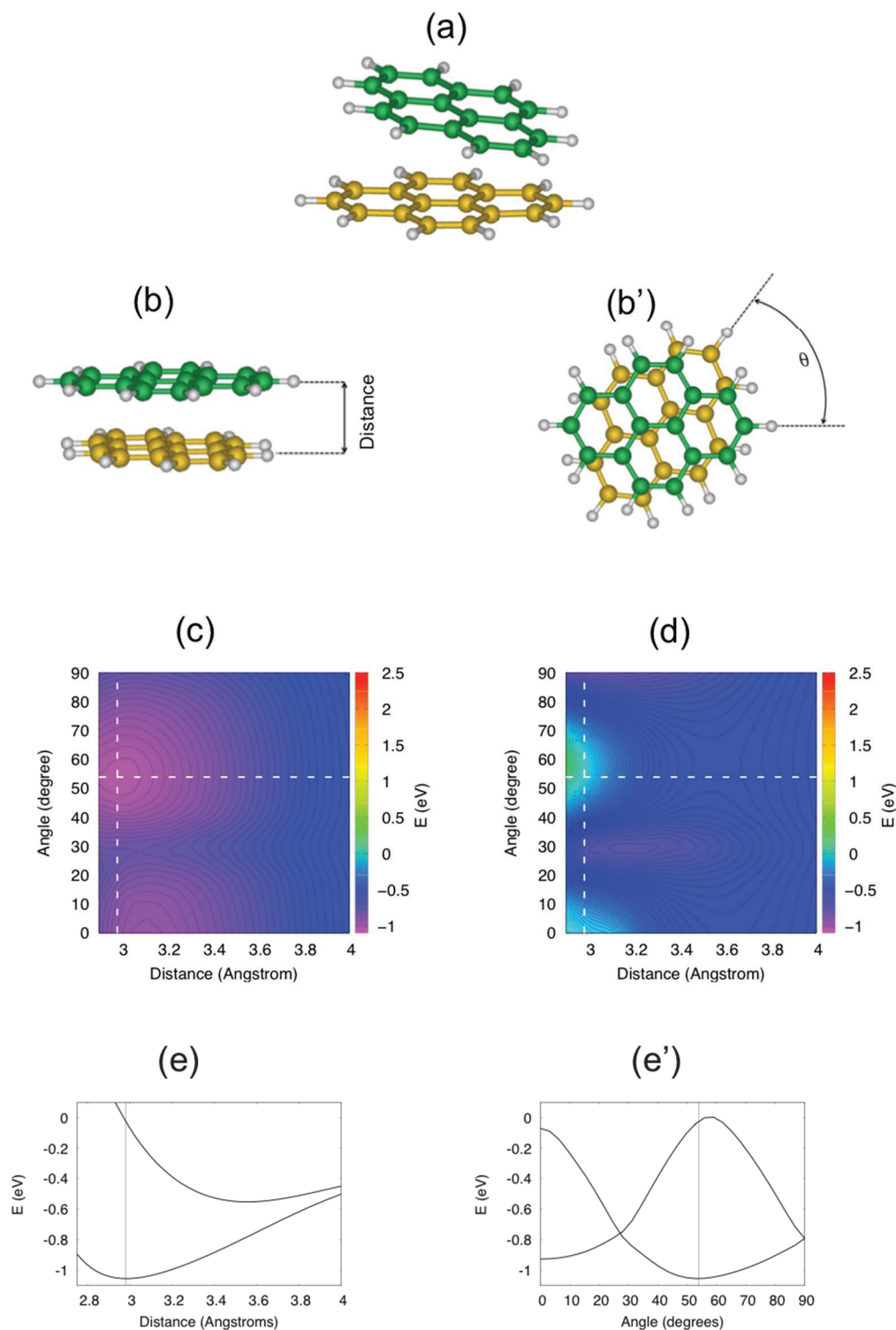


Figure 6-25 : (a) Equilibrium structure of the pyrene cationic dimers, without freezing any degree of freedom; (b, b') Definition of the intermolecular distance and twist angle in sandwich structures (molecular planes parallel); PES reduced to the two aforementioned dimensions for the ground (c) and first excited (d) states, involved in the CR transition. Cuts of these surfaces along a dissociation at 54° (e) and twist mode at 2.98 \AA (e').

6.6.3 The potential energy surfaces in reduced dimensionality

To characterize the CR absorption bands, PESs have been examined in reduced dimensionality, including the degrees of freedom corresponding to intermolecular separation and the twisting angle only. The corresponding PESs for the ground and first excited states are displayed in Figure 6-25(b) and Figure 6-25(b'), respectively. PESs for the ground state and first excited CR state can be shown in Figure 6-25(c) and Figure 6-25(d). The evolution of the

EXPERIMENTAL RESULTS FOR DIMER CATIONS

two states along with the chosen dissociation coordinate and twist cuts, are displayed in Figure 6-25(e) and Figure 6-25(e'), respectively. The CR splitting decreases with increasing intermolecular distance and strongly varies with the twisting angle with two maxima for twist angles of 0 and 54 degrees. The most stable geometry is found at 54 degrees. At low temperatures, the motion of cationic dimers of pyrene is expected to remain close to this geometry, i.e., inside the first isocontour centered at the crossing point between the white dashed line of Figure 6-25(c). At higher temperatures, the system potentially explores a more extended region of the ground state PES limited by higher energy isocontours of Figure 6-25(c). Figure 6-25(e) and Figure 6-25(e') show that the increased amplitude of both motions results in a decrease of the CR splitting. Therefore, a broadening of the CR absorption band decreases with a shift toward lower energies is expected from the calculations.

6.6.4 Comparison of the theoretical absorption spectrum with the experimental photodissociation spectrum

Figure 6-26 shows a comparison of the theoretical absorption spectrum with the experimental photodissociation spectrum. Amongst the calculated spectra, the one at 320 K is in best agreement with the experimental one. The theoretical broad band in the range 0.65-1.3 eV (\sim 950-1900 nm) is associated with the experimental CR absorption band centered at about 1.0 eV (1240 nm). This band extends between 1200 and 2000 nm (1.03-0.62 eV) with a maximum of around 1530 nm (0.79 eV). The shift of 0.2 eV may be at least partly attributed to the precision of the calculations.

The experimental LE band at 2.3 eV is not expected to result from the dimer states asymptotically correlated with the dipole-forbidden D_1 state of the monomer. However, there is a weak and flat plateau in the theoretical spectrum between 1.2 and 1.6 eV, for which the D_1 state may contribute. Accordingly, in the experimental spectrum, in between the CR and LE bands between 1.1 and 1.6 eV, the signal remains small but significantly above zero.

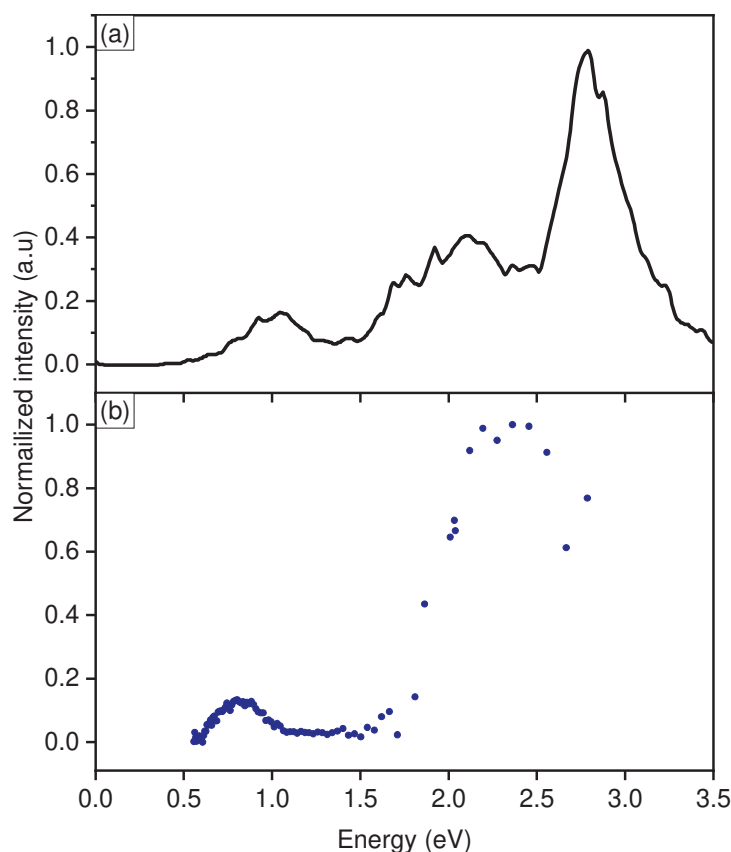


Figure 6-26: Comparison of the calculated photoabsorption spectrum of the cationic dimers of pyrene at $T=320$ K (a) with the experimental photodissociation spectrum (b).

EXPERIMENTAL RESULTS FOR DIMER CATIONS

The states above 2 eV are to be assigned to dimer states correlating to monomer asymptotes from D_2 and above states. The simulated spectrum at 320 K presents two intense bands in this higher energy region. The first one centered at 2.1 eV likely derives from monomer states D_2 - D_4 and is quite close to the experimental peak. The second band at 2.8 eV with maximal intensity corresponds to states directly correlated or having significant weights on the strongly absorbing monomer state D_5 . It is possible that both contributions (at 2.1 and 2.8 eV) predicted by the theory are present in the experimental spectrum but mixed within the recorded broad band. The ratio between the maximal intensities attributed to the LE and CR bands band is roughly 5 in the experimental spectrum, which appears to be rather consistent with the peak intensity ratio of the theoretical bands at 2.1 and 1.0 eV (about 3). However, as the experiment does not provide results above 2.9 eV, it is difficult to ascertain the former assignment with absolute confidence. Despite remaining discrepancies or uncertainties in the comparison between theory and experiment, we conclude that the measured photo-dissociation spectrum is consistent with an experimental temperature in the range 300-400 K for the stored pyrene dimer cations.

6.7 IR radiative cooling of the dimer of naphthalene at DESIREE

As already mentioned in chapter 4, one-week beam time at DESIREE has been spent to investigate the evolution of the photo-dissociation spectrum of naphthalene dimer cations as a function of the internal energy (or temperature). The CR line of the naphthalene dimer was recorded as a function of the storage time in the range 0-30 s. Naphthalene dimer cations were produced in the Nanogan ECR ion source and stored in the asymmetric ring of DESIREE for 30 s. The dissociation spectrum in the 900-1700 nm range has been recorded at different storage times for 0.1 s to 30 s every 0.1 s using an OPO laser (with ns laser pulses).

It is expected that the internal energy of dimer cations is reduced with the storage time due to the IR radiative cooling such that the dimer naphthalene approaches equilibrium with the temperature of the surrounding environment at 13 K.

In DESIREE, the photo-dissociation spectrum could be built by recording the neutral fragments on the ID detector or the charged fragments of the 'Frag' detector, or the coincidence counts between neutral and charged fragments as a function of the laser wavelength. Corrections of the ion beam fluctuations, laser beam intensity (more precisely: number of photons per laser pulse), etc., have been done in the same way as described for the Mini-Ring experiment.

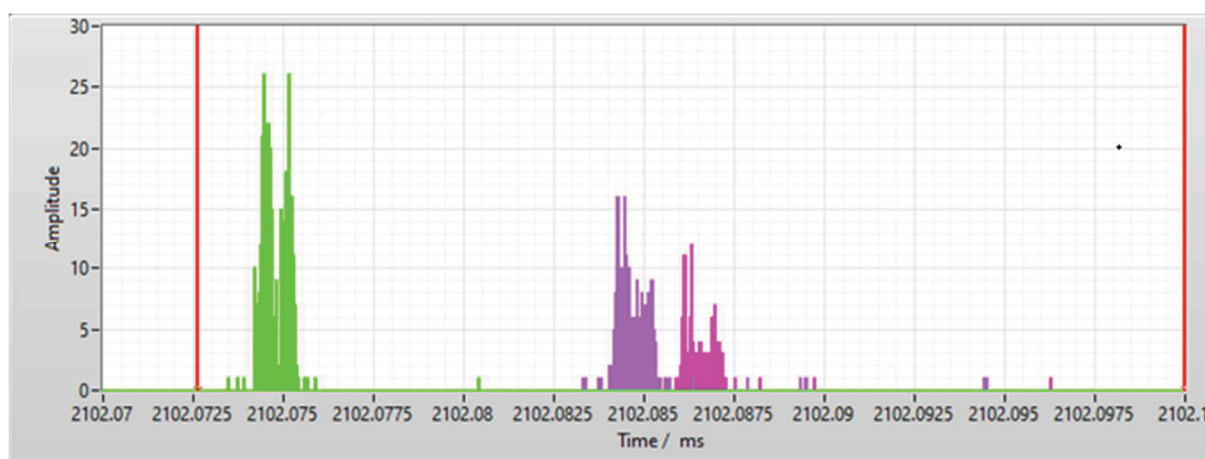


Figure 6-27: Raw data recorded for the cationic dimers of Naphthalene for laser shots at a storage time of about 2.1s. Green: Charged fragment count; purple: neutral fragment count; pink: coincidence count.

Figure 6-27 displays typical raw data of the charged fragment (green), neutral fragment (purple), coincidence counts (pink) for laser shots at a storage time of about 2.1s. It is noteworthy that detection efficiency is slightly higher for the charged fragments than for the neutral fragments. It is also important to note that the position of the 'Frag' detector was

EXPERIMENTAL RESULTS FOR DIMER CATIONS

optimized to detect charged fragments whose mass corresponded to half of the mass of the stored ions. It is then assumed, as already observed for the pyrene dimer cations (section 6.3), that the naphthalene dimer cations dissociate in two fragments of equal masses, i.e., a neutral and a charged monomer.

Figure 6-28 displays a 2D representation of the corrected charged fragment counts as functions of storage time and laser wavelength. It shows the time evolution of the CR band as the naphthalene dimer cations are cooling down during storage. As expected, the bandwidth of the CR line is reduced during the cooling of naphthalene dimer cations. Moreover, the center of the band is significantly shifted towards a shorter wavelength, i.e., higher photon energy, with the storage time. Thus, the CR band of naphthalene dimer cations shows a similar behavior as that of the theoretical pyrene dimer cations discussed in section 6.6.2.

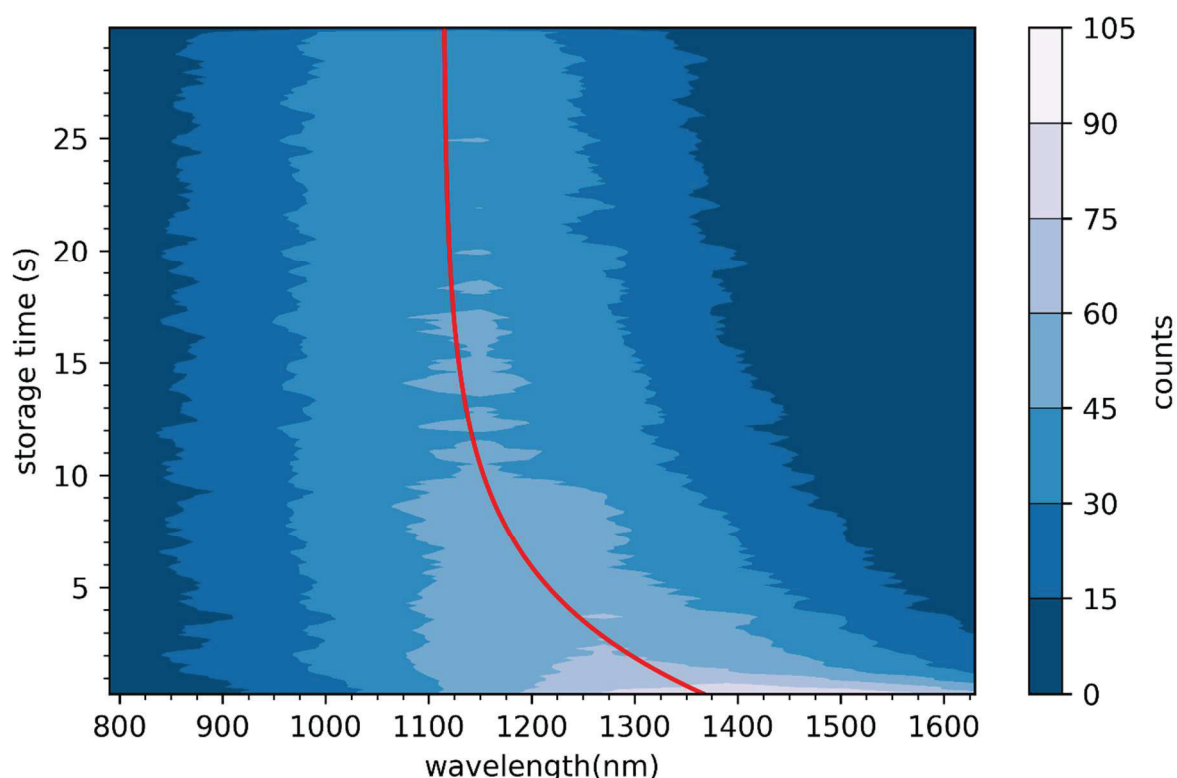


Figure 6-28: 2D diagram displaying the evolution of the recorded CR line of naphthalene dimer cations as a function of the storage time. Each row corresponds to a photo-absorption spectrum recorded at a given storage time. The red line shows the position of the center of the CR line using the fit function of Eq. (6-7).

At long storage times (several seconds), the center of the CR band is found at about 1100 nm (1.1 eV), very close to the value obtained by Inokuchi et al. [10], which means that the temperatures achieved in both cases are rather similar. However, Inokuchi et al. were not able to determine the temperature of the naphthalene dimer cations in their experiment. At short storage times, the center of the CR band is found at about 1400 nm (0.87 eV), i.e., at possibly significantly smaller energy than that we obtained with the Mini-Ring (1 eV). It could be an indication that the naphthalene dimer cations have been produced with a rather higher internal energy in DESIREE's ion source than in Mini-Ring's one. Indeed, in the experiments with Mini-Ring, the source set-up allowed us to reach higher naphthalene pressures and, therefore, to prepare a colder plasma.

Figure 6-29 displays the center and width of the CR band calculated from the data of Figure 6-28 as a function of storage time. To estimate the typical time at which the center of the CR band tends to its asymptotic wavelength value, we tentatively fit the center data points with an exponential curve:

$$\lambda(t) = \Delta\lambda \exp\left(-\frac{t}{\tau}\right) + \lambda_0 \quad \text{Eq. (6-7)}$$

where λ_0 is the center wavelength at $t \rightarrow \infty$ (i.e., cold conditions), $\Delta\lambda$ is the maximum wavelength shift at $t = 0$ (dependant on the initial temperature in the ions source) and τ is the typical cooling time. The best fit is obtained for $\tau \approx 5.2$ s and $\lambda_0 \approx 1100$ nm (see Figure 6-29). There is, however, a small deviation of the experimental values from fit at short storage time, indicating a possible faster cooling when the ions are still hot.

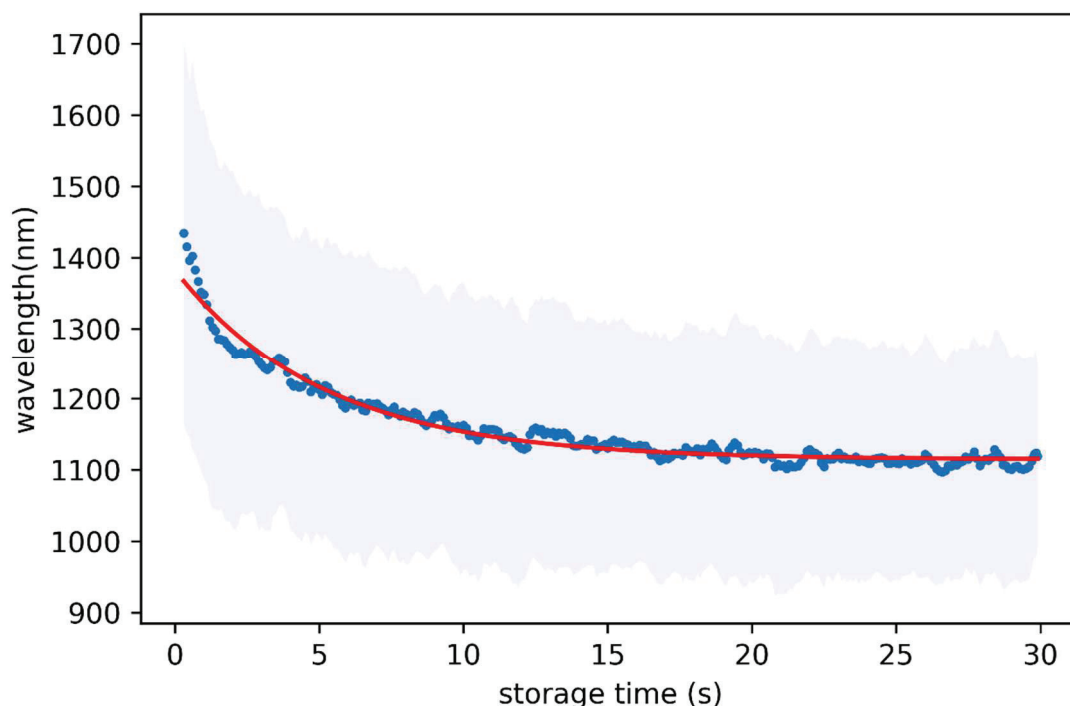


Figure 6-29: Center (blue dots) and width (light blue area) of the CR band as a function of storage time of cationic dimers of Naphthalene (computed from the data of Figure 6-28). The red line is an exponential fit to the center of the CR band with a characteristic time of 5.2 s.

To go further with the interpretation of the time evolution of the present photo-dissociation spectrum, more theoretical calculations, possibly using the same DFTB-EXCI scheme as for the pyrene dimer cations, are needed for the naphthalene dimer cations. These calculations are presently on the way in collaborative work with the group of M. Rapacioli at LCPQ Toulouse. The main conclusion from this work is that we have been able to quantify the cooling rate of naphthalene dimer cations by following the time evolution of the center of the CR band.

6.8 Fragmented dimer cations

In chapter 4, we have shown that, depending on the ion source conditions, it was possible to observe fragmented dimers in the mass spectra, especially dimers with one or more missing H atoms. These ions of mass corresponding to the mass of the dimer minus one or several H atoms may not be bound by charge resonance as the intact dimers. However, although it might be improper, we will keep, for simplicity, the name of ‘fragmented dimer cations’ in the following. The following discussions could have been made for fragmented naphthalene or pyrene dimer cations; however, we have chosen to focus on the example of dimer benzene-H cations.

Dimer benzene-H cations were store in the Mini-Ring for 10 ms. Figure 6-30 displays the neutral fragment yield recorded with the PSD for a 480 nm OPO-laser excitation of the stored ions between D₁-D₂ (merged beam configuration) with a repetition rate of 1 kHz. Every laser shot is followed by delayed dissociation with long decays that last for more than 700 μ s after

EXPERIMENTAL RESULTS FOR DIMER CATIONS

the laser shots, as can be seen in Figure 6-30(b). This delayed dissociation observed in the case of dimer benzene-H is a striking difference with the case of dimer benzene for which delayed dissociation was not observed at all after laser excitation. The observation of delayed dissociation is attributed to the population of bound electronic excited states, which was not possible for the intact cationic dimers.

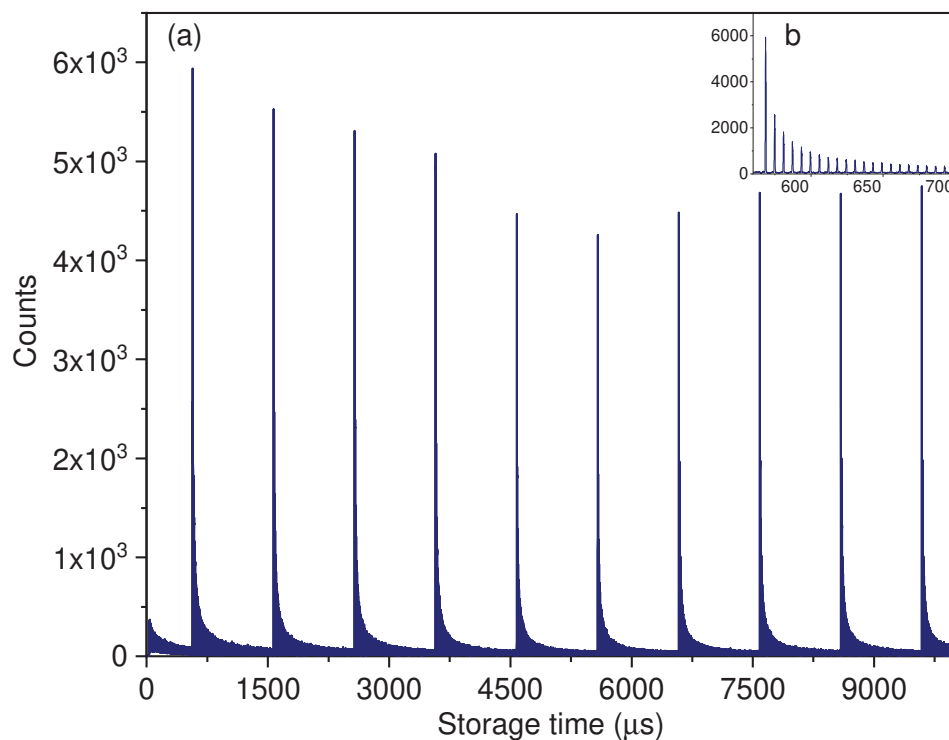


Figure 6-30: Neutral fragment counts recorded for a storage time of 10 ms with 450 nm laser pulses shot every 1 ms for dimer benzene-H cations.

In order to study the evolution of the distribution of internal energy, we have plotted the neutral fragment yields as a function of time t' , for the first ten turns after each laser shot, laser shot time being taken as the time reference (Figure 6-31). All the laser-induced decays could be nicely fitted with a power-law, as shown in Figure 6-31(b). All the decay curves are parallel in the log-log scale, and the exponent of the power-fit is found close to -1. The observation of this common trend shows that the energy distribution is broad and remains broad for 10 ms. Therefore, although delayed dissociation is observed in the case of dimer benzene-H, there is no fast cooling. We conclude that the RF cooling process does not occur in this case, most probably due to the absence of the IIC process, because the structure of the electronic states is not favorable for IIC. Therefore, after laser photon absorption, the IC process populates the ground electronic state with high vibrational energy, leading to statistical delayed dissociation.

Although the completed photo-dissociation spectrum was not performed for dimer-benzene-H cations, we have verified that no absorption could be observed in the near IR range where the CR lies for the intact dimer cations. The photon energy of 2.58 eV used in Figure 6-30 matches rather well with the LE band of the intact dimer cations.

We conclude that dimer benzene-H cations behave differently than the intact dimers. Therefore structure and the kind of bounding must be very different. Instead of a CR bounding, the dimer-benzene-H is probably bound covalently, forming a more stable system than the intact dimers.

This may have consequences in the growing route of PAH in the ISM, in regions where neutral, ionized, and fragmented PAHs may coexist. The formation of 'fragmented dimers', which may isomerize to rather stable structures, although they do not present any fast radiative

EXPERIMENTAL RESULTS FOR DIMER CATIONS

cooling via the RF process (they can still cool on longer timescales by IR cooling), might be suggested as a possible route towards the formation of big PAHs in the ISM.

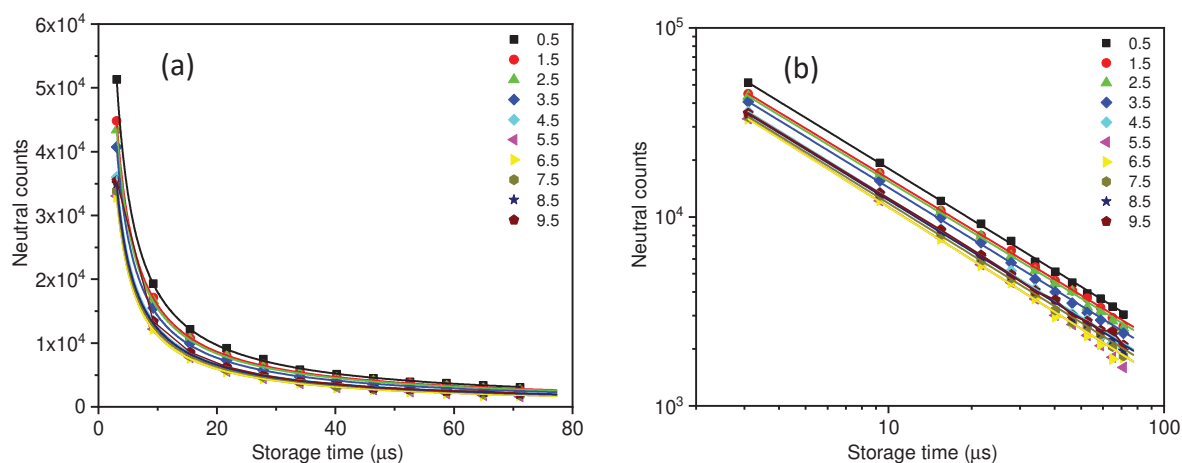


Figure 6-31: Laser-induced decay curves for the cationic dimer of benzene -H with decay factor close to 1.

6.9 Conclusion

In this chapter, we discussed the cationic dimers of PAHs, i.e., dimer benzene, naphthalene, pyrene stored in the Mini-Ring for storage times up to 100 ms. The natural decay of such dimers has been investigated and has shown the absence of fast radiative cooling due to recurrent fluorescence process, in opposition to the monomer cations of the phenanthrene, which, as demonstrated in chapter 6, is cooled down radiatively by recurrent fluorescence process. A coincidence experiment was performed in order to identify the neutral fragments, confirming the dissociation by splitting the cationic dimers into two fragments of equal masses. The photodissociation spectrum of these dimers has been recorded by scanning the wavelength in the range of 400-2400 nm. Two broad bands were assigned, namely the CR and the LE. The modeling of the experimental photodissociation spectra of these dimers has also been carried out using different approaches, a semi-empirical approach based on Morse potentials, and more accurate DFTB-EXCI calculations performed in LCPQ Toulouse. For dimer pyrene, the width and center of the CR line have been studied as a function of temperature, showing temperature sensitivity. The evolution of the CR line for the dimer of naphthalene was recorded for a long storage time in DESIREE, and the results show the evolution of the center of the CR band towards higher energies with the storage time, i.e., as the dimer temperature decrease. This experimental result obtained for naphthalene dimer cations is in line with the DFTB-EXCI theoretical results obtained for pyrene dimer cations. Finally, the fragmented dimer benzene -H was also investigated, showing a different case than the monomer and intact dimer cations, where the recurrent fluorescence is not observed, although the laser-induced delayed dissociation is observed.

7 CONCLUSION AND OUTLOOK

Owing to their presence in different regions of the universe, in particular in the interstellar medium, the Polycyclic Aromatic Hydrocarbons were supposed, in the mid of 1850s, to be possible carriers of observational Infrared emission features, the so-called unidentified infrared bands, and to be responsible for the visible emission bands, known as DIBs. This hypothesis has triggered a wide range of investigations to understand the energy relaxation dynamics of such isolated species and then their stability. Electrostatic storage devices (ESDs) proved to be suitable tools to study such ultra-slow processes of such species over a long observation time, under controlled conditions compatible with those found in the ISM, which allow the internal degrees of freedom to be vibrationally cooled

In the present thesis, the electrostatic storage ion rings, the Mini-Ring and DESIREE, have been used to investigate the small cationic PAHs monomers and dimers. Due to the compactness of Mini-Ring, with a circumference of about 0.7 m, the short revolution period of stored ions of several microseconds enabled the investigation of the cooling dynamics of molecular ions up to a long observation time with a fine sampling of the recorded dissociation decays. In this works, the Mini-Ring is employed primarily to study the cooling dynamics of small PAHs, particularly the singly charged phenanthrene cations and dimer cations of benzene, naphthalene, and pyrene, and to record photodissociation spectra of those dimer PAH cations. Moreover, due to the need for longer storage times up to seconds and cryogenic temperature, allowing the stored ions to be vibrationally cooled, a one-week beam time has been performed on the DESIREE facility to study the naphthalene dimer cations.

The studied species (cations of PAH monomers or dimers) have been prepared in the plasma of an electron cyclotron resonance (ECR) ion source and accelerated with 12 keV, and transported via a set of ion-optics to be stored in the Mini-Ring for storage times up to 100 ms. Special tuning conditions of the ECR ion source to produce phenanthrene cations: low HF and rather high pressure to keep the plasma as cold as possible. Such special conditions are critical for the production of dimer cations.

For phenanthrene monomer cations, the neutral fragment yield has been recorded at every single turn of the molecular ion bunch in the Mini-Ring as a function of well-defined storage time. During the first milliseconds of storage, the internal energy is dissipated either by unimolecular dissociation or fast radiative cooling via the recurrent fluorescence process. The natural decay of phenanthrene monomer cations presents three distinct regions: at short times (1-2 ms), the unimolecular dissociation dominates, then the dissociation processes are quenched by the fast radiative cooling due to recurrent fluorescence, finally radiative cooling dominates and the observed neutral fragments are due to collision-induced dissociation with the rest gas.

To quantify the effect of the RF process on the evolution of the internal energy distribution (IED), laser-induced dissociation was used at different storage times and with different wavelengths. The neutral fragment yields resulting from the laser-induced dissociation are analyzed using two different methods to determine the energy shift rate of IED: (i) the decay curves are fitted with the power-law decay $t^{-\alpha}$ and hence characterized by decay factor(α), which is tightly related to the shape of the high-energy edge of the IED. It was found that the decay factor decreases with decreasing internal energy. The cooling rate has been estimated to be about 100 eV/s for the ions in the observation time range (below 10 ms). (ii) simulated decays calculated from dissociation rates as a function of the internal energy, and gaussian IEDs are fitted to the experimental laser-induced decays. The energy at the high-energy edge of the gaussian IED is found to decrease regularly as a function of storage time with an average rate

CONCLUSION AND OUTLOOK

of about 100 eV/s, in good agreement with the previous method. This cooling rate is too fast to be attributed to IR radiative cooling, whose rate is expected to be in the range of one or several seconds. This fast rate is indeed attributed to the RF process, whose cooling rate is expected to be in the order of magnitude one or several hundreds of s^{-1} . The measured cooling rate of the phenanthrene cations is of comparable magnitude as that of its isomer, the anthracene cations.

In the last part of the present work, we showed that small PAH dimer cations behave very differently than monomers. For benzene, naphthalene, and pyrene dimer cations, the natural decay curve did not show any evidence of quenching of the dissociation. This result demonstrates that the radiative cooling of such dimer cations is much slower than isolated monomer cations and that the conditions for the recurrent fluorescence, i.e., the possibility to populate a stable excited state via the inverse internal conversion process, are not fulfilled by these dimer cations.

The photo-dissociation spectra of these three dimer cations have been measured in the range 400 to 2400 nm range. Two broad bands have been observed for all studied dimer cations: the charge resonance band (CR) is due to the electronic transition from the ground state to the first excited state, and the local excitation band (LE) due to the electronic transition from the ground state to the second excited state. The dissociation energy has been estimated as well. For naphthalene dimer cations [283], the CR and LE bands have been found at about 1 and 2.2 eV, respectively; the dissociation energy, estimated from half of the CR transition energy, was found to be 0.5 eV. This estimated value was found to be in good agreement with the previous experimental work, and yet smaller than theoretical works by a factor of 2. The disagreement can possibly be attributed to the temperature effect with possible isomerization, or maybe more probably, to a too crude estimation of its value via the half of the CR line. Other effects may contribute to an increase or decrease of the level splitting, like, e.g., polarization. A tentative semi-empirical model based on effective Morse potentials has been proposed for the interpretation of the photodissociation spectra. These effective potentials are expected to average temperature effects. The averaged effect would give rise to a smaller energy difference between the fundamental and dissociation states due to the twisting vibration modes of the dimer cations.

The photo-dissociation of free-flying pyrene dimer cations has been recorded, for the first time [189], in the 400 to 2000 nm range. Again, the two broad absorption bands observed at 550 (2.25 eV) and 1560 nm (0.79 eV) are attributed to LE and CR bands. Theoretical simulations carried out by our collaborators (M. Rapacioli et al., LCPQ, Toulouse) of the absorption spectrum as a function of the temperature were performed using the Density Functional based Tight Binding approach within the Extended Configuration Interaction scheme (DFTB-EXCI) to determine the electronic structure. The simulation involved all excited electronic states correlated asymptotically with the five lowest, dipole-allowed, excited states D_2 – D_6 of the monomer cations and a Monte Carlo exploration of the electronic ground state potential energy surface. The simulations exhibit three major bands at 1.0, 2.1, and 2.8 eV, respectively. They allow assigning the experimental band at 1560 nm to absorption by the charge resonance (CR) excited state correlated with the ground state of the monomer D_0 . The band at 550 nm is tentatively attributed to dimer states correlated with excited states D_2 – D_4 in the monomer cations. Simulations also show that the CR band broadens and shifts towards a longer wavelength with increasing temperature. It results from the dependence on the geometry of the energy gap between the ground state and the lowest excited state. The comparison of the experimental spectrum with theoretical spectra at various temperatures allowed us to estimate the temperature of the stored pyrene dimer cations in the 300–400 K range, which is in line with the expected temperatures of the ions deduced from the analysis of the natural decay curve.

During a one-week run-time, naphthalene dimer cations were stored up to 30 s in the cryogenic ring DESIREE to perform photo-dissociation spectroscopy. The evolution of the CR

CONCLUSION AND OUTLOOK

line as a function of storage time and the cryogenic temperature was measured. The time evolution of the center of the CR line was used to estimate a radiative cooling rate of about 5.2 s^{-1} .

In future studies, it is planned to investigate much larger PAHs, which are more relevant for astrophysics, in laboratory conditions that mimic those of the interstellar medium. Therefore, the Mini-Ring is intended to be operated at cryogenic temperature, which is expected to come along with much lower background gas pressure and, therefore, much longer storage times. One of the goals would be to quantify the lower IED energy region where IR radiative cooling competes with RF cooling or become the dominant cooling process. It is also expected that dissociation rates could be measured directly if photon absorption leads to narrow internal energy distributions. However, with conventional lasers, multi-photon absorption would be needed to reach the regime of internal energies where dissociation dominates. Instead, it is envisaged to use VUV synchrotron radiation to excite the stored in the single-photon absorption regime.

BIBLIOGRAPHY

- [1] B. T. Draine, *Physics of the Interstellar and Intergalactic Medium* (Princeton University Press, Princeton, N.J, 2011).
- [2] F. Salama, E. L. O. Bakes, L. J. Allamandola, and A. G. G. M. Tielens, *Assessment of the Polycyclic Aromatic Hydrocarbon--Diffuse Interstellar Band Proposal*, *Astrophys. J.* **458**, 621 (1996).
- [3] H. A. B. Johansson, *Ionization and Fragmentation of Complex Molecules and Clusters Biomolecules and Polycyclic Aromatic Hydrocarbons*, Department of Physics, Stockholm University, 2011.
- [4] T. Allain, S. Leach, and E. Sedlmayr, *Photodestruction of PAHs in the Interstellar Medium. I. Photodissociation Rates for the Loss of an Acetylenic Group.*, *Astron. Astrophys.* **305**, 602 (1996).
- [5] T. Allain, S. Leach, and E. Sedlmayr, *Photodestruction of PAHs in the Interstellar Medium. II. Influence of the States of Ionization and Hydrogenation.*, *Astron. Astrophys.* **305**, 616 (1996).
- [6] F. Salama and L. J. Allamandola, *Is a Pyrene-like Molecular Ion the Cause of the 4,430-Å Diffuse Interstellar Absorption Band?*, *Nature* **358**, 42 (1992).
- [7] F. Salama and L. J. Allamandola, *Electronic Absorption Spectroscopy of Matrix-isolated Polycyclic Aromatic Hydrocarbon Cations. I. The Naphthalene Cation (C₁₀H⁺₈)*, *J. Chem. Phys.* **94**, 6964 (1991).
- [8] A. Léger, P. Boissel, and L. d'Hendecourt, *Predicted Fluorescence Mechanism in Highly Isolated Molecules: The Poincaré Fluorescence*, *Phys. Rev. Lett.* **60**, 921 (1988).
- [9] P. Boissel, P. de Parseval, P. Marty, and G. Lefèvre, *Fragmentation of Isolated Ions by Multiple Photon Absorption: A Quantitative Study*, *J. Chem. Phys.* **106**, 4973 (1997).
- [10] Y. Inokuchi, K. Ohashi, M. Matsumoto, and N. Nishi, *Photodissociation Spectrum of Naphthalene Dimer Cation*, *J. Phys. Chem.* **99**, 3416 (1995).
- [11] A. G. G. M. Tielens, *The Physics and Chemistry of the Interstellar Medium* (Cambridge University Press, 2005).
- [12] *Astronomers Unveiling Life's Cosmic Origins*, <https://public.nrao.edu/news/astronomers-unveiling-life-s-cosmic-origins/>.
- [13] T. P. Snow and B. J. McCall, *Diffuse Atomic and Molecular Clouds*, *Annu. Rev. Astron. Astrophys.* **44**, 367 (2006).
- [14] B. McGuire, *2018 Census of Interstellar, Circumstellar, Extragalactic, Protoplanetary Disk, and Exoplanetary Molecules*, *Astrophys. J. Suppl. Ser.* **239**, 17 (2018).
- [15] A. G. G. M. Tielens, *The Molecular Universe*, *Rev. Mod. Phys.* **85**, 1021 (2013).
- [16] C. Arumainayagam, R. Garrod, M. Boyer, A. Hay, S. Bao, J. Campbell, J. Wang, C. Nowak, M. Arumainayagam, and P. Hodge, *Extraterrestrial Prebiotic Molecules: Photochemistry vs. Radiation Chemistry of Interstellar Ices*, *Chem. Soc. Rev.* **48**, (2019).
- [17] A. G. G. M. Tielens, *Interstellar Polycyclic Aromatic Hydrocarbon Molecules**, *Annu Rev Astron Astr* **46**, 289 (2008).
- [18] J. Groen, D. W. Deamer, A. Kros, and P. Ehrenfreund, *Polycyclic Aromatic Hydrocarbons as Plausible Prebiotic Membrane Components*, *Orig. Life Evol. Biosphere J. Int. Soc. Study Orig. Life* **42**, 295 (2012).

Bibliography

- [19] M. P. Bernstein, S. A. Sandford, L. J. Allamandola, J. S. Gillette, S. J. Clemett, and R. N. Zare, *UV Irradiation of Polycyclic Aromatic Hydrocarbons in Ices: Production of Alcohols, Quinones, and Ethers*, *Science* **283**, 1135 (1999).
- [20] *Story of Stellar Birth*, <http://www.spitzer.caltech.edu/images/2234-sig06-021-Story-of-Stellar-Birth>.
- [21] F. C. Gillett, W. J. Forrest, and K. M. Merrill, *8 - 13-Micron Spectra of NGC 7027, BD +30 3639, and NGC 6572.*, *Astrophys. J.* **183**, 87 (1973).
- [22] R. W. Russell, B. T. Soifer, and S. P. Willner, *The 4 to 8 Micron Spectrum of NGC 7027*, *Astrophys. J.* **217**, L149 (1977).
- [23] F. C. Gillett, D. E. Kleinmann, E. L. Wright, and R. W. Capps, *Observations of M82 and NGC 253 at 8 - 13 Microns.*, *Astrophys. J.* **198**, L65 (1975).
- [24] M. Cohen, C. M. Anderson, A. Cowley, G. V. Coyne, W. Fawley, T. R. Gull, E. A. Harlan, G. H. Herbig, F. Holden, H. S. Hudson, R. O. Jakoubek, H. M. Johnson, K. M. Merrill, F. H. Schiffer, B. T. Soifer, and B. Zuckerman, *The Peculiar Object HD 44179 ("The Red Rectangle")*, *Astrophys. J.* **196**, 179 (1975).
- [25] E. Dwek, K. Sellgren, B. T. Soifer, and M. W. Werner, *Excitation Mechanisms for the Unidentified Infrared Emission Features*, *Astrophys. J.* **238**, 140 (1980).
- [26] W. W. Duley and D. A. Williams, *The Infrared Spectrum of Interstellar Dust: Surface Functional Groups on Carbon*, *Mon. Not. R. Astron. Soc.* **196**, 269 (1981).
- [27] A. Leger and J. L. Puget, *Identification of the "unidentified" IR Emission Features of Interstellar Dust?*, *Astron. Astrophys.* **137**, L5 (1984).
- [28] L. J. Allamandola, A. G. G. M. Tielens, and J. R. Barker, *Polycyclic Aromatic Hydrocarbons and the Unidentified Infrared Emission Bands - Auto Exhaust along the Milky Way*, *Astrophys. J. Lett.* **290**, L25 (1985).
- [29] E. Peeters, *The PAH Hypothesis after 25 Years*, *Proc. Int. Astron. Union* **7**, 149 (2011).
- [30] T. P. Snow, V. Le Page, Y. Keheyan, and V. M. Bierbaum, *The Interstellar Chemistry of PAH Cations*, *Nature* **391**, 259 (1998).
- [31] F. Salama, *ESO Diffuse Interstellar Bands Large Exploration Survey (EDIBLES) - Merging Observations and Laboratory Data*, in (Leiden, Netherlands, 2016).
- [32] E. K. Campbell, M. Holz, D. Gerlich, and J. P. Maier, *Laboratory Confirmation of C 60 + as the Carrier of Two Diffuse Interstellar Bands*, *Nature* **523**, 322 (2015).
- [33] A. Ricca, C. W. Bauschlicher, C. Boersma, A. G. G. M. Tielens, and L. J. Allamandola, *THE INFRARED SPECTROSCOPY OF COMPACT POLYCYCLIC AROMATIC HYDROCARBONS CONTAINING UP TO 384 CARBONS*, *Astrophys. J.* **754**, 75 (2012).
- [34] V. Le Page, T. P. Snow, and V. M. Bierbaum, *Hydrogenation and Charge States of Polycyclic Aromatic Hydrocarbons in Diffuse Clouds. II. Results*, *Astrophys. J.* **584**, 316 (2003).
- [35] B. T. Draine, *Interstellar Dust Grains*, *Annu. Rev. Astron. Astrophys.* **41**, 241 (2003).
- [36] M. Frenklach and E. D. Feigelson, *Formation of Polycyclic Aromatic Hydrocarbons in Circumstellar Envelopes*, *Astrophys. J.* **341**, 372 (1989).
- [37] T. J. Millar and D. A. Williams, *Dust and Chemistry in Astronomy* (CRC Press, 1993).
- [38] C. S. Contreras and F. Salama, *Laboratory Investigations of Polycyclic Aromatic Hydrocarbon Formation and Destruction in the Circumstellar Outflows of Carbon Stars*, *Astrophys. J. Suppl. Ser.* **208**, 6 (2013).
-

Bibliography

- [39] J. A. Miller and C. F. Melius, *Kinetic and Thermodynamic Issues in the Formation of Aromatic Compounds in Flames of Aliphatic Fuels*, *Combust. Flame* **91**, 21 (1992).
- [40] M. K. Crawford, A. G. G. M. Tielens, and L. J. Allamandola, *Ionized Polycyclic Aromatic Hydrocarbons and the Diffuse Interstellar Bands*, *Astrophys. J.* **293**, L45 (1985).
- [41] S. Stein, *On the High Temperature Chemical Equilibria of Polycyclic Aromatic Hydrocarbons*, *J. Phys. Chem.* **82**, 566 (1978).
- [42] M. Frenklach, D. W. Clary, W. C. Gardiner, and S. E. Stein, *Detailed Kinetic Modeling of Soot Formation in Shock-Tube Pyrolysis of Acetylene*, *Symp. Int. Combust.* **20**, 887 (1985).
- [43] I. Cherchneff, *The Formation of Polycyclic Aromatic Hydrocarbons in Evolved Circumstellar Environments*, *EAS Publ. Ser.* **46**, 177 (2011).
- [44] H. Sabbah, L. Biennier, S. J. Klippenstein, I. R. Sims, and B. R. Rowe, *Exploring the Role of PAHs in the Formation of Soot: Pyrene Dimerization*, *J. Phys. Chem. Lett.* **1**, 2962 (2010).
- [45] M. Rapacioli, F. Calvo, C. Joblin, P. Parneix, D. Toubanc, and F. Spiegelman, *Formation and Destruction of Polycyclic Aromatic Hydrocarbon Clusters in the Interstellar Medium*, *Astron. Astrophys.* **460**, 519 (2006).
- [46] M. Rapacioli, C. Joblin, and P. Boissel, *Spectroscopy of Polycyclic Aromatic Hydrocarbons and Very Small Grains in Photodissociation Regions*, *Astron. Astrophys.* **429**, 193 (2005).
- [47] O. Berné, C. Joblin, Y. Deville, J. D. Smith, M. Rapacioli, J. P. Bernard, J. Thomas, W. Reach, and A. Abergel, *Analysis of the Emission of Very Small Dust Particles from Spitzer Spectro-Imagery Data Using Blind Signal Separation Methods*, *Astron. Astrophys.* **469**, 575 (2007).
- [48] C. Joblin, O. Berne, A. Simon, and G. Mulas, *Laboratory Studies of Polycyclic Aromatic Hydrocarbons: The Search for Interstellar Candidates*, *ArXiv09043185 Astro-Ph* (2009).
- [49] J. Mukherjee, A. Sarofim, and J. Longwell, *Polycyclic Aromatic Hydrocarbons from the High-Temperature Pyrolysis of Pyrene*, *Combust. Flame - COMBUST FLAME* **96**, 191 (1994).
- [50] P. Merino, M. Švec, J. I. Martinez, P. Jelinek, P. Lacovig, M. Dalmiglio, S. Lizzit, P. Soukiassian, J. Cernicharo, and J. A. Martin-Gago, *Graphene Etching on SiC Grains as a Path to Interstellar Polycyclic Aromatic Hydrocarbons Formation*, *Nat. Commun.* **5**, 3054 (2014).
- [51] V. Le Page, T. P. Snow, and V. M. Bierbaum, *Hydrogenation and Charge States of PAHs in Diffuse Clouds. I. Development of a Model*, *Astrophys. J. Suppl. Ser.* **132**, 233 (2001).
- [52] J. Montillaud, C. Joblin, and D. Toubanc, *Evolution of Polycyclic Aromatic Hydrocarbons in Photodissociation Regions: Hydrogenation and Charge States*, *Astron. Astrophys.* **552**, A15 (2013).
- [53] J. Zhen, T. Chen, and A. G. G. M. Tielens, *Laboratory Photo-Chemistry of Pyrene Clusters: An Efficient Way to Form Large PAHs*, *Astrophys. J.* **863**, 128 (2018).
- [54] E. R. Micelotta, A. P. Jones, and A. G. G. M. Tielens, *Polycyclic Aromatic Hydrocarbon Processing in Interstellar Shocks*, *Astron. Astrophys.* **510**, A36 (2010).
- [55] E. R. Micelotta, A. P. Jones, and A. G. G. M. Tielens, *Polycyclic Aromatic Hydrocarbon Processing by Cosmic Rays*, *Astron. Astrophys.* **526**, A52 (2011).
-

Bibliography

- [70] J. Postma, R. Hoekstra, A. G. G. M. Tielens, and T. Schlathölter, *A Molecular Dynamics Study on Slow Ion Interactions with the Polycyclic Aromatic Hydrocarbon Molecule Anthracene*, *Astrophys. J.* **783**, 61 (2014).
- [71] E. L. O. Bakes and A. G. G. M. Tielens, *The Photoelectric Heating Mechanism for Very Small Graphitic Grains and Polycyclic Aromatic Hydrocarbons*, *Astrophys. J.* **427**, 822 (1994).
- [72] R. Visser, V. C. Geers, C. P. Dullemond, J.-C. Augereau, K. M. Pontoppidan, and E. F. van Dishoeck, *PAH Chemistry and IR Emission from Circumstellar Disks*, *Astron. Astrophys.* **466**, 229 (2007).
- [73] F. Useli-Bacchitta, A. Bonnamy, G. Mulas, G. Mallocci, D. Toubanc, and C. Joblin, *Visible Photodissociation Spectroscopy of PAH Cations and Derivatives in the PIRENEA Experiment*, *Chem. Phys.* **371**, 16 (2010).
- [74] *PIRENEA 2*, <https://nanocosmos.iff.csic.es/technology/pirenea-2-pirenea-and-espoirs-upgrades/>.
- [75] A. Leger, L. D'Hendecourt, P. Boissel, and F. X. Desert, *Photo-Thermo-Dissociation. I - A General Mechanism for Destroying Molecules*, *Astron. Astrophys.* **213**, 351 (1989).
- [76] S. Martin, J. Bernard, R. Brédy, B. Concina, C. Joblin, M. Ji, C. Ortega, and L. Chen, *Fast Radiative Cooling of Anthracene Observed in a Compact Electrostatic Storage Ring*, *Phys. Rev. Lett.* **110**, 063003 (2013).
- [77] S. Martin, M. Ji, J. Bernard, R. Brédy, B. Concina, A.-R. Allouche, C. Joblin, C. Ortega, G. Montagne, A. Cassimi, Y. Ngono-Ravache, and L. Chen, *Fast Radiative Cooling of Anthracene: Dependence on Internal Energy*, *Phys. Rev. A* **92**, (2015).
- [78] M. H. Stockett, J. N. Bull, J. T. Buntine, E. Carrascosa, M. Ji, N. Kono, H. T. Schmidt, and H. Zettergren, *Unimolecular Fragmentation and Radiative Cooling of Isolated PAH Ions: A Quantitative Study*, *J. Chem. Phys.* **153**, 154303 (2020).
- [79] S. P. Møller, *ELISA, and Electrostatic Storage Ring for Atomic Physics*, *Nucl. Instrum. Methods Phys. Res. A* **394**, 281 (1997).
- [80] D. Zajfman, O. Heber, L. Vejby-Christensen, I. Ben-Itzhak, M. Rappaport, R. Fishman, and M. Dahan, *Electrostatic Bottle for Long-Time Storage of Fast Ion Beams*, *Phys. Rev. A* **55**, R1577 (1997).
- [81] E. Bäckström, D. Hanstorp, O. M. Hole, M. Kaminska, R. F. Nascimento, M. Blom, M. Björkhage, A. Källberg, P. Löfgren, P. Reinhed, S. Rosén, A. Simonsson, R. D. Thomas, S. Mannervik, H. T. Schmidt, and H. Cederquist, *Storing KeV Negative Ions for an Hour: The Lifetime of the Metastable P_{21/2} o Level in S₃₂⁻*, *Phys. Rev. Lett.* **114**, 143003 (2015).
- [82] M. Goto, J. Matsumoto, H. Shiromaru, Y. Achiba, T. Majima, H. Tanuma, and T. Azuma, *Laser-Induced Thermal Detachment of Hot, Large Molecular Ions under Multiphoton-Absorption Conditions*, *Phys. Rev. A* **87**, 033406 (2013).
- [83] A. E. K. Sundén, M. Goto, J. Matsumoto, H. Shiromaru, H. Tanuma, T. Azuma, J. U. Andersen, S. E. Canton, and K. Hansen, *Absolute Cooling Rates of Freely Decaying Fullerenes*, *Phys. Rev. Lett.* **103**, 143001 (2009).
- [84] S. Tomita, J. U. Andersen, H. Cederquist, B. Concina, O. Echt, J. S. Forster, K. Hansen, B. A. Huber, P. Hvelplund, J. Jensen, B. Liu, B. Manil, L. Maunoury, S. Brøndsted Nielsen, J. Rangama, H. T. Schmidt, and H. Zettergren, *Lifetimes of C₆₀(²⁻) and C₇₀(²⁻) Dianions in a Storage Ring*, *J. Chem. Phys.* **124**, 024310 (2006).

Bibliography

- [85] L. H. Andersen, *Thermionic Electron Emission from SF₆-*, Phys. Rev. A **78**, 032512 (2008).
- [86] B. Klærke, A. I. S. Holm, and L. H. Andersen, *UV Action Spectroscopy of Protonated PAH Derivatives. Methyl Substituted Quinolines*, Astron. Astrophys. **532**, A132 (2011).
- [87] C. J. Johnson, B. B. Shen, B. L. J. Poad, and R. E. Continetti, *Photoelectron-Photofragment Coincidence Spectroscopy in a Cryogenically Cooled Linear Electrostatic Ion Beam Trap*, Rev. Sci. Instrum. **82**, 105105 (2011).
- [88] B. B. Shen, B. L. J. Poad, and R. E. Continetti, *Photoelectron–Photofragment Coincidence Studies of the Tert-Butoxide Anion (CH₃)₃CO⁻, the Carbanion Isomer (CH₃)₂CH₂COH⁻, and Corresponding Radicals*, J. Phys. Chem. A **118**, 10223 (2014).
- [89] B. B. Shen, K. G. Lunny, Y. Benitez, and R. E. Continetti, *Photoelectron-Photofragment Coincidence Spectroscopy With Ions Prepared in a Cryogenic Octopole Accumulation Trap: Collisional Excitation and Buffer Gas Cooling*, Front. Chem. **7**, (2019).
- [90] F. Chen, N. Kono, R. Suzuki, T. Furukawa, H. Tanuma, P. Ferrari, T. Azuma, J. Matsumoto, H. Shiromaru, V. Zhaunerchyk, and K. Hansen, *Radiative Cooling of Cationic Carbon Clusters, C N + , N=8,10,13-16*, Phys. Chem. Chem. Phys. **21**, (2018).
- [91] P. Ferrari, E. Janssens, P. Lievens, and K. Hansen, *Radiative Cooling of Size-Selected Gas Phase Clusters*, Int. Rev. Phys. Chem. **38**, 405 (2019).
- [92] J. W. Farley, *Photodetachment Cross Sections of Negative Ions: The Range of Validity of the Wigner Threshold Law*, Phys. Rev. Gen. Phys. **40**, 6286 (1989).
- [93] M. Goto, A. E. K. Sundén, H. Shiromaru, J. Matsumoto, H. Tanuma, T. Azuma, and K. Hansen, *Direct Observation of Internal Energy Distributions of C₅⁻*, J Chem Phys **8** (2013).
- [94] G. Ito, T. Furukawa, H. Tanuma, J. Matsumoto, H. Shiromaru, T. Majima, M. Goto, T. Azuma, and K. Hansen, *Cooling Dynamics of Photoexcited C₆⁻ and C₆H⁻*, Phys. Rev. Lett. **112**, 183001 (2014).
- [95] Y. Toker, O. Aviv, M. Eritt, M. L. Rappaport, O. Heber, D. Schwalm, and D. Zajfman, *Radiative Cooling of Al₄⁻ Clusters*, Phys. Rev. A **76**, 053201 (2007).
- [96] E. K. Anderson, M. Kamińska, K. C. Chartkunchand, G. Eklund, M. Gatchell, K. Hansen, H. Zettergren, H. Cederquist, and H. T. Schmidt, *Decays of Excited Silver-Cluster Anions Ag_n, N=4 to 7, in the Double ElectroStatic Ion Ring Experiment*, Phys. Rev. A **98**, 022705 (2018).
- [97] O. Aviv, Y. Toker, M. Eritt, K. G. Bhushan, H. B. Pedersen, M. L. Rappaport, O. Heber, D. Schwalm, and D. Zajfman, *A Bent Electrostatic Ion Beam Trap for Simultaneous Measurements of Fragmentation and Ionization of Cluster Ions*, Rev. Sci. Instrum. **79**, 083110 (2008).
- [98] C. Breitenfeldt, K. Blaum, M. W. Froese, S. George, G. Guzmán-Ramírez, M. Lange, S. Menk, L. Schweikhard, and A. Wolf, *Decay Processes and Radiative Cooling of Small Anionic Copper Clusters*, Phys. Rev. A **94**, 033407 (2016).
- [99] O. Aviv, Y. Toker, D. Strasser, M. L. Rappaport, O. Heber, D. Schwalm, and D. Zajfman, *Competition between Ionization and Fragmentation of Small Aluminum Cluster Anions*, J. Phys. Conf. Ser. **194**, 152017 (2009).
- [100] F. Martinez, S. Bandelow, C. Breitenfeldt, G. Marx, L. Schweikhard, F. Wienholtz, and F. Ziegler, *Appearance Size of Poly-Anionic Aluminum Clusters, Al_n^{-z}, z = 2–5**, (2013).
-

Bibliography

- [101] R. Antoine, T. Doussineau, P. Dugourd, and F. Calvo, *Multiphoton Dissociation of Macromolecular Ions at the Single-Molecule Level*, Phys. Rev. A **87**, 013435 (2013).
- [102] T. Doussineau, C. Mathevon, L. Altamura, C. Vendrely, P. Dugourd, V. Forge, and R. Antoine, *Mass Determination of Entire Amyloid Fibrils by Using Mass Spectrometry*, Angew. Chem. Int. Ed Engl. **55**, 2340 (2016).
- [103] Y. Toker, A. Svendsen, A. V. Bochenkova, and L. H. Andersen, *Probing the Barrier for Internal Rotation of the Retinal Chromophore*, Angew. Chem. Int. Ed. **51**, 8757 (2012).
- [104] S. Nielsen, J. Andersen, P. Hvelplund, B. Liu, and S. Tomita, *TOPICAL REVIEW: Biomolecular Ions in Accelerators and Storage Rings*, J. Phys. B-At. Mol. Opt. Phys. - J PHYS-B- MOL OPT PHYS **37**, (2004).
- [105] J. U. Andersen, H. Cederquist, J. S. Forster, B. A. Huber, P. Hvelplund, J. Jensen, B. Liu, B. Manil, L. Maunoury, S. Brøndsted Nielsen, U. V. Pedersen, H. T. Schmidt, S. Tomita, and H. Zettergren, *Power-Law Decay of Collisionally Excited Amino Acids and Quenching by Radiative Cooling*, Eur. Phys. J. D **25**, 139 (2003).
- [106] E. Gruber, C. Kjaer, S. B. Nielsen, and L. H. Andersen, *Intrinsic Photophysics of Light-Harvesting Charge-Tagged Chlorophyll a and b Pigments*, Chem. Weinh. Bergstr. Ger. **25**, 9153 (2019).
- [107] K. Hansen, *DECAY DYNAMICS IN MOLECULAR BEAMS*, Mass Spectrom. Rev. (2020).
- [108] L. H. Andersen, O. Heber, and D. Zajfman, *TOPICAL REVIEW: Physics with Electrostatic Rings and Traps*, J. Phys. B At. Mol. Phys. **37**, R57 (2004).
- [109] J. Bernard, G. Montagne, R. Brédy, B. Terpend-Ordacière, A. Bourgey, M. Kerleroux, L. Chen, H. T Schmidt, H. Cederquist, and S. Martin, *A "Tabletop" Electrostatic Ion Storage Ring: Mini-Ring*, Rev. Sci. Instrum. **79**, 075109 (2008).
- [110] R. von Hahn, F. Berg, K. Blaum, J. R. Crespo Lopez-Urrutia, F. Fellenberger, M. Froese, M. Grieser, C. Krantz, K.-U. Kühnel, M. Lange, S. Menk, F. Laux, D. A. Orlov, R. Repnow, C. D. Schröter, A. Shornikov, T. Sieber, J. Ullrich, A. Wolf, M. Rappaport, and D. Zajfman, *The Electrostatic Cryogenic Storage Ring CSR - Mechanical Concept and Realization*, Nucl. Instrum. Methods Phys. Res. B **269**, 2871 (2011).
- [111] K. E. Stiebing, V. Alexandrov, R. Dörner, S. Enz, N. Yu. Kazarinov, T. Kruppi, A. Schempp, H. Schmidt Böcking, M. Völp, P. Ziel, M. Dworak, and W. Dilfer, *FLSR - The Frankfurt Low Energy Storage Ring*, Nucl. Instrum. Methods Phys. Res. A **614**, 10 (2010).
- [112] H. T. Schmidt, H. A. B. Johansson, R. D. Thomas, W. D. Geppert, N. Haag, P. Reinhard, S. Rosén, M. Larsson, H. Danared, K.-G. Rensfelt, L. Liljeby, L. Bagge, M. Björkhage, M. Blom, P. Löfgren, A. Källberg, A. Simonsson, A. Paál, H. Zettergren, and H. Cederquist, *DESIREE as a New Tool for Interstellar Ion Chemistry*, Int. J. Astrobiol. **7**, 205 (2008).
- [113] D. Zajfman, A. Wolf, D. Schwalm, D. A. Orlov, M. Grieser, R. von Hahn, C. P. Welsch, J. R. C. Lopez-Urrutia, C. D. Schröter, X. Urbain, and J. Ullrich, *Physics with Colder Molecular Ions: The Heidelberg Cryogenic Storage Ring CSR*, J. Phys. Conf. Ser. **4**, 296 (2005).
- [114] M. Knoop, N. Madsen, and R. C. Thompson, *Physics with Trapped Charged Particles: Lectures from the Les Houches Winter School* (IMPERIAL COLLEGE PRESS, 2014).
- [115] K. Hansen, J. Andersen, P. Hvelplund, S. Møller, U. Elstrøm, and V. Petrunin, *Observation of a $1/t$ Decay Law for Hot Clusters and Molecules in a Storage Ring*, Phys. Rev. Lett. **87**, 123401 (2001).
-

Bibliography

- [116] S. P. Møller, *Design and First Operation of the Electrostatic Storage Ring, ELISA*, in *6th European Particle Accelerator Conference, ECAC 98*, (Sweden, 1998).
- [117] U. V. Pedersen, M. Hyde, S. P. Møller, and T. Andersen, *Lifetime Measurement of He- Utilizing an Electrostatic Ion Storage Ring*, *Phys. Rev. A* **64**, 012503 (2001).
- [118] U. V. Pedersen, A. Svendsen, P. Blæsild, and T. Andersen, *Lifetime Measurement of the Metastable Be- Ion Using an Electrostatic Ion Storage Ring*, *J. Phys. B At. Mol. Phys.* **35**, 2811 (2002).
- [119] M. J. Jensen, U. V. Pedersen, and L. H. Andersen, *Stability of the Ground State Vinylidene Anion H₂CC-*, *Phys. Rev. Lett.* **84**, 1128 (2000).
- [120] A. Svendsen, H. Bluhme, M. O. A. E. Ghazaly, K. Seiersen, S. B. Nielsen, and L. H. Andersen, *Tuning the Continuum Ground State Energy of NO₂- by Water Molecules*, *Phys. Rev. Lett.* **94**, 223401 (2005).
- [121] M. O. A. El Ghazaly, A. Svendsen, H. Bluhme, A. B. Nielsen, S. B. Nielsen, and L. H. Andersen, *Electron Scattering on Centrosymmetric Molecular Dianions Pt(CN)₄(2-) and Pt(CN)₆(2-)*, *Phys. Rev. Lett.* **93**, 203201 (2004).
- [122] S. Boyé, S. B. Nielsen, H. Krogh, I. B. Nielsen, U. V. Pedersen, A. F. Bell, X. He, P. J. Tonge, and L. H. Andersen, *Gas-Phase Absorption Properties of DsRed Model Chromophores*, *Phys. Chem. Chem. Phys.* **5**, 3021 (2003).
- [123] L. H. Andersen, H. Bluhme, S. Boyé, T. J. D. Jørgensen, H. Krogh, I. B. Nielsen, S. B. Nielsen, and A. Svendsen, *Experimental Studies of the Photophysics of Gas-Phase Fluorescent Protein Chromophores*, *Phys. Chem. Chem. Phys.* **6**, 2617 (2004).
- [124] S. Boyé, H. Krogh, I. B. Nielsen, S. B. Nielsen, S. U. Pedersen, U. V. Pedersen, L. H. Andersen, A. F. Bell, X. He, and P. J. Tonge, *Vibrationally Resolved Photoabsorption Spectroscopy of Red Fluorescent Protein Chromophore Anions*, *Phys. Rev. Lett.* **90**, 118103 (2003).
- [125] S. B. Nielsen, A. Lapierre, J. U. Andersen, U. V. Pedersen, S. Tomita, and L. H. Andersen, *Absorption Spectrum of the Green Fluorescent Protein Chromophore Anion in Vacuo*, *Phys. Rev. Lett.* **87**, 228102 (2001).
- [126] L. H. Andersen, A. Lapierre, S. B. Nielsen, I. B. Nielsen, S. U. Pedersen, U. V. Pedersen, and S. Tomita, *Chromophores of the Green Fluorescent Protein Studied in the Gas Phase*, *Eur. Phys. J. - At. Mol. Opt. Plasma Phys.* **20**, 597 (2002).
- [127] T. Tanabe, K. Chida, K. Noda, and I. Watanabe, *An Electrostatic Storage Ring for Atomic and Molecular Science*, *Nucl. Instrum. Methods Phys. Res. A* **482**, 595 (2002).
- [128] T. Tanabe, K. Noda, and E. Syresin, *An Electrostatic Storage Ring with a Merging Electron Beam Device at KEK*, *Nucl. Instrum. Methods Phys. Res. Sect. Accel. Spectrometers Detect. Assoc. Equip.* **532**, 105 (2004).
- [129] T. Tanabe, M. Saito, K. Noda, and E. B. Starikov, *Molecular Structure Conversion of Fluorescein Monoanions in an Electrostatic Storage Ring*, *Eur. Phys. J. D* **66**, 163 (2012).
- [130] M. Saito, T. Tanabe, M. Lintuluoto, E. Starikov, K. Noda, T. Majima, S. Tomita, and K. Takahashi, *Photodissociation of Orange I Monoanion Studied Using an Electrostatic Storage Ring*, *J. Phys. Conf. Ser.* **875**, 032035 (2017).
- [131] S. Jinno, T. Takao, Y. Omata, A. Satou, H. Tanuma, T. Azuma, H. Shiromaru, K. Okuno, N. Kobayashi, and I. Watanabe, *TMU Electrostatic Ion Storage Ring Designed for Operation at Liquid Nitrogen Temperature*, *Nucl. Instrum. Methods Phys. Res. A* **532**, 477 (2004).
-

Bibliography

- [132] Y. Ebara, T. Furukawa, J. Matsumoto, H. Tanuma, T. Azuma, H. Shiromaru, and K. Hansen, *Detection of Recurrent Fluorescence Photons*, Phys. Rev. Lett. **117**, 133004 (2016).
- [133] C. Ortéga, R. Brédy, L. Chen, J. Bernard, M. Ji, G. Montagne, A. R. Allouche, A. Cassimi, C. Joblin, and S. Martin, *The Cooling of Naphthalene Cations Studied within an Electrostatic Storage Ring*, J. Phys. Conf. Ser. **583**, 012038 (2015).
- [134] M. Ji, J. Bernard, L. Chen, R. Brédy, C. Ortéga, C. Joblin, A. Cassimi, and S. Martin, *Cooling of Isolated Anthracene Cations Probed with Photons of Different Wavelengths in the Mini-Ring*, J. Chem. Phys. **146**, 044301 (2017).
- [135] J. Bernard, L. Chen, R. Brédy, M. Ji, C. Ortéga, J. Matsumoto, and S. Martin, *Cooling of PAH Cations Studied with an Electrostatic Storage Ring*, Nucl. Instrum. Methods Phys. Res. Sect. B Beam Interact. Mater. At. **408**, 21 (2017).
- [136] S. Martin, J. Matsumoto, N. Kono, M.-C. Ji, R. Brédy, J. Bernard, A. Cassimi, and L. Chen, *Fluorescence Decay of Naphthalene Studied in an Electrostatic Storage Ring, the Mini-Ring*, Nucl. Instrum. Methods Phys. Res. Sect. B Beam Interact. Mater. At. **408**, 209 (2017).
- [137] M. Saito, H. Kubota, K. Yamasa, K. Suzuki, T. Majima, and H. Tsuchida, *Direct Measurement of Recurrent Fluorescence Emission from Naphthalene Ions*, Phys. Rev. A **102**, 012820 (2020).
- [138] M. Gatchell, H. T. Schmidt, R. D. Thomas, S. Rosén, P. Reinhed, P. Löfgren, L. Brännholm, M. Blom, M. Björkhage, E. Bäckström, J. D. Alexander, S. Leontein, D. Hanstorp, H. Zettergren, L. Liljeby, A. Källberg, A. Simonsson, F. Hellberg, S. Mannervik, M. Larsson, W. D. Geppert, K. G. Rensfelt, H. Danared, A. Paál, M. Masuda, P. Halldén, G. Andler, M. H. Stockett, T. Chen, G. Källersjö, J. Weimer, K. Hansen, H. Hartman, and H. Cederquist, *Commissioning of the DESIREE Storage Rings – a New Facility for Cold Ion-Ion Collisions*, J. Phys. Conf. Ser. **488**, 012040 (2014).
- [139] H. T. Schmidt, R. D. Thomas, M. Gatchell, S. Rosén, P. Reinhed, P. Löfgren, L. Brännholm, M. Blom, M. Björkhage, E. Bäckström, J. D. Alexander, S. Leontein, D. Hanstorp, H. Zettergren, L. Liljeby, A. Källberg, A. Simonsson, F. Hellberg, S. Mannervik, M. Larsson, W. D. Geppert, K. G. Rensfelt, H. Danared, A. Paál, M. Masuda, P. Halldén, G. Andler, M. H. Stockett, T. Chen, G. Källersjö, J. Weimer, K. Hansen, H. Hartman, and H. Cederquist, *First Storage of Ion Beams in the Double Electrostatic Ion-Ring Experiment: DESIREE*, Rev. Sci. Instrum. **84**, 055115 (2013).
- [140] E. K. Anderson, A. F. Schmidt-May, N. Pk, G. Eklund, K. C. Chartkunchand, S. Rosén, Å. Larson, K. Hansen, H. Cederquist, H. Zettergren, and H. T. Schmidt, *Spontaneous Electron Emission from Hot Silver Dimer Anions: Breakdown of the Born-Oppenheimer Approximation*, Phys. Rev. Lett. **124**, (2020).
- [141] H. B. Pedersen, A. Svendsen, L. S. Harbo, H. V. Kiefer, H. Kjeldsen, L. Lammich, Y. Toker, and L. H. Andersen, *Characterization of a New Electrostatic Storage Ring for Photofragmentation Experiments*, Rev. Sci. Instrum. **86**, 063107 (2015).
- [142] H. V. Kiefer, E. Gruber, J. Langeland, P. A. Kusochek, A. V. Bochenkova, and L. H. Andersen, *Intrinsic Photoisomerization Dynamics of Protonated Schiff-Base Retinal*, Nat. Commun. **10**, 1 (2019).
- [143] Y. Nakano, Y. Enomoto, T. Masunaga, S. Menk, P. Bertier, and T. Azuma, *Design and Commissioning of the RIKEN Cryogenic Electrostatic Ring (RICE)*, Rev. Sci. Instrum. **88**, 033110 (2017).

Bibliography

- [144] R. Igosawa, N. Kimura, S. Kuma, K. C. Chartkunchand, P. M. Mishra, M. Lindley, T. Yamaguchi, Y. Nakano, T. Azuma, and A. Hirota, *Radiative Cooling Dynamics of Isolated N_2O^+ Ions in a Cryogenic Electrostatic Ion Storage Ring*, Phys. Rev. A **102**, 023119 (2020).
- [145] R. Igosawa, A. Hirota, N. Kimura, S. Kuma, K. C. Chartkunchand, P. M. Mishra, M. Lindley, T. Yamaguchi, Y. Nakano, and T. Azuma, *Photodissociation Spectroscopy of N_2O^+ in the Ion Storage Ring RICE*, J. Chem. Phys. **153**, 184305 (2020).
- [146] M. O. A. El Ghazaly, S. M. Alshammari, C. P. Welsch, and H. H. Alharbi, *Design of a Novel Electrostatic Ion Storage Ring at KACST*, Nucl. Instrum. Methods Phys. Res. A **709**, 76 (2013).
- [147] M. O. A. El Ghazaly, *ELASR- an ELECTROSTATIC Storage Ring in Riyadh for Atomic Collisions*, in Vol. 635 (2015), p. 032098.
- [148] M. O. A. E. Ghazaly, *Design of a Low-Energy Electrostatic Storage Ring under Consideration of 3D Fields*, Microsc. Microanal. **21**, 44 (2015).
- [149] K. E. Stiebing, V. Alexandrov, R. Dörner, S. Enz, N. Yu. Kazarinov, T. Kruppi, A. Schempp, H. Schmidt Böcking, M. Völp, P. Ziel, M. Dworak, and W. Dilfer, *FLSR – The Frankfurt Low Energy Storage Ring*, Nucl. Instrum. Methods Phys. Res. Sect. Accel. Spectrometers Detect. Assoc. Equip. **614**, 10 (2010).
- [150] F. King, T. Kruppi, J. Müller, R. Dörner, L. P. H. Schmidt, H. Schmidt-Böcking, and K. E. Stiebing, *Status of the Frankfurt Low Energy Electrostatic Storage Ring (FLSR)*, Phys. Scr. Vol. T **166**, 014064 (2015).
- [151] J. C. Müller, R. Dörner, F. King, L. P. H. Schmidt, M. S. Schöffler, and K. E. Stiebing, *Measurements of the Kinetic-Energy-Release (KER) of Vibrational Cooled HeH^+ and H_3^+ at the Electrostatic Frankfurt Low Energy Storage Ring (FLSR)*, in Vol. 875 (2017).
- [152] J. C. Müller, R. Dörner, L. P. H. Schmidt, M. S. Schöffler, and K. E. Stiebing, *Kinetic Energy Release (KER) of Vibrationally Cold HeH^+ : Experiments at the Reaction Microscope in the Frankfurt Low-Energy Storage Ring (FLSR)*, in Vol. 1412 (2020).
- [153] O. Forstner, J. Müller, and K. Stiebing, *Opportunities for Negative Ions Studies at the Frankfurt Low-Energy Storage Ring (FLSR)*, Hyperfine Interact. **241**, (2020).
- [154] R. von Hahn, A. Becker, F. Berg, K. Blaum, C. Breitenfeldt, H. Fadil, F. Fellenberger, M. Froese, S. George, J. Göck, M. Grieser, F. Grussie, E. A. Guerin, O. Heber, P. Herwig, J. Karthein, C. Krantz, H. Kreckel, M. Lange, F. Laux, S. Lohmann, S. Menk, C. Meyer, P. M. Mishra, O. Novotný, A. P. O'Connor, D. A. Orlov, M. L. Rappaport, R. Repnow, S. Saurabh, S. Schippers, C. D. Schröter, D. Schwalm, L. Schweikhard, T. Sieber, A. Shornikov, K. Spruck, S. Sunil Kumar, J. Ullrich, X. Urbain, S. Vogel, P. Wilhelm, A. Wolf, and D. Zajfman, *The Cryogenic Storage Ring CSR*, Rev. Sci. Instrum. **87**, 063115 (2016).
- [155] C. Meyer, A. Becker, K. Blaum, C. Breitenfeldt, S. George, J. Göck, M. Grieser, F. Grussie, E. A. Guerin, R. von Hahn, P. Herwig, C. Krantz, H. Kreckel, J. Lion, S. Lohmann, P. M. Mishra, O. Novotný, A. P. O'Connor, R. Repnow, S. Saurabh, D. Schwalm, L. Schweikhard, K. Spruck, S. Sunil Kumar, S. Vogel, and A. Wolf, *Radiative Rotational Lifetimes and State-Resolved Relative Detachment Cross Sections from Photodetachment Thermometry of Molecular Anions in a Cryogenic Storage Ring*, Phys. Rev. Lett. **119**, 023202 (2017).
- [156] H. Kreckel, O. Novotný, and A. Wolf, *Astrochemical Studies at the Cryogenic Storage Ring*, Philos. Trans. R. Soc. Math. Phys. Eng. Sci. **377**, 20180412 (2019).
-

Bibliography

- [157] O. Novotný, P. Wilhelm, D. Paul, Á. Kálosi, S. Saurabh, A. Becker, K. Blaum, S. George, J. Göck, M. Grieser, F. Grussie, R. von Hahn, C. Krantz, H. Kreckel, C. Meyer, P. M. Mishra, D. Muell, F. Nuesslein, D. A. Orlov, M. Rimmler, V. C. Schmidt, A. Shornikov, A. S. Terekhov, S. Vogel, D. Zajfman, and A. Wolf, *Quantum-State-Selective Electron Recombination Studies Suggest Enhanced Abundance of Primordial HeH⁺*, *Science* **365**, 676 (2019).
- [158] J. Matsumoto, R. Saiba, and H. Shiromaru, *Storage Test of a Table-Top Electrostatic Ion Storage Ring (ME-Ring)*, *J. Phys. Conf. Ser.* **875**, 092018 (2017).
- [159] J. Matsumoto, R. Saiba, K. Gouda, E. Makino, K. Hashimoto, K. Fueta, N. Kondo, and H. Shiromaru, *Construction of a Table-Top Ion Storage Ring and Its Application to Cross Section Measurements*, *Nucl. Instrum. Methods Phys. Res. Sect. B Beam Interact. Mater. At.* **454**, 23 (2019).
- [160] C. Welsch, A. Papash, J. Harasimowicz, O. Karamyshev, G. Karamysheva, D. Newton, M. Panniello, M. Putignano, M. Siggel-King, and A. Smirnov, *Beam Life Time Studies and Design Optimization of the Ultra-Low Energy Storage Ring*, *Hyperfine Interact.* **229**, (2014).
- [161] W. H. Benner, *A Gated Electrostatic Ion Trap To Repetitiously Measure the Charge and m/z of Large Electrospray Ions*, *Anal. Chem.* **69**, 4162 (1997).
- [162] M. Lange, M. W. Froese, S. Menk, D. Bing, F. Fellenberger, M. Grieser, F. Laux, D. A. Orlov, R. Repnow, T. Sieber, Y. Toker, R. von Hahn, A. Wolf, and K. Blaum, *Radiative Cooling of Al-4 and Al-5 in a Cryogenic Environment*, *New J. Phys.* **14**, 065007 (2012).
- [163] V. Lepère, B. Lucas, M. Barat, J. A. Fayeton, V. J. Picard, C. Jouvet, P. Carçabal, I. Nielsen, C. Dedonder-Lardeux, G. Grégoire, and A. Fujii, *Comprehensive Characterization of the Photodissociation Pathways of Protonated Tryptophan*, *J. Chem. Phys.* **127**, 134313 (2007).
- [164] P. Micke, S. Kühn, L. Buchauer, J. R. Harries, T. M. Bücking, K. Blaum, A. Cieluch, A. Egl, D. Hollain, S. Kraemer, T. Pfeifer, P. O. Schmidt, R. X. Schüssler, Ch. Schweiger, T. Stöhlker, S. Sturm, R. N. Wolf, S. Bernitt, and J. R. Crespo López-Urrutia, *The Heidelberg Compact Electron Beam Ion Traps*, *Rev. Sci. Instrum.* **89**, 063109 (2018).
- [165] C. R. Calvert, L. Belshaw, M. J. Duffy, O. Kelly, R. B. King, A. G. Smyth, T. J. Kelly, J. T. Costello, D. J. Timson, W. A. Bryan, T. Kierspel, P. Rice, I. C. E. Turcu, C. M. Cacho, E. Springate, I. D. Williams, and J. B. Greenwood, *LIAD-Fs Scheme for Studies of Ultrafast Laser Interactions with Gas Phase Biomolecules*, *Phys. Chem. Chem. Phys.* **14**, 6289 (2012).
- [166] M. Saito, H. Kubota, T. Majima, M. Imai, H. Tsuchida, and Y. Haruyama, *Radiative Lifetime Measurements of Metastable Levels in Kr³⁺ Using Electrostatic Ion Beam Trap*, *X-Ray Spectrom.* **49**, 37 (2020).
- [167] A. Wolf, K. G. Bhushan, I. Ben-Itzhak, N. Altstein, D. Zajfman, O. Heber, and M. L. Rappaport, *Lifetime Measurement of He⁻ Using an Electrostatic Ion Trap*, *Phys. Rev. A* **59**, 267 (1999).
- [168] L. Knoll, K. G. Bhushan, N. Altstein, D. Zajfman, O. Heber, and M. L. Rappaport, *Lifetime Measurement of Be⁻(2s2p² 4P^{3/2}) Using an Electrostatic Ion Trap*, *Phys. Rev. A* **60**, 1710 (1999).
- [169] D. Zajfman, Y. Rudich, I. Sagi, D. Strasser, D. W. Savin, S. Goldberg, M. Rappaport, and O. Heber, *High Resolution Mass Spectrometry Using a Linear Electrostatic Ion Beam Trap*, *Int. J. Mass Spectrom.* **229**, 55 (2003).
-

Bibliography

- [170] O. Heber, P. D. Witte, A. Diner, K. Bhushan, D. Strasser, Y. Toker, M. Rappaport, I. Ben-Itzhak, N. Altstein, D. Schwalm, A. Wolf, and D. Zajfman, *Electrostatic Ion Beam Trap for Electron Collision Studies*, Rev. Sci. Instrum. **76**, 013104 (2004).
- [171] A. Diner, Y. Toker, D. Strasser, O. Heber, I. Ben-Itzhak, P. D. Witte, A. Wolf, D. Schwalm, M. Rappaport, K. Bhushan, and D. Zajfman, *Size-Dependent Electron-Impact Detachment of Internally Cold C_n – and Al_n – Clusters*, Phys. Rev. Lett. **93**, 063402 (2004).
- [172] K. Saha, V. Chandrasekaran, O. Heber, M. A. Iron, M. L. Rappaport, and D. Zajfman, *Ultraslow Isomerization in Photoexcited Gas-Phase Carbon Cluster C₁₀ –*, Nat. Commun. **9**, 1 (2018).
- [173] M. W. Froese, M. Lange, S. Menk, M. Grieser, O. Heber, F. Laux, R. Repnow, T. Sieber, Y. Toker, R. von Hahn, A. Wolf, and K. Blaum, *The Decay of Ion Bunches in the Self-Bunching Mode*, New J. Phys. **14**, 073010 (2012).
- [174] C. Breitenfeldt, K. Blaum, S. George, J. Göck, G. Guzmán-Ramírez, J. Karthein, T. Kolling, M. Lange, S. Menk, C. Meyer, J. Mohrbach, G. Niedner-Schatteburg, D. Schwalm, L. Schweikhard, and A. Wolf, *Long-Term Monitoring of the Internal Energy Distribution of Isolated Cluster Systems*, Phys. Rev. Lett. **120**, 253001 (2018).
- [175] A. Shahi, R. Singh, Y. Ossia, M. L. Rappaport, O. Heber, D. Zajfman, and D. Strasser, *Hybrid Electrostatic Ion Beam Trap (HEIBT): Design and Simulation of Ion-Ion and Ion-Neutral Low-Energy Collisions and Ion-Laser Photoreactions*, J. Phys. Conf. Ser. **1412**, 122028 (2020).
- [176] H. T. Schmidt, H. Cederquist, J. Jensen, and A. Fardi, *Conetrap: A Compact Electrostatic Ion Trap*, Nucl. Instrum. Methods Phys. Res. B **173**, 523 (2001).
- [177] P. Reinhed, A. Orbán, J. Werner, S. Rosén, R. D. Thomas, I. Kashperka, H. A. B. Johansson, D. Misra, L. Brännholm, M. Björkhage, H. Cederquist, and H. T. Schmidt, *Precision Lifetime Measurements of He⁺ in a Cryogenic Electrostatic Ion-Beam Trap*, Phys. Rev. Lett. **103**, 213002 (2009).
- [178] P. Reinhed, A. Orbán, S. Rosén, R. D. Thomas, I. Kashperka, H. A. B. Johansson, D. Misra, A. Fardi, L. Brännholm, M. Björkhage, H. Cederquist, and H. T. Schmidt, *Cryogenic KeV Ion-Beam Storage in ConeTrap—A Tool for Ion-Temperature Control*, Nucl. Instrum. Methods Phys. Res. Sect. Accel. Spectrometers Detect. Assoc. Equip. **621**, 83 (2010).
- [179] C. C. Harper, A. G. Elliott, L. M. Oltrogge, D. F. Savage, and E. R. Williams, *Multiplexed Charge Detection Mass Spectrometry for High-Throughput Single Ion Analysis of Large Molecules*, Anal. Chem. **91**, 7458 (2019).
- [180] G. Herzberg and J. W. T. Spinks, *Atomic Spectra and Atomic Structure* (Courier Corporation, 1944).
- [181] B. H. Bransden, C. J. Joachain, and T. J. Plivier, *Physics of Atoms and Molecules* (Prentice Hall, 2003).
- [182] V. P. Gupta, *Principles and Applications of Quantum Chemistry* (Academic Press, 2015).
- [183] I. N. Levine, *Quantum Chemistry* (Pearson Prentice Hall, 2009).
- [184] A. Szabo and N. S. Ostlund, *Modern Quantum Chemistry: Introduction to Advanced Electronic Structure Theory* (Courier Corporation, 2012).
- [185] W. Demtröder, *Molecular Physics: Theoretical Principles and Experimental Methods* (John Wiley & Sons, 2008).
-

Bibliography

- [186] M. Baer, *Beyond Born-Oppenheimer: Electronic Nonadiabatic Coupling Terms and Conical Intersections* (John Wiley & Sons, 2006).
- [187] E. G. Lewars, *Computational Chemistry: Introduction to the Theory and Applications of Molecular and Quantum Mechanics*, 2. ed (Springer, Dordrecht, 2011).
- [188] I. Mayer, *Simple Theorems, Proofs, and Derivations in Quantum Chemistry* (Springer Science & Business Media, 2003).
- [189] J. Bernard, A. Al-Moogeth, S. Martin, G. Montagne, C. Joblin, L. Dontot, F. Spiegelman, and M. Rapacioli, *Experimental and Theoretical Study of Photo-Dissociation Spectroscopy of Pyrene Dimer Cations Stored in a Compact Electrostatic Ion Storage Ring*, Phys. Chem. Chem. Phys. (2021).
- [190] E. Schrödinger, *An Undulatory Theory of the Mechanics of Atoms and Molecules*, Phys. Rev. **28**, 1049 (1926).
- [191] D. R. Hartree, *The Wave Mechanics of an Atom with a Non-Coulomb Central Field. Part I. Theory and Methods*, Math. Proc. Camb. Philos. Soc. **24**, 89 (1928).
- [192] V. Fock, *Näherungsmethode zur Lösung des quantenmechanischen Mehrkörperproblems*, Z. Für Phys. **61**, 126 (1930).
- [193] Chr. Møller and M. S. Plesset, *Note on an Approximation Treatment for Many-Electron Systems*, Phys. Rev. **46**, 618 (1934).
- [194] C. David Sherrill and H. F. Schaefer, *The Configuration Interaction Method: Advances in Highly Correlated Approaches*, in *Advances in Quantum Chemistry*, edited by P.-O. Löwdin, J. R. Sabin, M. C. Zerner, and E. Brändas, Vol. 34 (Academic Press, 1999), pp. 143–269.
- [195] H.-J. WERNER, *Third-Order Multireference Perturbation Theory The CASPT3 Method*, Mol. Phys. **89**, 645 (1996).
- [196] W. Koch and M. C. Holthausen, *A Chemist's Guide to Density Functional Theory* (John Wiley & Sons, 2015).
- [197] P. Hohenberg and W. Kohn, *Inhomogeneous Electron Gas*, Phys. Rev. **136**, B864 (1964).
- [198] M. Baer, *Beyond Born-Oppenheimer: Electronic Nonadiabatic Coupling Terms and Conical Intersections* (John Wiley & Sons, 2006).
- [199] G. Herzberg and J. W. T. Spinks, *Molecular Spectra and Molecular Structure : Diatomic Molecules* (Van Nostrand, 1950).
- [200] D. Willock, *Molecular Symmetry* (John Wiley & Sons, 2009).
- [201] J. Huh, *Unified Description of Vibronic Transitions with Coherent States*, 2011.
- [202] H. Friha, G. Féraud, T. Pino, P. Parneix, D. Zoubeida, and P. Brechignac, *Electronic Spectra of Cationic PAH and PAH Clusters*, in Vol. 58 (2012).
- [203] H. Friha, *Spectroscopie des transitions électroniques des cations hydrocarbures aromatiques polycycliques et de leurs agrégats*, 2015.
- [204] L. Dontot, N. Suaud, M. Rapacioli, and F. Spiegelman, *An Extended DFTB-CI Model for Charge-Transfer Excited States in Cationic Molecular Clusters: Model Studies versus Ab Initio Calculations in Small PAH Clusters*, Phys. Chem. Chem. Phys. **18**, 3545 (2016).
- [205] R. Schinke, *Photodissociation Dynamics: Spectroscopy and Fragmentation of Small Polyatomic Molecules* (Cambridge University Press, 1995).
-

Bibliography

- [206] O. K. Rice and H. C. Ramsperger, *THEORIES OF UNIMOLECULAR GAS REACTIONS AT LOW PRESSURES*, **49**, 13 (1927).
- [207] L. S. Kassel, *Studies in Homogeneous Gas Reactions. I*, J. Phys. Chem. **32**, 225 (1928).
- [208] R. A. Marcus, *Unimolecular Dissociations and Free Radical Recombination Reactions*, J. Chem. Phys. **20**, 359 (1952).
- [209] H. Haberland, *Clusters of Atoms and Molecules: Theory, Experiment, and Clusters of Atoms* (Springer Science & Business Media, 2013).
- [210] J. U. Andersen, E. Bonderup, and K. Hansen, *On the Concept of Temperature for a Small Isolated System*, J. Chem. Phys. **114**, 6518 (2001).
- [211] A. Leger, L. D'Hendecourt, and D. Defourneau, *Physics of IR Emission by Interstellar PAH Molecules*, Astron. Astrophys. **216**, 148 (1989).
- [212] JI Ming Chao, *Molecular Relaxation Dynamics Of Anthracene Cations Studied In An Electrostatic Storage Ring*, 2015.
- [214] L. D'Hendecourt, A. Léger, P. Boissel, and F. Désert, *Infrared Emission Mechanism in Large Isolated Molecules*, **135**, 207 (1989).
- [216] T. Beyer and D. F. Swinehart, *Algorithm 448: Number of Multiply-Restricted Partitions*, Commun. ACM **16**, 379 (1973).
- [217] J. H. Moon, M. Sun, and M. S. Kim, *Efficient and Reliable Calculation of Rice–Ramsperger–Kassel–Marcus Unimolecular Reaction Rate Constants for Biopolymers: Modification of Beyer–Swinehart Algorithm for Degenerate Vibrations*, J. Am. Soc. Mass Spectrom. **18**, 1063 (2007).
- [218] G. Z. Whitten and B. S. Rabinovitch, *Accurate and Facile Approximation for Vibrational Energy-Level Sums*, J. Chem. Phys. **38**, 2466 (1963).
- [219] S. Stein and B. Rabinovitch, *Accurate Evaluation of Internal Energy Level Sums and Densities Including Anharmonic Oscillators and Hindered Rotors*, (1973).
- [220] C. P. Welsch, J. Ullrich, and C. Glaßner, *Electrostatic Ring as the Central Machine of the Frankfurt Ion Storage Experiments*, 7 (2004).
- [221] R. Geller, *Electron Cyclotron Resonance Ion Sources and ECR Plasmas* (CRC Press, 1996).
- [222] R. Geller, *ECRIS: The Electron Cyclotron Resonance Ion Sources*, Annu. Rev. Nucl. Part. Sci. **40**, 15 (1990).
- [223] S. Iida, S. Kuma, J. Matsumoto, T. Furukawa, H. Tanuma, T. Azuma, H. Shiromaru, V. Zhaunerchyk, and K. Hansen, *Rotationally Resolved Excitation Spectra Measured by Slow Electron Detachment from Si²⁻*, (2020).
- [224] E. Gruber, M. Strauss, H. Wegner, and L. Andersen, *Action-Spectroscopy Studies of Positively Charge-Tagged Azobenzene in Solution and in the Gas-Phase*, J. Chem. Phys. **150**, 084303 (2019).
- [225] C. Ortega, *Dynamique de refroidissement du cation naphthalène dans un anneau de stockage électrostatique*, 2015.
- [226] R. Geller, *Electron Cyclotron Resonance Multiply Charged Ion Sources*, IEEE Trans. Nucl. Sci. **23**, 904 (1976).
- [227] C. Lyneis, D. Leitner, M. Leitner, C. Taylor, and S. Abbott, *The Third Generation Superconducting 28 GHz Electron Cyclotron Resonance Ion Source VENUS (Invited)a*, Rev. Sci. Instrum. **81**, 02A201 (2010).
-

Bibliography

- [228] D. Hitz, A. Girard, K. Serebrennikov, G. Melin, D. Cormier, J. M. Mathonnet, J. Chartier, L. Sun, J. P. Briand, and M. Benhachoum, *Production of Highly Charged Ion Beams with the Grenoble Test Electron Cyclotron Resonance Ion Source (Plenary)*, Rev. Sci. Instrum. **75**, 1403 (2004).
- [229] P. Sortais, P. Attal, M. Bisch, M. Bourgarel, P. Leherissier, and J. Pacquet, *Ecris Development at GANIL*, Rev. Sci. Instrum. **61**, 288 (1990).
- [230] Z. Xie and C. Lyneis, *Production of High Charge State Ions with the Advanced Electron Cyclotron Resonance Ion Source at LBNL*, Rev. Sci. Instrum. **67**, 886 (1996).
- [231] D. Hitz, F. Bourg, M. Delaunay, P. Ludwig, G. Melin, M. Pontonnier, and T. NGuyen, *The New 1.2 T–14.5 GHz Caprice Source of Multicharged Ions: Results with Metallic Elements*, Rev. Sci. Instrum. **67**, 883 (1996).
- [232] C. Lyneis, D. Leitner, S. Abbott, R. Dwinell, M. Leitner, C. Silver, and C. Taylor, *Results with the Superconducting Electron Cyclotron Resonance Ion Source VENUS (Invited)*, Rev. Sci. Instrum. **75**, 1389 (2004).
- [233] H. Zhao, L. Sun, J. W. Guo, W. Zhang, W. Lu, W. Wu, B. Wu, G. Sabbi, M. Juchno, R. Hafalia, E. Ravaioli, and D. Xie, *Superconducting ECR Ion Source: From 24-28 GHz SECRAL to 45 GHz Fourth Generation ECR*, Rev. Sci. Instrum. **89**, 052301 (2018).
- [234] Y. Higurashi, J. Ohnishi, K. Ozeki, M. Kidera, and T. Nakagawa, *Recent Development of RIKEN 28 GHz Superconducting Electron Cyclotron Resonance Ion Source*, Rev. Sci. Instrum. **85**, 02A953 (2014).
- [235] P. A. Zavodszky, B. Arend, D. Cole, J. DeKamp, G. Machicoane, F. Marti, P. Miller, J. Moskalik, W. Nurnberger, J. Ottarson, J. Vincent, X. Wu, and A. Zeller, *Design, Construction and Commissioning of the SuSI ECR*, in (2007), pp. 3766–3770.
- [236] L. Sun, H. W. Zhao, W. Lu, J. W. Guo, Y. Yang, H. Jia, L. Lu, and W. Wu, *Review of Highly Charged Ion Production with ECR Ion Source and the Future Opportunities for HCI Physics*, X-Ray Spectrom. **49**, 47 (2020).
- [237] I. G. Brown, *The Physics and Technology of Ion Sources* (John Wiley & Sons, 2006).
- [238] M. M. Abdelrahman, *Factors Enhancing Production of Multicharged Ion Sources and Their Applications*, Sci. Technol. **2**, 98 (2012).
- [239] B. L. Peko and T. M. Stephen, *Absolute Detection Efficiencies of Low Energy H, H⁻, H⁺, H₂⁺ and H₃⁺ Incident on a Multichannel Plate Detector*, Nucl. Instrum. Methods Phys. Res. Sect. B Beam Interact. Mater. At. **171**, 597 (2000).
- [240] N. Takahashi, Y. Adachi, M. Saito, and Y. Haruyama, *Absolute Detection Efficiencies for KeV Energy Atoms Incident on a Microchannel Plate Detector*, Nucl. Instrum. Methods Phys. Res. Sect. B Beam Interact. Mater. At. **315**, 51 (2013).
- [241] M. Ji, R. Brédy, L. Chen, J. Bernard, B. Concina, G. Montagne, A. Cassimi, and S. Martin, *Time Evolution of the Internal Energy Distribution of Singly Charged Anthracene in a Storage Ring*, Phys. Scr. Vol. T **2013**, 4091 (2013).
- [242] S. Martin, J. Matsumoto, N. Kono, M.-C. Ji, R. Brédy, J. Bernard, A. Cassimi, and L. Chen, *Fluorescence Decay of Naphthalene Studied in an Electrostatic Storage Ring, the Mini-Ring*, Nucl. Instrum. Methods Phys. Res. Sect. B Beam Interact. Mater. At. **408**, 209 (2017).
- [243] M. Ji, R. Brédy, L. Chen, J. Bernard, B. Concina, G. Montagne, A. Cassimi, and S. Martin, *Time Evolution of the Internal Energy Distribution of Singly Charged Anthracene in a Storage Ring*, Phys. Scr. **2013**, 014091 (2013).
-

Bibliography

- [244] R. D. Thomas, H. T. Schmidt, G. Andler, M. Björkhage, M. Blom, L. Brännholm, E. Bäckström, H. Danared, S. Das, N. Haag, P. Halldén, F. Hellberg, A. I. S. Holm, H. A. B. Johansson, A. Källberg, G. Källersjö, M. Larsson, S. Leontein, L. Liljeby, P. Löfgren, B. Malm, S. Mannervik, M. Masuda, D. Misra, A. Orbán, A. Paál, P. Reinhed, K.-G. Rensfelt, S. Rosén, K. Schmidt, F. Seitz, A. Simonsson, J. Weimer, H. Zettergren, and H. Cederquist, *The Double Electrostatic Ion Ring Experiment: A Unique Cryogenic Electrostatic Storage Ring for Merged Ion-Beams Studies*, Rev. Sci. Instrum. **82**, 065112 (2011).
- [245] R. D. Thomas, H. T. Schmidt, M. Gatchell, S. Rosén, P. Reinhed, P. Löfgren, L. Brännholm, M. Blom, M. Björkhage, E. Bäckström, J. D. Alexander, S. Leontein, D. Hanstorp, H. Zettergren, M. Kaminska, R. Nascimento, L. Liljeby, A. Källberg, A. Simonsson, F. Hellberg, S. Mannervik, M. Larsson, W. D. Geppert, K. G. Rensfelt, A. Paál, M. Masuda, P. Halldén, G. Andler, M. H. Stockett, T. Chen, G. Källersjö, J. Weimer, K. Hansen, H. Hartman, and H. Cederquist, *DESIREE: Physics with Cold Stored Ion Beams*, in Vol. 84 (2015), p. 01004.
- [246] *DESIREE: The Double ElectroStatic Ion Ring ExpERiment*, <https://www.desiree-infrastructure.com>.
- [247] G. Eklund, Experiments on Mutual Neutralization Using Storage Rings with Merged Ion Beams, Department of Physics, Stockholm University, 2020.
- [248] B. Badger and B. Brocklehurst, *Absorption Spectra of Dimer Cations. Part 3. Naphthalene and Anthracene Derivatives and Pyrene*, Trans. Faraday Soc. **65**, (1969).
- [249] T. Shida and W. H. Hamill, *Molecular Ions in Radiation Chemistry. III. Absorption Spectra of Aromatic-Hydrocarbon Cations and Anions in Organic Glasses*, J. Chem. Phys. **44**, 4372 (1966).
- [250] A. Kira and M. Imamura, *Absorption Spectra of Dimer Cations and Other Cationic Species Produced by Warming of γ -Irradiated Glassy Solutions of Aromatic Hydrocarbons*, J Phys Chem **83**, (1979).
- [251] A. Kira, M. Imamura, and T. Shida, *Spectroscopic Study on Aggregate Ion Radicals of Naphthalene and Pyrene in γ -Irradiated Alkane Glasses*, J Phys Chem **80**, (1976).
- [252] H. Saigusa and E. Lim, *Photochemistry of Naphthalene Cluster Ions (C₁₀H₈)ⁿ⁺, n = 2-7: Formation of C₁₁H₉⁺ Ion via Intervalence Band Excitation*, J. Am. Chem. Soc. - J AM CHEM SOC **117**, (1995).
- [253] Y. Inokuchi, M. Matsumoto, K. Ohashi, and N. Nishi, *Charge Resonance and Charge Transfer Interactions in Naphthalene Homo- and Hetero-Dimers*, in (State College, Pennsylvania (USA), 1997), pp. 231–236.
- [254] Y. Inokuchi and N. Nishi, *Photodissociation Spectroscopy of Benzene Cluster Ions in Ultraviolet and Infrared Regions: Static and Dynamic Behavior of Positive Charge in Cluster Ions*, J. Chem. Phys. **114**, 7059 (2001).
- [255] K. Ohashi and N. Nishi, *Photodissociation Dynamics of (C₆H₆)₃⁺: Role of the Extra Benzene Molecule Weakly Bound to the Dimer Core*, J. Chem. Phys. **109**, 3971 (1998).
- [256] C. Joblin, L. Dontot, G. A. Garcia, F. Spiegelman, M. Rapacioli, L. Nahon, P. Parneix, T. Pino, and P. Bréchnignac, *Size Effect in the Ionization Energy of PAH Clusters*, J. Phys. Chem. Lett. **8**, 3697 (2017).
- [257] S. Zamith, J.-M. L'Hermite, L. Dontot, L. Zheng, M. Rapacioli, F. Spiegelman, and C. Joblin, *Threshold Collision Induced Dissociation of Pyrene Cluster Cations*, J. Chem. Phys. **153**, 054311 (2020).
-

Bibliography

- [258] I. Braud, S. Zamith, and J.-M. L'Hermite, *A Gas Aggregation Source for the Production of Heterogeneous Molecular Clusters*, Rev. Sci. Instrum. **88**, 043102 (2017).
- [259] C. Ortega, N. Kono, M. Ji, R. Brédy, J. Bernard, C. Joblin, A. Cassimi, Y. Ngonoravache, L. Chen, and S. Martin, *Dissociation Rate, Fluorescence and Infrared Radiative Cooling Rates of Naphthalene Studied in Electrostatic Storage Miniring*, in Vol. 635 (2015), p. 032051.
- [260] Brandi West, Priv. Commun. (2019).
- [261] P. Brechignac and T. Pino, *Electronic Spectra of Cold Gas Phase PAH Cations: Towards the Identification of the Diffuse Interstellar Bands Carriers*, Astron. Astrophys. **343**, L49 (1999).
- [262] B. Badger and B. Brocklehurst, *Absorption Spectra of Dimer Cations. Part 4.—Theoretical Considerations and Dimer Structure*, Trans Faraday Soc **66**, 2939 (1970).
- [263] M. Meot-Ner, *Dimer Cations of Polycyclic Aromatics. Experimental Bonding Energies and Resonance Stabilization*, J. Phys. Chem. **84**, 2724 (1980).
- [264] T. Fujiwara and E. C. Lim, *Binding Energies of the Neutral and Ionic Clusters of Naphthalene in Their Ground Electronic States*, J. Phys. Chem. A **107**, 4381 (2003).
- [265] B. Bouvier, V. Brenner, P. Millie, and J.-M. Soudan, *A Model Potential Approach to Charge Resonance Phenomena in Aromatic Cluster Ions*, J. Phys. Chem. A **106**, (2002).
- [266] T. Beitz, R. Laudien, H.-G. Löhmannsröben, and B. Kallies, *Ion Mobility Spectrometric Investigation of Aromatic Cations in the Gas Phase*, J. Phys. Chem. A **110**, 3514 (2006).
- [267] T. N. Das, *Monomer and Dimer Radical Cations of Benzene, Toluene, and Naphthalene*, J. Phys. Chem. A **113**, 6489 (2009).
- [268] X. Cai, S. Tojo, M. Fujitsuka, and T. Majima, *Photodissociation of Naphthalene Dimer Radical Cation during the Two-Color Two-Laser Flash Photolysis and Pulse Radiolysis—Laser Flash Photolysis*, J. Phys. Chem. A **110**, 9319 (2006).
- [269] B. BADGER and B. BROCKLEHURST, *Formation of Dimer Cations of Aromatic Hydrocarbons*, Nature **219**, (1968).
- [270] T. Fujiwara and E. C. Lim, *Binding Energies of the Neutral and Ionic Clusters of Naphthalene in Their Ground Electronic States*, J. Phys. Chem. A **107**, 4381 (2003).
- [271] K. Müller-Dethlefs and P. Hobza, *Noncovalent Interactions: A Challenge for Experiment and Theory*, Chem. Rev. **100**, 143 (2000).
- [272] P. A. Pieniasek, A. I. Krylov, and S. E. Bradforth, *Electronic Structure of the Benzene Dimer Cation*, J. Chem. Phys. **127**, 044317 (2007).
- [273] K. Ohashi and N. Nishi, *Photodissociation Spectroscopy of Benzene Cluster Ions: (C₆H₆)⁺ + 2 and (C₆H₆)⁺ + 3*, J. Chem. Phys. **95**, 4002 (1991).
- [274] K. Ohashi, Y. Inokuchi, and N. Nishi, *Pump-Probe Photodepletion Spectroscopy of (C₆H₆)₂²⁺. Identification of Spectrum in the Charge Resonance Band Region*, Chem. Phys. Lett. **263**, 167 (1996).
- [275] K. Ohashi and N. Nishi, *Photodepletion Spectroscopy on Charge Resonance Band of Benzene Clusters (C₆H₆)₂²⁺ and (C₆H₆)₃³⁺*, J. Phys. Chem. **96**, 2931 (1992).
- [276] K. Ohashi, Y. Nakai, T. Shibata, and N. Nishi, *Photodissociation Spectroscopy of (C₆H₆)₂ PLU*, Laser Chem. **14**, 3 (1994).
- [277] B. Badger and B. Brocklehurst, *Absorption Spectra of Dimer Cations. Part 2.—Benzene Derivatives*, Trans. Faraday Soc. **65**, 2582 (1969).
-

Bibliography

- [278] E. Miyoshi, T. Ichikawa, T. Sumi, Y. Sakai, and N. Shida, *Ab Initio CASSCF and MRSDCI Calculations of the (C₆H₆)²⁺ Radical*, Chem. Phys. Lett. **275**, 404 (1997).
- [279] H. Krause, B. Ernstberger, and H. J. Neusser, *Binding Energies of Small Benzene Clusters*, Chem. Phys. Lett. **184**, 411 (1991).
- [280] J. R. Grover, E. A. Walters, and E. T. Hui, *Dissociation Energies of the Benzene Dimer and Dimer Cation*, J. Phys. Chem. **91**, 3233 (1987).
- [281] K. Hiraoka, S. Fujimaki, K. Aruga, and S. Yamabe, *Stability and Structure of Benzene Dimer Cation (C₆H₆)⁺₂ in the Gas Phase*, J. Chem. Phys. **95**, 8413 (1991).
- [282] K. Hiraoka, S. Fujimaki, K. Aruga, and S. Yamabe, *Stability and Structure of Benzene Dimer Cation (C₆H₆)⁺₂ in the Gas Phase*, J. Chem. Phys. **95**, 8413 (1991).
- [283] J. Bernard, A. Al-Mogeeth, A.-R. Allouche, L. Chen, G. Montagne, and S. Martin, *Photo-Dissociation of Naphthalene Dimer Cations Stored in a Compact Electrostatic Ion Storage Ring*, J. Chem. Phys. **150**, 054303 (2019).
- [284] S. Grimme, J. Antony, S. Ehrlich, and H. Krieg, *A Consistent and Accurate Ab Initio Parametrization of Density Functional Dispersion Correction (DFT-D) for the 94 Elements H-Pu*, J. Chem. Phys. **132**, 154104 (2010).
- [285] J. Tao, J. P. Perdew, V. N. Staroverov, and G. E. Scuseria, *Climbing the Density Functional Ladder: Nonempirical Meta--Generalized Gradient Approximation Designed for Molecules and Solids*, Phys. Rev. Lett. **91**, 146401 (2003).
- [286] S. Grimme, S. Ehrlich, and L. Goerigk, *Effect of the Damping Function in Dispersion Corrected Density Functional Theory*, J. Comput. Chem. **32**, 1456 (2011).
- [287] F. Negri and M. Z. Zgierski, *On the Vibronic Structure of the Absorption Spectra of Radical Cations of Some Polycyclic Aromatic Hydrocarbons*, J. Chem. Phys. **100**, 1387 (1994).
- [288] S. Hirata, M. Head-Gordon, J. Szczepanski, and M. Vala, *Time-Dependent Density Functional Study of the Electronic Excited States of Polycyclic Aromatic Hydrocarbon Radical Ions*, J. Phys. Chem. A **107**, 4940 (2003).
- [289] M. Vala, J. Szczepanski, F. Pauzat, O. Parisel, D. Talbi, and Y. Ellinger, *Electronic and Vibrational Spectra Of Matrix-Isolated Pyrene Radical Cations: Theoretical and Experimental Aspects*, J. Phys. Chem. **98**, 9187 (1994).
- [290] J. Szczepanski, M. Vala, D. Talbi, O. Parisel, and Y. Ellinger, *Electronic and Vibrational Spectra of Matrix Isolated Anthracene Radical Cations: Experimental and Theoretical Aspects*, J. Chem. Phys. **98**, 4494 (1993).
- [291] Z. H. Khan, *Electronic Spectra of Radical Cations and Their Correlation with Photoelectron Spectra—V. Pyrenes*, Spectrochim. Acta Part Mol. Spectrosc. **45**, 253 (1989).
- [292] F. Salama, C. Joblin, and L. J. Allamandola, *Neutral and Ionized PAHs: Contribution to the Interstellar Extinction*, Planet. Space Sci. **43**, 1165 (1995).